

UNIVERSITY OF BIRMINGHAM

LUMINESCENT IRIDIUM(III) COMPLEXES AS SOLUTION-BASED AND SURFACE-ACTIVE PROBES FOR OPTICAL DETECTION OF ANALYTES

Andrew James Carrod

A thesis submitted to the University of Birmingham for the degree of

Doctor of Philosophy

School of Chemistry, October 2020

UNIVERSITY OF
BIRMINGHAM

University of Birmingham Research Archive

e-theses repository

This unpublished thesis/dissertation is copyright of the author and/or third parties. The intellectual property rights of the author or third parties in respect of this work are as defined by The Copyright Designs and Patents Act 1988 or as modified by any successor legislation.

Any use made of information contained in this thesis/dissertation must be in accordance with that legislation and must be properly acknowledged. Further distribution or reproduction in any format is prohibited without the permission of the copyright holder.

Abstract

The development of luminescent Ir(III) complexes for application in small analyte sensing is of great interest in the scientific community. Iridium cyclometalated complexes provide ideal sensing probes with photo- and electro- chemical characteristics which are sensitive to changes in the local environment.

Consequently, we have designed and synthesised a series of cyclometalated iridium complexes based upon the archetypal $[Ir(ppy)_2bpy]^+$ compound (ppy = 2-phenylpyridine, bpy = 2,2'-bipyridine). This complex is emissive, at λ_{max} = 602 nm with a quantum yield of 14 % in deaerated acetonitrile. Previous studies have determined that bpy is the chromophoric ligand, and the lowest energy triplet states are mixed metal-ligand charge transfer (MLCT) and ligand-ligand charge transfer (LLCT) states.

We synthetically modify 2-phenylpyridine and 2,2'-bipyridine ligands to create analogues with desired functionality. Through synthesis of novel Ir(III) complexes based on these ppy and bpy analogues we incorporate desired functionality into a luminescent metal complex.

In our first approach a boronic acid moiety was appended to the 2-phenylpyridine ligands of the metal complexes, in either the 3- or 4- position of the phenyl ring. Boronic acid groups are widely reported as fluorescent chemosensors for saccharides; of which glucose is the most relevant to human physiology. Glucose concentration in the blood of patients is a good measure of the successful control and treatment of diabetes. Photophysical properties of the two novel iridium complexes **Ir-4-BOH** and **Ir-3-BOH** were investigated in deaerated acetonitrile to compared with the $[Ir(ppy)_2bpy]^+$ complex. We found both complexes were emissive with λ_{max} = 610 nm and 594 nm, for **Ir-4-BOH** and **Ir-3-BOH** respectively, with quantum yields of 12 and 8 %. We subsequently investigate the saccharide binding ability of the synthesised Ir(III)

complexes in aqueous solutions at physiological pH. We utilise the dual photoluminescence and electrochemiluminescence response permitted by the use of the transition metal core to report on the binding event, and to allow a readout of the saccharide concentration. A 70 % maximum decrease in photoluminescence intensity and 90 % maximum decrease in electrochemiluminescence intensity for the **Ir-4-BOH** upon addition of fructose demonstrates that the emission intensity of the complexes is highly susceptible to the binding of saccharide. Formation of the boronic ester is probed by ^{11}B and ^{19}F nuclear magnetic resonance spectroscopy, and mass spectrometry. We have equally incorporated the **Ir-4-BOH** into hydrogel devices, which are shown to be non-toxic, stable, and have potential as wearable devices for the monitoring of saccharide concentration in interstitial fluid. This is the first report of the use of a transition metal complex with dual photoluminescence and electrochemiluminescent response to saccharide binding, and the first report of a functional saccharide sensing device based on a transition metal complex.

To extend the approach of analyte detection with Ir(III) complexes to functional devices, we report the formation of iridium transition metal probes containing a previously reported 2,2'-bipyridine ligand (**bpySS**) with a lipoic acid moiety for specific attachment to gold surfaces. The synthesised complexes **IrC6bpySS** and **IrC12bpySS** are also modified with hexyl or dodecyl hydrophobic chains respectively, this chain is incorporated on each of the 2-phenylpyridine ligands at the 2- position of the phenyl ring (C6 = 2-(2-hexylphenyl)pyridine and C12 = 2-(2-hexylphenyl)pyridine). The photophysical properties of the metal complexes are investigated in degassed acetonitrile where both have the same emission maxima, λ_{max} = 606 nm, and show relatively small quantum yields of 3 % and 5 % for **IrC6bpySS** and **IrC12bpySS** respectively. Luminescent lifetimes of 210 and 260 ns are measured for **IrC6bpySS** and **IrC12bpySS** under the same conditions. The C6 containing compound has been previously synthesised and attached to gold nanoparticles for cell imaging and we expand

on the use of hydrophobic metal complexes through attachment to planar and patterned gold surfaces. Select physical and chemical properties of the transition metal decorated gold surfaces are reported; with the surface morphology and chemistry probed through atomic force microscopy and X-ray photoelectron spectroscopy. Contact angle is used to probe the hydrophobicity of the surfaces, and sequentially increased hydrophobicity of the decorated gold surfaces is observed with increasing alkyl chain length. We propose that the hydrophobic nature of the iridium probes inferred by the alkyl chain on the cyclometalating ligand lends itself to the sensing of hydrophobic molecules, one analyte of interest is the persistent organic pollutant perfluorooctanoic acid. This pollutant is an environmental contaminant widely monitored by liquid chromatography-mass spectrometry, due to its known hepatotoxic and carcinogenic properties. The design of the iridium complex incorporates gold binding ligands with sufficient height to minimise quenching of the luminescence by the gold surface meaning luminescence studies may be undertaken using the photoluminescence signal of the Ir(III) complex. We assess the ability of the devices to sense fluorosurfactant concentrations through monitoring of the luminescence lifetime of the Ir(III) complex and observe augmentation of the lifetime at high fluorosurfactant concentrations. To improve the efficiency of sensing we detail attachment of the Zonyl FSA fluorosurfactant, and characterise these surfaces by time of flight secondary ion mass spectrometry. It is reasoned fluorine-fluorine interactions between Zonyl and the analyte will aid in the adsorption of the analyte. We observe high sensitivity and can report significant changes in the luminescence lifetime (710 to 860 ns) upon additions of pM concentrations of analyte rivalling reported electrochemical techniques. The sample preparation time is greatly reduced from the gold standard HPLC methods currently employed. This is the first report of a transition metal complex-based device for optical sensing of the environmental pollutant perfluorooctanoic acid and will provide a solid foundation for further optimisation of the binding event.

Acknowledgements

The author would like to thank all people over the last 4 years, who have started any sentence with “You should include……”; until fearful of the extra chapters, one had to stop advertising that this thesis was in progress.

I would like to thank my supervisor, Professor Zoe Pikramenou and my second supervisor, Dr Haider Butt. Their support and guidance over the past few years has been a great motivator and has facilitated the enjoyable passing of 4 years in research.

Tribute must be paid to the members of the ZP group, they have past and present left an indelible impression. In no particular order I thank; Patrícia Gírio, Zhilin Guo, Menisha Manhota, Elena del Giorgio, Jamie Bradley, Luke Watson, Sarah Akponasa, Irene Theophilou, and Sajni Haria. To the wider postgraduate community at the School of Chemistry, a big thanks, it is just a shame there are too many people to reasonably list.

Thanks are given to the School of Chemistry at the University of Birmingham, the RSC and to BAM (Bundesanstalt für materialforschung und -Prüfung) for funding throughout my postgraduate career.

I would like to acknowledge the analytical facility in the school of chemistry, Chi Tsang and Peter Ashton for their help with MS; Cecile Le Duff for help with NMR; and Louise Male for help with crystallography. In the School of Mechanical Engineering, University of Birmingham, thanks are given to Peter Simpson, and Muhammad Elsherif for their help with the hydrogels and laser ablation equipment. At the Institute of Inflammation and Ageing, University of Birmingham, thanks is given to Prof. Zubair Ahmed who carried out the cell studies with the hydrogels.

To our collaborators at Swansea University, Paolo Bertoncello and Francesco Graglia, a thanks for all their help and input on electrochemiluminescence and cyclic voltammetry.

We thank the members of the BAM teams that aided in the collection of data. Francesca Bennet, Dan Hodoroaba and Oded Sobol.

My friends outside of university, without the support of whom I would have been far less jolly: Ben Humphrey; Julie Jackson; Ashley Henderson; Jon Ford, Morgan Pearce, Ben Liu, and Adam Leckenby. Thank you to my family, they have no idea what I do but offer their full support nonetheless: John Carrod, Michelle Carrod and David Carrod.

Contents

Abstract II

Acknowledgements V

Abbreviations XI

1 Introduction 1

1.1 Overview of the photophysical properties of Ir(III) cyclometalated complexes 1

1.2 Electrochemiluminescence properties of Ir(III) cyclometalated complexes 4

1.3 Sensors 5

1.3.1 Sensing by luminescence with Ir(III) complexes with structure $[Ir(C\hat{}N)_2(N\hat{}N)]^+$ ... 6

1.3.2 Sensing by electrochemistry with Ir(III) complexes with structure $[Ir(C\hat{}N)_2(N\hat{}N)]^+$ 13

1.4 Our Work 18

1.5 References 20

2 Photoluminescent and Electrochemical Sensing of Sugars at Physiological pH via an iridium(III) Complex Bearing Directly Boronated Ligands. 25

2.1 Introduction 25

2.1.1 General Remarks on saccharide importance and chemical sensing 25

2.1.2 NMR sensors for saccharides 28

2.1.3 Electrochemical sensors for saccharides 30

2.1.4 Archetypal examples of boronic acid sensors for fluorescent sensing of saccharides 36

2.1.5 Recent examples of boronic acid sensors for fluorescent sensing of saccharides in solution 38

2.1.6 Boronic acid containing transition metal-based sensors of saccharides by luminescence 45

2.1.7 Luminescent hydrogel-based saccharide sensors 48

2.1.8 Our aims 52

2.2 Results and discussion 55

2.2.1 Synthesis and characterisation of boronic acid containing compounds 55

2.2.2 Photophysical properties of Ir(III) complexes 59

2.2.3 Sugar sensing by photophysical effects in solution 63

2.2.4 Binding Constants for Ir(III) complexes with glucose and fructose 68

2.2.5 Characterisation of the boronic ester complex 70

2.2.6 Electrochemical properties and saccharide sensing of Ir-4-BOH 75

2.2.7 Saccharide sensing via hydrogel device incorporating Ir-4-BOH 78

2.2.8 Stability and toxicity of Ir(III) implanted hydrogels 81

2.3 Conclusion 83

2.4 References 84

3 Sensing of Environmentally Harmful Fluorosurfactant *via* Luminescent Lifetime Augmentation of a Cyclometalated Ir(III) Complex in Solution and Immobilised on Gold... 93

3.1 Introduction 93

3.1.1 General remarks on surfaces, SAMs and their patterning 93

3.1.2 Organic and mixed organic/inorganic SAMs as sensors by fluorescence 97

3.1.3 SAMs of Ru(II) and Ir(III) transition metal complexes 101

3.1.4 General comments on perfluorooctanoic acid toxicity and monitoring.....117

3.1.5 PFOA detection by fluorometric methods 121

3.1.6 Our Aims.....125

3.2 Results and Discussion 126

3.2.1 Synthesis and characterisation of ligands and Ir(III) complexes 126

3.2.2 Photophysical Properties of metal complexes in solution.....131

3.2.3 Sensing of fluorosurfactants in solution.....134

3.2.4 Immobilisation of IrC6bpySS and IrC12bpySS on planar and patterned surfaces .137

3.2.5 Photoluminescence properties of Ir(III) complexes immobilised on Au surfaces ..141

3.2.6 Sensing of PFOA using Ir(III) complex coated gold surfaces 144

3.2.7 Sensing of PFOA using Ir(III) complex coated gold surfaces co-coated with Zonyl FSA 146

3.2.8 Investigation of the Zonyl FSA mediated enhancement of PFOA detection.....147

3.2.9 Quantitative determination of the surface composition of IrC6bpySS.Au.Z and IrC12bpySS.Au.Z devices 148

3.3 Conclusions.....151

3.4 References.....153

4 General conclusions and future work 161

5 Appendix.....A

5.1 Experimental and Supplementary Information for Chapter 2: Photoluminescent and Electrochemical Sensing of Sugars at Physiological pH via an iridium(III) Complex Bearing Directly Boronated Ligands. ..... A

5.1.1 Experimental ..... A

5.1.2 Supplementary Information L

5.2 Experimental and Supplementary Information for Chapter 3: Sensing of Environmentally Harmful Fluorosurfactant via Luminescent Lifetime Augmentation of a Cyclometalated Ir(III) Complex in Solution and Immobilised on Gold. ..... Z

5.2.1 Experimental ..... Z

5.2.2 Supplementary information ..... KK

5.3 Conferences Attended III

5.4 Publications III

Abbreviations

^{13}C NMR	Carbon Nuclear Magnetic Resonance
^{1}H NMR	Proton Nuclear Magnetic Resonance
bpy	2,2'-bipyridine
COSY	Correlation Spectroscopy
DCM	Dichloromethane
DMF	Dimethyl Formaldehyde
DMSO	Dimethyl Sulfoxide
EDC	1-Ethyl-3-(3-dimethylaminopropyl)carbodiimide
HMBC	Heteronuclear multiple-bond correlation spectroscopy
HOMO	Highest Occupied Molecular Orbital
HSQC	Heteronuclear single-quantum correlation spectroscopy
IC	Internal conversion
IR	Infrared Spectroscopy
ISC	Intersystem crossing
LC	Ligand Centre Transfer
LUMO	Lowest Unoccupied Molecular Orbital

MALDI	Matrix assisted laser desorption ionisation
MeCN	Acetonitrile
MeOH	Methanol
MLCT	Metal to Ligand Charge Transfer
MS	Mass Spectrometry
NOESY	Nuclear Overhauser Effect Spectroscopy
OLED	Organic Light Emitting Diode
PDT	Photodynamic Therapy
PET	Photoinduced Electron Transfer
PFOA	perfluorooctanoic acid
PMT	Photomultiplier tube
ppy	2-phenylpyridine
SMBG	Self-Monitored Blood Glucose
SPR	Surface Plasmon Resonance
TFA	Trifluoroacetic Acid
THF	Tetrahydrofuran
TOF	Time of flight

UCNP	Upconverting Nanoparticle
UV	Ultraviolet
Vis	Visible Spectrum
XPS	X-ray photoelectron spectroscopy
ε	Molar Absorptivity
λ_{max}	Wavelength with Maximum Intensity
τ	Luminescence lifetime
Φ	Luminescence quantum Yield

1 Introduction

Iridium, a metal originally thought to be useless due to its inert nature,[1] has become a widely used metal centre for the fabrication of luminescent compounds. Iridium(III) cyclometalated complexes are a class of compound that has found use in areas spanning organic light-emitting diodes (OLEDs),[2-4] singlet oxygen sensitisers (often for PDT),[5, 6] imaging agents,[7-9] and photocatalysts.[10-12] They exhibit this diversity of application due to their efficient phosphorescence, emission colour tunability and high thermal and photostability.[13] Modification of the ligands surrounding the metal core are determinate of the photophysical and chemical properties, and iridium complexes may be cationic, anionic, or neutral dependant on this design.[14] These complexes also display relatively long lived lifetimes (in the order of hundreds of nanoseconds to microseconds) at room temperature with emission approaching the red region of the electromagnetic spectrum for the archetypal $[Ir(ppy)(bpy)]^+$ complex.[4] Thus, with all the properties that are listed we are motivated to investigate the use of Ir(III) complexes for sensing purposes, in applications where a sensitive, red emissive and long-lived phosphorescent reporter will provide advantages over organic molecules that are investigated for the same purpose. In this chapter focus will be placed on examples of Ir(III) cationic complexes applied to small molecule sensing,[15-19] in particular using their attractive photophysical and electrochemical properties to generate sensitive luminescent reporter compounds.

1.1 Overview of the photophysical properties of Ir(III) cyclometalated complexes

This section will focus on the photophysical processes observed in the archetypal $[Ir(C\hat{}N)_2(N\hat{}N)]^+$ complexes where C^N denotes a ligand bound through both a carbon and nitrogen to the metal centre (e.g. 2-phenylpyridine) and N^N denotes a diimine ligand (often an analogue of a 2,2'-bipyridine ligand). The simplest and arguable most well studied example

is $[Ir(ppy)_2(bpy)]^+$ (ppy = 2-phenylpyridine, and bpy = 2,2'-bipyridine). These heteroleptic, d^6 complexes display strong spin orbit coupling. The 5d-orbitals of the Ir(III) ion in these complexes are split into the t_{2g} (d_{xy}, d_{xz}, and d_{yz}) and e_g (d_{z2} and d_{y2}) orbitals allowing for an octahedral splitting energy Δ_o which is determined by oxidation state, atomic number, and ligand field strength. The molecular orbitals of the metal complex can be assigned depending on which ligand they lie, and electronic transitions are named in accordance. In general, transitions are labelled as ligand centred (LC), ligand to ligand charge transfer (LLCT), metal to ligand charge transfer (MLCT), ligand to metal charge transfer (LMCT), or metal centred (MC). The different transitions are shown in Figure 1.1 below. In the $[Ir(C\hat{}N)_2(N\hat{}N)]^+$ there is not one dominant transition and often a mixture of MLCT and LLCT character is observed, allowing for electronic transitions over a broad energy range. In some cases direct excitation to the triplet manifold denoted as ^{3}MLCT is observed, though spin forbidden transitions of this kind are characteristically weaker, still must be considered a further boon to the utility of Ir(III) complexes.[14, 20]

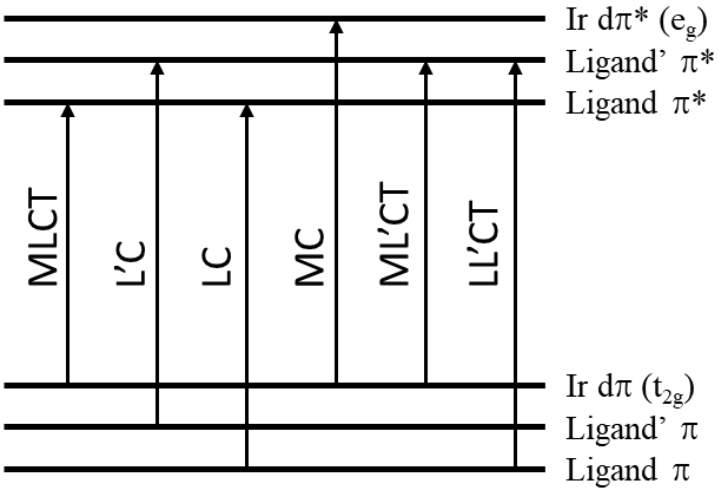


Figure 1.1: Electronic energy level diagram for an $[Ir(C\hat{}N)_2(N\hat{}N)]^+$ type complex: where Ligand (C^N) is 2'-phenylpyridine, Ligand' (N^N) is 2,2'-bipyridine, MC is metal centered, LC or L'C is ligand centered, and LL'CT is ligand to ligand charge transfers (in the direction of C^N to N^N) and MLCT or ML'CT are metal to ligand charge transfers, onto both the phenylpyridine and bipyridine ligands respectively.

The intersystem crossing facilitated by the Ir(III) core allows access to triplet excited states, with the intersystem crossing occurring on a timescale of 100 fs, faster than the fluorescence

processes possible from the singlet manifold. With the large ligand field splitting of the metal d* orbitals the accessible MC triplet excited states are limited and the non-radiative transitions from these excited states to the ground state are reduced, further helping to increase phosphorescence quantum yields. Generally accepted emission pathways of the $[Ir(C\hat{}N)_2(N\hat{}N)]^+$ complexes are summarised in Figure 1.2.[21, 22]

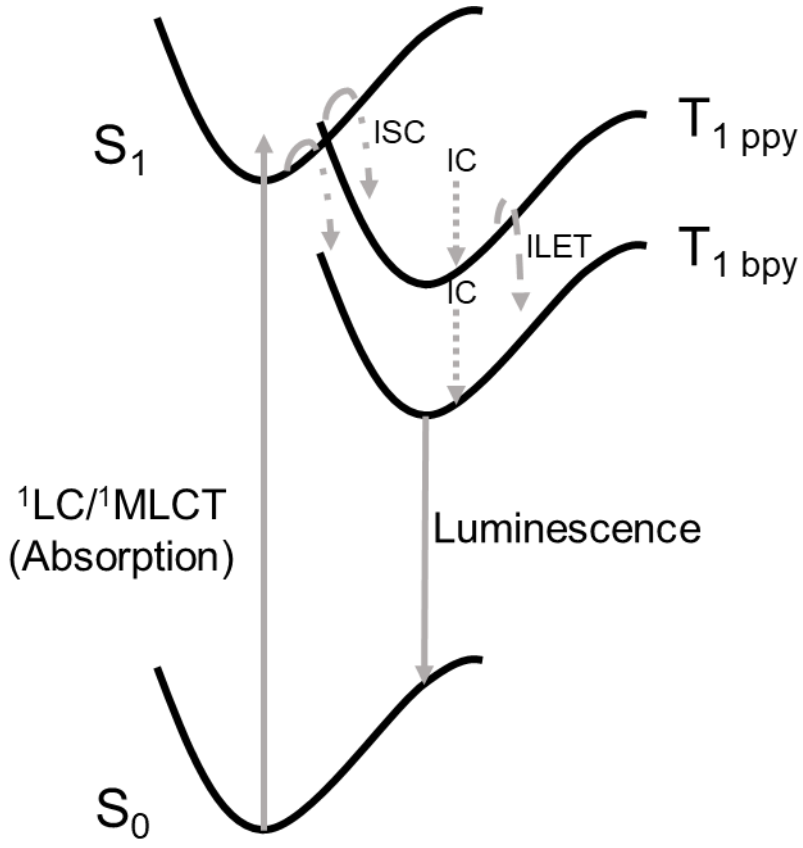


Figure 1.2: Energy level diagram showing common excitation and emission pathways for the $[Ir(C\hat{}N)_2(N\hat{}N)]^+$ archetypal complex.

Utilising Ir(III) cyclometalated complexes then allows for distinct chemical and photophysical properties such as versatile ligand design, thermal stability, photostability, modulation of the position of the excited state, high Φ_p, long-lived and tuneable luminescence lifetimes, as well as large Stokes shifts.

1.2 Electrochemiluminescence properties of Ir(III) cyclometalated complexes

The electrogenerated luminescence (ECL) of *fac*-$Ir(ppy)_3$ complex has been well explored.[23, 24] There are in essence two routes proposed for the ECL generation in *fac*-$Ir(ppy)_3$ dependent on the presence of a so called co-reactant, a sacrificial electron donor or acceptor. The first is the annihilation method in which the luminophore is concurrently oxidised and reduced forming both the cationic and anionic species at the same electrode. The mechanism and equations for this reaction type can be found below in Equation 1-3.

$$Ir(ppy)_3 + e^- \rightarrow Ir(ppy)_3^- \quad (1)$$

$$Ir(ppy)_3 - e^- \rightarrow Ir(ppy)_3^+ \quad (2)$$

$$Ir(ppy)_3^+ + Ir(ppy)_3^- \rightarrow {}^3*Ir(ppy)_3 + Ir(ppy)_3 \quad (3)$$

The second reaction type in the production of ECL in *fac*-$Ir(ppy)_3$ relies on the presence of a sacrificial reagent (N.B. this is often referred to as a co-reactant), and the reaction proceeds via the mechanism shown in Equation 4-7, where 5' indicates a secondary possible simultaneous reaction to lead to the same reaction products as in Equation 5.

$$Ir(ppy)_3 - e^- \rightarrow Ir(ppy)_3^{+\bullet} \quad (4)$$

$$TPA - e^- \rightarrow TPA^{+\bullet} \quad (5)$$

$$Ir(ppy)_3^{+\bullet} + TPA \rightarrow Ir(ppy)_3 + TPA^{+\bullet} \quad (5')$$

$$TPA^{+\bullet} \rightarrow TPA^{\bullet} + H^+ \quad (6)$$

$$Ir(ppy)_3^{+\bullet} + TPA^{\bullet} \rightarrow {}^3*Ir(ppy)_3 + TPA' \text{ (side product)} \quad (7)$$

The first examples of the practical use of the incredibly interesting electrochemiluminescence properties of *fac*-Ir(ppy)$_3$ were described in relation to OLED devices, which were described first in solid state,[25, 26] and later in solution.[27]

In 2005 Kim *et al.* reported the first ECL study of $[Ir(ppy)_2(bpy)]^+$ to determine the mechanism and efficiency of ECL. The complex is assumed to follow similar electron transfer pathways as *fac*-Ir(ppy)$_3$ albeit somewhat more efficiently in presence of a co-reactant.[28] After this study, many groups realised the utility of these cationic Ir(III) complexes as sensors for a variety of small molecules in challenging conditions and matrices.

Selected published examples of the $[Ir(C\hat{}N)_2(N\hat{}N)]^+$ complex type as ECL sensors will be covered in a later section.

1.3 Sensors

Sensors may be generally defined as any compound or device that allows a measurable signal transduction in response to a stimulus, and chemosensing is but one of the areas of focus within this broader field. Many reviews have focussed on the ever-expanding topic of chemosensing, and many focus on supramolecular sensing by fluorescence,[29-34] which is often described as a host-guest system in which reversible binding or interaction of a target substrate with the host molecule facilitates a signal modulation measurable by one or several desired techniques.[35] Supramolecular sensing and self-assembly has been applied to a variety of analytes and with correct chemical modulation of the host molecule this method of detection is extremely versatile.

A visual representation of the host-guest interaction is given in Figure 1.3.

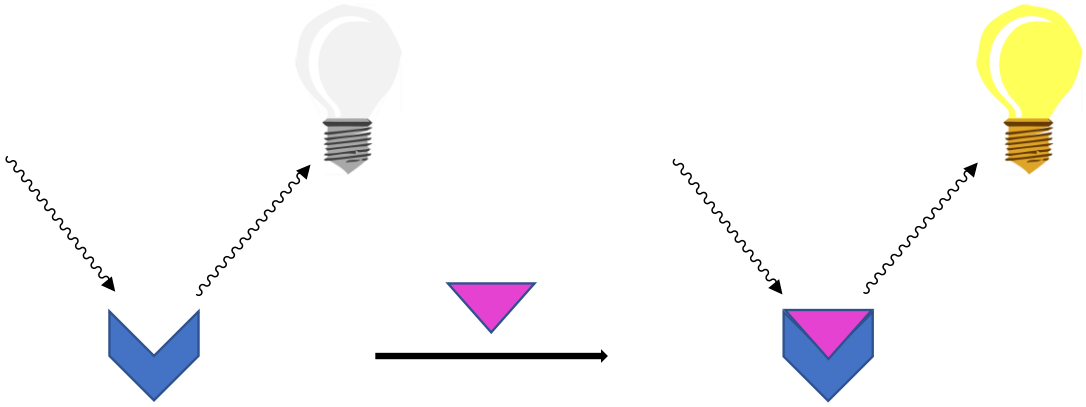


Figure 1.3: Schematic representation of Host-Guest interaction in which the host is represented by the blue chevron and the guest by the pink triangle. Arrows represent the signal in/out, which may be envisaged as the signal arising from, UV-vis, fluorescence, NMR, ITC or any technique in which direct measurement of change to the Host is possible.

1.3.1 Sensing by luminescence with Ir(III) complexes with structure $[Ir(C\hat{}N)_2(N\hat{}N)]^+$

Luminescence techniques are arguably some of the most sensitive optical methods for sensing. Generally, spectra can be obtained quickly and efficiently at low concentration with no need for a reference beam, as the background in luminescence measurements is theoretically zero assuming complete dark and a perfect detector. Spectra may often be obtained at low concentrations, as low as nM with observable changes upon analyte addition, giving a stark advantage over UV-Vis measurements wherein only small percentage changes can be observed at low concentrations due to the high subtraction needed from the reference beam. The limiting factor in both techniques is often therefore the optics sensitivity. In this regard fluorescence single photon counting has the advantage over subtraction from the reference used in UV-Vis.[36]

Using luminescence techniques also allows for samples to be analysed for response in the solid state, which is far easier than analysing solid state samples by transmission or reflectance

measurements, which are inherently difficult especially on solid substrates with high reflectivity.

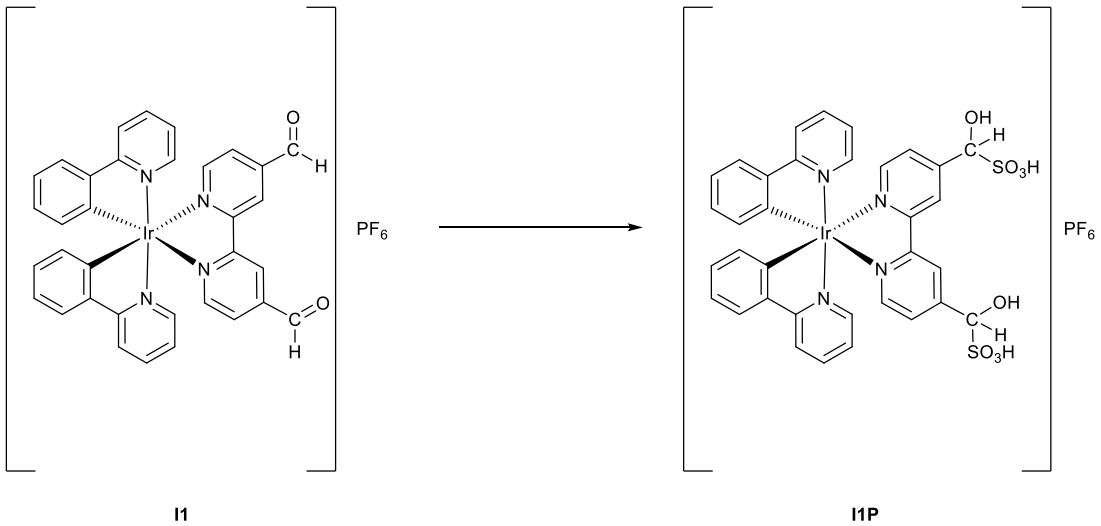
Whilst luminescent techniques have advantages over other solution-based detection methods, the choice of chromophore is important, and application dependent, one may consider that the requirements of an OLED and a biological imaging reagents will be fairly different. In relation to molecular sensors, organic fluorophores have been popular in the field of sensing, owing to their high molar absorptivities, high quantum yields, and synthetically facile access to varied scaffolds.

Upon considering the photophysical properties of the $[Ir(C\hat{}N)_2(N\hat{}N)]^+$ explained in section 1.1, it becomes clear why transition metal complexes are attractive agents in the field of chemosensing. Transition metal complex-based chemosensors of this type are generally accessible with relative ease through conventional synthetic techniques. Owing to the highly ligand dependent nature of the photophysical properties, modification can lead to surprisingly advantageous effects. Moreover, compared to the short-lived fluorescent emission of conventional organic dyes which is generally below 10 nanoseconds;[37] the luminescence lifetime of Ir(III) complexes often lies in the tens or hundreds of nanoseconds even in unfavourable conditions (aerated samples, aqueous solvents), if not in the microsecond range. This luminescence is often distinguishable from so called "autofluorescence" observed from either scattering, or other molecules within the matrix of the sample. Commonly this is achieved by use of time-resolved emission spectroscopy.[38, 39] Additionally, with their sizable Stokes shifts, transition metal complex-based luminescent sensors circumvent the issue of self-quenching,[40] and can penetrate tissue samples to a higher depth based upon how far into the red or near-IR the emission stretches. Finally, metal complexes can be synthesised to show

high luminescent quantum yields and sensitivity towards variation of the local environment, making them ideal scaffolds for developing luminescent chemosensors.[17, 18]

To demonstrate these principles, some select recent examples of chemosensors based upon luminescence detection by an Ir(III) complex with structure $[Ir(C\hat{}N)_2(N\hat{}N)]^+$ are detailed below.

In a 2017 study by Ma *et al*. a bisulfite reactive Ir(III) complex **I1** (Figure 1.4) was synthesised from 4,4'-dicarboxaldehyde-2,2'-bipyridine and the well-known $[Ir(ppy)_2Cl]_2$ dimer. The aldehyde group will react with bisulfite to form an adduct with differing MLCT state. The emission intensity of the luminescent complex was measured in MeCN:H_2O (9:1 v/v) with increasing concentrations of HSO_3^- through the range 0-30 μM. Good linear relationship between $[HSO_3]$ and emission intensity was found between 0-10 μM, after which plateau was reached with a maximum 4-fold intensity increase. *In vivo* luminescence imaging in zebra fish shows no detectable emission signal from **I1** until the samples are incubated with 200 μM of HSO_3^-.[41]



I1 **I1P**

Figure 1.4: Ir(III) complex **I1** bearing bisulfite reactive ketone groups on the side of the molecule, the presence of these groups allows for a "light up" detection of $[HSO_3^-]$ via transformation to product **I1P**

The same group later used a similar methodology to test for periodate concentration in aqueous solution. An iridium(III) complex **I2** was synthesised with an ancillary phenanthroline ligand bearing a methylthio group, which is oxidised to the methylsulfinyl group by periodate anions through a known mechanism with intermediate and product **I3** and **I4** (Figure 1.5).[42] The oxidation of the thiol group leads to a shift of the HOMO from the phenyl to the sulfoxide thus a reduction in the emission intensity with increasing [IO_4^-]. Linearity of the emission intensity reduction of the Ir(III) complex in PBS vs. [IO_4^-] across 0-1.5 μM was found, furthermore plateau of the emission intensity reduction was found at ~100 μM. *In vitro* luminescence imaging serves to highlight how reductions in intensity can be observed through microscopy when cells are incubated with increasing [IO_4^-].[43]

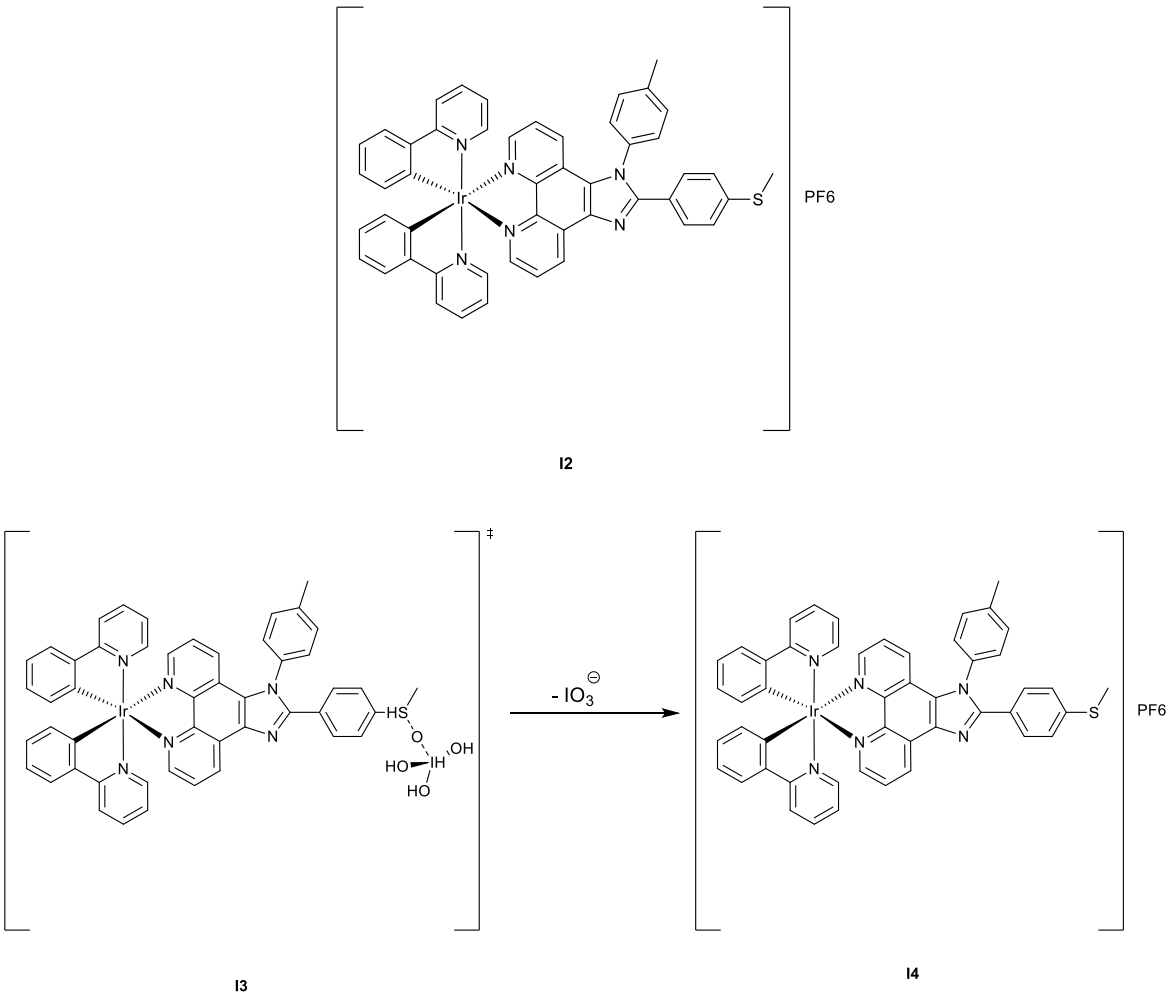
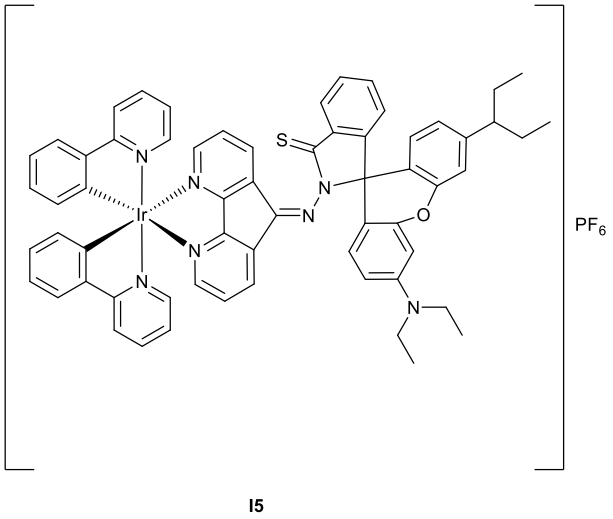


Figure 1.5: Structures of the synthesised iridium complex (**I2**) and reaction intermediate (**I3**) and product (**I4**) upon IO_4^- addition

Wang *et al*. describe the selective detection Hg^{2+} ions utilising chelation by ancillary ligands of an Ir(III) complex **I5** (Figure 1.6).[44] The addition of 1 eq. Hg^{2+} ions to a solution of **I5** at a concentration of 10 μM in DMF:PBS (4:96, pH 7.4) induced large changes to the UV-Visible spectrum in the region 500-600 nm. The changes were assigned to the formation of a π-conjugated system in the ancillary ligand brought about by chelation of Hg^{2+}. Linear relationships were deduced between increases in the emission intensity at 587 nm (λ_{exc} = 530 nm) when measured across a 0.1-1 eq. range. The authors suggest a detection limit for Hg^{2+} of 8 x 10^{-8} M and a working pH range of 7-8 in aqueous solution, clearly denoting the usefulness of this complex in environmental Hg^{2+} sensing.

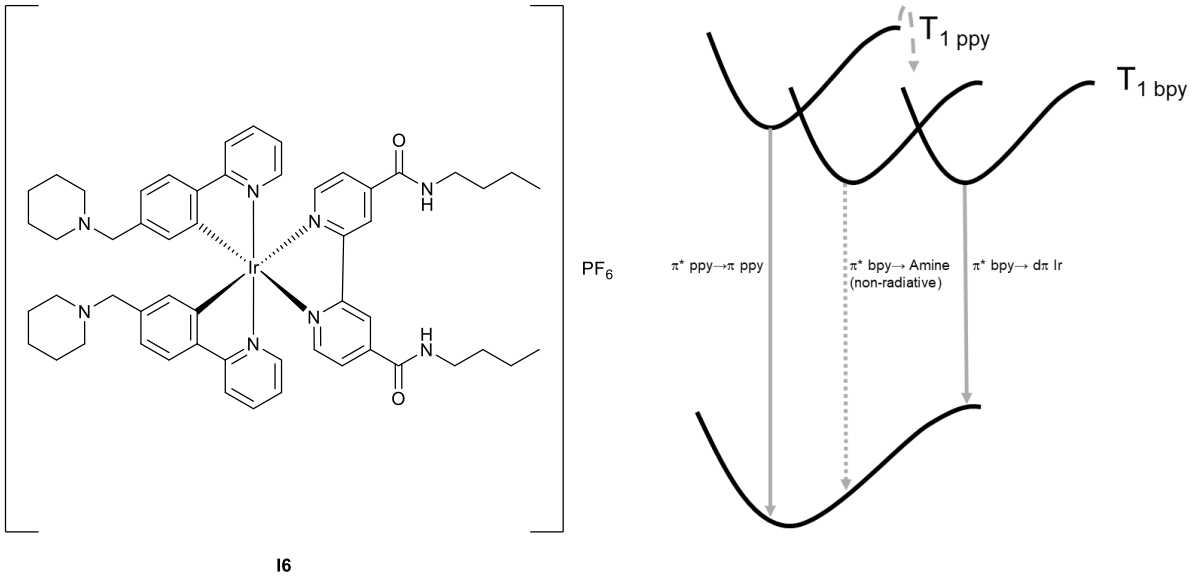


I5

Figure 1.6: Structure of **I5** synthesised by Wang et al. for the purposes of selective Hg^{2+} sensing, chelation occurs between the imine and the thioketone, to form a polycycle

Lo *et al*. detailed a new class of dual emissive Ir(III) complexes for sensing based upon dual emission several years ago,[45, 46] with two possible emissive states. The existence of both low and high energy emission features is due to a separation and interruption of charge transfer between excited states by a third non-emissive state (Figure 1.7). Emission intensity ratios of the high and low energy features can be controlled by modifying polarity, viscosity and presence of biomolecules. Utilising their understanding of the earlier findings, Lo *et al*. in 2018 used a particularly successful Ir(III) complex **I6** (Figure 1.7) for oxygen sensing through from

hypoxia to hyperoxia.[47] By again manipulating the efficiency of internal conversion between the two emissive states, this time by increasing the oxygen content of the sample, changes to both luminescent lifetime and emission intensity/ratio are clearly observed when the Ir(III) complex is irradiated in aqueous buffer solution. The authors note this is the first single molecular probe suitable for sensing across the hypoxic to hyperoxic range.

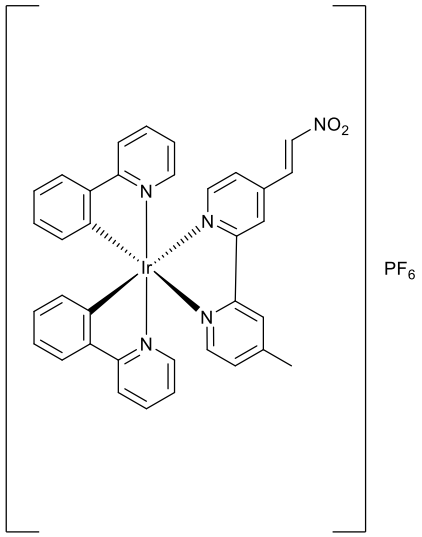


I6

Figure 1.7: Structure of the Ir(III) complex used by Lo *et al.* in Ref. 45. (left) Along with the proposed energy diagram which demonstrates the interruption of the internal conversion process and emission from the lowest lying transition by a non-radiative quenching process between the LUMO and the methylpiperidine moiety attached to the ppy ligand (right)

Yuan *et al*. demonstrated a long-lifetime turn-on luminescence sensor for cysteine, mediated by the reaction of the cysteine with the nitroalkene group substituted onto the 2,2'-bipyridine ligand of Ir(III) complex **I7** (Figure 1.8).[48] The specific interaction induces changes to the location of the LUMO, which moves from localisation on the vinyl group to the 2,2'-bipyridine after reaction with cysteine. This change in LUMO energy "turns on" the luminescence, and allows for readout of a concentration of cysteine. Owing to the relatively long luminescent lifetimes ~100 ns; time-gated luminescence images are taken of the iridium(III) complex incubated in MCF-7 cells. Delaying the capture of a luminescence image by 12 ns affords an

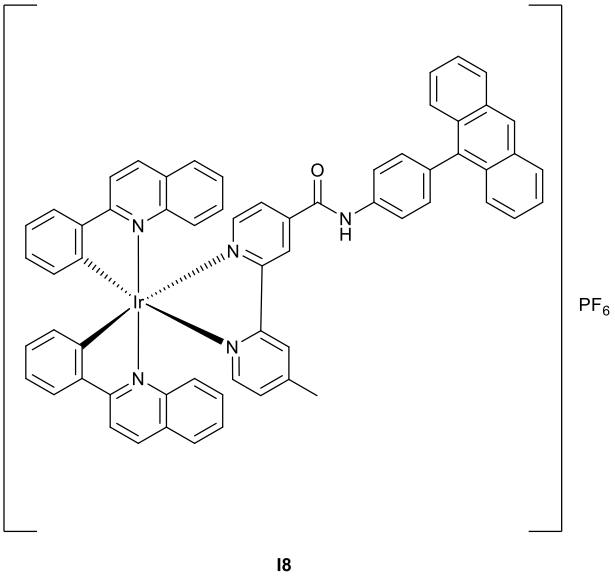
impressive signal to noise ratio of ~1.6 compared to 0.6 at 0 ns delay. The utility of this probe in challenging bio-imaging applications further highlights Ir(III) complex versatility.



I7

Figure 1.8: cysteine reactive iridium(III) complex **I7** bearing the nitroalkene group on the 4-position on the 2,2'-bipyridine ligand. Synthesised by Yuan *et al.*

An anthracene-Ir(III) conjugate **I8** (Figure 1.9) was developed for detection of singlet oxygen by Zhao *et al.*,[15] with a turn on effect upon oxidation of the anthracene moiety. The complex has extremely low quantum yield of <0.1 % due to the highly effective quenching by a photoinduced electron transfer in the direction Ir(III) to anthracene. The electron transfer mechanism is turned off upon singlet oxygen addition on the anthracene, a well-known reaction and photobleaching mechanism;[49] thus leading to a 20-fold emission signal intensity enhancement arising from the Ir(III) complex. The complexes were tested for cellular toxicity and below 10 μM were found to be not toxic. Cell localisation studies revealed the complex was localised in the mitochondria, and irradiation of the cells across 40 mins revealed a light up effect of the complex, which matched with the result of known ROS reporter DCFH-DA.



I8

Figure 1.9: Structure of the anthracene-Ir(III) complex synthesised by Zhao *et al.*, the effective photoinduced electron transfer between the Ir(III) core and the anthracene moiety, can be halted by reaction of the anthracene with singlet oxygen.

1.3.2 Sensing by electrochemistry with Ir(III) complexes with structure $[Ir(C\hat{}N)_2(N\hat{}N)]^+$

ECL based sensors for diagnostic applications have gained some traction in recent years. Traditional steady state fluorophores require a carefully chosen excitation source and emission detection pathway that can limit their application in samples with large "autofluorescence" backgrounds (see discussion above). Conversely, ECL sensors do not require excitation by this method, and as such many background effects can be limited or negated entirely. Modulation of the output signal by control of the potential allows for high accuracy, reproducibility, and simplicity of experimental design.[50] Often ruthenium(II) complexes are employed in sensing assays due to the well understood mechanisms and documented efficiency, with the first report of the ECL of $[Ru(bpy)_3]^{2+}$ from Tokel and Bard appearing as early as 1972.[51] ECL reviews have particularly focussed on the large number of these Ru(II) polypyridyl complexes.[52-55] Over 90 % of all iridium(III) complexes for luminescence applications have been reported since 2000, with this late bloom in the refining and understanding of the photophysics of these

complexes, it is unsurprising that there is an equally late bloom in the interest towards their application to ECL sensing.[56]

There are now many examples of ECL based sensing via Ir(III) complexes in the scientific literature, and this section will detail a small number of complexes with structure $[Ir(C\hat{}N)_2(N\hat{}N)]^+$ from recent literature to give an overview of the field.

In 2010 an ECL assay for barium cations (Ba^{2+}) was developed, with the ECL active complexes being Ir(III) complexes (**I9**-**I11**, Figure 1.10) appended with crown-ethers,[57] in a similar manner as was previously reported for ruthenium(II) analogues developed by the same group.[58] Upon increasing the concentration of barium cations in solutions of the **I10** in MeCN, the ECL intensity increases whilst simultaneously displaying bathochromic shifts which are not observed in the analogous Ru(II) complex. Through DFT calculations the authors suggest that placing the cation recognition site on the ligand where the LUMO is localised (phenanthroline) will stabilise the LUMO, and lead to the red shift in emission.

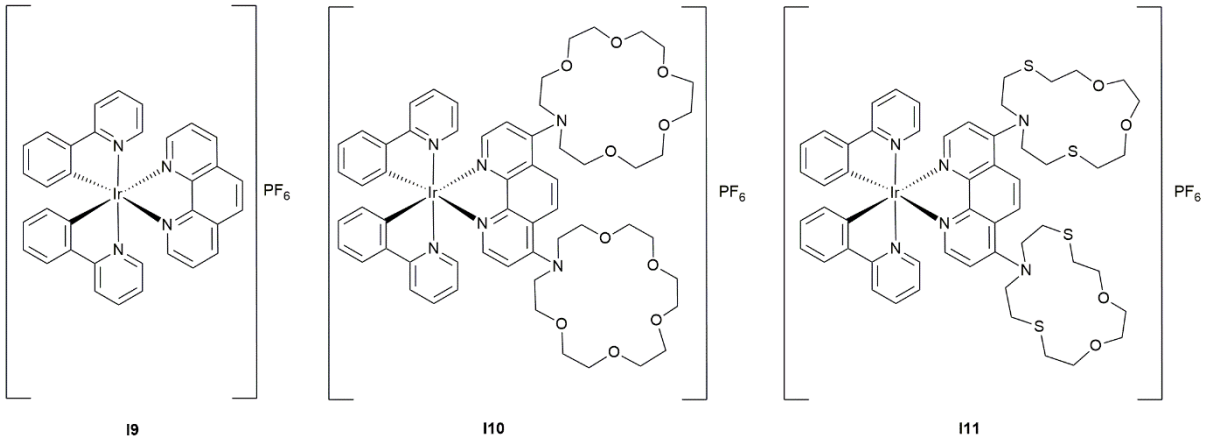


Figure 1.10: Structures of the crown ether appended Ir(III) complexes synthesised by Schmittel *et al.* for the purposes of selective Ba^{2+} sensing by ECL

In another example, increasing target DNA concentrations were reported by the ECL intensity increase of complex **I12** immobilised on a gold nanoparticle carrier.[59] A gold electrode was primed with capture-DNA, and placed in an aqueous solution of sensor-DNA coated nanocarrier (AuNP). The AuNP's show low ECL intensity as they are unbound at this point. On addition of the target-DNA the ECL intensity increases, the increases are proportional to the concentration of target-DNA as the target DNA binds concurrently to the capture- and sensor-DNA (Figure 1.11). The authors suggest this assay may be applied to clinical testing and were able to show 200-fold higher sensitivity than in a ruthenium(II) analogue.

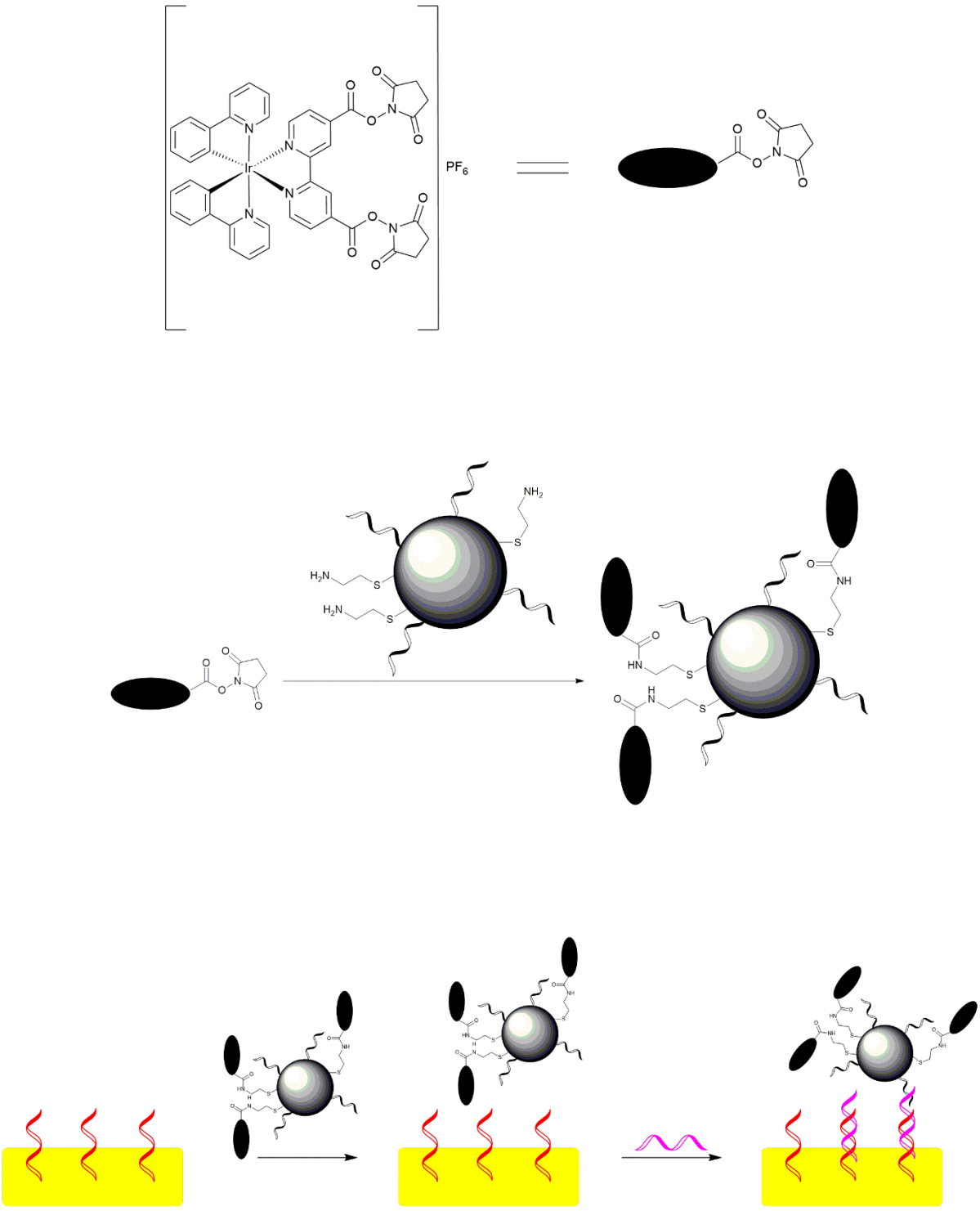


Figure 1.11: The structure of the NHS ester **I12** synthesised in the work of Zhang *et al.* (top). The synthesis of the final gold nanoparticles, by mixing of **I12** with nanoparticles in solution. Nanoparticles are represented with grey spheres coated with cysteamine and sensor DNA represented by black strand. (middle). Assay to evaluate target DNA concentration via immobilisation and therefore ECL intensity increase of the active iridium complex. The capture DNA and target DNA are represented in red and pink respectively. (bottom)

In a 2018 paper, ECL arising from both Ir(III) and Ru(II) complexes was used as the readout method in an immunoassay. Three different ECL active luminophores (**I13-I15**, Figure 1.12) were synthesised and used. The differing oxidation potentials of these complexes allows for selective 'switching on' of the ECL. To create an immunoassay, polymer beads were loaded with the luminophore of interest, before tagging with the antibody of interest. Potential dependent outputs are observed in the immunoassay, with the oxidation potential of each complex sufficiently different to allow for specific ECL signal, with specific wavelength associated (see Figure 1.12 for oxidation potential, and emission wavelength of each complex). Through measuring the emission at set oxidation potentials allows for identification of a positive response for selected antigens. The authors once again highlight the potential use of an Ir(III) complex for application in a rapid clinical diagnoses.[60]

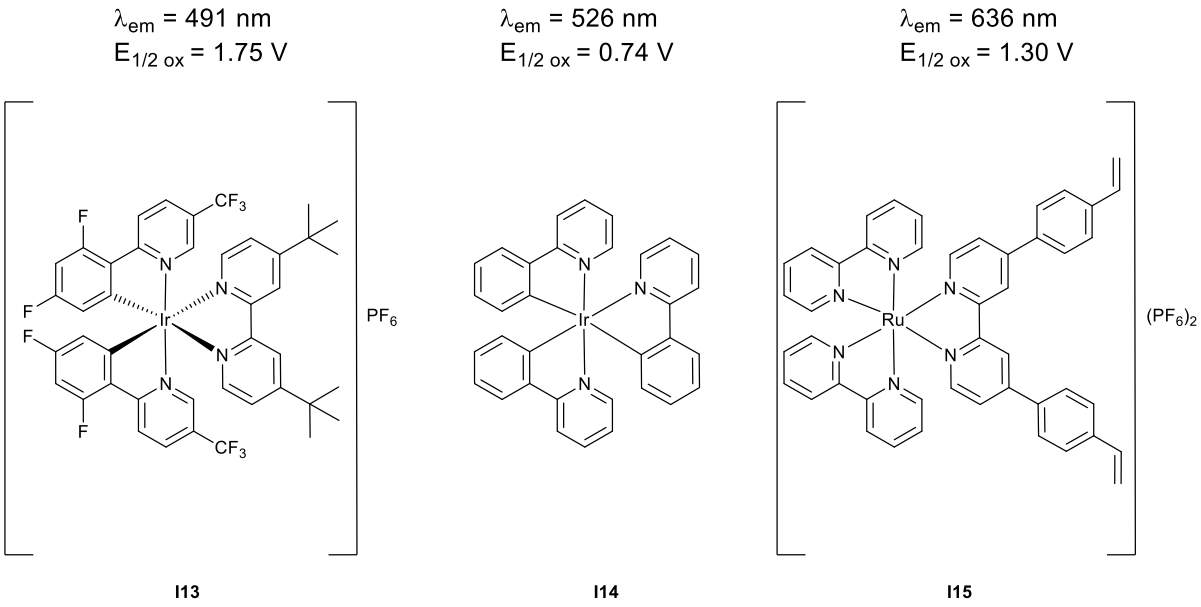
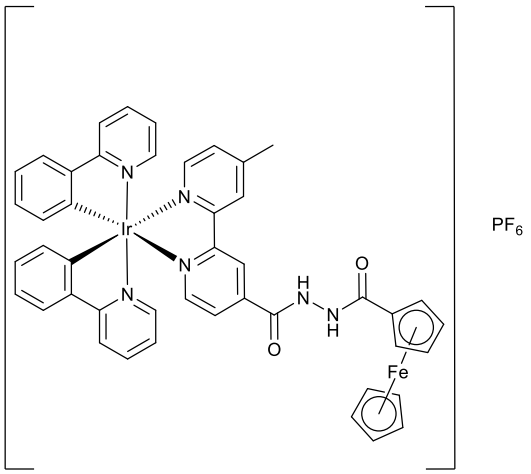


Figure 1.12: Structures of complexes **I13-I15**. Stereochemistry of **I14** and **I15** is not explicitly shown as they are isolated as racemic mixtures. $E_{1/2}$ ox values and ECL emission maxima for each complex are displayed above the complex.

Most recently, in 2019, the group of Zhang *et al.* synthesised an ECL active Ir(III) complex bearing both acylhydrazine and ferrocene moieties.[61] The acylhydrazine group is known to be sensitive to cleavage by hypochlorous acid,[62] whereas the ferrocene moiety is chemically inert

in the test conditions, but known to quench the ECL of ruthenium(II) complexes.[63] The inclusion of both groups gives scope for a "turn-on" ECL sensor for hypochlorous acid. The complex in question was able to show a > 100 fold increase in the photoluminescent intensity, whilst simultaneously displaying a > 3 fold increase in the ECL intensity in aqueous solutions at physiological pH. The complex therefore is a promising first step towards Ir(III) complexes as biological HClO sensors with ECL readout.



I16

Figure 1.13: Ir(III) complex **I16** for efficient and specific electrochemical sensing of hypochlorite, the ferrocene group is linked through an acylhydrazine group, which is cleaved in the presence of hypochlorite ions..

1.4 Our Work

This thesis aims to detail detection of analytes through optical effects arising from Ir(III) complexes. We report the synthesis and use of several novel cyclometalated Ir(III) complexes as luminescent reporters in both the solution-phase and immobilised on a gold surface. The first sensor type contains a boronic acid for recognition, whilst the second sensor type contains hydrophobic chains and a surface anchoring group, which can be used to anchor this complex to a gold substrate.

We chose Ir(III) complexes due to their advantageous photophysical and chemical properties described above; continuing to be actively explored.[64-66] With the Ir(III) luminescence heavily reliant on the local environment,[17] this provides an ideal platform for molecular sensing.[67-79] It offers, as shown above, a platform to sense optically by UV-Vis, photoluminescence intensity, photoluminescence lifetime and electrochemiluminescence. Confirmation of interaction can often be coupled with NMR, and mass spectrometry, with iridium(III) complexes offering an advantage over organic counterparts due to the unique isotope pattern produced.[80] The interaction and binding modes of surface-immobilised complexes can be further investigated by surface chemistry techniques. We have utilised confocal microscopy, contact angle, XPS, TOF-SIMS, and EDX to investigate the surface morphologies.

The triggering of the signal modulation in the solution-based boronic acid sensors is due to a well-known supramolecular binding event between the analyte and the luminescent complex.[81-83] In the highly hydrophobic sensors, the immobilisation and interaction has been preliminarily studied by our group.[84, 85] One of the complexes has been demonstrated to be a nuclear targeting agent for bio-imaging with gold nanoparticles.[8]

This thesis is split into 3 main chapters, with this chapter giving a brief overview of the photophysical properties of Ir(III) complexes, with an introduction to the field of sensing by Ir(III).

The second chapter details the synthesis, characterisation and use of Ir(III)-boronic acid complexes as supramolecular sensors for saccharides. The photoluminescent and electrochemiluminescence response to the saccharide binding event will be described and the structure of the sugar conjugates probed by mass spectrometry and NMR spectroscopy. We will also demonstrate the immobilisation of these complexes into a hydrogel matrix in an attempt to construct a glucose sensing device that is non-toxic, stable and wearable.

The third chapter will cover the synthesis and characterisation of hydrophobic, surface-active iridium(III) complexes with the ability to interact with perfluorooctanoic acid (PFOA); an extremely harmful and widely monitored environmental contaminant. We further detail the preparation, surface morphology and properties of iridium coated gold surfaces before and after immersion of the device in aqueous solutions of PFOA. The coated surfaces can be used as a sensing tool, based upon the luminescent lifetime of the immobilised Ir(III) complex.

1.5 References

1. J. L. Comstock, *Elements of chemistry: in which the recent discoveries in the science are included and its doctrines familiarly explained ; illustrated by numerous engravings and designed for the use of schools and academies*, Published by Robinson Pratt, & Co. ... New-York, 1838.
2. A. F. Henwood, A. K. Bansal, D. B. Cordes, A. M. Z. Slawin, I. D. W. Samuel and E. Zysman-Colman, *J. Mater. Chem. C*, 2016, **4**, 3726-3737.
3. A. F. Henwood and E. Zysman-Colman, *Chem. Commun.*, 2017, **53**, 807-826.
4. R. D. Costa, E. Ortí, D. Tordera, A. Pertegás, H. J. Bolink, S. Graber, C. E. Housecroft, L. Sachno, M. Neuburger and E. C. Constable, *Advanced Energy Materials*, 2011, **1**, 282-290.
5. J. S. Nam, M.-G. Kang, J. Kang, S.-Y. Park, S. J. C. Lee, H.-T. Kim, J. K. Seo, O.-H. Kwon, M. H. Lim, H.-W. Rhee and T.-H. Kwon, *J. Am. Chem. Soc.*, 2016, **138**, 10968-10977.
6. R. Bevernaegie, B. Doix, E. Bastien, A. Diman, A. Decottignies, O. Feron and B. Elias, *J. Am. Chem. Soc.*, 2019, **141**, 18486-18491.
7. K. K.-W. Lo and K. K.-S. Tso, *Inorg. Chem. Front.*, 2015, **2**, 510-524.
8. S. M. King, S. Claire, R. I. Teixeira, A. N. Dosumu, A. J. Carrod, H. Dehghani, M. J. Hannon, A. D. Ward, R. Bicknell, S. W. Botchway, N. J. Hodges and Z. Pikramenou, *J. Am. Chem. Soc.*, 2018, **140**, 10242-10249.
9. K. K.-W. Lo, *Acc. Chem. Res.*, 2020, **53**, 32-44.
10. Y. Kuramochi and O. Ishitani, *Frontiers in Chemistry*, 2019, **7**.
11. H. Ren, G.-F. Li, B. Zhu, X.-D. Lv, L.-S. Yao, X.-L. Wang, Z.-M. Su and W. Guan, *ACS Catal.*, 2019, **9**, 3858-3865.
12. S. Mühmel, D. Alpers, F. Hoffmann and M. Brasholz, *Chemistry – A European Journal*, 2015, **21**, 12308-12312.
13. Z. Liu, Z. Bian and C. Huang, in *Molecular Organometallic Materials for Optics*, eds. H. Bozec and V. Guerchais, Springer Berlin Heidelberg, Berlin, Heidelberg, 2010, DOI: 10.1007/978-3-642-01866-4_4, pp. 113-142.

14. J. C. Deaton and F. N. Castellano, *Iridium(III) in Optoelectronic and Photonics Applications*, 2017, DOI: doi:10.1002/9781119007166.ch1, 1-69.

15. X. Liu, P. Dai, T. Gu, Q. Wu, H. Wei, S. Liu, K. Y. Zhang and Q. Zhao, *J. Inorg. Biochem.*, 2020, **209**, 111106.

16. Z. Lu, M. Shangguan, X. Jiang, P. Xu, L. Hou and T. Wang, *Dyes Pigm.*, 2019, **171**, 107715.

17. D.-L. Ma, S. Lin, W. Wang, C. Yang and C.-H. Leung, *Chem. Sci.*, 2017, **8**, 878-889.

18. D.-L. Ma, S.-Y. Wong, T.-S. Kang, H.-P. Ng, Q.-B. Han and C.-H. Leung, *Methods*, 2019, **168**, 3-17.

19. T. Ramón-Márquez, M. Marín-Suárez, A. Fernández-Gutiérrez and J. F. Fernández-Sánchez, *Iridium(III) in Optoelectronic and Photonics Applications*, 2017, DOI: doi:10.1002/9781119007166.ch10, 479-539.

20. E. Longhi and L. De Cola, *Iridium(III) in Optoelectronic and Photonics Applications*, 2017, DOI: doi:10.1002/9781119007166.ch6, 205-274.

21. R. Bevernaegie, L. Marcélis, A. Moreno-Betancourt, B. Laramée-Milette, G. S. Hanan, F. Loiseau, M. Sliwa and B. Elias, *PCCP*, 2018, **20**, 27256-27260.

22. E. Pomarico, M. Silatani, F. Messina, O. Braem, A. Cannizzo, E. Barranoff, J. H. Klein, C. Lambert and M. Chergui, *The Journal of Physical Chemistry C*, 2016, **120**, 16459-16469.

23. A. Kapturkiewicz and G. Angulo, *Dalton Trans.*, 2003, DOI: 10.1039/B308964A, 3907-3913.

24. E. M. Gross, N. R. Armstrong and R. M. Wightman, *J. Electrochem. Soc.*, 2002, **149**, E137.

25. M. A. Baldo, S. Lamansky, P. E. Burrows, M. E. Thompson and S. R. Forrest, *Appl. Phys. Lett.*, 1999, **75**, 4-6.

26. C. Adachi, M. A. Baldo, S. R. Forrest and M. E. Thompson, *Appl. Phys. Lett.*, 2000, **77**, 904-906.

27. K. Nishimura, Y. Hamada, T. Tsujioka, K. Shibata and T. Fuyuki, *Jpn. J. Appl. Phys.*, 2001, **40**, L945-L947.

28. J. I. Kim, I.-S. Shin, H. Kim and J.-K. Lee, *J. Am. Chem. Soc.*, 2005, **127**, 1614-1615.

29. H. Cao and M. D. Heagy, *J. Fluoresc.*, 2004, **14**, 569-584.

30. J. Ma, M. Song, I. Boussouar, D. Tian and H. Li, *Supramol. Chem.*, 2015, **27**, 444-452.

31. X. Zhou, S. Lee, Z. Xu and J. Yoon, *Chem. Rev.*, 2015, **115**, 7944-8000.

32. N. Kwon, Y. Hu and J. Yoon, *ACS Omega*, 2018, **3**, 13731-13751.

33. D. Cao, Z. Liu, P. Verwilst, S. Koo, P. Jangjili, J. S. Kim and W. Lin, *Chem. Rev.*, 2019, **119**, 10403-10519.

34. D. Wu, A. C. Sedgwick, T. Gunnlaugsson, E. U. Akkaya, J. Yoon and T. D. James, *Chem. Soc. Rev.*, 2017, **46**, 7105-7123.

35. T. L. Mako, J. M. Racicot and M. Levine, *Chem. Rev.*, 2019, **119**, 322-477.

36. in *Principles of Fluorescence Spectroscopy*, ed. J. R. Lakowicz, Springer US, Boston, MA, 2006, DOI: 10.1007/978-0-387-46312-4_19, pp. 623-673.

37. N. Boens, W. Qin, N. Basarić, J. Hofkens, M. Ameloot, J. Pouget, J.-P. Lefèvre, B. Valeur, E. Gratton, M. vandeVen, N. D. Silva, Y. Engelborghs, K. Willaert, A. Sillen, G. Rumbles, D. Phillips, A. J. W. G. Visser, A. van Hoek, J. R. Lakowicz, H. Malak, I. Gryczynski, A. G. Szabo, D. T. Krajcarski, N. Tamai and A. Miura, *Anal. Chem.*, 2007, **79**, 2137-2149.

38. E. Baggaley, J. A. Weinstein and J. A. G. Williams, in *Luminescent and Photoactive Transition Metal Complexes as Biomolecular Probes and Cellular Reagents*, ed. K. K.-W. Lo, Springer Berlin Heidelberg, Berlin, Heidelberg, 2015, DOI: 10.1007/430_2014_168, pp. 205-256.

39. Y. Li, Y. Wu, L. Chen, H. Zeng, X. Chen, W. Lun, X. Fan and W.-Y. Wong, *Journal of Materials Chemistry B*, 2019, **7**, 7612-7618.

40. K. K.-W. Lo, A. W.-T. Choi and W. H.-T. Law, *Dalton Trans.*, 2012, **41**, 6021-6047.

41. J.-B. Liu, C. Yang, C.-N. Ko, K. Vellaisamy, B. Yang, M.-Y. Lee, C.-H. Leung and D.-L. Ma, *Sens. Actuators B: Chem.*, 2017, **243**, 971-976.

42. F. Ruff, A. Fábián, Ö. Farkas and Á. Kucsman, *Eur. J. Org. Chem.*, 2009, **2009**, 2102-2111.

43. W. Wang, L. Lu, K.-J. Wu, J. Liu, C.-H. Leung, C.-Y. Wong and D.-L. Ma, *Sens. Actuators B: Chem.*, 2019, **288**, 392-398.

44. Z. Chen, G. Meng, H. Tang, Y. Ye, R. Sun, M. Chen and K.-M. Wang, *New J. Chem.*, 2017, **41**, 8312-8319.

45. K. K.-W. Lo, K. Y. Zhang, S.-K. Leung and M.-C. Tang, *Angew. Chem. Int. Ed.*, 2008, **47**, 2213-2216.

46. K. Y. Zhang, H.-W. Liu, M.-C. Tang, A. W.-T. Choi, N. Zhu, X.-G. Wei, K.-C. Lau and K. K.-W. Lo, *Inorg. Chem.*, 2015, **54**, 6582-6593.

47. K. Y. Zhang, P. Gao, G. Sun, T. Zhang, X. Li, S. Liu, Q. Zhao, K. K.-W. Lo and W. Huang, *J. Am. Chem. Soc.*, 2018, **140**, 7827-7834.

48. Z. Du, R. Zhang, B. Song, W. Zhang, Y.-L. Wang, J. Liu, C. Liu, Z. P. Xu and J. Yuan, *Chemistry – A European Journal*, 2019, **25**, 1498-1506.

49. W. Fudickar and T. Linker, *Chem. Commun.*, 2008, DOI: 10.1039/B719637G, 1771-1773.

50. J. Shen, T. Zhou and R. Huang, *Micromachines*, 2019, **10**.

51. N. E. Tokel and A. J. Bard, *J. Am. Chem. Soc.*, 1972, **94**, 2862-2863.

52. E. M. Gross, S. S. Maddipati and S. M. Snyder, *Bioanalysis*, 2016, **8**, 2071-2089.

53. S. E. K. Kirschbaum and A. J. Baeumner, *Anal. Bioanal. Chem.*, 2015, **407**, 3911-3926.

54. H. Wei and E. Wang, *Luminescence*, 2011, **26**, 77-85.

55. H. Liu, X. Zhou, J. Shen and D. Xing, *ChemElectroChem*, 2017, **4**, 1681-1685.

56. S. E. Laird and C. F. Hogan, *Iridium(III) in Optoelectronic and Photonics Applications*, 2017, DOI: doi:10.1002/9781119007166.ch8, 359-414.

57. H. Lin, M. E. Cinar and M. Schmittel, *Dalton Trans.*, 2010, **39**, 5130-5138.

58. M. Schmittel and H.-W. Lin, *Angew. Chem. Int. Ed.*, 2007, **46**, 893-896.

59. C. Li, J. Lin, Y. Guo and S. Zhang, *Chem. Commun.*, 2011, **47**, 4442-4444.

60. W. Guo, H. Ding, C. Gu, Y. Liu, X. Jiang, B. Su and Y. Shao, *J. Am. Chem. Soc.*, 2018, **140**, 15904-15915.

61. D. Han, M. Qian, H. Gao, B. Wang, H. Qi and C. Zhang, *Anal. Chim. Acta*, 2019, **1074**, 98-107.

62. L. Cao, R. Zhang, W. Zhang, Z. Du, C. Liu, Z. Ye, B. Song and J. Yuan, *Biomaterials*, 2015, **68**, 21-31.

63. W. Cao, J. P. Ferrance, J. Demas and J. P. Landers, *J. Am. Chem. Soc.*, 2006, **128**, 7572-7578.

64. J. R. Shakirova, O. A. Tomashenko, E. E. Galenko, A. F. Khlebnikov, P. Hirva, G. L. Starova, S.-H. Su, P.-T. Chou and S. P. Tunik, *Inorg. Chem.*, 2018, **57**, 6853-6864.

65. P.-Y. Ho, C.-L. Ho and W.-Y. Wong, *Coord. Chem. Rev.*, 2020, **413**, 213267.

66. A. B. Kajjam and S. Vaidyanathan, *J. Photochem. Photobiol. A: Chem.*, 2018, **350**, 130-141.

67. Z. Mao, J. Liu, T.-S. Kang, W. Wang, Q.-B. Han, C.-M. Wang, C.-H. Leung and D.-L. Ma, *Science and Technology of Advanced Materials*, 2016, **17**, 109-114.

68. H. J. Kim, T. Kim and J.-I. Hong, *Sens. Actuators B: Chem.*, 2020, **307**, 127656.

69. X. Miao, C. Yang, C.-H. Leung and D.-L. Ma, *Sci. Rep.*, 2016, **6**, 25774.

70. Q. Chen, S. Sheth, Y. Zhao and Q. Song, *Analytical Methods*, 2019, **11**, 3033-3040.

71. C. Wu, J.-B. Liu, G. Li, S.-Y. Wong, Q.-B. Han, C.-H. Leung and D.-L. Ma, *Dyes Pigm.*, 2018, **159**, 479-482.

72. M. Zhao, Y. Pan, X. Wang, X.-W. Gao and D. Chao, *New J. Chem.*, 2018, **42**, 5508-5513.

73. T. Kim and J.-I. Hong, *ACS Omega*, 2019, **4**, 12616-12625.

74. Z. Yang, C. Huang, C. Wang, Y. Zhao and Q. Song, *ACS Sustainable Chemistry & Engineering*, 2017, **5**, 4443-4448.

75. N. Lin, H.-D. Ou, Q. Xu, Y. Jin, W. Deng and Z.-J. Yao, *ACS Omega*, 2020, **5**, 4636-4645.

76. S. Yi, Z. Lu, J. Zhang, J. Wang, Z. Xie and L. Hou, *ACS Appl. Mater. Interfaces*, 2019, **11**, 15276-15289.

77. X. Miao, C.-N. Ko, K. Vellaisamy, Z. Li, G. Yang, C.-H. Leung and D.-L. Ma, *Sci. Rep.*, 2017, **7**, 42740.

78. C. Liu, C. Yang, L. Lu, W. Wang, W. Tan, C.-H. Leung and D.-L. Ma, *Chem. Commun.*, 2017, **53**, 2822-2825.

79. J.-B. Liu, L.-J. Liu, Z.-Z. Dong, G.-J. Yang, C.-H. Leung and D.-L. Ma, *Sci. Rep.*, 2016, **6**, 36509.

80. K. S. Choung, K. Marroquin and T. S. Teets, *Chem. Sci.*, 2019, **10**, 5124-5132.

81. X.-t. Zhang, G.-j. Liu, Z.-w. Ning and G.-w. Xing, *Carbohydr. Res.*, 2017, **452**, 129-148.

82. X. Sun, B. M. Chapin, P. Metola, B. Collins, B. Wang, T. D. James and E. V. Anslyn, *Nat. Chem.*, 2019, **11**, 768-778.

83. Z. Bian, A. Liu, Y. Li, G. Fang, Q. Yao, G. Zhang and Z. Wu, *Analyst*, 2020, **145**, 719-744.

84. S. J. Adams, D. J. Lewis, J. A. Preece and Z. Pikramenou, *ACS Appl. Mater. Interfaces*, 2014, **6**, 11598-11608.

85. S. J. Adams, A. J. Carrod, L. A. Rochford, M. Walker and Z. Pikramenou, *ChemistrySelect*, 2018, **3**, 3251-3257.

2 Photoluminescent and Electrochemical Sensing of Sugars at Physiological pH via an iridium(III) Complex Bearing Directly Boronated Ligands.

2.1 Introduction

2.1.1 General Remarks on saccharide importance and chemical sensing

As consumption of carbohydrate rich, ultra-processed food becomes increasingly prevalent, clinician's advice to governments is to enact legislation to limit the sale of these foodstuffs.[1] Whilst the long-term advantages of certain calorie controlled diets are still a matter of debate among medical professionals,[2] one thing is clear, that the prevalence of obesity and diabetes in certain countries has been increasing rapidly for some time, with unfavourable outcomes.[3, 4] Diabetes detection, and subsequent control is of critical importance to nearly 400 million people directly, with that number predicted to rise significantly in the coming years.[5] Diabetes leads to issues with many bodily functions including retinopathy,[6] renal failure,[7] cardiovascular events[8, 9] and ulceration.[10] It is therefore vital globally there is in place a method for cheap, facile, high throughput methods for accurate blood glucose measurement.[11]

Many people still utilise self-monitored blood glucose (SMBG) more colloquially known as "finger prick" testing, to inform their decisions on appropriate treatment.[12, 13] Unfortunately, this method has been shown in numerous studies to lead to patients unwillingness to adhere to an effective testing regimen, often due to psychological barriers such as pain and low expectations.[13-16] Further studies reveal that many of the devices currently approved by the FDA were in fact not performant in home use to the same standards that led to their approval.[17, 18] FDA guidelines for the approval of SMBG devices currently set an accuracy level of ±15 % in the measurement of blood glucose in 95 % of sample pairs (one tested by standardised

method such as HPLC); in one particular study this standard was found to be consistently met by only 6 of 18 tested devices.[19] Clearly then patients may be misled by these values into taking actions when unnecessary. Recent efforts have focussed on continuous glucose monitoring (CGM) as a method of overcoming limitations in patient adherence and depth of data from glucose monitoring.[20, 21] To create a CGM device, one must have an accurate, stable, biocompatible and externally referenceable monitor.

In assessing a chemical approach to this goal then, one must consider at its most basic the principle of supramolecular chemistry, in which a host-guest interaction will mediate a measurable signal output as shown in Figure 2.1.[22, 23] To this end, the synthetic challenge for chemists is to create a monosaccharide sensitive supramolecular sensor. Accordingly, the boronic acid functional group is well known to reversibly bind to *cis*-1,2 and 1,3 diols, the basic feature of monosaccharides such as glucose.[24] Many reviews exist on the nature of the formation of the boronate ester upon saccharide binding, and the inherent use of boronic acid containing compounds for the purpose of saccharide sensing.[25-32]

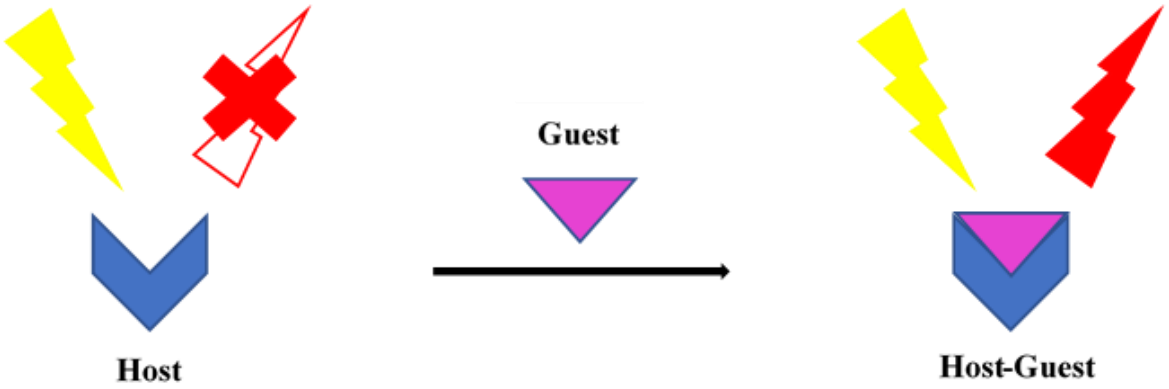
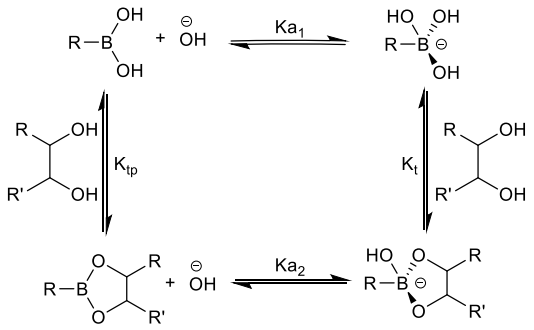


Figure 2.1: Visual representation of supramolecular sensing via luminescence intensity increase or "turn on", common for many boronic acids. The incident light is represented by the yellow arrow. The red arrow represents emitted photons at the wavelength of detection.

To detail in brief, Scheme 2.1 below details the basic process of ester formation. The boronic acid group is initially an sp^2-hybrid with a trigonal planar configuration, upon diol binding

shifts of 120° (boronic acid) to 113° (boronic ester) are apparent, however, the bond angle of sp^3-hybrid tetrahedral boronic acid anion is ~109.5°. Boronic acids are known to become more acidic upon diol binding, with pKa_2 of the boronate ester lower by 2–4 units than the pKa_1 of the boronic acid.[24, 33, 34] Elucidating from this we may assume two things, that formation constants are much higher in the anionic tetrahedral form ($Ka_1K_t = Ka_2K_{tp}$, therefore lower values of Ka_1 generate higher values for K_t). The second assumption we therefore make is that higher pH will therefore allow for more efficient saccharide binding (i.e. increasing formation of the tetrahedral anionic form will promote binding).[35]



Scheme 2.1: Binding pathway for the boronic acid complexes based upon thermodynamic equilibria. Ka_1 and Ka_2 are the boronic acid and the ester forms ionisation constants, respectively. K_t and K_{tp} are the binding constants of the tetrahedral anionic form and the trigonal planar form respectively

After the basic principles of saccharide binding by boronic acid functionalities were detailed in 1959, it took 33 years for the work of Yoon and Czarnik to disseminate the first example of a fluorescent monosaccharide sensor based on a boronic acid substituted anthracene now considered to be seminal work in the field.[36] Since, many groups have used the principle of fluorescence to sense saccharides,[37-47] amongst many methods.

This section will have an in-depth focus on the literature surrounding boronic acid containing compounds from the preceding 10 years, as well as outlining any seminal work in each of the listed fields. Studies of supramolecular interactions of boronic acids with diols through several techniques including NMR, electrochemistry, and luminescence will be highlighted, with focus placed on photoluminescent monitoring of these interactions. Due to the scope of the boronic

acid field only a few examples have been depicted to give the best overview of the broad subject. The section will also briefly cover our aim in this field and detail some key expectations for our findings.

2.1.2 NMR sensors for saccharides

NMR has long been utilised as a tool for visualising the occurrence of supramolecular interactions and for shedding light on the mechanism behind them.[48-50] This technique has been successfully applied to the field of boronic acids in saccharide detection. In the past 10 years several NMR active nuclei have been investigated for their application in saccharide recognition *via* boronic acid containing complexes.

Sporzyński *et al.* reported in 2013 the use of phenylboronic acid in ^{17}O NMR studies, for the determination of boronic ester formation and structural discrimination of the bound group. The cyclic ester formed with catechol gives a distinct ^{17}O chemical shift from the phenylboronic acid (**B1**) alone, structures are shown in Figure 2.2. In $CDCl_3$ the chemical shift of the phenylboronic acid is 70.7 ppm, this shift is compared to that of the synthesised catechol bound boronic ester compound (**B2**) with a ^{17}O chemical shift of 148.1 ppm ($\Delta\delta$ = 77.4 ppm). Boronic esters wherein the bound acid is non-symmetric in nature such as in the ortho- methylated catechol (**B3**) lead to 2 distinguishable ^{17}O shifts (155.2 and 149.1 ppm).[51] These results suggest that ^{17}O can be used as a tool for probing not only the binding of sugars, but also the differentiation of sugar type by structure specific ^{17}O chemical shifts. Significant drawbacks of ^{17}O NMR however are the low natural abundance of the isotope (0.037%), the difficulties with an aqueous solvent and low sensitivity compared to the ^{1}H nuclei.[52]

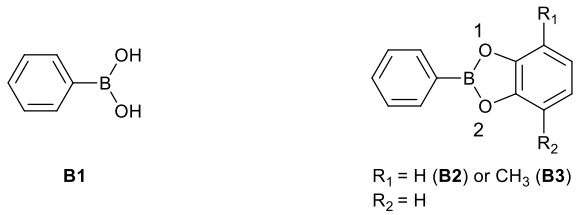


Figure 2.2: Structures of notable.compounds in the study of Sporzyński *et al.* with asymmetric catechol adduct shown

To overcome then the problems with ^{17}O NMR, in recent years ^{19}F NMR has become an attractive method of sensing. Many papers have used the fluorine nuclei as a sensitive reporter for saccharide binding. Of note is a study by Schiller *et al.*, wherein a fluorine appended boronic acid was linked to a pyridinium salt via a methyl bridge (**B4**, Figure 2.3). The complexes display high aqueous binding constants 1600 and 130 M^{-1} for fructose and glucose respectively at pH 7.4, which allows for rapid biological screening. Perhaps most impressive is the ability of these compounds to distinguish between sugars, and indeed a distinct ^{19}F NMR pattern is observed dependent on the sugar added. Further to this, complex mixtures of up to 9:1 molar ratio of fructose to glucose can still be analysed and the sugars distinguished. The rapid testing was applied to synthetic urine samples, and with a 188 MHz spectrometer the limit of detection was as low as 1 mM. The drawback of the technique itself is the relatively high concentration requirements for the boronic acid when compared to fluorimetric methods.[53]

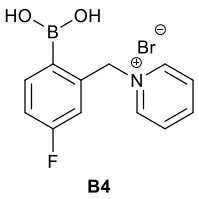


Figure 2.3: structure of the pyridinium salt appended to 4-fluorophenylboronic acid for the selective detection and discrimination of saccharides developed by Schiller *et al.*

In a more recent study fluorinated sugars in place of fluorinated probes were used to measure the diol-boronic acid interaction. A multinuclear approach in which ^{11}B and ^{19}F NMR were used in conjunction, was attempted with differing boronic acids (Figure 2.4). The authors note that ^{11}B nuclei whilst abundant offers low sensitivity, and is a quadrupolar nuclei (spin-3/2)

therefore ^{19}F NMR spectra taken in the region of fluorinated sugars could give a better insight into the diol interaction. Indeed, the authors note that there is a ^{11}B shift from 28 to 11 ppm observed upon addition of 3-fluorocatechol in a 50:50 molar ratio to phenylboronic acid (**B1**) at pH 7.4 in PBS buffer. This signal is broad, and may be problematic to analyse if several different boron species/functionalities are present. The concurrent ^{19}F NMR shows a shift of -137 ppm to -143 ppm upon diol binding to the boronic acid, the signals are sharp and well resolved. The authors also applied the ^{19}F NMR to samples containing 3-fluorocatechol and 1,4-phenylenediboronic acid (**B5**), again in a 50:50 molar ratio. An extremely weak signal was observed arising from the 2:1 sugar:boronic acid complex formed. The study therefore suggests that there is a simplistic route to utilise commercially available fluorinated sugars in lieu of synthetic modification of the boronic acid containing compound.[54]

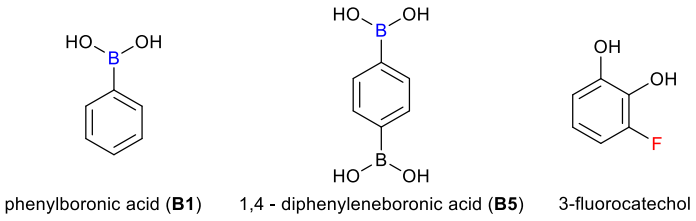


Figure 2.4: Selected structures used by Larcher *et al.*, reporter nuclei for ^{11}B and ^{19}F NMR are highlighted in blue and red respectively.

2.1.3 Electrochemical sensors for saccharides

Electrochemical sensing and monitoring of biological events often geared towards point-of-care testing has been apparent and well documented in the literature,[55, 56] in the context of boronic acids, one might utilise such compounds in electrochemical systems as a rather facile glucose monitoring system for diabetes.

Perhaps the most well-known and widely studied of all electrochemically applicable boronic acids is the ferrocene-boronic acid first prepared by Nesmejanow *et al.*.[57] Building on this

original work the group of James *et al.* apply a di-boronic acid group linked to ferrocene (**B6**, Figure 2.5),[58] to improve the capability of other ferrocene-boronic acid complexes previously synthesised (**B7,** Figure 2.5).[59] The authors measure the complexes electrochemical signal through differential pulse voltammetry (DPV), with the complexes shifting in potential to higher voltages, becoming harder to oxidise upon subsequent additions of monosaccharide (the structure of the glucose adduct of **B7** is shown in Figure 2.5). The paper details the binding constants found between sugars and the synthesised complexes via the DPV method; the diboronic acid species displays far superior binding capability to the mono- analogue as expected, 680 vs 20 M^{-1} respectively. Unfortunately, the complexes are sparingly soluble in aqueous solutions, with 52% methanol by volume needed to solubilise the ferrocene complexes.

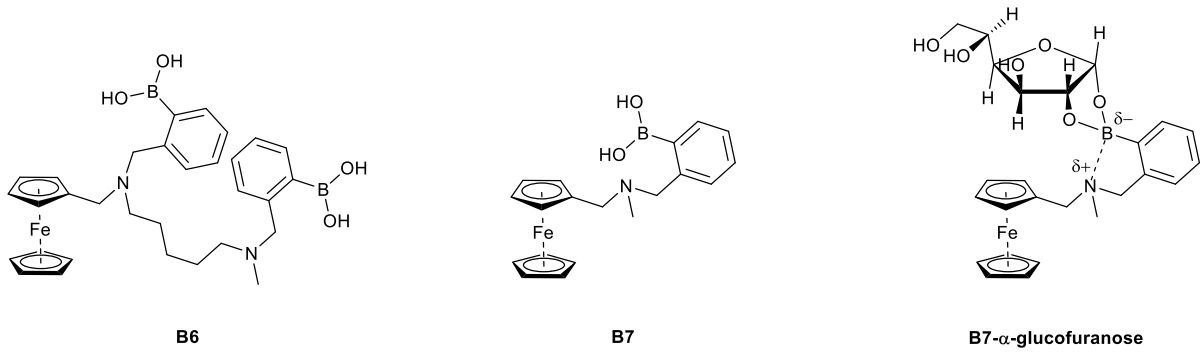


Figure 2.5: Structures of the diboronic and monoboric acid ferrocene complexes **B6** and **B7** reported by James *et al.*, alongside the glucose adduct of the monoboronic acid, which increases the oxidation potential of the ferrocene complex.

Ruthenium is another important metal in electrochemical sensing, ever since the first detailed studies of $[Ru(bpy)_3](PF_6)_2$ electrochemically generated luminescence by Tokel and Bard,[60] many groups have used complexes of Ru(II) as general electrochemical sensors for a large variety of analytes.[61, 62]

Ru(II) complexes have been studied in solution and in dendritic systems. Dendrimers of G2-$PAMAM_{16}$ were mixed with the ruthenium complex (**B8**, Figure 2.6) at 1.25 molar equivalents in 8:2, H_2O:MeOH mixtures. Binding was reasoned to occur through carboxylic acids on the

ruthenium complex. After preparation of dendrimers, DPV was again used to assess electrochemical signal variation over a concentration range of glucose and fructose of 0-30 mM (Figure 2.6). The binding constants were assessed of both the ruthenium complex alone in solution (8:2, H_2O:MeOH) and as a dendrimer preparation in the same conditions; surprisingly far higher constants were observed for the dendrimer bound Ru(II) than in solution. The constants for fructose measured were 1300 M^{-1} for the dendrimer and 80 M^{-1} in solution.[63]

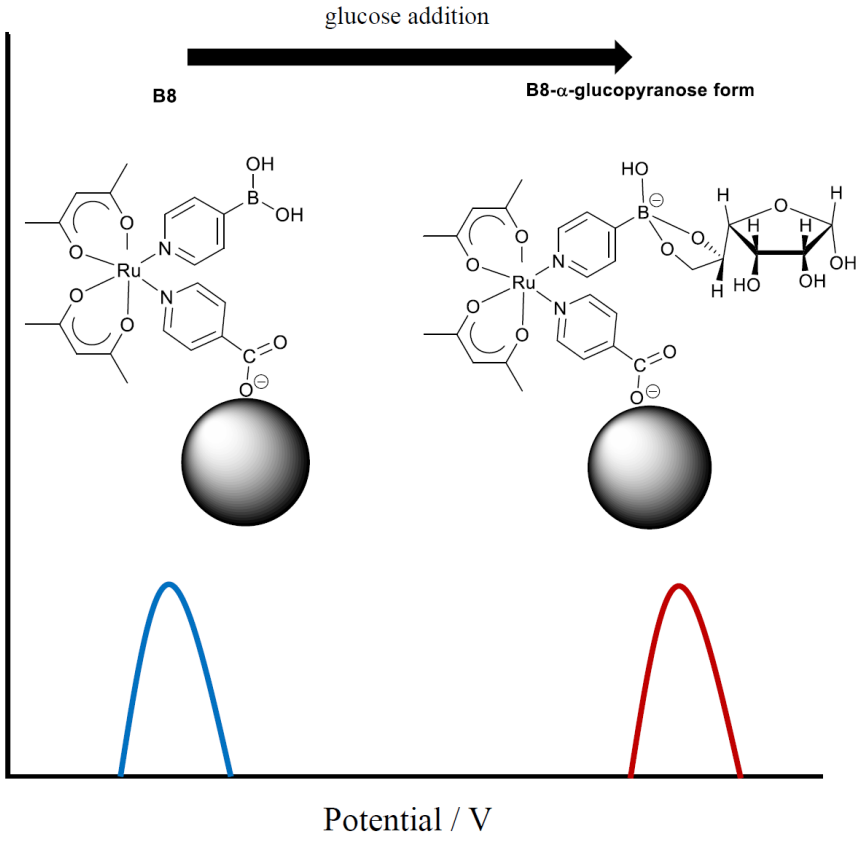


Figure 2.6: Graphical depiction of the modulation of the dpv signal dependent on glucose concentration. The blue curve represents the dpv spectrum for the Ru complex unbound to glucose, and the red curve represents that of the glucose bound complex. The bound and unbound forms of the complex are displayed above the relevant curve.

The same group followed with more work in Ru(II) based sensing of saccharides, this time utilising gold nanoparticles as nanocarriers for both the ruthenium complex and an aromatic compound containing a boronic acid functionality. Several different lengths of sulfur capped-alkyl linker to the gold nanoparticle were used for both the ruthenium and the boronic acid containing aromatic. Four varied combinations of the ruthenium/boronic acid were attached to

the nanoparticle (Figure 2.7), and the DPV signal of the gold nanoparticles in solution (3:1, H_2O:EtOH), in 3 of the cases (**B9 + B11**, **B10 + B11**, **B10 + B12**) extremely high and similar binding constants of ~10^6 M^{-1} were calculated with D-glucose. The notable exception to this is with the short linked boronic acid but longer linker on the ruthenium (**B9 + B12**), the binding constant was not determined as the spectral changes were small. Based upon this result and concurrent UV-Vis spectra taken, which showed no changes upon saccharide binding suggesting no aggregation of the gold nanoparticles, it was determined that the changes in the DPV spectra arise from the shielding of the ruthenium from the detecting electrode by bound saccharide.[64]

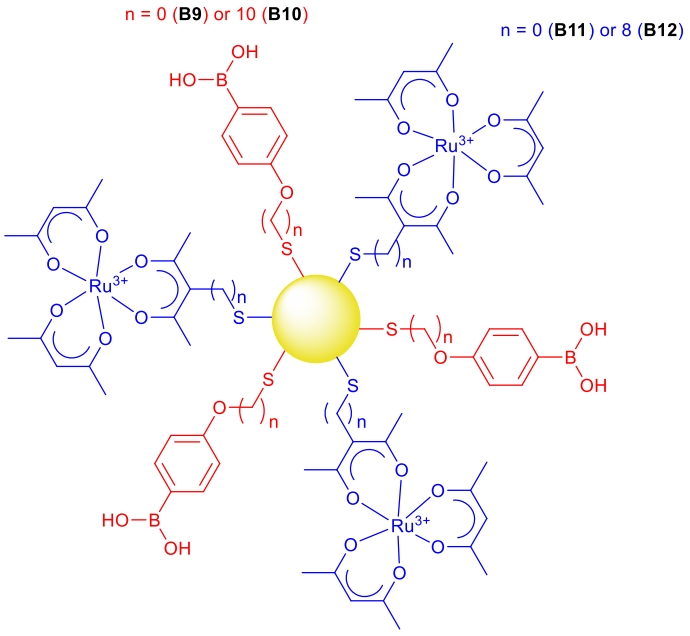


Figure 2.7: Nanoparticle systems developed for dpv sensing of saccharides with the possible structures of all ruthenium reporter and the boronic acid sensing group attachments shown

The group of James *et al.*, used the electrochemiluminescence intensity of $[Ru(bpy)_3](PF_6)_2$ as a measurable parameter for determination of saccharide concentration. $[Ru(bpy)_3](PF_6)_2$ has been well document to respond to amine co-reactants that increase the ECL signal observed,[65] and in light of this the authors synthesised a small selection amine containing boronic acid structures, the di-boronic acids of which had been previously synthesised and for which the saccharide binding properties were investigated through fluorescence spectroscopy.[66] In the

study in question these amines were used as the co-reactant in the ECL experiments. As a proof of principle, the authors first used the simplest of all the acids synthesised, 2-((dipropylamino)methyl)phenylboronic acid (**B13**, Figure 2.8), in conjunction with $[Ru(bpy)_3](PF_6)_2$ in PBS solution at pH 7.4. It is important to note that the concentration of the lumiphore was 10 μM but the co-reactant was used at a relatively high concentration of 0.2 mM. The combination displayed measurable reduction in ECL intensity upon glucose or fructose addition (around 40 % and 80 % respectively at 50 mM of the relevant saccharide), but showed no discrimination between D-glucose and D-fructose. The solution found by the authors was to use the aforementioned di-boronic acid (**B14**, Figure 2.8) which would only show efficient quenching if both boronic acids were bound to saccharide, which is the case in the cyclic glucose bound form. The authors note that in the same conditions as the previous experiment, successful discrimination was achieved only observing a <5 % reduction in ECL intensity on addition of the fructose to 50 mM, whereas the same concentration of glucose inferred a 40 % reduction in ECL intensity. This system therefore is highly efficient and simplistic but seemingly high concentrations of co-reactant are needed in comparison to photoluminescence sensors.[67]

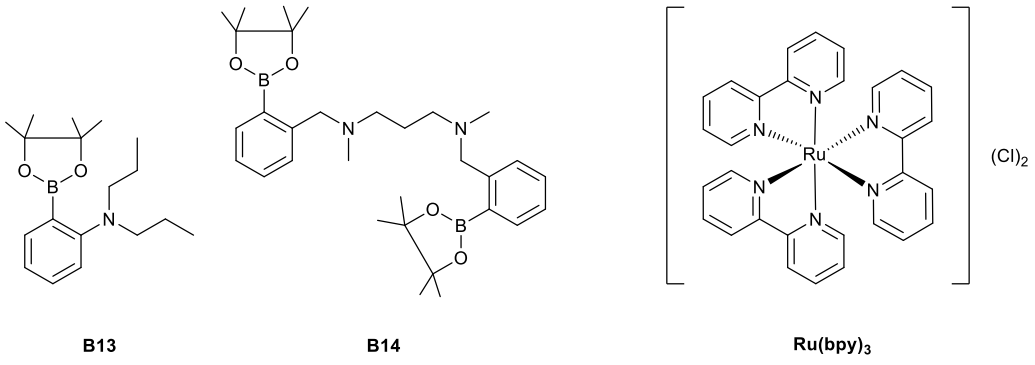


Figure 2.8: Structures used in as co reactants in the study of James *et al*., with the structure of ruthenium(II) tris-bipyridine as its chloride salt, as used in the publication

More recently Fabre *et al*. have developed a glucose sensor based upon boronic acids covalently attached to Si(111) surfaces, electrochemical impedance spectroscopy

measurements of these 4-ethylbenzeneboronic acid (**B15**, Figure 2.9) functionalised surfaces in the presence of a reporter couple, in this case $[Fe(CN)_6]^{3-}/[Fe(CN)_6]^{4-}$ (Figure 2.9) showed specific dopamine-induced changes. It is assumed that the boronate anion increases charge transfer resistance (R_{ct}). With measurements performed at pH 7.4 in aqueous solutions the R_{ct} was found to decrease from 4.9 MΩ to 14 KΩ upon increasing dopamine concentration from 10 μM–1 mM. A reference surface containing ethylbenzene in place of the 4-ethylbenzeneboronic acid was used and no significant changes were observed in the impedence spectra in solutions containing up to 10 mM of dopamine.[68]

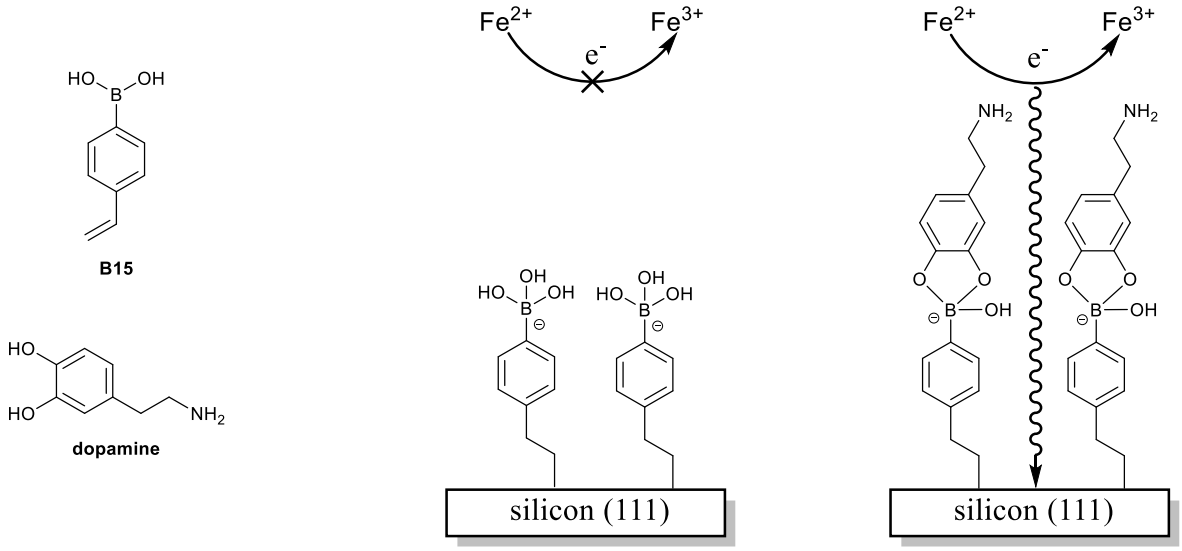
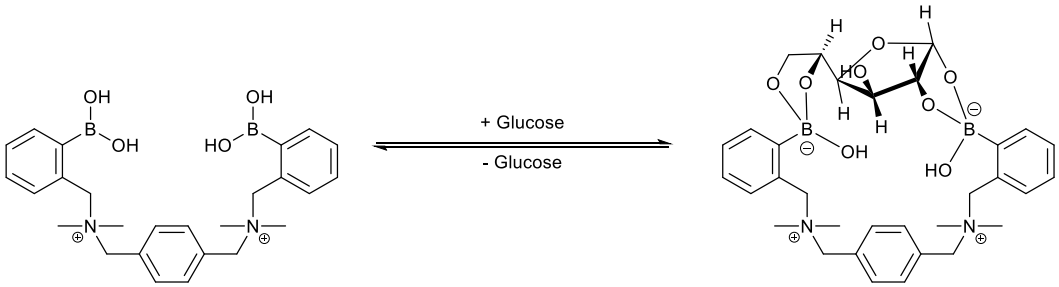


Figure 2.9: Structures of the 4-ethylbenzeneboronic acid (**B15**) and the dopamine analyte. Also shown are the Si(111) surfaces before and after immersion in dopamine solutions. The electron transfer process is denoted by curly arrows, and is shown to occur only in the dopamine bound sample

Bazan et al. recently detail a boronic acid sensor for solution phase monitoring of saccharide concentrations, based upon a conductimetric response. The complex was found to lower the conductivity of an aqueous solution at pH 7.4 containing the HPO_4^{2-} salt, through the formation of $H_2PO_4^-$, mediated by the lowering of the pK_a of the boronic acid containing compound upon diol binding (Figure 2.10). The binding constants for glucose and fructose are found to be 1000 M^{-1} and 600 M^{-1} respectively, inferring that the complex may be used in a biological application to sense glucose selectively. Conductimetric measurements confirmed that incremental

changes in glucose can be measured via an increase in resistance between 0-30 mM, the correct range for biological application. On addition of the interfering fructose to a concentration of 1 mM – at least 10 times the maximum found in human blood plasma, to a solution of boronic acid complex (2 mM) and glucose (5 mM), only a 3 % change in resistance was measured; this confirms that the compound may be used in biological assays for glucose.[69]



B16

Figure 2.10: schematic representation of the glucose bound and unbound forms, of **B16,** introduced in the work of *Bazan et al*., the plus and minus symbols pertain to increasing and decreasing glucose concentrations.

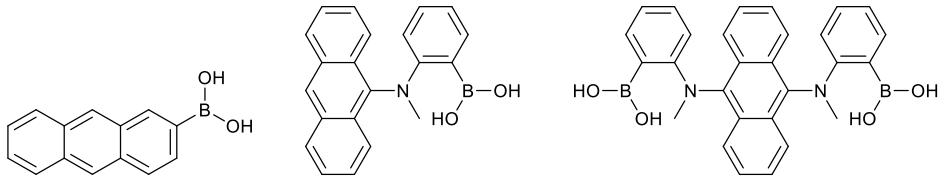
2.1.4 Archetypal examples of boronic acid sensors for fluorescent sensing of saccharides

Yoon and Czarnik in 1992 detailed the first boronic acid compound anthracen-2-ylboronic acid, (**B17**, Figure 2.11), to sense saccharide binding by fluorescence.[36] The boronic acid was appended to the anthracene fluorophore directly, and the pKa of the acid and the ester measured in aqueous solution (1% DMSO in water), producing a value of 8.9 for the anthracene-boronic acid. The study found that the pKa lowered by 3 units after repeating the experiment in the presence of 100 mM of fructose. It was therefore decided that this lent itself to sensing of saccharides through titrations of the sugar into aqueous solutions containing the boronic acid at physiological pH. Upon addition of monosaccharides or diols to the solutions of boronic acid, the fluorescence intensity decreased. After fitting the binding curves, a value for overall binding constant for fructose was calculated to be 270 M^{-1} at that physiological pH.

The second fluorescence based sensor of note, (**B18**, Figure 2.11), was also based on an anthracene moiety, to report saccharide concentration by fluorescent enhancement (Figure 2.1).[70] First assumed to be a photo-electron transfer mediated mechanism, the compound displayed turn on fluorescence upon saccharide binding, opposite to that of Czarnik's early work. In the publication an optimal pH range of between 6-9 is shown via measurement of the pH dependent fluorescence intensity behaviour of compound **B18**. It was later measured that the binding constants between **B18** and fructose or glucose were 1000 and 60 respectively, measured in 2:1 MeOH:H_2O solutions at pH 7.8.[71] Whilst this compound introduced a new opportunity for fluorescent sensing the drawback of its aqueous insolubility to biological application is evident.

The third and final archetypal boronic acid containing compound of note is that synthesised again by Shinkai *et al.*, the 9,10-diaminomethylanthracene backbone sensor (**B19**, Figure 2.11). The design of the boronic acid incorporates 2 spaced boronic acid moieties, with such an arrangement allowing for preferential binding to 1,2- and 4,6-hydroxyl groups of glucose. The efficient spacing leads to the binding constant between **B19** and glucose being higher than that of fructose, at 4000 and 300 respectively in 2:1 MeOH:H_2O solutions at pH 7.8 quantified by fluorescent signal enhancement. ^{1}H and 2D COSY NMR studies support the 1:1 binding model with glucose, as a notable upfield shift of -0.3 ppm in the glucose H3 indicates orientation toward the anthracene π-electrons. 1:1 glucose:anthracene complexes were also observed by mass spectrometry, and the ordering of saccharide affinity in sugars apart from glucose,

believed to be dependent on the stability of the 2:1 saccharide:anthracene complex, which were only observed in mass spectrometry for glucose conjugates.[72]



B17 **B18** **B19**

Figure 2.11: structures of selected archetypal boronic acid complexes developed by Yoon and Czarnik, as well as Shinkai *et al.*

2.1.5 Recent examples of boronic acid sensors for fluorescent sensing of saccharides in solution

The group of James *et al.*, investigated the possibility of excimer formation via a boronic acid containing compound selectively with glucose rather than fructose (**B20**, Figure 2.12). The rationale behind this approach is the formation of 1:2 glucose:boronic acid aggregates upon addition of this saccharide, whereas 1:1 amorphous conjugates will be formed upon addition of fructose. The 1:2 complexes formed show an increase in the emission intensity at 510 nm, whereas only an increase at 377 nm is observed in the 1:1 fructose complex. These luminescence measurements are made in aqueous solution containing 2 % methanol at pH 10 at 0.1 mM boronic acid concentration. In pH range 6.5-9.5 **B20** alone in solution formed excimers, therefore measurements could not be carried out in this pH range, rendering the compound unsuitable for biological application. Further disadvantage is evident of the emission peak appearing at 377 nm, outside of the range of visible light. Despite this, fitting of the intensity increase observed at either 510 nm or 377 nm in the titrations to a 1:2 model in the glucose containing samples, and 1:1 model in fructose led to impressive binding constants of around 1400 and 350 M^{-1} respectively. Further selectivity towards glucose can be achieved

by mixing the boronic acid complex with phenylboronic acid, which preferentially binds to fructose "knocking out" this saccharide from binding to the studied boronic acid.[73]

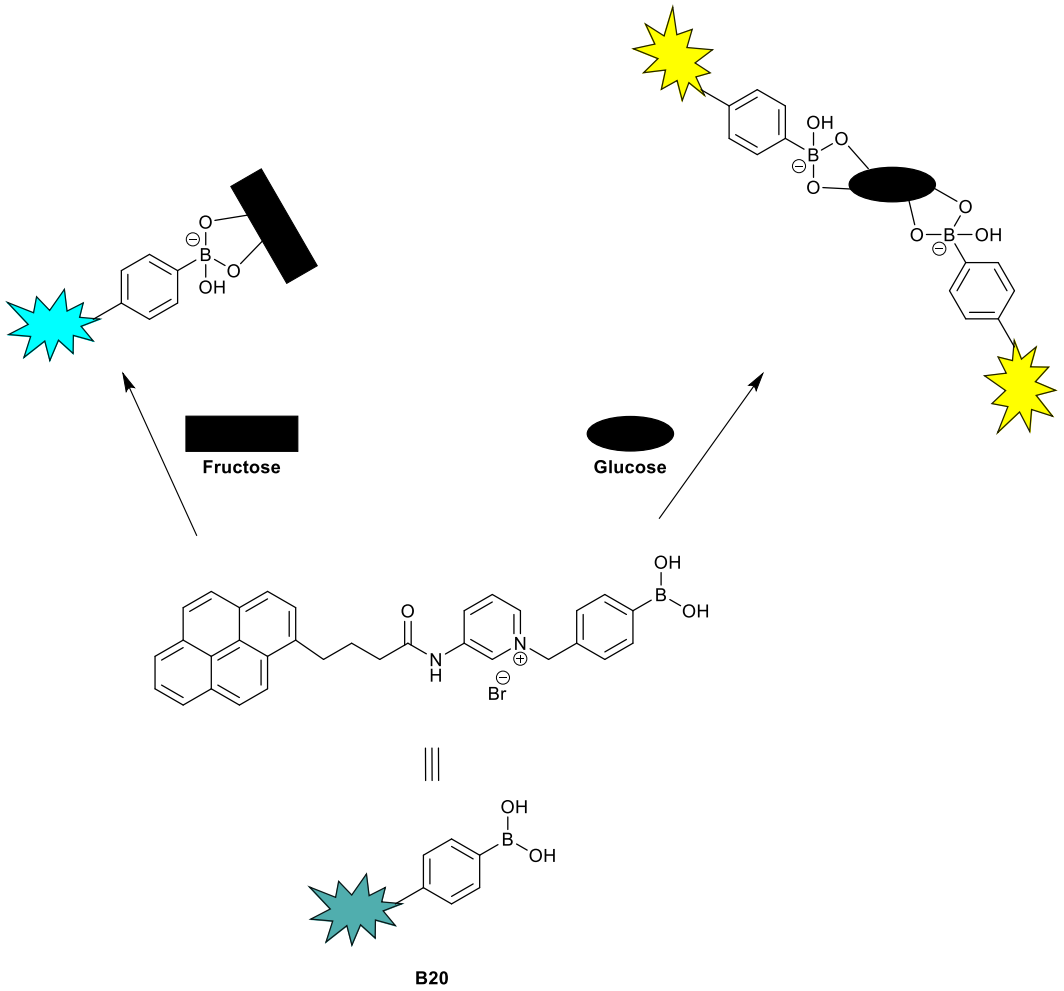
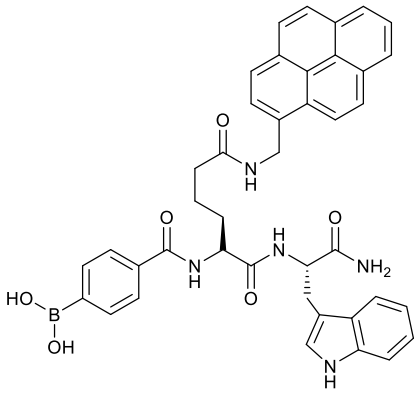


Figure 2.12: Schematic representation of the sensing mechanism in aqueous solutions at pH 10 of **B20** developed by James *et al.*, with cartoon representations of fructose and glucose. The colour of the fluorophore is representative of emission wavelength and intensity of the sugar conjugates, (blue = 377 nm, yellow = 510 nm)

The group of Lee *et al.*, employ a similar technique in ratiometric sensing of saccharides. A pyrene and tryptophan containing compound was synthesised as a water-soluble amphiphilic molecule aggregated in aqueous solutions by pyrene-pyrene stacking (**B21**, Figure 2.13). The titration of saccharides into aqueous solutions (pH 7.4, 1 % DMSO) of this compound led to the disaggregation and decrease in the excimer emission intensity measured at 470 nm, concurrently an increase of the emission intensity arising from the monomer is observed at 378 nm. As the binding is reliant on phenylboronic acid, and the compound is a mono-boronic acid,

a preferential binding is observed for fructose over glucose with binding constants of 1200 and 40 M^{-1} respectively.[74]



B21

Figure 2.13: Structure of the pyrene based dis-aggregation sensor, with the ability to measure saccharide concentration in aqueous solution at pH 7.4 via fluorescence, developed by Lee *et al.*

In 2018 a collective of two eminent names in boronic acid chemistry joined to give a consensus on the fluorescence "turn on" effect in *ortho*-methylaminophenylboronic acids. This type of compound first proposed by Shinkai *et al.* has already been discussed. There have been several mechanisms for the turn on fluorescence proposed in previous literature, including a PET mechanism,[70] and a pK_a switch.[75] Neither methods hold up entirely under scrutiny as they do not account for various phenomena observed. The authors synthesise a variety of known boronic acids (**B18**, **B22-B24**, Figure 2.14), and use them to test a hypothesis that the fluorescence changes occur due to an elimination of quenching via internal conversion, a non-radiative process in this case mediated by the presence of the $-B(OH)_2$ groups. The key finding in proving this theory is that addition of saccharide to a solution of every synthesised complex to saturation (judged by concentration at which there is plateau of fluorescence intensity increase) leads to an extremely similar emission intensity measured for compounds bare in deuterated solvent at pH 7.4. The authors therefore conclude that both previously suggested mechanisms are incorrect, and the new mechanism proposed fits all observed trends. The paper

therefore provides a unified theory and puts to bed any competing conclusions from past literature.[76]

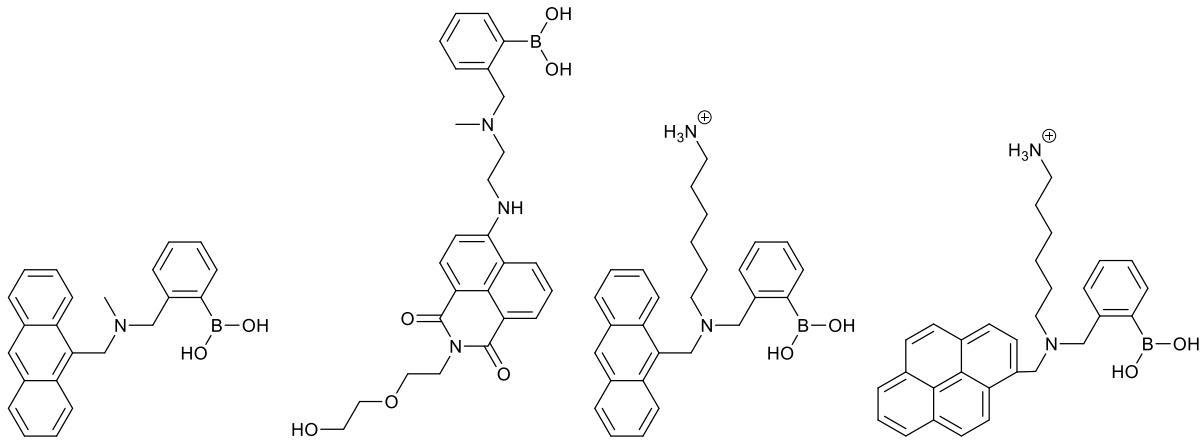
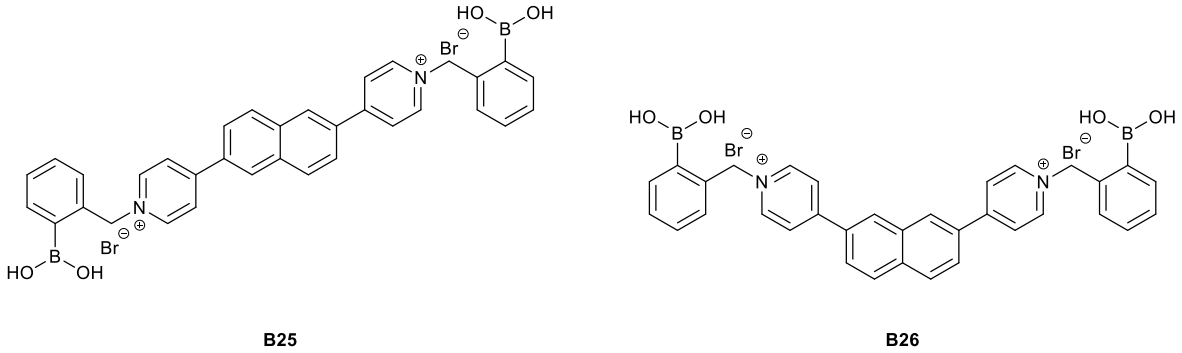


Figure 2.14: Compounds studied by James *et al.*, to elucidate a mechanism to aid in understanding the fluorescent intensity enhancement upon saccharide binding in *ortho*-methylaminophenylboronic acids

Resendez and Malhotra propose naphthyl-pyridinium receptors as saccharide sensing groups, that report through changes in the intensity of the fluorescence spectra. The authors hoped that the complexes may be used in binding assays for lactulose and mannitol, sugars that are utilised in gut permeability assays. The study mainly focuses on the binding of two di-boronic acid containing compounds to these sugars (**B25** and **B26**, Figure 2.15). Titrations were carried out in 0.1 M PBS solutions at pH 7.4 to mimic biological pH. An increase in the emission intensity is observed with subsequent additions of lactulose up to 4 mM for both boronic acid complexes wherein the emission intensity plateaus at a maximum. The authors subsequently studied the boronic acid complexes in a fluorescence recovery assay in which alizarin red dye is used to bind to the boronic acid complex and the release of this dye upon binding of an analyte, in this case saccharide, elicits an increased fluorescent signal. The binding of multiple saccharides is assessed through this method, and the binding constant between **B25** and the saccharides are determined at 2000 M^{-1} for fructose, 1000 M^{-1} for lactulose, and 20 M^{-1} for glucose. **B26** has lower but still high binding constants of 300 M^{-1} for both fructose and lactulose, and 20 M^{-1}

for glucose. Considering the discussion above (c.f. archetypal boronic acid sensors), it is somewhat surprising that the di-boronic acids do not show an increased affinity to glucose, the authors do not comment, however the reason could be the lack of flexibility in the mainly aromatic backbone to bind efficiently through both boronic acid moieties. It is also interesting to note that the authors assume 1:1 binding despite two boronic acid moieties, this is again not justified by the authors. In any case, high affinities to lactulose across the relevant concentration range for the permeability studies (100-900 μM) at physiological pH were observed and quantification with low interference in this range should therefore be possible.[77]



B25 **B26**

Figure 2.15: Di-boronic acids based on the napthyl-pyridinium backbone synthesised by Resendez and Malhotra, for the detection of lactulose

Wellington *et al.*, described the pH dependent sensing of 4-isoquinolineboronic acid, **B27**, assessed through fluorescence spectroscopy. Although the 4-isoquinolineboronic acid complex is commercially available, the authors wanted to test the affinity for sialic acid under acidic conditions, the resonance forms of this structure are shown in Figure 2.16. The sialic acid contains an α-hydroxycarboxylate moiety which is not the case in most of the commonly studies saccharides and diols (fructose, glucose, catechol). Fluorescent enhancement is observed in the 4-isoquinolineboronic acid complexes even at pH 7, and binding curves may be fit from the fluorescence enhancement at λ_{em} = 377 nm measured in 0.04 M aqueous phosphate buffer. Apparent binding constants at pH 7 are 1400 M^{-1} for fructose, 9 M^{-1} for glucose and 80 M^{-1} for Neu5Ac. After acidification to pH 3 the authors re-measured the binding constants and found a marked increase for the binding constant with Neu5Ac to 5400 M^{-1},

whilst both fructose and glucose displayed markedly less affinity at this pH, with binding constants of around 0.1 M^{-1} for both sugars. The marked decrease of glucose and fructose binding affinities is likely due to the protonation of hydroxyl groups found in the sugars. Conversely the increase in the binding affinity is suggested by the authors to come from the good match of this pH to the protonation of the nitrogen heterocycle whilst maintaining the ionisation in the α-hydroxycarboxylate moiety not found in the vicinal diols commonly studied.[78]

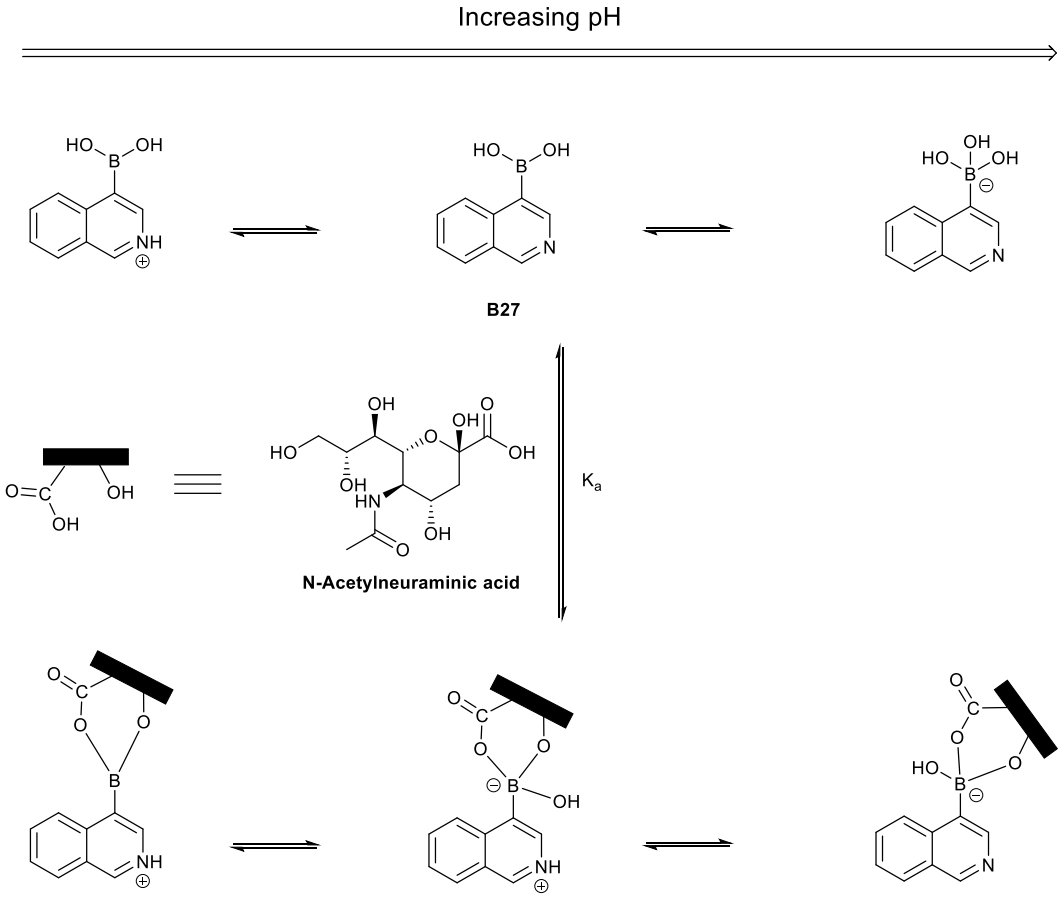
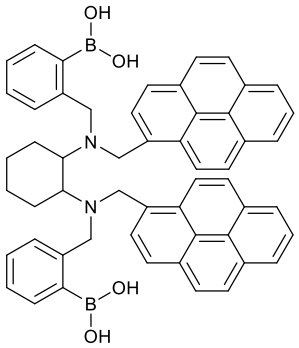


Figure 2.16: Resonance forms of 4-isoquinolineboronic acid, with the structure of Neu5Ac (N-acetylneuraminic acid) drawn. Also displayed are the resonance forms of the bound boronic ester with this sugar. The central resonance structure is presumed to be the fluorescently active form at pH 3.

An enantiomerically selective fluorescent sensor for D- and L-tartaric acid based upon chiral pyrene based boronic acids (**B28**, Figure 2.17) was developed by Xiao *et al.*. The emission spectra were recorded in DMSO:HEPES buffer 7:3, at a pH of 7.4. The complexes displayed remarkable enantioselectivity with (S,S)- enantiomer selective to L-tartaric acid with a K_S:K_R

(where K_S represents the binding constant of the (S,S)- enantiomer and K_R the (R,R)-enantiomer) of 7:1. The (R,R)- enantiomer displays a K_S:K_R of 1:5 with D-tartaric acid. The relative fluorescence enhancements upon the more selective sugar addition to are both around 40-fold when plateau in the emission intensity is reached (8 mM of D/L-tartaric acid) a rather large increase. The authors do not present any wholly aqueous studies likely due to aggregation effects in this solvent, the authors acknowledge the difficulty in solubilising this complex at high concentrations even for NMR characterisation.[79]



B28

Figure 2.17: Structure of the chiral boronic acid developed by Xiao *et al.*, the chiral centres lie on the cyclohexane ring, indicated by stars.

Glass *et al*., applied a boronic acid functionalised quinoline complex (**B29**, Figure 2.18) to catecholamine sensing. The sensor was able to be used as a fluorescent sensor with a "turn on" response to the catecholamines, with fluorescence intensity of the quinoline increasing upon diol binding when measured at λ_{exc} = 488 nm, λ_{em} = 510 nm. Several diols were titrated to ensure selectivity towards catecholamines (Figure 2.18). All catecholamines show strong binding constants $K_a > 10000\ M^{-1}$ in aqueous solutions at pH 7.4; conversely glutamate, lysine and glucosamine show binding constants $K_a < 100\ M^{-1}$ in the same conditions. The sensor also allowed differentiation of norepinephrine from dopamine due to the fluorescence increase upon norepinephrine binding and slight quenching on dopamine binding. The authors claim that this is the first time this discrimination is observed with a fluorescent sensor, making this a useful compound in biological assays for catecholamines.[80]

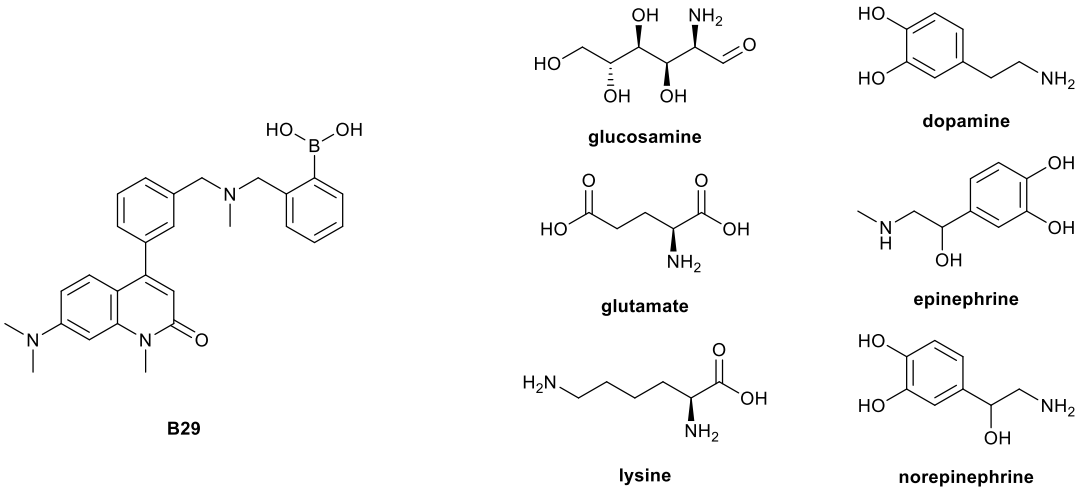
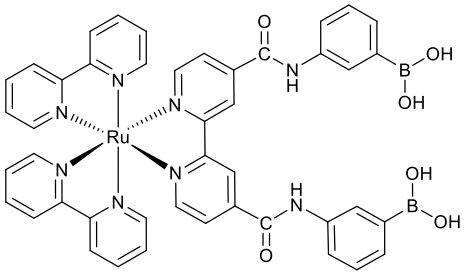


Figure 2.18: Structure of the quinoline derived boronic acid complex synthesised by Glass *et al*., B29, and the structures of the amines studied for their binding affinity.

2.1.6 Boronic acid containing transition metal-based sensors of saccharides by luminescence

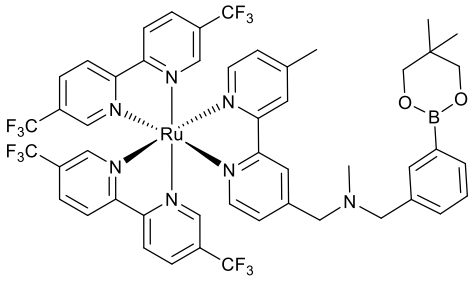
Ruthenium has been shown in the previous sections to be a useful electrochemical reporter for saccharide sensing, but only a few groups have used the metal for luminescent sensing of saccharides. The group of Deetz and Smith used a ruthenium(II) complex (**B30**, Figure 2.19) based upon the tris-bipyridyl analogue $[Ru(bpy)_3](PF_6)_2$ to efficiently bind phosphates of fructose and glucose. The sensor relies on the synergetic binding of phosphate and saccharide, as evidenced by the low binding constant in water vs. phosphate buffer for glucose, 30 vs. 1600 M^{-1} respectively. Binding studies of fructose-6-phosphate in water gave rise to similar binding constants of fructose in phosphate buffer, K_a = 1300 M^{-1}. The luminescence enhancement observed in these complexes is relatively small at I/I_0 of around 1.3 in water after diol binding.[81]



B30

Figure 2.19: Ru(II) complex synthesised by Deetz and Smith, the heteroditopic complex requires cooperative binding of both phosphate and diol containing units to efficiently bind.

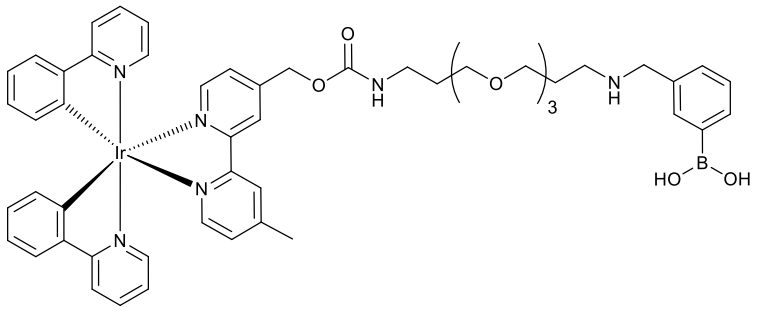
Cary *et al.* developed another ruthenium(II) complex (**B31**, Figure 2.20) for saccharide sensing based with a tethered phenylboronic acid.[82] It was found that this complex was not water soluble, despite the use of CF_3 groups to aid this, and could only be used in methanol. In spite of dissolution in methanol only small luminescence intensity increases of around 10 % were observed for the Ru(II) complex at 88 mM of glucose. This signal modification is neither as good as the previous ruthenium(II) complex, nor the ortho-methylaminophenylboronic acids published by Shinkai *et al*., furthermore the group had previously published rhenium(I) complexes for sugar sensing that were more sensitive.[83]



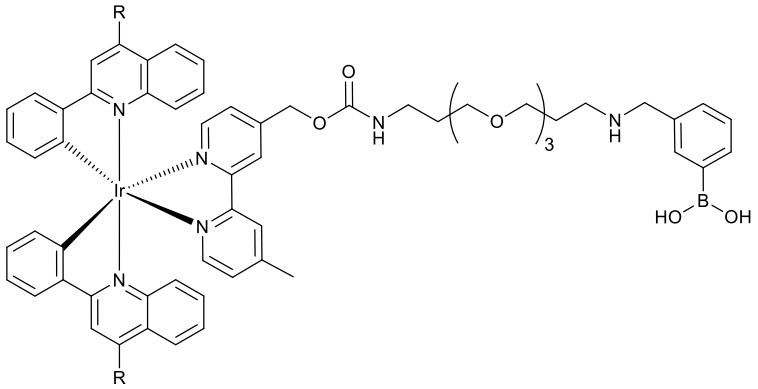
B31

Figure 2.20: Saccharide sensing ruthenium(II) complex synthesised by Cary *et al*., the complex is displayed with the boronic acid shown as the protected ester, the titrations were done as the ester and it is assumed that the ester is deprotected under measurement conditions

In 2017 the first example of an iridium(III) complex for saccharide sensing was developed by Lo *et al.* utilising a phenylboronic acid saccharide sensitive group bound to the bipyridine ligand through a triethylene glycol linker. The complexes show limited solubility in aqueous solutions requiring aqueous solutions with 10% DMSO during the binding studies. Binding is assessed through spectrophotometric measurements, with around a 10 % maximum change in absorbance from 0-10 mM of any sugar. Small changes are perhaps to be expected as the ^{1}MLCT transitions monitored in this titration are perhaps unlikely to change based on the lack of electronic communication between the PBA unit and the metal centre owing to its distance. Equally the ^{1}MLCT transitions of the Ir(III) metal centre to the 2-phenylpyridine/phenylquinoline ligands would likely be unaffected. The complexes binding to sugars was not assessed through luminescence spectroscopy, but the complexes were put into cell studies wherein the intensity of the luminescent signal decreased upon addition of free Neu5AC into the cells.[84]



B32



B33 R = H
B34 R = COOH

Figure 2.21: Ir(III) complexes designed by Lo *et al*., the tethered boronic acid groups allow for saccharide sensing.

2.1.7 Luminescent hydrogel-based saccharide sensors

A luminescent hydrogel developed by Singaram *et al.* includes a pyranine derivatised dye into the hydrogel network created by polymerising an acrylamide monomer containing pyranine-type dye with monomeric boronic acid species (**B35** and **B36**, Figure 2.22). The solution-based binding of the monomeric boronic acid species to saccharide was assessed by luminescence intensity increase and binding constants were elucidated at around 100 M^{-1} for both boronic acids at physiological pH. After polymerisation, the hydrogel slabs were affixed to the side of a quartz cuvette, buffered solutions of saccharide at varying concentrations were added to the cuvettes and the binding constants and response times were both assessed by luminescence intensity increases. Binding constants reflected those in solution with values for both hydrogels around 100 M^{-1}, surprisingly response times were high with stabilisation of the gels luminescent signal requiring roughly 15 mins after application of the saccharide solution.[85]

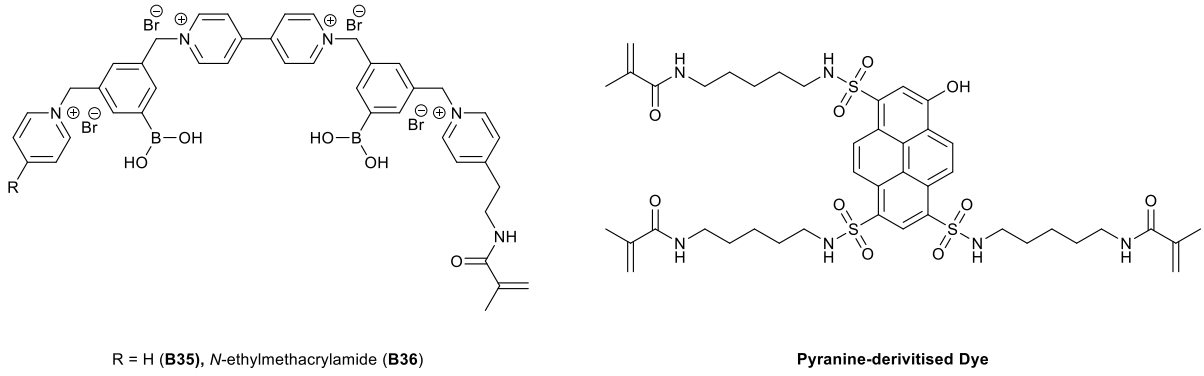


Figure 2.22: Boronic acid containing compounds **B35** and **B36** with acrylamide polymerizable groups synthesised by Singaram *et al*.. Also shown is the pyranine-derivitised dye that is used as a fluorescent reporter group for saccharide binding in the hydrogel systems.

Another pyranine dye-based hydrogel sensor for saccharides was developed by Florea *et al.*, with boronic acid monomers containing phenylboronic acid (Figure 2.23). Pyranine binds to the boronic acid moieties and the binding induces a quenching of the dye luminescence (λ_{exc} = 460 nm, λ_{em} = 510 nm). The recovery of the fluorescence when sugar is added both in solution and in crosslinked hydrogels is examined. In solution binding studies carried out in

buffered solutions at pH 7.4 authors report a binding constant of around 30 M^{-1} for both the ortho- and meta- boronic acid monomers that were synthesised. Hydrogel discs were synthesised through polymerisation of the boronic acid monomer of the meta-boronic acid with acrylamide and bis-acrylamide. The discs were immersed in the same pH 7.4 buffer and assessed for their glucose affinity through fluorescence recovery, with binding constant of around 100 M^{-1} reported for the hydrogel disc. It is important to also note however that the hydrogel luminescence is only increased by around 40 % upon glucose binding at 100 mM^{-1} whereas the dye-bound monomeric boronic acids in solution display a 5-fold increase in the luminescence intensity upon saccharide binding, clearly making this method more sensitive despite similar binding constants.[86]

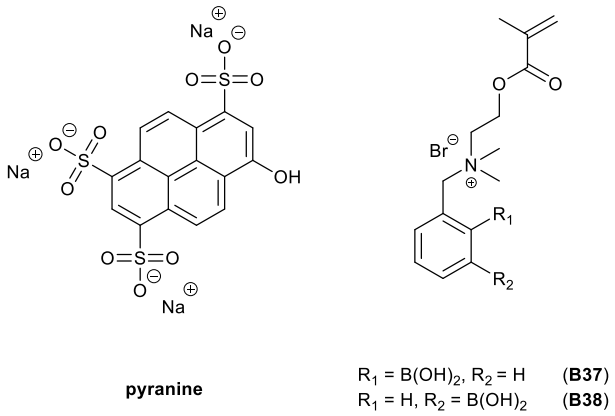


Figure 2.23: Pyranine dye structure, with the synthesised ortho- and meta- substituted phenylboronic acid derivatives synthesised by Florea *et al*.

ARS based fluorescence recovery is utilised by James *et al.*, in hydrogels with saccharide binding reliant upon benzoxaborole and phenylboronic acid moieties. To create the gels water, acrylamide, bis-acrylamide, and either 6-methacryloylamino benzoxaborole monomer, or 3-methacyryloylamino phenylboronic acid pinacol ester monomer (**B39** and **B40** repectively, Figure 2.24). Blank gels were also prepared wherein no boron containing compounds were added to the gels. Binding studies were performed through saturation of the gels with ARS after formation by immersion in 2 x 10^{-4} M solutions of the dye in PBS at pH 7.4. After

washing, only the dye specifically bound should remain, although it is important to note this is not the case and non-specific binding is observed in the blank gels. Despite this, the authors took the gels forward to binding studies using spectrophotometric titrations with glucose and upon immersion in glucose solutions. Increasing concentrations of glucose across a range of 0-1 M led to absorbance changes of 0.53 abs/g for the benzoxaborole gel, 0.34 abs/g for the phenylboronic acid, compared to a 0.19 abs/g change in the blank. The mechanism for the dye displacement is shown below (Figure 2.24). The binding constants were not assessed in this study, but fructose gives rise to higher absorbance changes of 0.94 abs/g as expected and shown in many other studies.[87]

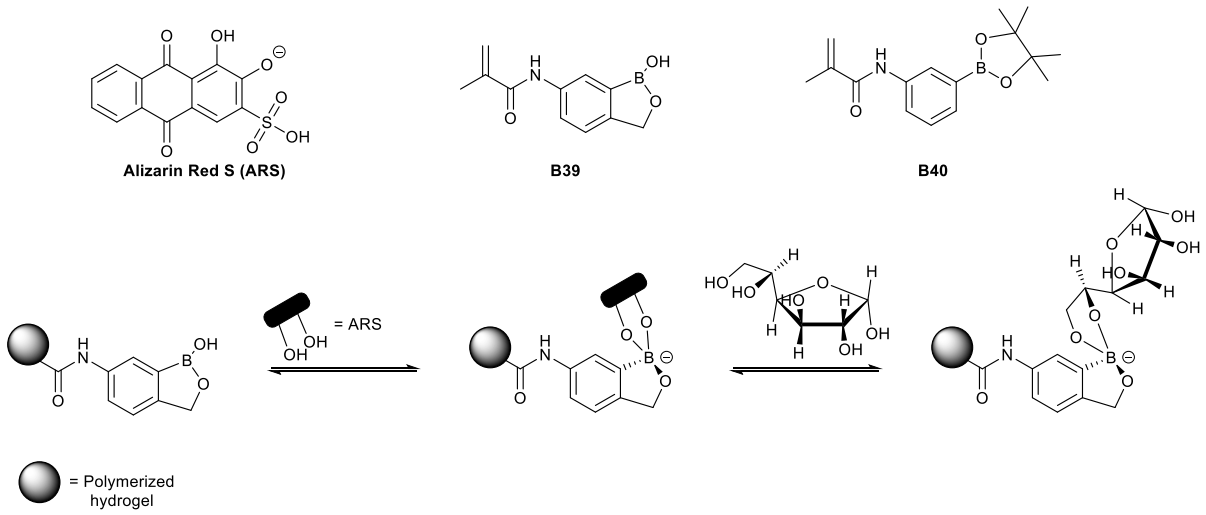


Figure 2.24: Structures of the boronic acid, benzoxaborole and ARS dye used by James *et al*. in a saccharide sensitive displacement assay, the dye displacement mechanism inside the polymerised gels is also displayed for the benzoxaborole gel with α-D-glucose

The group of Takeuchi *et al*. created injectable hydrogel beads which contain a crosslinked monomeric dye, **B42** which is based upon an anthracene backbone with bis-boronic acid developed by Shinkai *et al*.,[88] **B41** (Figure 2.25). The hydrogel beads were formed from the monomeric dye, and cross linkers widely commercially available, acrylamide and bis-acrylamide. Droplets were formed through dispersion of aqueous droplets in silicone oil before cross linking at 37 °C. Once synthesised the gels fluorescence intensity changes (λ_{em} = 488 nm)

over a glucose concentration range of 0-55 mM in a buffered aqueous solution at pH 7.4 was measured, and further tested for reversibility. The fluorescence at 55 mM is roughly 4-fold higher that that at 0 mM of glucose. Owing to their organic anthracene backbone one might expect photobleaching to hinder the effectiveness of these dyes as is previously observed in anthracene photodegradation studies.[89] Indeed, the authors report 20 % photobleaching after 25 mins of irradiation (405 nm, 5.7 mW cm^{-2}). Although the measurement times will be kept short <1 ms every 5 mins the issue may still arise that sun exposure will damage the beads limiting their use *in vivo*. Despite this, the authors took the studies into a mouse model, wherein the beads were injected into the interstitial space of the mice. Good agreement was found between fluorescent intensity changes in the hydrogel beads and induced fluctuations in the blood glucose of the mice with only a short time delay <30 mins, mostly accounted for by the known delay between interstitial concentrations and blood concentrations.[90]

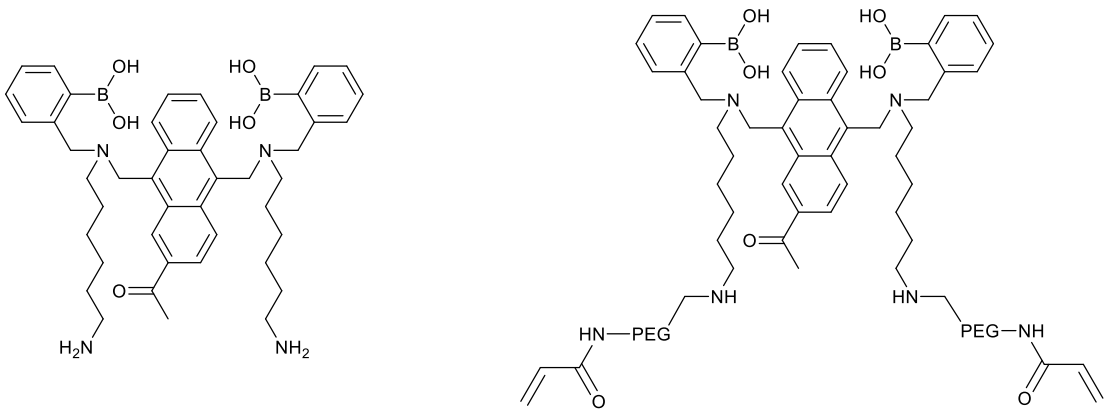
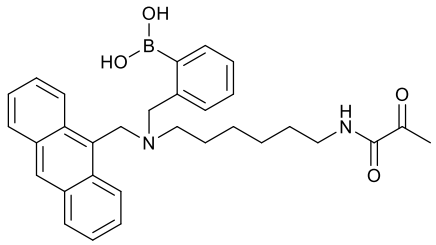


Figure 2.25: Structures of anthracene based bis-boronic acid complexes, **B41** developed by Shinkai *et al*., and **B42** with polymerizable moieties, synthesised by Takeuchi *et al*.

James *et al.*, followed with a further hydrogel synthesised from a monomeric sensing group based on the ortho-methylaminophenylboronic acid backbone developed by the same author previously (**B43**, Figure 2.26). The gel containing the boronic acid was polymerised based upon a radical polymerisation of the complex with acrylamide and bis-acrylamide. After, synthesis

the gels were compared to the solution binding characteristics of the monomer. A direct comparison is somewhat difficult though, as the monomer needs an aqueous potassium phosphate solution at pH 8 containing 52% methanol. The gels are also assessed for binding at pH 8 but are in a solely aqueous potassium phosphate solution. The binding constant for fructose is found to be around K_a = 1400 M^{-1} and 50 M^{-1} for the monomer and the hydrogel, respectively. The authors ascribe the difference to the inability of saccharide to diffuse through the gel although it may be unwise to directly compare binding in different solvents. The authors also state that the binding constant for glucose is too low to measure. The difficulty in solubilising the monomer in aqueous solvent and the pH necessary for the sensing of this hydrogel means that this sensor is slightly outside of the scope of biological applications.[91]



B43

Figure 2.26: Polymerizable boronic acid monomer designed by James *et al*. with anthracene-boronic acid backbone eliciting fluorescent enhancement upon saccharide binding in 52 % methanolic solutions at pH 8

2.1.8 Our aims

Dual-modality sensing *via* optical and electrochemical techniques allows for highly sensitive detection of analytes, and is less prone to false-positives due to the differing signal transduction pathways in each detection method.[92] In recent years dual-modality optical and electrochemical sensing has been applied to various analytes across the biological, and chemical sciences,[93-98] but has not been widely reported in saccharide sensing.

Supramolecular binding of boronic acid containing compounds with *cis*-1,2 and 1,3 diols is widely studied, and several reviews exist on this topic.[31, 32, 99] As the sections above clearly

demonstrate boronic acids have previously been evaluated as saccharide or diol responsive moieties through a multitude of methods including differential pulse voltammetry,[58, 63, 64] NMR spectroscopy,[51, 53, 54, 100] UV-Visible and circular dichroism spectroscopies.[43, 46, 101, 102]

Many more recent examples of boronic acids for detection of saccharides have utilized fluorescence based techniques,[73, 76, 77, 80, 90, 103, 104] and electrochemical techniques,[67-69, 105] but in the vast majority of cases have not combined the two. Only one exception is found, wherein a dipyrido[3,2-α:2′3′-χ]phenazine (dppz) molecule functionalised with boronic acid groups was used as a dual optical and electrochemical sensor through fluorescence enhancement and cyclic voltammetry. The compound however is only partially soluble in water, displays short emission wavelengths (<450 nm) and displays very small binding constants for glucose (K_a = 10^{-4} M^{-2}).[106]

Transition metal complexes are well poised to offer dual-mode electrochemical and photoluminescence signals,[107, 108] with examples of Ru(II) complexes and Ir(III) complexes previously having been shown to display sensing capabilities in both modalities simultaneously,[109-112] however this has not translated well to saccharide sensing. Limited examples of Ru(II) complexes have been published for saccharide sensing, the first needing the saccharide or solvent to contain phosphate groups for efficient sensing.[81] Alternatively, a second compound was found insoluble in water,[82] however in either study only the photoluminescence response was reported. Only one example of an iridium(III)-boronic acid complex exists for saccharide sensing. The complex displays poor water solubility, and the authors only report a binding response through spectrophotometry.[84] It is noted that the transition metal complexes have relied on tethering of a phenylboronic acid to the metal centre through an alkyl coupling leaving the metal centre far away from the sensing motif. A directly boronated ligand may increase electrochemical and luminescence signal modulation.

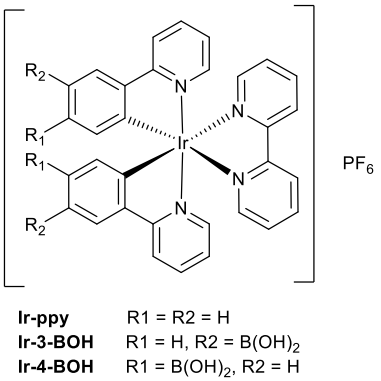
Iridium(III) complexes have been well documented by many groups as water soluble, low toxicity, photostable probes for biological imaging and luminescent detection of a variety of analytes.[113-116] Our group has previously investigated the use of heteroleptic iridium(III) complexes as luminescent biomolecular sensors for proteins,[117] and microscopy imaging agents.[118] It is worthwhile to note we have used heteroleptic phenylpyridine/bipyridine complexes often used in biological sensing, due to the LUMO (located on the bipyridine ligand) possessing a lower energy than in the homoleptic [Ir(ppy)$_3$] species, aiding in detection at longer wavelengths which in turn is useful for microscopy. We propose then the use of novel heteroleptic Ir(III) metal complexes as saccharide sensors that can overcome challenges currently observed in the field, from solubility, working pH range, and small spectroscopic changes whilst providing a framework to sense saccharides both electrochemically and through use of photoluminescence. The joint use of both techniques should also allow detection over varied concentration ranges.

We detail herein the properties of two novel, directly boronated heteroleptic Ir(III) complexes, **Ir-4-BOH** synthesised from the 2-(4-phenylboronic acid)pyridine ligand, **ppy-4-BOH**, and an Ir(III) structural analogue **Ir-3-BOH**, incorporating boronic acids for both photoluminescent and electrochemical detection of monosaccharides in aqueous solution at physiological pH. This will be the first work to use the same transition metal complex to sense saccharides through both detection techniques and will also offer an emission maximum above 600 nm. This is advantageous for microscopy studies, as when a bandpass filter is used it allows for deconvolution of the luminescence signal from autofluorescence displayed by proteins in the cell and matrix. We have also utilized the **Ir-4-BOH** complex in the fabrication of a luminescent hydrogel that is shown to be non-toxic and easy to synthesise.

2.2 Results and discussion

2.2.1 Synthesis and characterisation of boronic acid containing compounds

Two ligands based upon 2-phenylpyridine were synthesised in this work, subsequently allowing two iridium(III) complexes with boronic acid moieties **Ir-4-BOH** and **Ir-3-BOH**, and one previously reported analogous iridium(III) complex **Ir-ppy**, without the boronic acid moiety to be synthesised (Figure 2.27). The synthesis and characterisation of these complexes and relevant ligands is detailed in this section.

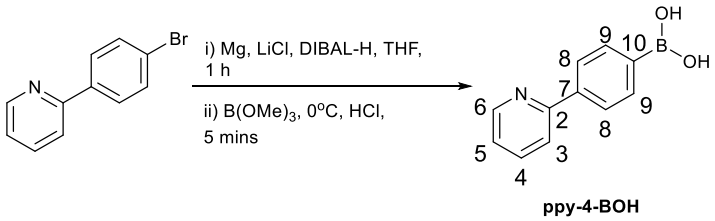


Ir-ppy R1 = R2 = H
Ir-3-BOH R1 = H, R2 = $B(OH)_2$
Ir-4-BOH R1 = $B(OH)_2$, R2 = H

Figure 2.27: Structures of all Ir(III) cyclometalated structures presented in this chapter. All complexes were isolated and studied as their PF_6 salts

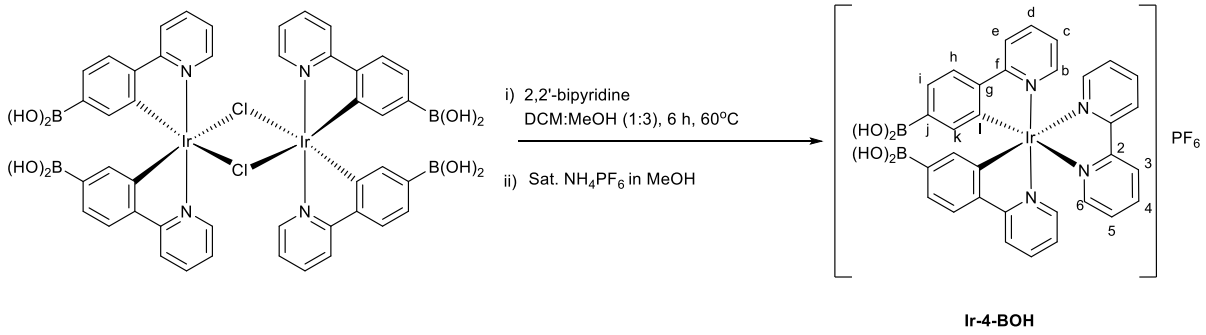
The ligand **ppy-4-BOH** was synthesised by a one pot Grignard reaction in accordance with previously published literature procedures for analogous boronic acid compounds.[119] The synthesis proceeds as per Scheme 2.2 and utilises the starting material 2-(4-bromophenyl)pyridine. The synthetic procedure is a general and convenient protocol for electrophilic borylation of aryl Grignard reagents by direct insertion of magnesium in the presence of LiCl; this is useful in avoiding the widely utilised cryogenic (-78^{o}C) reaction of aryllithium intermediates with trialkylborates. The product was synthesised in good yield and is characterised by both ^{1}H, ^{13}C, and ^{11}B NMR spectroscopies, as well as mass spectrometry (Supporting Information). Single crystals suitable for X-ray crystal structure analysis of **ppy-4-BOH** were also prepared by slow evaporation of a methanolic solution of the ligand. Meta-

substituted **ppy-3-BOH** was synthesised in a similar manner, but the characterisation is not presented due to discontinuation of this synthetic route (see later).



Scheme 2.2: Synthesis of boronic acid ppy-4-BOH

The iridium(III) complexes **Ir-4-BOH** and **Ir-ppy** are synthesised using an adapted method from Ohsawa *et al.*,[120] first synthesising a chloro-bridged dimer with the appropriate cyclometallating ppy ligands, before addition of an ancillary bpy ligand and purification using flash column chromatography on silica gel. The synthesis of **Ir-4-BOH** from the bpy, and the chloro-bridged dimer is detailed in Scheme 2.3. The **Ir-ppy** was characterised by ^{1}H, ^{13}C spectroscopies and mass spectrometry with data agreeing with that previously published for this complex.[120] **Ir-4-BOH** was characterised by ^{1}H, ^{11}B NMR spectroscopies, as well as by mass spectrometry, and elemental analysis (Supporting Information).



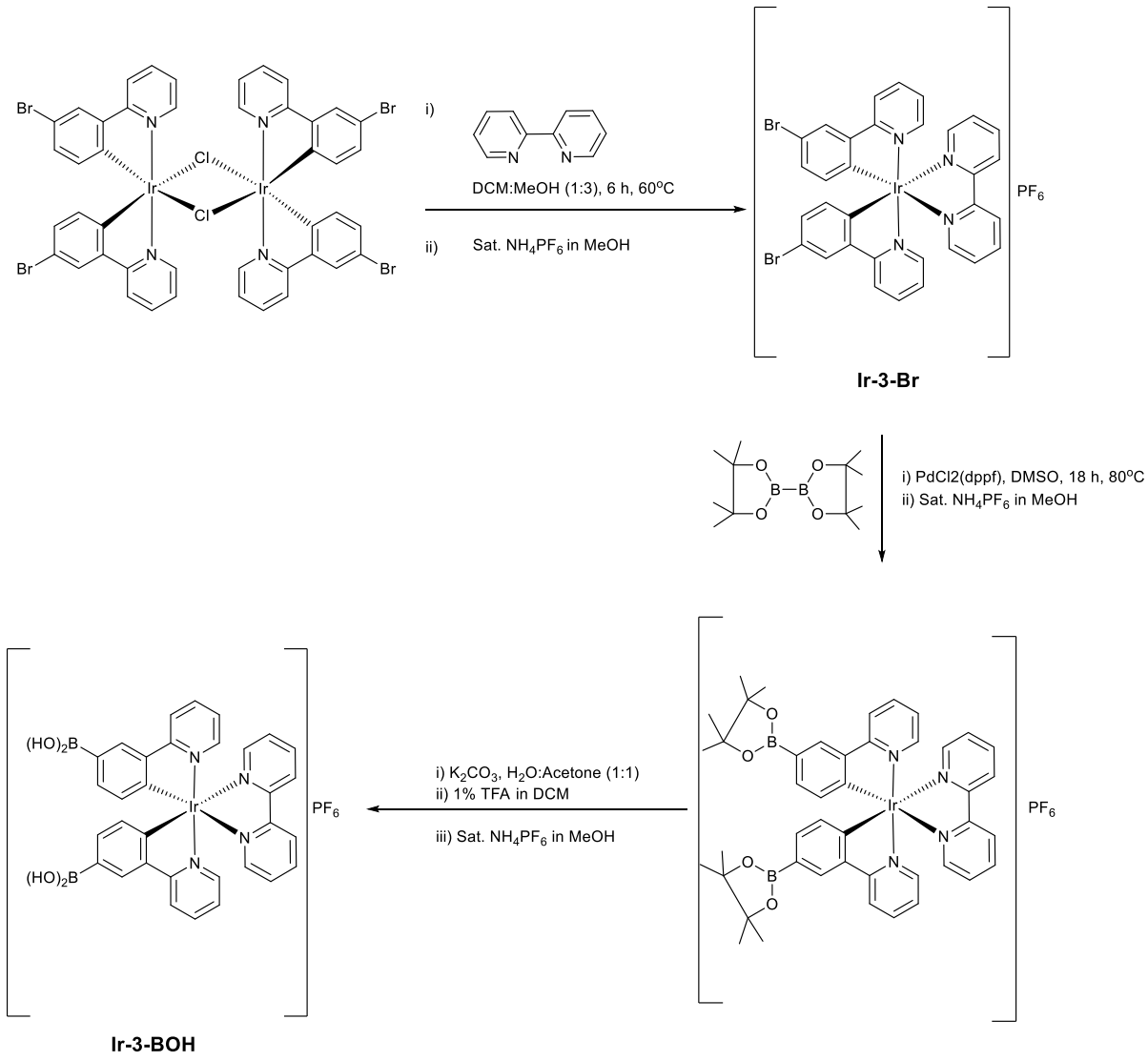
Scheme 2.3: Synthesis of Ir-4-BOH from the chloride bridged dimer

The ^{1}H NMR spectrum of **Ir-4-BOH** (Supporting Information) shows variation from the spectrum of **Ir-ppy** (Supporting Information) in protons H-i, H-j, and H-k, along with the disappearance of the ^{1}H signal arising from H-j. The ^{1}H signal arising from the $B(OH)_2$ moiety is also clearly visible as a broad singlet at 5.74 ppm. The accompanying ^{11}B spectra shows a

peak at 29.3 ppm, this fits with chemical shifts commonly assigned to $B(OH)_2$ groups.[51, 54] In the electrospray mass spectrometry (Supporting Information) a mass at m/z = 745.1769 is observed, the calculated monoisotopic mass is m/z = 745.1768. This is a difference of <1 ppm and therefore with other evidence confirms the presence of the desired species.

In the case of the **Ir-4-BOH** and the **Ir-ppy** complexes the synthesis proceeded directly from the relevant ppy ligand to the final complex without need for protecting groups or modifications. Conversely in the **Ir-3-BOH** complex, attempted synthesis directly from the boronated ligand ppy-3-BOH yielded only the unsubstituted **Ir-ppy** complex. Successful synthesis of **Ir-3-BOH** was therefore carried out by a multi-step synthesis detailed in Scheme 2.4.

In the first step **Ir-3-Br** is synthesised using the aforementioned method adapted from Ohsawa *et al.*, and characterised by ^{1}H and ^{13}C NMR and mass spectrometry (Supporting Information).[120] In the second stage the iridium(III) complex was converted to a pinacol protected boronate ester via an adapted Miyaura borylation utilising a palladium(0) catalyst $PdCl_2(dppf)$.[121] The presence of the desired protected product was confirmed by mass spectrometry, but the crude compound was used in the next step without purification. The final step concerned the deprotection of the boronic ester to yield the boronic acid **Ir-3-BOH**. This was achieved through adapting existing literature methods, first stirring in an alkaline solution of sodium bicarbonate before acidifying with 1 % TFA in DCM.[122] The desired product was purified via preparatory TLC on alumina. The final two steps of the reaction were low yielding, with an overall yield of 3 %. This is likely due to complete removal of the boronic acid group, which is indeed observed when running TLC, as a spot with a matching R_f to the **Ir-ppy** complex is observed. However, the product was isolated in sufficient yield and purity to



Scheme 2.4: Full synthetic route to **Ir-3-BOH** from chloride bridged dimer containing bromine substituents.

continue with photophysical studies. The characterisation of the product by ^{1}H NMR in DMSO-d_6 reveals the presence of the $B(OH)_2$ peak at 7.91 ppm. Mass spectrometry reveals many ionised species, the principle of which is found at 787.10 m/z (Supporting Information). This corresponds to the trimethylated complex. Methylation during electrospray mass spectrometry is commonly observed in boronic acid species, alongside dehydration products and boronate esters.[123] This mass however confirms presence of both boronic acids within the structure.

2.2.2 Photophysical properties of Ir(III) complexes

The UV-Visible and steady state emission spectra of complexes **Ir-4-BOH**, **Ir-3-BOH**, and **Ir-ppy** were investigated in solution, both in pure CH_3CN, and aqueous PBS (0.01 M) containing 2% CH_3CN. The photophysical properties of all complexes are summarised in Table 2.1. UV-Visible, steady state emission and lifetime values have been reported for **Ir-ppy**, and whilst experimentally obtained data has been reported in this study, the values match well with previous literature values from several sources.[107, 124-128]

Table 2.1: Summary of experimentally obtained photophysical data for Ir(III) complexes in various solvents. a) 298 K λ_{exc} = 350 nm b) 298 K λ_{exc} = 375 nm c) H_2O was an aqueous solution of PBS (0.01 M) containing 2% CH_3CN. Errors are estimated for emission wavelengths at ± 1 nm, emission lifetimes ± 10%, emission quantum yields ± 20%.

		Absorption	emission				
	Solvent	λ /nm (ε / 10^4 M^{-1} cm^{-1})	λ_{max} /nm	Φ^a		τ^b / ns	
				aerated	deaerated	aerated	deaerated
Ir-4-BOH	CH_3CN	261(4.12), 291 sh(2.70), 307 sh(2.22), 349 sh(0.71), 415 sh(0.34)	610	0.042	0.118	55	320
	H_2O^c	261(4.32), 292 sh(2.70), 310 sh(2.09), 350 sh(0.69), 400 sh(0.38)	618	0.004	0.014	40	45
Ir-ppy	CH_3CN	254(4.48), 265 (4.33), 310 sh(1.98), 375 sh(0.56), 410 sh(0.33)	606	0.049	0.165	65	320
	H_2O^c	254 (4.31), 310 (1.86), 375 sh(0.52), 405 sh(0.33)	618	0.022	0.035	40	45
Ir-3-BOH	CH_3CN	257(4.07), 265(3.97), 310(1.82), 339sh(0.76)	594	0.037	0.076	60	350
	H_2O^c	255(3.88), 310(1.98), 340(0.96)	593	0.022	0.042	70	70

UV-Visible absorption spectra reveal that all novel synthesised complexes display archetypal electronic transition features of Ir(III) cyclometallated complexes (Figure 2.28a-f).[107, 126, 128] For the Ir(III) complexes in CH_3CN there is a transition observed at 265 nm for **Ir-ppy**, 261

nm for **Ir-4-BOH** and at 255 nm for **Ir-3-BOH**, assigned to a ligand centred transition of the phenylpyridine ligand (^{1}LC, $\pi-\pi^*$), which is spin-allowed and gives rise to highly absorptive band with $\varepsilon > 10000$ M^{-1} cm^{-1}.[120, 124, 129-134] The hypsochromic shift of 4 nm **Ir-ppy** to **Ir-4-BOH**, and subsequent 6 nm from the **Ir-4-BOH** to the **Ir-3-BOH** can be explained by the addition and position of the boronic acid moiety. The regiochemistry of the substituent with respect to the Ir–C bond is given a Hammett value ($\sigma_{m/p}$), which parameterises the electron-withdrawing or donating character of a functional group based on whether it is situated meta or para- to the substituent of interest. In this case the $B(OH)_2$ group is acting as a weakly electron withdrawing group, as evidenced by reported values of $\sigma_{m/p}$ of -0.01 and 0.12 for meta- and para- substituted respectively.[135]

The absorption spectra also display less intense shoulders in the region 320 – 415 nm. These transitions are assigned as arising from ^{1}MLCT transitions ($d\pi(Ir)\rightarrow\pi^*$(2,2'-bipyridine and phenylpyridine type ligand)) and are characteristically weaker than the ^{1}LC bands, with molar absorptivity in the range $3000 < \varepsilon < 10000$. [120, 124, 129-134]

Upon excitation all Ir(III) complexes in this study exhibit sub-microsecond luminescence with intense orange to red colour, exact wavelengths are recorded in Table 2.1, whilst emission spectra are displayed graphically below (Figure 2.28a-f). **Ir-ppy** displays emission at a measured maxima of 606 nm, matching well with the reported value of 602 nm.[126] The emission maxima for **Ir-4-BOH** is found at 610 nm in CH_3CN and 618 nm in PBS; for **Ir-3-BOH** these values are 594 and 593 nm respectively. The blue shift apparent in the complexes emission wavelength is due to the more electron withdrawing effect of the $B(OH)_2$ group when para to the iridium-carbon bond (c.f. Hammett values).[135] The electron withdrawing effect of the substituent appended to the phenyl ring of the 2-phenylpridine type ligand serves to stabilise

the HOMO, increasing the HOMO-LUMO energy gap and leading to a blue shift in the emission wavelength.[107, 136]

The luminescence lifetimes of both complexes at room temperature were measured in deaerated 0.01 M aq. PBS solutions containing 2% MeCN, and in pure MeCN. **Ir-4-BOH** and **Ir-3-BOH** in the PBS solutions show lifetimes of 45 ns and 70 ns respectively. In deaerated MeCN lifetimes are 320 ns and 350 ns for **Ir-4-BOH** and **Ir-3-BOH** respectively, in a similar range to that reported for **Ir-ppy** (τ = 370 ns).[124] The quantum yield is of 1 % and 4 % for **Ir-4-BOH** and **Ir-3-BOH** respectively in the PBS solution, whereas quantum yields for **Ir-4-BOH** and **Ir-3-BOH** are 12 % and 8 % respectively in deaerated MeCN, similar to the reported value for **Irppy** (14 %).[125] The quantum yield of all complexes decreases significantly in water which can be explained by the sensitivity of the charge transfer state to the external environment.[113] Luminescence lifetimes and quantum yields of the **Ir-4-BOH** and **Ir-ppy** complexes show a sizeable decrease versus those in MeCN. Luminescence lifetimes decrease from 320 ns to 45 ns in both complexes and the quantum yield decreases to 1 % and 4 % respectively in deaerated PBS solution. The **Ir-3-BOH** show a more modest decrease from 8 % to 4 %, switching from MeCN to PBS but concurrently shows a large drop in the luminescence lifetime from 350 ns to 70 ns, suggesting structure may play a large part in the solvent sensitivity of these boronic acid substituted Ir(III) complexes.

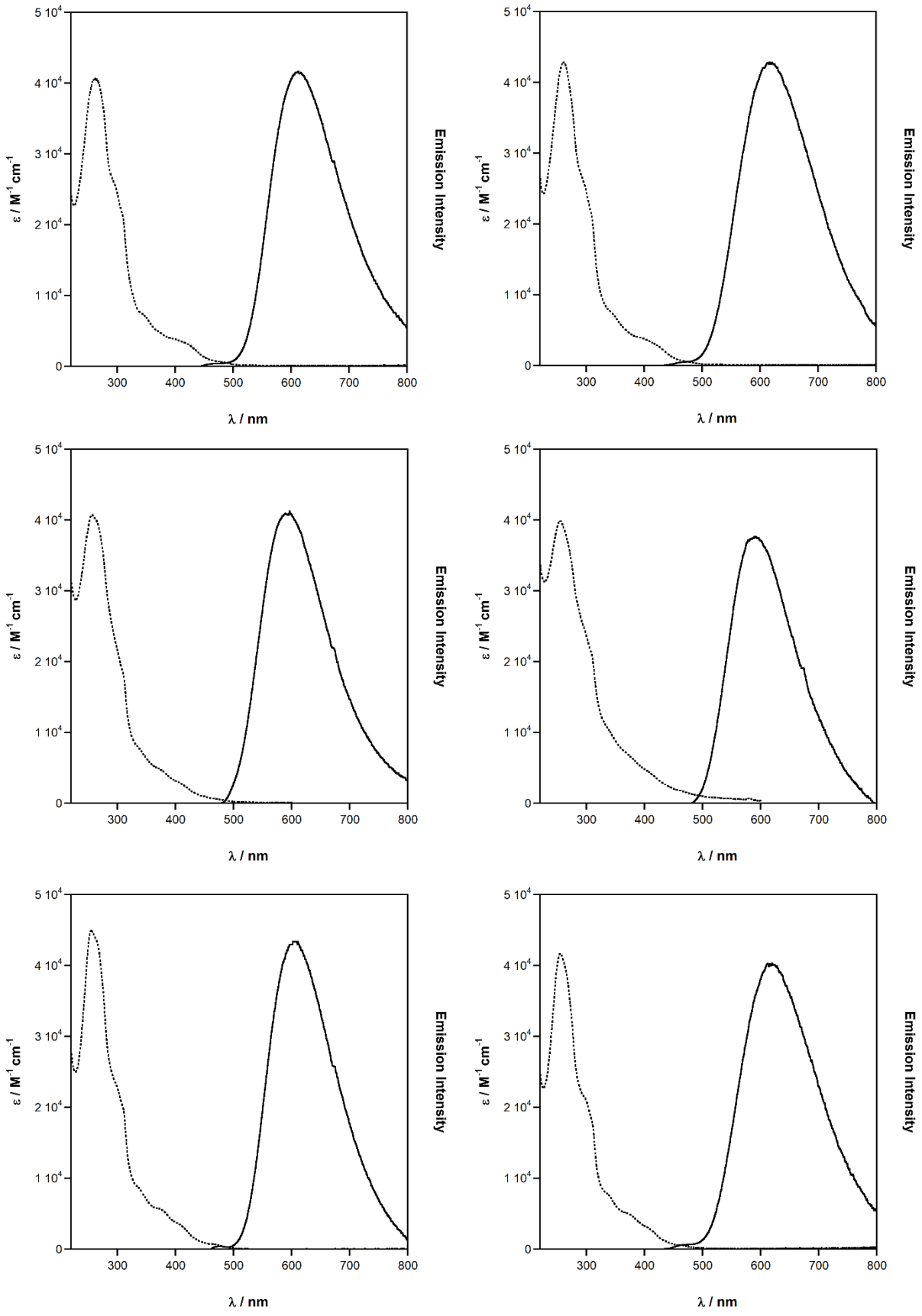


Figure 2.28: Electronic absorption spectra (dotted line) and emission spectra (solid line) of a) **Ir-4-BOH** in CH_3CN b) **Ir-4-BOH** in aqueous PBS (0.01 M) containing 2% CH_3CN c) **Ir-3-BOH** in CH_3CN d) **Ir-3-BOH** in aqueous PBS (0.01 M) containing 2% CH_3CN e) $[Ir(ppy)_2bpy](PF_6)$ in CH_3CN f) $[Ir(ppy)_2bpy](PF_6)$ in aqueous PBS (0.01 M) containing 2% CH_3CN

2.2.3 Sugar sensing by photophysical effects in solution

Complexes **Ir-4-BOH** and **Ir-3-BOH** contain a boronic acid functional group which should facilitate monosaccharide binding, leading to a change in the UV-Vis, photoluminescence properties of the complex. The **Ir-ppy** complex is used as a control, and due to the lack of functional group should remain unaffected by addition of monosaccharides into solution. To verify this, the monosaccharide glucose was added to solutions of complexes **Ir-4-BOH**, **Ir-3-BOH** and **Ir-ppy** in PBS (0.01 M aq. PBS with 2% CH_3CN, pH 7.4) mimicking biological pH conditions. In the case of **Ir-4-BOH** and **Ir-ppy** titrations were also carried out with fructose. Sugars were first added as a solution in 0.01 M PBS (aliquots of 2.5 μL, 2 M saccharide solution) up to 10 mM and then as powder to avoid dilution effects. The UV-Vis spectrum of the complexes was measured at each addition point of the relevant sugar. Decreases in the absorption intensity of boronic acid complexes upon selective binding to a diol is not uncommon in the literature, and is in some cases used to fit the binding constants of boronic acid complexes.[38, 47, 69]

Upon monosaccharide addition to **Ir-4-BOH**, the absorption peaks centered at 261 nm decreased in intensity, display a total reduction in intensity of 18 % for glucose and 15 % for fructose, at a concentration of 50 mM of the respective sugar (Figure 2.29). The charge transfer bands at wavelengths >350 nm remain largely unaffected by the addition of monosaccharide.

In the case of **Ir-3-BOH** when glucose is added to the solution the absorption peak at 255 nm decreases in intensity by 25 % (Figure 2.30). Similarly to the spectra taken for **Ir-4-BOH** the peaks at wavelengths >350 nm seemingly are less affected by the increasing concentration of monosaccharide.

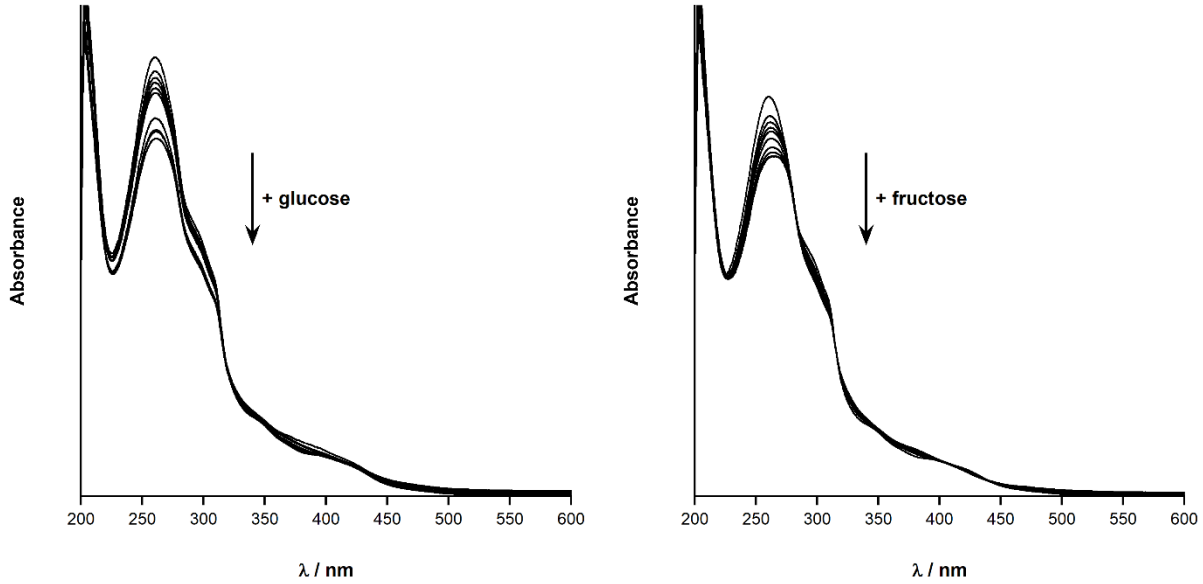


Figure 2.29: UV-Visible absorption spectra (40 μM in 0.01 M aq. PBS with 2% CH_3CN, pH 7.4) of (left) Ir-4-BOH with glucose additions to 50 mM. (right) Ir-4-BOH with fructose additions to 50 mM. Concentrations shown are 0, 2, 4, 6, 8, 10, 20, 30, 40 and 50 mM

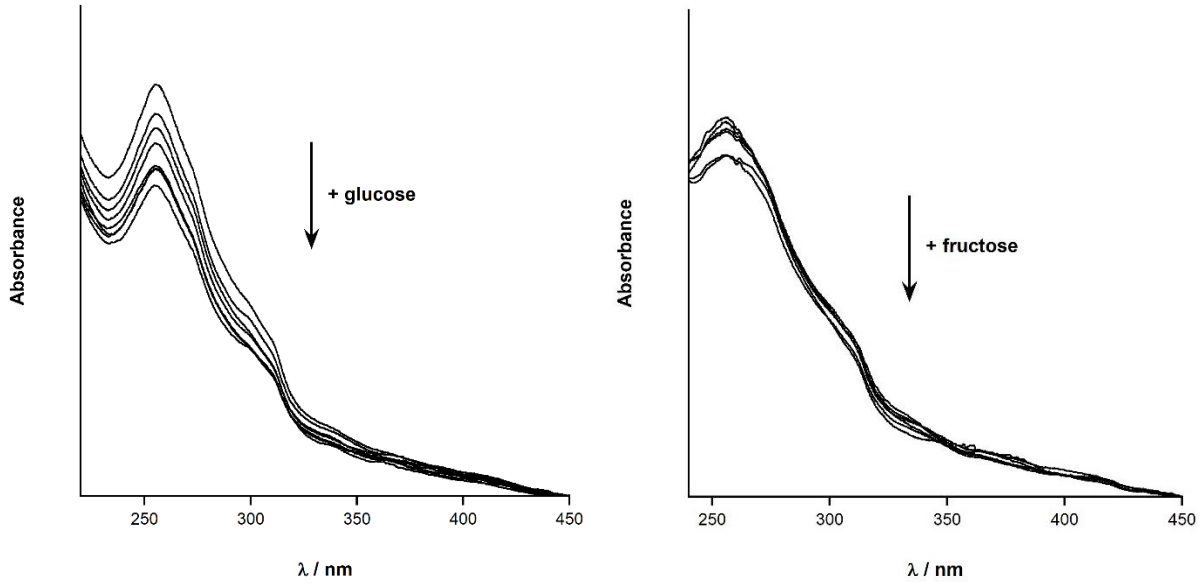


Figure 2.30: UV-Visible spectra of complex **Ir-3-BOH** (4 μM in 0.01 M aq. PBS with 2% CH_3CN) with varying amounts of monosaccharide

As previously mentioned, controls to these sugar binding experiments were carried out in the form of titrations of monosaccharide into a solution of **Ir-ppy**. The spectra display negligible changes through the concentration range of 0 - 30 mM of monosaccharide (Figure 2.31). These results therefore confirm a specific interaction with the boronic acid moiety, as expected.

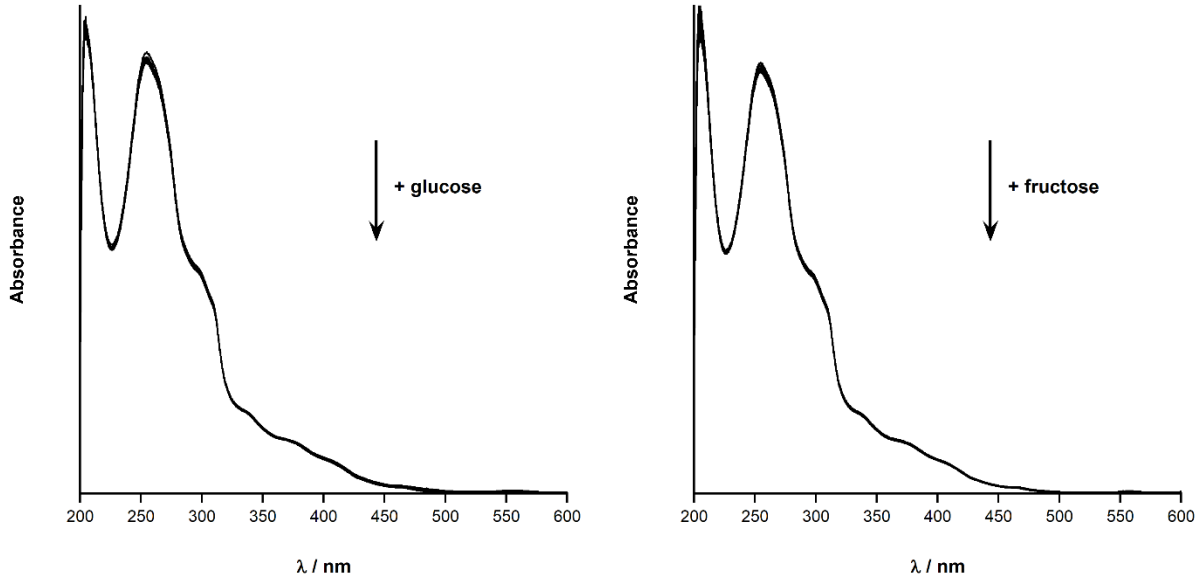


Figure 2.31: UV-Vis spectra of complex Ir-ppy (40 μM in 0.01 M aq. PBS with 2% CH_3CN) with varying amounts of monosaccharide. (left) Ir-ppy with glucose additions to 30 mM, (right) Ir-ppy with fructose additions to 30 mM. Concentrations shown are 0, 2, 4, 6, 10, 15, 20, 25 and 30 mM

More often than UV-Visible absorption, fluorescence is used as the monitoring tool for boronic acid-diol binding.[37, 38, 40, 42, 47, 76, 77, 79, 85, 91, 137-139] In accordance with this convention the emission spectra of the Ir(III) complexes were also measured upon each addition of diol. The spectra for **Ir-4-BOH** (Figure 2.32) and **Ir-3-BOH** (Figure 2.33) display decreases in intensity upon each successive addition of monosaccharide, in both the case of glucose and fructose.

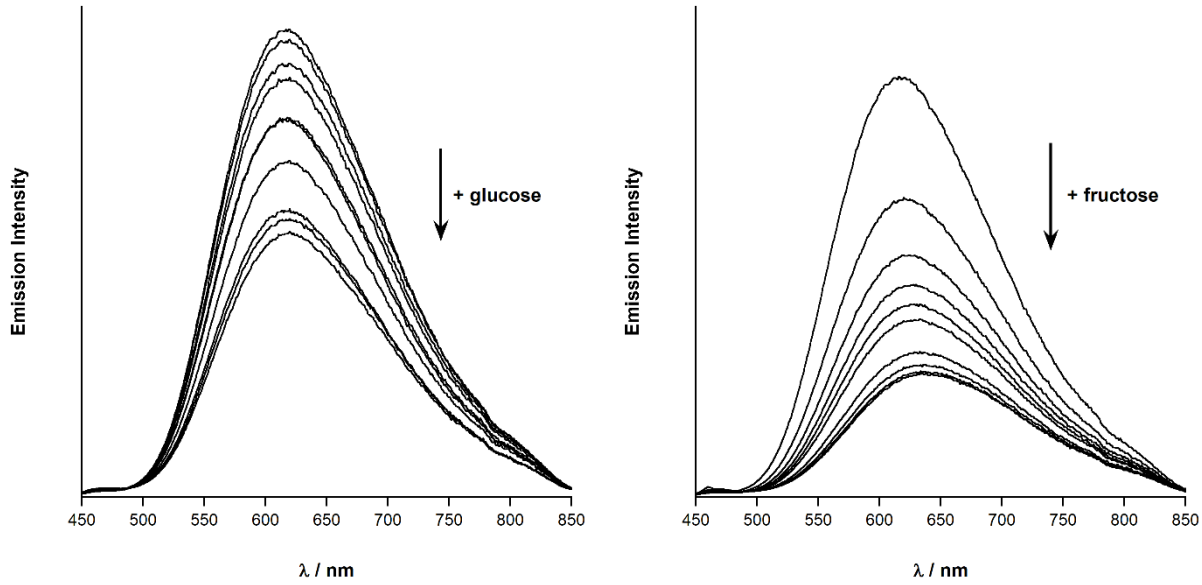


Figure 2.32: Emission spectra (40 μM in 0.01 M aq. PBS with 2% CH_3CN) of (left) Ir-4-BOH with glucose additions to 50 mM. (right) Ir-4-BOH with fructose additions to 50 mM. Concentrations shown are 0, 2, 4, 6, 8, 10, 20, 30, 40 and 50 mM. (λ_{exc} = 350 nm).

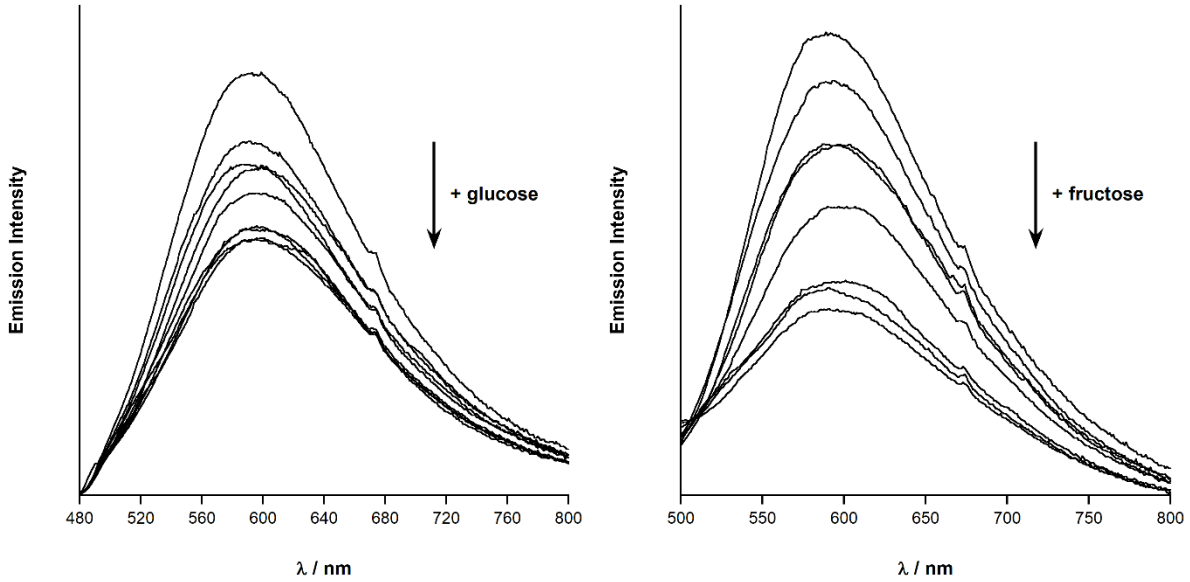


Figure 2.33: Emission spectra of **Ir-3-BOH** (4 μM in 0.01 M aq. PBS with 2% CH_3CN) with varying amounts of monosaccharide. (left) **Ir-3-BOH** with glucose additions to 70 mM. (right) **Ir-3-BOH** with fructose additions to 70 mM. Concentrations of saccharide shown are 0, 2, 4, 6, 8, 20, 30, 50 and 70 mM. (λ_{exc} = 350 nm).

There is no shift in the emission maxima; with luminescence suppression reasoned to be due to the binding of the sugars through the boronic acid moiety. To confirm this, the same experiment was performed on **Ir-ppy**, with no decrease in the luminescent intensity observed (Figure 2.34). This therefore confirms a specific interaction with the boronic acid is responsible for the decrease in emission intensity.

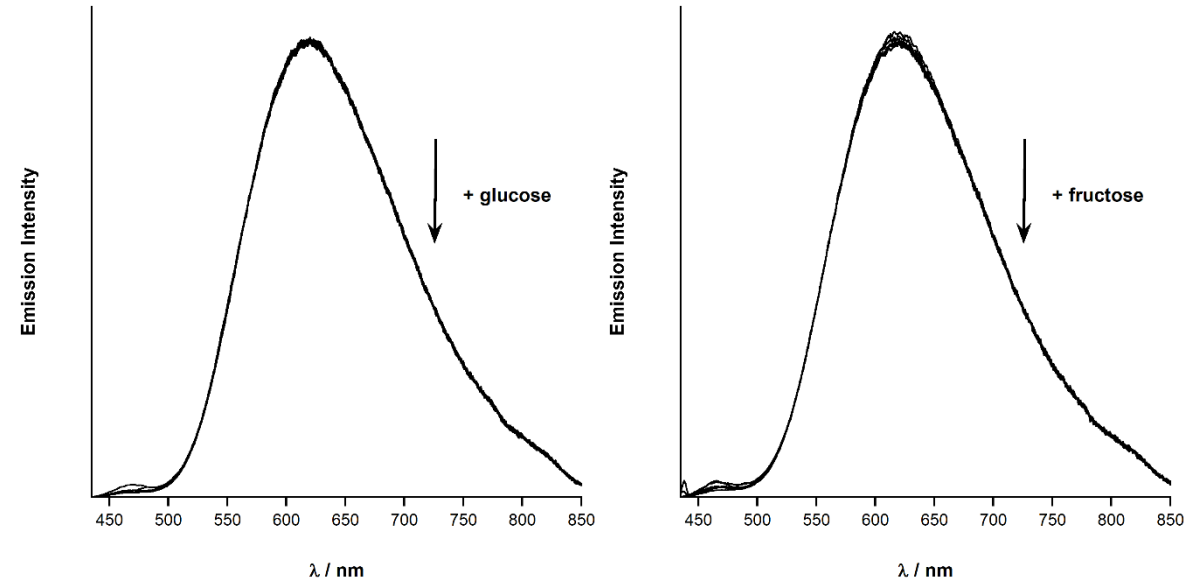


Figure 2.34: Emission spectra of Ir-ppy (40 μM in 0.01 M aq. PBS with 2% CH_3CN) with varying amounts of monosaccharide. (left) Ir-ppy with glucose additions to 30 mM. (right) Ir-ppy with fructose additions to 30 mM. Concentrations of saccharide shown are 0, 6, 10, 15, 20, 25 and 30 mM. (λ_{exc} = 350 nm).

One possible explanation for changes in the luminescence properties of fluorescent boronic acid compounds upon diol binding was investigated by Anslyn *et al.* in which study it is suggested that the -$B(OH)_2$ groups are mediators for radiationless relaxation.[76] The authors describe a "loose bolt" effect in which transformation of the -$B(OH)_2$ group into either a -$B(OMe)_2$, -$B(OD)_2$, or -$B(OR)_2$ where R = sugar, leads to an increase in the fluorescence intensity.[76] Seemingly, similar logic could be applied to the Ir(III) complexes, wherein a transformation of -$B(OH)_2$ to -$B(OR)_2$ where R = sugar, leads to a luminescence decrease. In this work the weakening of the ^{3}LLCT (ILET, ppy to bpy) contribution in addition to a less efficient π-π* transition of the phenylpyridine mediated by the -$B(OH)_2$ to -$B(OR)_2$ transformation would explain both the UV-Vis and luminescence observations, explain why the MLCTs observed are quenched to a lesser extent than those of the LC transitions, and further explain the lack of signal change in the **Ir-ppy** complex. The suspected charge transfer pathways in **Ir-4-BOH** are shown in Figure 2.35 and are based off those reported for **Ir-ppy**.[140-142]

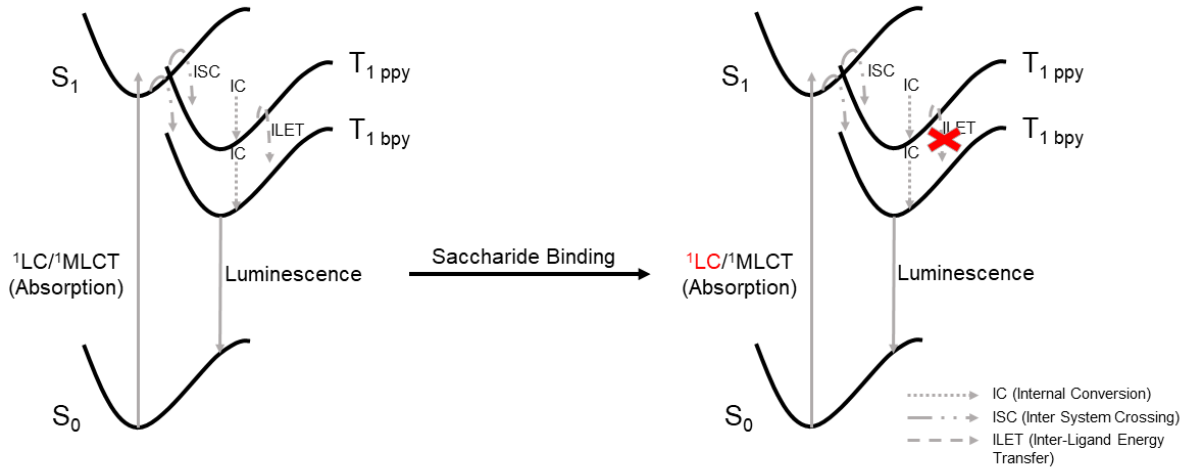


Figure 2.35: Schematic representation of the proposed relaxation processes apparent in Ir-4-BOH before and after addition of monosaccharides into solution. Absorption from S_0 to S_1 is representative of all ^{1}MLCT and ^{1}LC charge transfers to the respective ppy or bpy ligands. Relaxation can occur radiatively or non-radiatively denoted by solid or dashed arrows respectively. Non-radiative relaxation pathways to the S_0 state are not shown for clarity. Red highlights the photophysical processes suspected to be affected by saccharide binding.

2.2.4 Binding Constants for Ir(III) complexes with glucose and fructose

Using the data collected from the luminescence titrations it is possible to fit binding curves for **Ir-4-BOH** and **Ir-3-BOH** with both glucose and fructose. Careful selection of a method for binding constant determination is required. Within the literature several differing spectroscopic titration fitting methods have been detailed in the determination of saccharide association constants with boronic acids, including the Benesi-Hildebrand method,[41, 143, 144] Stern-Volmer plots,[39, 40, 45, 77, 145] and through 1:1 quadratic fitting with mean of least-squares iteration.

In this work we chose to fit all binding constants via a quadratic equation, adapted for use with luminescence spectroscopy. The underlying reason for this is that there is no need to make assumptions in the excess of the sugar, or that the quenching pathway leads to a completely non-emissive complex, assumptions inherent when using other fitting methods.[146] The derivation of the equation used is detailed in the experimental section of this chapter. It has been previously described for UV-Vis, NMR and fluorescence titration.[146-148]

The binding constant determination relies on measurement of (F_0-F) vs. [monosaccharide], where F is defined as the area of the luminescence spectrum found by integration. As such binding curves were plotted for each sugar with both **Ir-4-BOH** and **Ir-3-BOH**, these plots therefore offer a value for the saccharide association constant (Figure 2.36 and 37); values are summarized in Table 2.2.

Table 2.2: Summary of the binding constant values elucidated by 1:1 quadratic fitting of the values for F_0-F vs. concentration of saccharide. Values are obtained from the mean of least squares iteration with error expressed as error in the fitted value.

Complex	Sugar	Binding Constant / M^{-1}
Ir-4-BOH	glucose	82 ± 11
	fructose	331 ± 25
Ir-3-BOH	glucose	305 ± 42
	fructose	139 ± 16

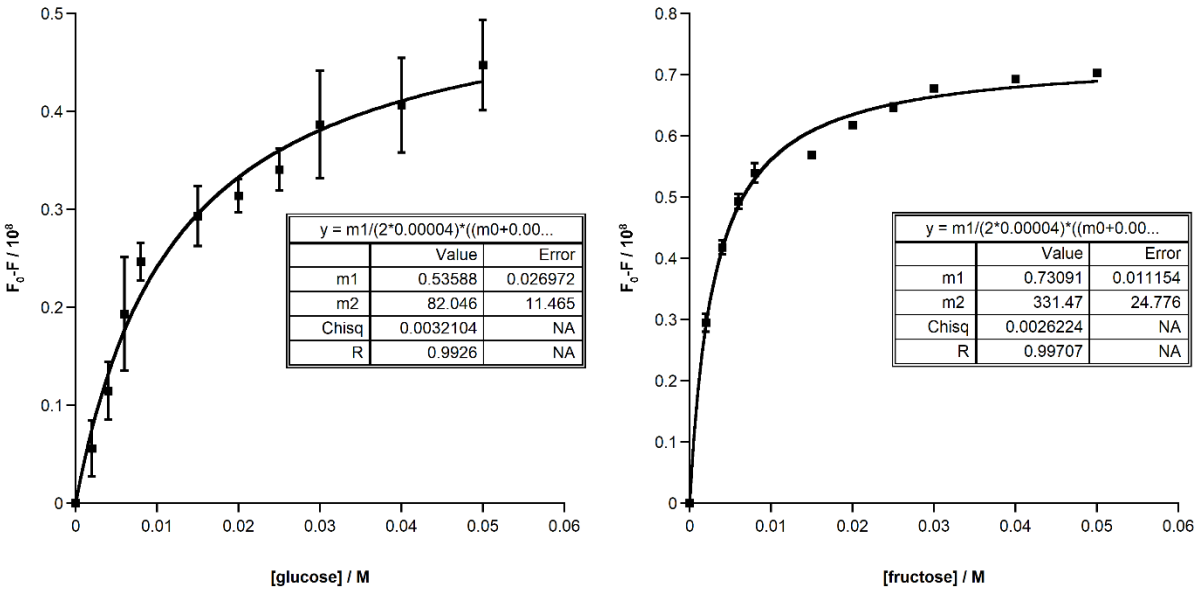


Figure 2.36: 1:1 quadratic fits of the binding of Ir-4-BOH to each sugar in solution (40 mM Ir(III), 0.01 M aq. PBS with 2% CH_3CN, pH 7.4). Points are an average determined from 3 runs. Error bars are standard deviation in the repeat measurements.

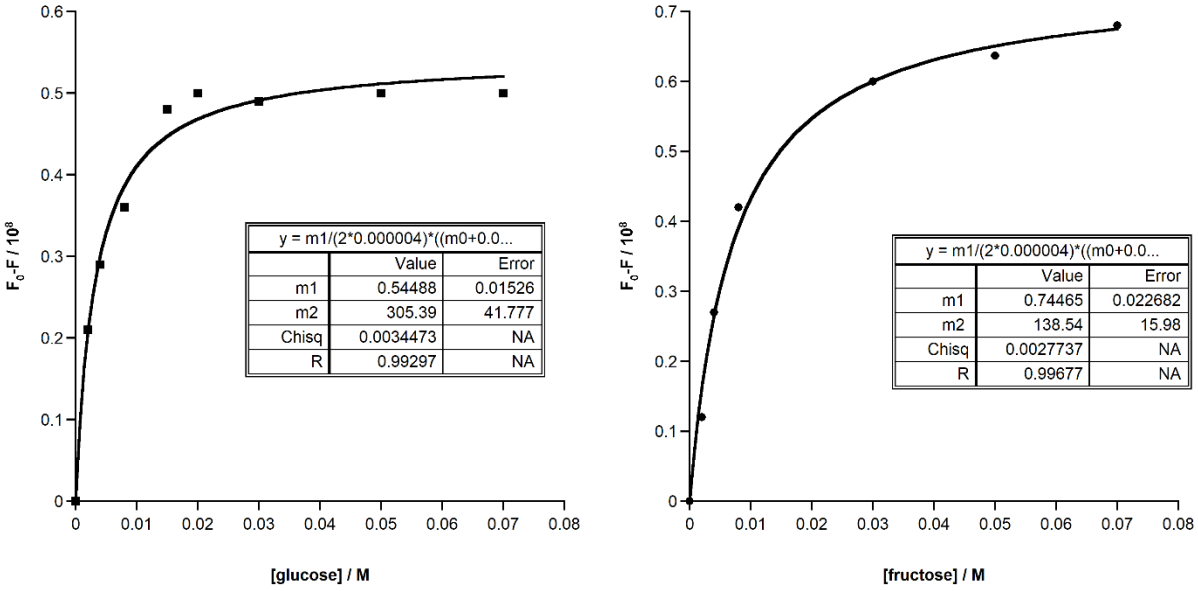


Figure 2.37: 1:1 quadratic fits of the binding of **Ir-3-BOH** to each sugar in solution (4 mM Ir(III), 0.01 M aq. PBS with 2% CH_3CN, pH 7.4)

Apparent binding constants for **Ir-4-BOH** with glucose and fructose are 82 ± 11 and 331 ± 25 M^{-1} respectively which sit higher than some recently seen examples of boronic acids in the literature.[78, 86, 103, 149, 150] These values are also high compared to the simple phenylboronic acid binding constants at pH 7.4; of 4.6 and 180 M^{-1}, for glucose and fructose respectively.[37] For **Ir-3-BOH** the binding constant is much higher in the case of glucose and lower in the case of fructose. Binding constants are calculated in the same manner and give values of 305 ± 42 and 139 ± 16 M^{-1} for glucose and fructose respectively. As we did not separate the **Ir-4-BOH** and **Ir-3-BOH** reaction products into their component stereoisomers, there was likely presence of more than one conformation of each Ir(III) complex in the saccharide sensing solutions. With non-equivalent boronic acid binding sites present within the Ir(III) complexes, and the knock on effect of binding chiral sugars we likely form diastereoisomers. The Ir(III) stereoisomers potentially have differing binding constants, although the binding constants given reflect the overall average of the as synthesised complexes.

For **Ir-3-BOH** saturation is reached around 20 mM of glucose this is slightly lower than the upper end of the biologically relevant range for glucose sensing which is around 30 mM.[151-153] The **Ir-3-BOH** complex could however be of use in scenarios where accurate determination of glucose concentration is needed in a lower concentration range. It was therefore decided to continue with structural studies, and to fabricate devices solely for **Ir-4-BOH**.

2.2.5 Characterisation of the boronic ester complex

Whilst the UV-Visible and steady state emission experiments provide near refutable evidence for the specific interaction of diol with the boronic acid moiety, empirical evidence should be obtained by other methodologies. Mass spectrometric analysis of solutions containing diol and boronic acid,[154-156] and multinuclear NMR studies,[53, 54, 76, 157] are common methodologies used

to provide evidence of boronic ester formation. It was therefore decided to probe the formation of Ir(III)-boronic ester complexes with the aforementioned techniques.

MALDI mass spectrometry was used to confirm the presence of both mono- or di-substituted boronic esters of the metal complexes. Mass spectra show several peaks, found at 889.2, 903.2 and 1033.3 m/z. The calculated monoisotopic masses for **Ir-4-BOH** bound to glucose are 889.2 m/z for $IrC_{38}H_{34}N_4O_8B_2$ (**Ir-4-BOH**-α-D-glucofuranose) and 1033.3 m/z for $IrC_{44}H_{42}N_4O_{12}B_2$ (**Ir-4-BOH**-(α-D-glucofuranose)$_2$) which relate to the single glucose boronic ester complex, di-glucose boronic ester respectively (Figure 2.38 and 39). The observed peak at 903.2 m/z can be assigned to a methylated adduct of the single substituted boronic ester, the methylation effect has previously been observed in mass spectrometry of boronic acids, adding validity to the observed masses.[123] In the case of **Ir-3-BOH** the mass observed is 889.6 m/z which fits well to the expected monoisotopic mass of 889.2 m/z as shown (Supporting Information).

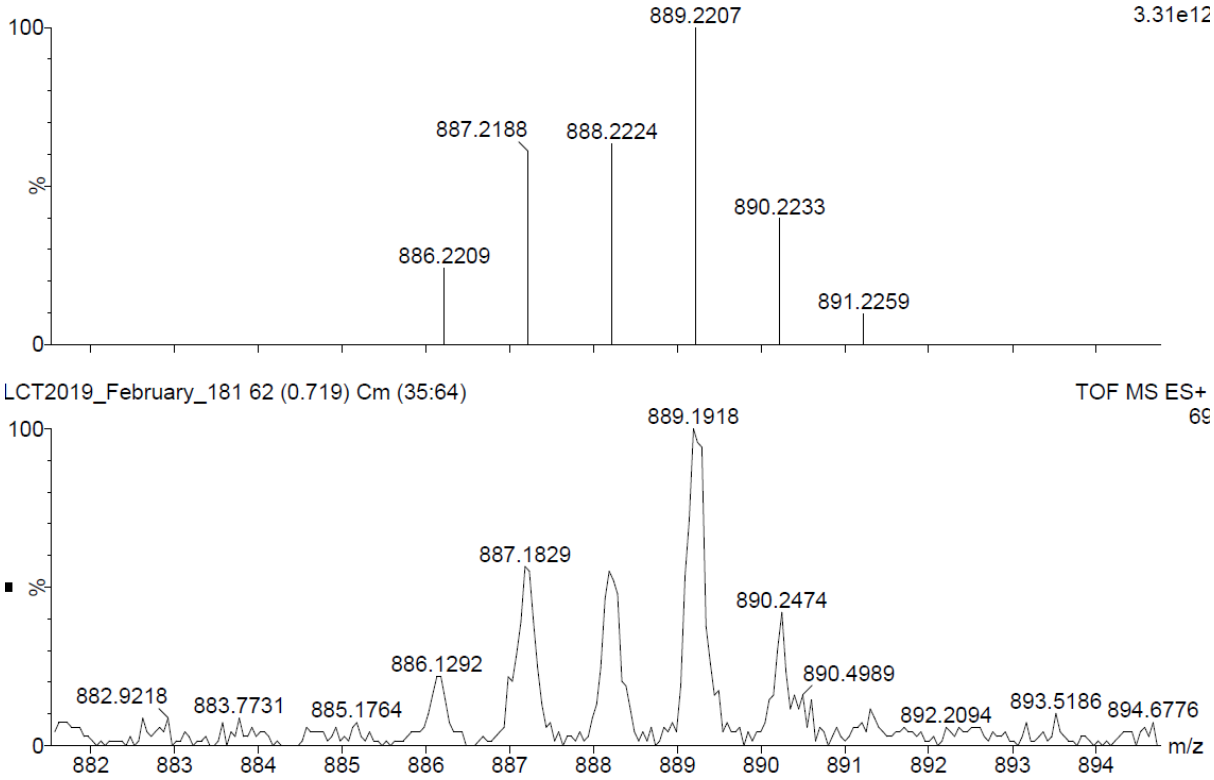


Figure 2.38: (top) Modelled Isotope pattern for Ir-4-BOH-α-D-glucofuranose, (bottom) Experimentally obtained MALDI mass spectrum for Ir-4-BOH after addition of 100 mM of glucose. (1:1, CH_3CN:H_2O) using DHB matrix.

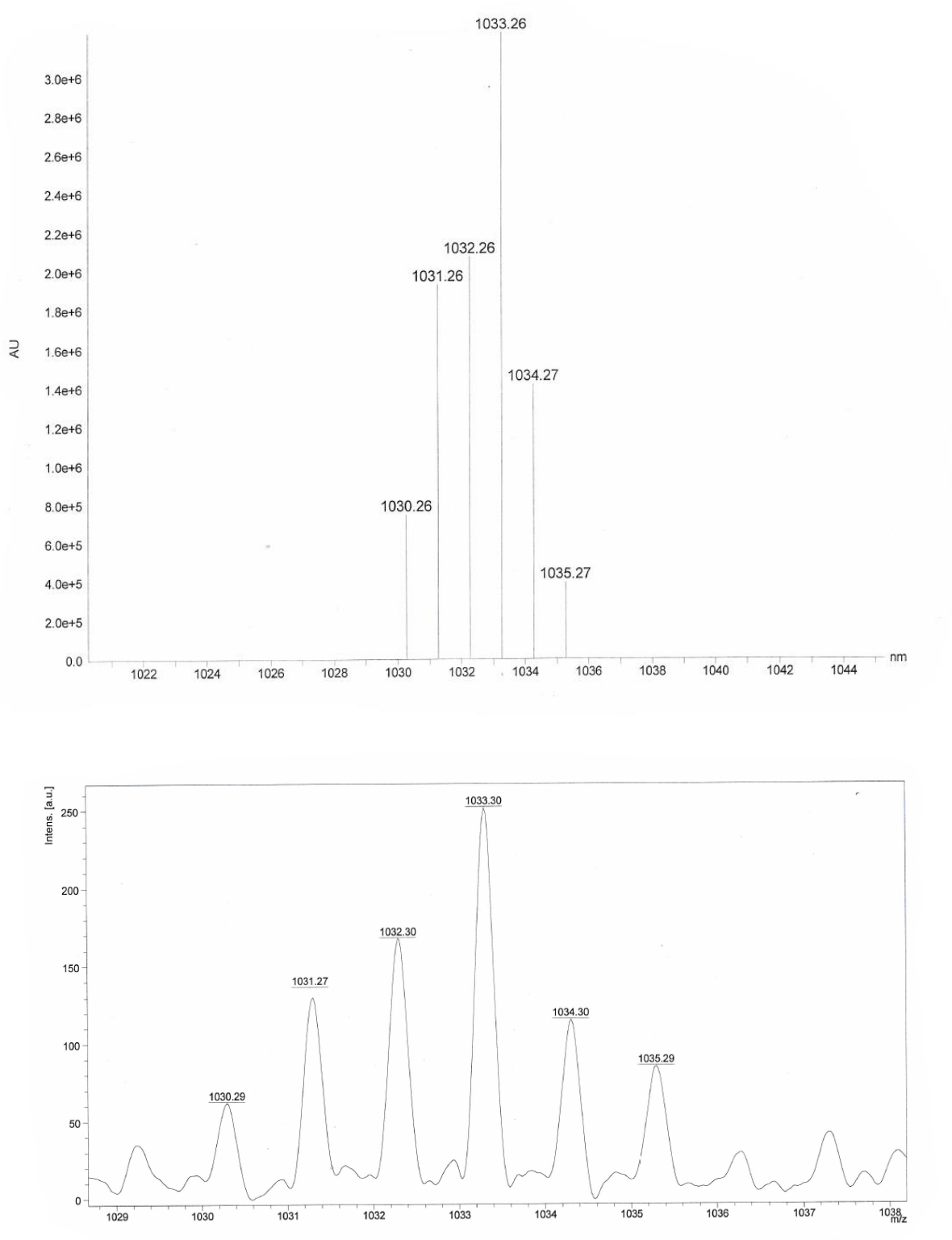


Figure 2.39: (top) Modelled Isotope pattern for Ir-4-BOH-(α-D-glucofuranose)$_2$, (bottom) experimental mass spectrum gained via MALDI experiment for Ir-4-BOH after addition of 100 mM of glucose. (1:1, CH_3CN:H_2O) using DHB matrix.

As previously mentioned NMR spectroscopy has also been utilized in previous papers to yield binding information of boronic acids.[158] The main goal of NMR in these compounds is to confirm the binding of *cis*-diols by shifts in both the boronic acid ^{11}B signal, and as in recent studies by a ^{19}F active reporter moiety on the diol itself.[54] In this work we used the fluorinated diol, 3-fluorocatechol; as well as the fluorinated analogue of glucose, 2-fluoro-2-deoxy-D-glucose (FDG). Experiments pertaining to the binding of the **Ir-4-BOH** complex to 3-fluorocatechol were carried out in CH_3CN, and in the case of FDG in DMSO, this is due to the precipitation of the Ir(III) complex in D_2O at the high concentrations needed to perform NMR studies.

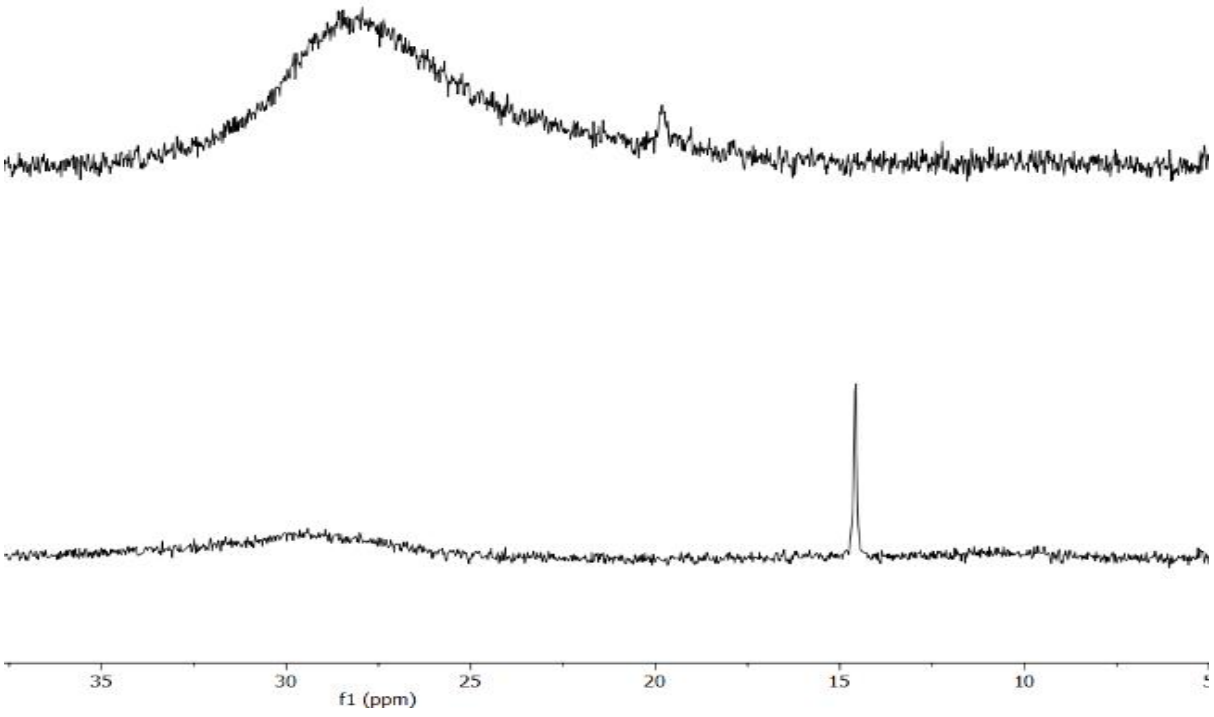


Figure 2.40: (top), ^{11}B NMR of Ir-4-BOH in acetonitrile-d_3 (~3mM). (bottom) ^{11}B NMR of Ir-4-BOH in acetonitrile-d_3 after addition to 100 mM 3-fluorocatechol

The ^{11}B NMR spectra of Ir-4-BOH under varying conditions were recorded in CH_3CN (Figure 2.40). In the absence of the 3-fluorocatechol the ^{11}B signal observed at 29.3 ppm can be

assigned to the boronic acid on the phenylpyridine ligand of the bare metal complex, a shift that is in the previously observed region for boronic acids.[54, 119] The peak at 19.9 ppm fits with previous assignment for boric acid, a common by-product in boronic acid syntheses regularly observed in ^{11}B studies of boronic acid compounds.[86] After addition of 3-fluorocatechol to the sample, the boron signal shifts to 14.6 ppm. The results demonstrate that the binding event is occurring through a boronic ester formation, with a change to the electronic properties of the boron group, which would in turn explain the changing photophysical properties upon sugar addition.

Both 3-fluorocatechol and 2-fluoro-2-deoxy-D-glucose were used for their ability to report binding based upon ^{19}F NMR. As such, each sample was run for this isotope too and a shift of the ^{19}F signal at -138 ppm to -144 ppm is assigned to the unbound to bound state of 3-Fluorocatechol respectively (Figure 2.41); which agrees well with previous studies.[54]

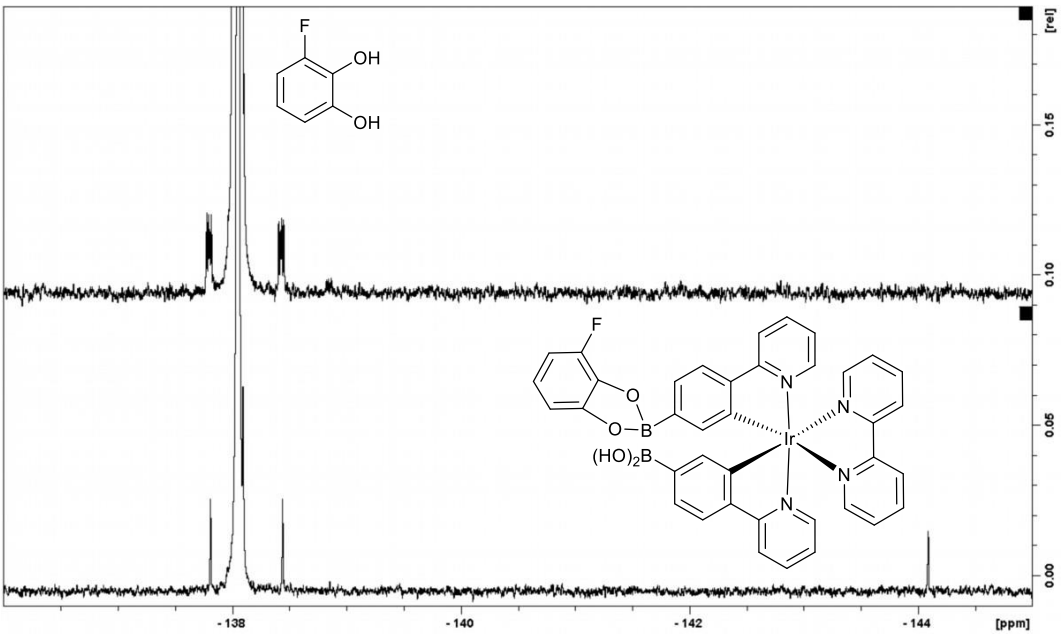


Figure 2.41: A) ^{19}F NMR of 100 mM 3-fluorocatechol in acetonitrile-d_3 containing NH_4PF_6. All spectra are referenced to the the RPF_6 peak present in both samples. B) ^{19}F NMR of **Ir-4-BOH** in acetonitrile-d_3 (~3mM).after addition to 100 mM 3-fluorocatechol

For the ^{19}F NMR of 2-fluoro-2-deoxy-D-glucose in DMSO there are two signals appearing at -195.7 ppm and -196.7 ppm, the α and β forms of the sugar (Figure 2.42).[159, 160] Upon addition of complex **Ir-4-BOH** a third peak appears at -197.8 ppm assigned to the iridium-sugar conjugate. Only one peak is observed as only the α–FDG complex contains syn-periplanar –OH groups, and therfore will be the only form to bind the boronic acid complex.

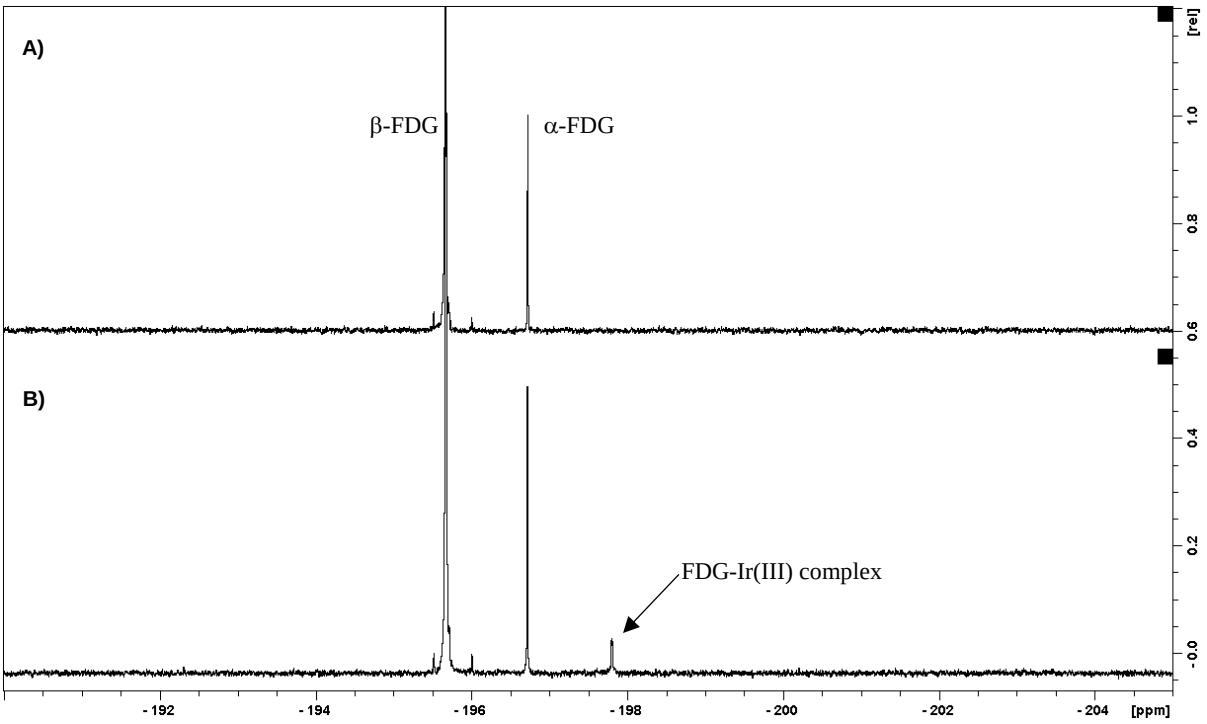


Figure 2.42: A) ^{19}F NMR of 50 mM 2-Fluoro-2-deoxy-D-glucose in DMSO-d_6, B) ^{19}F NMR of 50 mM 2-Fluoro-2-deoxy-D-glucose in DMSO-d_6, after addition of 3 mM of Ir-4-BOH

2.2.6 Electrochemical properties and saccharide sensing of Ir-4-BOH

Following on from the luminescence, mass spectrometry, and NMR experiments, the electrochemical properties of **Ir-4-BOH** and **Ir-ppy** were investigated. Firstly, the electrochemical properties were investigated by cyclic voltammetry. Commonly, this technique is used to elucidate the oxidation of the Ir(III)/(IV) couple and the reduction in the N^N ligand in this case 2,2'-bipyridine. Values for positions of the oxidation and reduction peaks can be found in Table 2.3 below.

Table 2.3: Electrochemical data for complexes **Ir-4-BOH** and **Ir-3-BOH**, taken at 298 K and pH 7.5. Recorded in a 0.1 M aqueous NaCl solution at scan rate of 50mV/s, referenced to Ag/AgCl electrode.

Complex	Oxidation $E_{1/2}$ or E_a / V	Reduction $E_{1/2}$ or E_a / V
Ir-4-BOH	+1.19	-1.37
Ir-ppy	+1.27	-1.40

The oxidation at +1.19 V is assigned to the of iridium(IV)/(III) couple in **Ir-4-BOH**, significantly shifted from the +1.27 V of the complex without this group **Ir-ppy**, however the assignment fits well with previously reported Ir(III) complexes substituted at the same position.[128] We propose that the cathodic shift observed in the oxidative couple of the metal complex is due to the -BOH groups electron withdrawing effect. This is interesting as this is not observed in earlier example of a boronic acid-iridium(III) complex, likely due to the distance between the metal centre and the phenylboronic acid moiety.[84]

Values for the reduction of the bpy ligand are -1.37 and -1.40 **Ir-4-BOH** and **Ir-ppy** respectively, these values align well with reported values for other iridium(III) complexes.[128,124] We therefore postulate, due to the lack of functionalisation, these ligands values are unaffected by the boronic acid electron withdrawing effect.

In light of the photoluminescence sensing ability of these complexes it was decided that the **Ir-4-BOH** should also be evaluated as an electrochemiluminescence (ECL) based sensor. Iridium complexes have become a staple class of compound for use in ECL studies with book chapters devoted to the field.[108] ECL itself is a sensitive and facile detection method for analytical applications.[161, 162] Iridium complexes have been utilized as mixed photoluminescent and ECL sensors for a variety of analytes, owing to their highly tuneable and therefore versatile nature they have become normalized in the analytical chemistry field.[111, 112, 163, 164] ECL is a technique

in which a luminescent signal is observed after application of a potential to a solution of the iridium(III) complex. This is particularly interesting as very few papers focus on electrochemiluminescence as a tool for monitoring saccharide binding. Where these studies are found, the ECL measurement to sense glucose is an indirect measurement, by changing the properties of solely the co-reactant and not of the reporter.[67]

In this study we observe electrochemiluminescence directly from the iridium(III) complexes, possibly a more sensitive sensing method. The ECL spectra of both **Ir-4-BOH** and **Ir-ppy** at pH 7.5 can be measured and show an ECL signal at ~+1.2 V. In the case of **Ir-4-BOH** the observed ECL signal can be suppressed by addition of fructose to the electrochemical cell (Figure 2.43), similarly to what has been observed in our photoluminescence studies. At a fructose concentration of 60 μM the ECL signal arising from **Ir-4-BOH** is decreased by 90 %. The ECL of **Ir-ppy** shows no correlation to the concentration of fructose. We can therefore conclude that the sensing of saccharides can be specifically monitored by **Ir-4-BOH**; not only through photophysical but also through electrochemical techniques, suggesting development of a dual mode sensor should be possible.

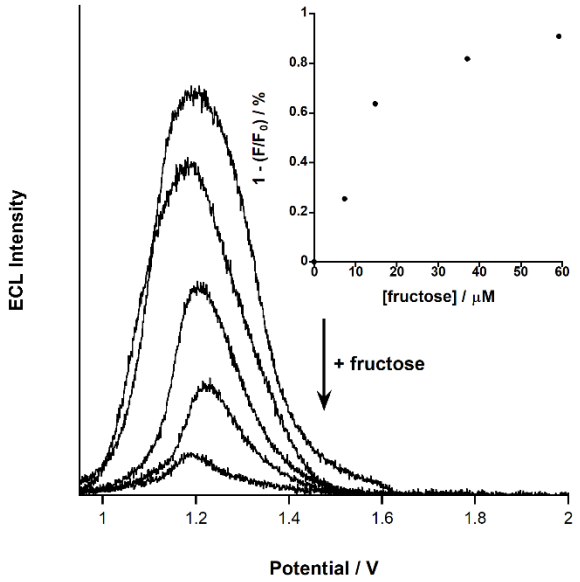


Figure 2.43: ECL spectra of complex Ir-4-BOH upon addition to increasing concentrations of fructose, the supporting electrolyte was 0.1 M aqueous NaCl at pH 7.5 and scan rate 50 mV s^{-1}. Inset: the integrated area of emission for each spectrum vs. concentration of fructose.

2.2.7 Saccharide sensing via hydrogel device incorporating Ir-4-BOH

The binding of sugars by the boronated complex in solution at physiological pH lends itself to subsequent sensing device fabrication. One area of research that has been established in recent years has been the fabrication of hydrogels for the sensing of glucose concentration in blood. There have been many sensors fabricated with a range of sensing modalities, some focussed on swelling of the gel or diffraction of the incident light.[165-169] Luminescence sensing in hydrogels has been explored, with work focusing on this technique using organic fluorophores to create a sensing system.[85, 91, 104, 170, 171] The aforementioned glucose sensitive hydrogel devices are ordinarily based on the emission of organic fluorophores, with emission wavelengths below 550 nm, this is not optimal for detection *in vivo* as the penetration depth of light to tissue increases with increasing wavelength.[172] We propose a method in which an iridium(III) complex is used in place of an organic dye. This system should provide advantages of photostability and ease of synthesis. A handheld laser attached to a fibre optic and relatively inexpensive detector are used. The gel is placed onto the aperture of the fibre optic and a

readout of the luminescence is given by the detector at the far end of the fibre optic, allowing in theory an *in vivo* implant to monitor the glucose levels of patients continuously.

Provided the gels exhibit permeability to the saccharides, luminescence of the gels was expected to decrease similarly to the luminescence of the complexes in solution. The photoluminescent signal from the gels was measured upon addition of an increasing concentration of saccharide, added into a solution of 0.01 M PBS in which the gel is immersed. When loaded with **Ir-4-BOH**, the gels show a decrease in intensity with each subsequent addition of sugar (Figure 2.44); whereas no reduction is observed when saccharide is added to gels loaded with compound **Ir-ppy** (Figure 2.45).

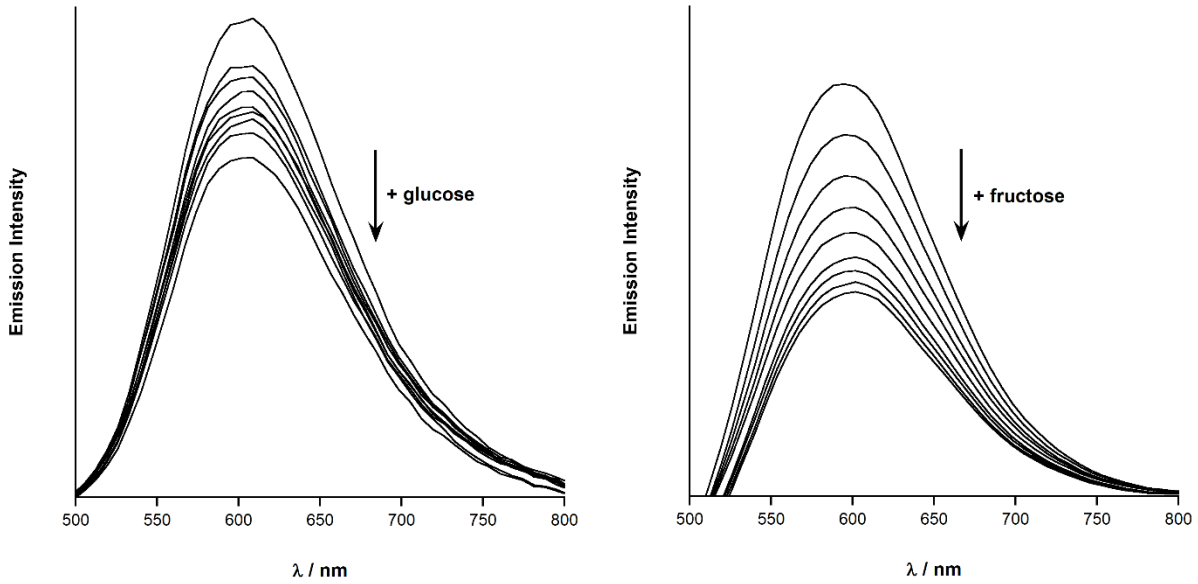


Figure 2.44: Emission spectra of hydrogel devices loaded with A) Ir-4-BOH, with glucose additions to 50 mM. B) Ir-4-BOH, with fructose additions to 100 mM. Concentrations shown are 0, 2, 4, 6, 8, 10, 25, 50, and 100 mM. (λ_{exc} = 450 nm)

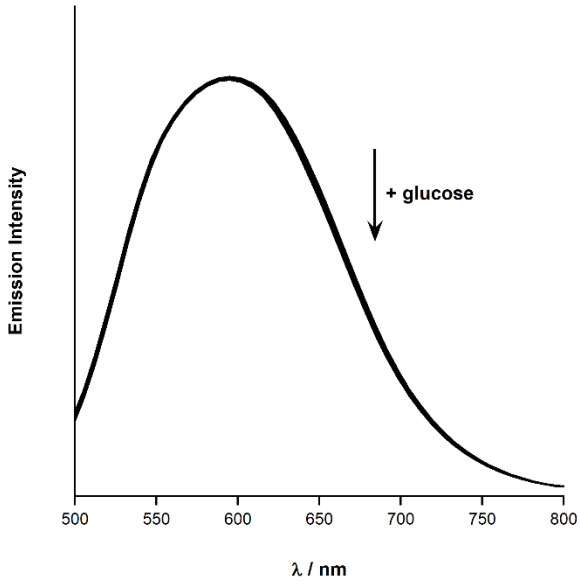


Figure 2.45: Emission spectra of hydrogel devices loaded with Ir-ppy, with glucose additions to 50 mM. Concentrations shown are 0, 2, 4, 6, 8, 10, 25, 50, and 100 mM. (λ_{exc} = 450 nm).

The luminescence percentage decrease is slightly smaller than that observed in solution, with luminescence plots revealing the maximum decrease in the luminescence by area is 34 % and 49 % for glucose and fructose respectively at 500 mM, the trend between sugars agrees well with solution studies and an observable decrease is apparent. Binding values for the hydrogels can also be obtained from 1:1 binding plots using the same method as that used in this study for solution based sensing (Figure 2.46).

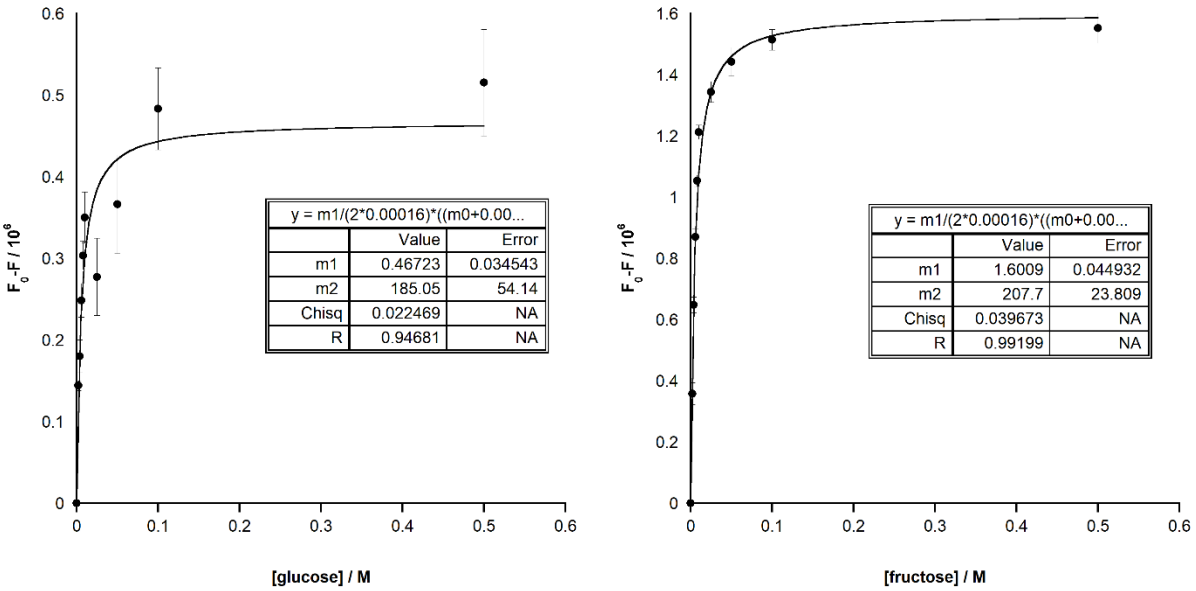


Figure 2.46: 1:1 quadratic fits of the binding of Ir-4-BOH hydrogels, to each sugar in solution (0.16 mM Ir(III), 0.01 M aqueous PBS, pH 7.4).

The binding constants of 185 and 208 M^{-1} for glucose and fructose respectively, do not match closely with those seen in PBS solution (82 and 331 M^{-1}). A possible explanation is that binding is influenced by the matrix due to the diffusion of sugars through the gel. The binding constants are however similar or higher than those observed for organic counterparts in devices, with binding constants typically in the range of 100 M^{-1} for glucose.[86, 91, 103]

The sensitivity of the complex **Ir-4-BOH** and the gels is larger to fructose, although human serum levels of fructose are low, with concentrations of around 10 μM,[173] which would not illicit a large response from the gel devices. Conversely the response of the gels fits well with the range of subcutaneous concentrations of glucose, which studies indicate would be in the range of 2 to 30 mM.[151-153] In this region the gel device would be a useful and accurate tool in monitoring glucose levels.

2.2.8 Stability and toxicity of Ir(III) implanted hydrogels

For real life application the gel devices must also be non-toxic and stable. As such, both stability and cell toxicity tests were performed. To probe the stability across a 48-hour window,

the emission intensity of the hydrogels was used as an indicator for the release of the boronic acid containing complex into solution from such a gel device. The devices were immersed in 2 mL PBS; which was removed before each measurement to ensure the signal was coming only from the gel. We observed no decrease within the 48-hour window and may conclude that the compound is entrapped in such a way that minimal release occurs at physiological pH (Figure 2.47).

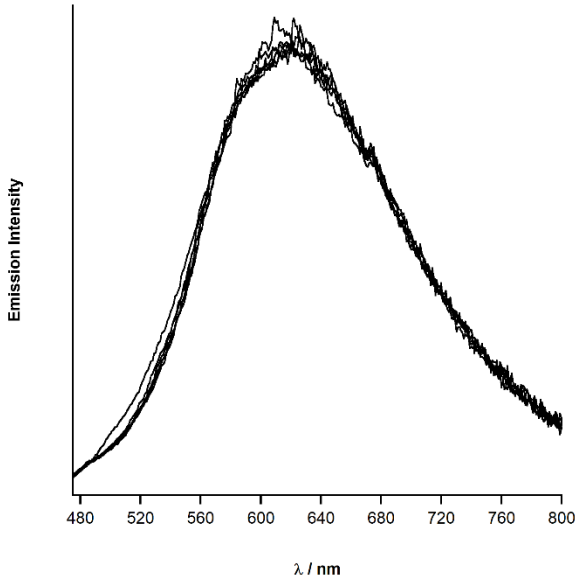


Figure 2.47: Luminescence spectra of hydrogel device loaded with Ir-4-BOH (λ_{exc} = 450 nm), taken over a 48-hour period. Excitation counts were monitored and matched at all measured points. Timepoints displayed are 5 min, 10 min, 30 min, 1.5 h, and 48 h.

Toxicity testing was carried out over a 72-hour period on several different cell lines found within human skin; human dermal fibroblasts, keratinocytes, melanocytes. No toxicity was observed, and it can be concluded that the gels are non-toxic and would have compatibility as a skin worn or sub-dermal device (Figure 2.48).

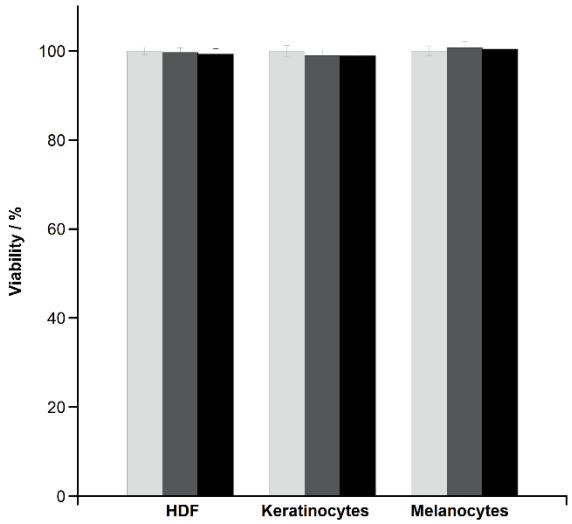


Figure 2.48: Cell viability of differing cell lines after 72 h incubation with non-loaded hydrogel (light grey), hydrogel loaded with Ir-ppy (dark grey), and hydrogel loaded with Ir-4-BOH (black). n = 5.

2.3 Conclusion

We have detailed the synthesis and photophysical properties of two novel Ir(III) complexes (**Ir-3-BOH** and **Ir-4-BOH**). Both of these complexes have been utilised in the detection of saccharides (glucose and fructose) in aqueous solutions at physiological pH and sugar concentration. The luminescence intensity of the Ir(III) complexes decreases with increasing concentration of saccharide, and we were able to elucidate the binding constants of each Ir(III) complex with each saccharide in solution (Table 2.4). Further to this, we investigated **Ir-4-BOH** as a dual modality Ir(III)-boronic acid sensor for saccharides, able to report binding through spectral changes in both photoluminescence and electroluminescence techniques, with spectral changes that are significant (up to 90 % quenching in ECL). Moreover, the **Ir-4-BOH** complex is incorporated into hydrogels to efficiently sense saccharides through photoluminescence readout, whilst the implantable Ir(III) containing gels are shown to be non-toxic, stable and easy to synthesise. Table 2.4 summarises the hydrogel binding constants alongside the data from solution. It can be observed that although different, the hydrogels offer

reasonable binding constants at physiological pH, with responses at physiological sugar concentrations.

Table 2.4: Summarised data for complexes **Ir-3-BOH**, and **Ir-4-BOH** in and out of the hydrogel device. Values were obtained by 1:1 quadratic fitting of the values for F_0-F vs. concentration of saccharide. Values are obtained from the mean of least squares iteration with error.

Complex	Binding constant with glucose / M^{-1}	Binding constant with fructose / M^{-1}
Ir-3-BOH	305 ± 42	139 ± 16
Ir-4-BOH	82 ± 11	331 ± 25
Ir-4-BOH in hydrogel	185 ± 54	208 ± 24

Overall this chapter has demonstrated the utility of the synthesised Ir(III) complexes in saccharide sensing. It is the first example of an Ir(III) complex able to show a dual photoluminescence and electroluminescence response to sugars. Moreover we have synthesised stimuli responsive Ir(III) containing hydrogels. As they are non-toxic, these gels could be further developed to be used as saccharide responsive devices *in vitro* or *in vivo*.

2.4 References

1. C. A. Monteiro, R. B. Levy, R. M. Claro, I. R. R. de Castro and G. Cannon, *Public Health Nutr.*, 2010, **14**, 5-13.
2. G. A. Bray, *JAMA*, 2003, **289**, 1853-1855.
3. K. M. Flegal, M. D. Carroll, C. L. Ogden and L. R. Curtin, *JAMA*, 2010, **303**, 235-241.
4. J. McKinlay and L. Marceau, *Lancet*, 2000, **356**, 757-761.
5. L. Guariguata, D. R. Whiting, I. Hambleton, J. Beagley, U. Linnenkamp and J. E. Shaw, *Diabetes Res. Clin. Pract.*, 2014, **103**, 137-149.
6. R. R. A. Bourne, G. A. Stevens, R. A. White, J. L. Smith, S. R. Flaxman, H. Price, J. B. Jonas, J. Keeffe, J. Leasher, K. Naidoo, K. Pesudovs, S. Resnikoff and H. R. Taylor, *Lancet Glob. Health*, 2013, **1**, e339-e349.
7. M. Afkarian, L. R. Zelnick, Y. N. Hall and et al., *JAMA*, 2016, **316**, 602-610.
8. C. The Emerging Risk Factors, *Lancet*, 2010, **375**, 2215-2222.

9. N. C. Barengo, S. Katoh, V. Moltchanov, N. Tajima and J. Tuomilehto, *Eur. Heart J.*, 2008, **29**, 1889-1895.

10. P. W. Moxey, P. Gogalniceanu, R. J. Hinchliffe, I. M. Loftus, K. J. Jones, M. M. Thompson and P. J. Holt, *Diabet. Med.*, 2011, **28**, 1144-1153.

11. D. Beran and J. S. Yudkin, *Diabetes Res. Clin. Pract.*, 2010, **88**, 217-221.

12. L. Olansky and L. Kennedy, *Diabetes Care*, 2010, **33**, 948.

13. S. R. Patton, *J. Diabetes Sci. Technol.*, 2015, **9**, 668-675.

14. W. H. Polonsky, L. Fisher, D. Hessler and S. V. Edelman, *Diabet. Med.*, 2014, **31**, 40-46.

15. D. Bruttomesso, L. Laviola, A. Avogaro, E. Bonora, S. Del Prato, S. Frontoni, E. Orsi, I. Rabbone, G. Sesti and F. Purrello, *Nutrition, Metabolism and Cardiovascular Diseases*, 2019, **29**, 421-431.

16. M. A. O'Connell, S. Donath and F. J. Cameron, *Pediatr. Diabetes*, 2011, **12**, 556-559.

17. D. C. Klonoff and P. Prahalad, *J. Diabetes Sci. Technol.*, 2015, **9**, 895-910.

18. L. Ekhlaspour, D. Mondesir, N. Lautsch, C. Balliro, M. Hillard, K. Magyar, L. G. Radocchia, A. Esmaeili, M. Sinha and S. J. Russell, *J. Diabetes Sci. Technol.*, 2016, **11**, 558-566.

19. D. C. Klonoff, J. L. Parkes, B. P. Kovatchev, D. Kerr, W. C. Bevier, R. L. Brazg, M. Christiansen, T. S. Bailey, J. H. Nichols and M. A. Kohn, *Diabetes Care*, 2018, **41**, 1681.

20. T. Danne, R. Nimri, T. Battelino, R. M. Bergenstal, K. L. Close, J. H. DeVries, S. Garg, L. Heinemann, I. Hirsch, S. A. Amiel, R. Beck, E. Bosi, B. Buckingham, C. Cobelli, E. Dassau, F. J. Doyle, S. Heller, R. Hovorka, W. Jia, T. Jones, O. Kordonouri, B. Kovatchev, A. Kowalski, L. Laffel, D. Maahs, H. R. Murphy, K. Nørgaard, C. G. Parkin, E. Renard, B. Saboo, M. Scharf, W. V. Tamborlane, S. A. Weinzimer and M. Phillip, *Diabetes Care*, 2017, **40**, 1631.

21. R. A. Ajjan, *Diabetes Technol. Ther.*, 2017, **19**, S-27-S-36.

22. J. M. Lehn, *Pure Appl. Chem.*, 1994, **66**, 1961-1966.

23. J.-M. Lehn, *Angewandte Chemie International Edition in English*, 1990, **29**, 1304-1319.

24. J. P. Lorand and J. O. Edwards, *J. Org. Chem.*, 1959, **24**, 769-774.

25. R. Nishiyabu, Y. Kubo, T. D. James and J. S. Fossey, *Chem. Commun.*, 2011, **47**, 1106-1123.

26. J. S. Fossey, F. D'Hooge, J. M. H. van den Elsen, M. P. Pereira Morais, S. I. Pascu, S. D. Bull, F. Marken, A. T. A. Jenkins, Y.-B. Jiang and T. D. James, *Chem. Rec.*, 2012, **12**, 464-478.

27. S. D. Bull, M. G. Davidson, J. M. H. van den Elsen, J. S. Fossey, A. T. A. Jenkins, Y.-B. Jiang, Y. Kubo, F. Marken, K. Sakurai, J. Zhao and T. D. James, *Acc. Chem. Res.*, 2013, **46**, 312-326.

28. S. J. Hansen and B. J. Christensen, *Biosensors*, 2013, **3**.

29. X. Wu, Z. Li, X.-X. Chen, J. S. Fossey, T. D. James and Y.-B. Jiang, *Chem. Soc. Rev.*, 2013, **42**, 8032-8048.

30. X.-t. Zhang, G.-j. Liu, Z.-w. Ning and G.-w. Xing, *Carbohydr. Res.*, 2017, **452**, 129-148.

31. G. Fang, H. Wang, Z. Bian, J. Sun, A. Liu, H. Fang, B. Liu, Q. Yao and Z. Wu, *RSC Advances*, 2018, **8**, 29400-29427.

32. Z. Bian, A. Liu, Y. Li, G. Fang, Q. Yao, G. Zhang and Z. Wu, *Analyst*, 2020, **145**, 719-744.

33. Y. Nagai, K. Kobayashi, H. Toi and Y. Aoyama, *Bull. Chem. Soc. Jpn.*, 1993, **66**, 2965-2971.

34. J. C. Norrild and I. Søtofte, *Journal of the Chemical Society, Perkin Transactions 2*, 2001, DOI: 10.1039/B102377M, 727-732.

35. R. Pizer and C. Tihal, *Inorg. Chem.*, 1992, **31**, 3243-3247.

36. J. Yoon and A. W. Czarnik, *J. Am. Chem. Soc.*, 1992, **114**, 5874-5875.

37. G. Springsteen and B. Wang, *Tetrahedron*, 2002, **58**, 5291-5300.

38. X. Gao, Y. Zhang and B. Wang, *Tetrahedron*, 2005, **61**, 9111-9117.

39. D. B. Cordes, S. Gamsey, Z. Sharrett, A. Miller, P. Thoniyot, R. A. Wessling and B. Singaram, *Langmuir*, 2005, **21**, 6540-6547.

40. A. Schiller, R. A. Wessling and B. Singaram, *Angew. Chem. Int. Ed.*, 2007, **46**, 6457-6459.

41. T. D. James, K. R. A. S. Sandanayake and S. Shinkai, *Angewandte Chemie International Edition in English*, 1996, **35**, 1910-1922.

42. L.-E. Guo, Y. Hong, S.-Y. Zhang, M. Zhang, X.-S. Yan, J.-L. Cao, Z. Li, T. D. James and Y.-B. Jiang, *J. Org. Chem.*, 2018, **83**, 15128-15135.

43. H. Kobayashi, K. Nakashima, E. Ohshima, Y. Hisaeda, I. Hamachi and S. Shinkai, *Journal of the Chemical Society, Perkin Transactions 2*, 2000, DOI: 10.1039/A909822D, 997-1002.

44. A.-J. Tong, A. Yamauchi, T. Hayashita, Z.-Y. Zhang, B. D. Smith and N. Teramae, *Anal. Chem.*, 2001, **73**, 1530-1536.

45. J. T. Suri, D. B. Cordes, F. E. Cappuccio, R. A. Wessling and B. Singaram, *Angew. Chem. Int. Ed.*, 2003, **42**, 5857-5859.

46. W. Ni, H. Fang, G. Springsteen and B. Wang, *J. Org. Chem.*, 2004, **69**, 1999-2007.

47. A. E. Hargrove, R. N. Reyes, I. Riddington, E. V. Anslyn and J. L. Sessler, *Org. Lett.*, 2010, **12**, 4804-4807.

48. H.-J. Schneider, *Recl. Trav. Chim. Pays-Bas*, 1993, **112**, 412-419.

49. N. Bampos, Z. Clyde-Watson, J. C. Hawley, C. C. Mak, A. Vidal-Ferran, S. J. Webb and J. K. M. Sanders, in *NMR in Supramolecular Chemistry*, ed. M. Pons, Springer Netherlands, Dordrecht, 1999, DOI: 10.1007/978-94-011-4615-9_3, pp. 37-44.

50. S. J. Cantrill, M. C. T. Fyfe, F. M. Raymo and J. F. Stoddart, in *NMR in Supramolecular Chemistry*, ed. M. Pons, Springer Netherlands, Dordrecht, 1999, DOI: 10.1007/978-94-011-4615-9_1, pp. 1-18.

51. B. Gierczyk, M. Kaźmierczak, G. Schroeder and A. Sporzyński, *New J. Chem.*, 2013, **37**, 1056-1072.

52. I. P. Gerothanassis, *Prog. Nucl. Magn. Reson. Spectrosc.*, 1994, **26**, 239-292.

53. J. Axthelm, S. H. C. Askes, M. Elstner, U. R. G, H. Görls, P. Bellstedt and A. Schiller, *J. Am. Chem. Soc.*, 2017, **139**, 11413-11420.

54. A. Larcher, A. Lebrun, M. Smietana and D. Laurencin, *New J. Chem.*, 2018, **42**, 2815-2823.

55. F. Sassa, G. C. Biswas and H. Suzuki, *Lab on a Chip*, 2020, **20**, 1358-1389.

56. P. B. Luppa, C. Müller, A. Schlichtiger and H. Schlebusch, *TrAC, Trends Anal. Chem.*, 2011, **30**, 887-898.

57. A. N. Nesmejanow, W. A. Ssasonowa and V. N. Drosd, *Chem. Ber.*, 1960, **93**, 2717-2729.

58. S. Arimori, S. Ushiroda, L. M. Peter, A. T. A. Jenkins and T. D. James, *Chem. Commun.*, 2002, DOI: 10.1039/B207643H, 2368-2369.

59. J. C. Norrild and I. Søtofte, *Journal of the Chemical Society, Perkin Transactions 2*, 2002, DOI: 10.1039/B107457A, 303-311.

60. N. E. Tokel and A. J. Bard, *J. Am. Chem. Soc.*, 1972, **94**, 2862-2863.

61. Z. Liu, W. Qi and G. Xu, *Chem. Soc. Rev.*, 2015, **44**, 3117-3142.

62. E. M. Gross, S. S. Maddipati and S. M. Snyder, *Bioanalysis*, 2016, **8**, 2071-2089.

63. A. Endo, H. Minesaka, T. Hashimoto and T. Hayashita, *Analytical Methods*, 2012, **4**, 2657-2660.

64. A. Endo, M. Kimura, T. Hashimoto and T. Hayashita, *Analytical Methods*, 2014, **6**, 8874-8877.

65. J. K. Leland, *J. Electrochem. Soc.*, 1990, **137**, 3127.

66. S. Arimori, M. L. Bell, C. S. Oh, K. A. Frimat and T. D. James, *J. Chem. Soc., Perkin Trans. 1*, 2002, DOI: 10.1039/B108998F, 803-808.

67. H. Li, A. C. Sedgwick, M. Li, R. A. R. Blackburn, S. D. Bull, S. Arbault, T. D. James and N. Sojic, *Chem. Commun.*, 2016, **52**, 12845-12848.

68. B. Fabre and F. Hauquier, *Langmuir*, 2017, **33**, 8693-8699.

69. B. Wang, K.-H. Chou, B. N. Queenan, S. Pennathur and G. C. Bazan, *Angew. Chem. Int. Ed.*, 2019, **58**, 10612-10615.

70. T. D. James, K. R. A. S. Sandanayake and S. Shinkai, *J. Chem. Soc., Chem. Commun.*, 1994, DOI: 10.1039/C39940000477, 477-478.

71. T. D. James, K. R. A. S. Sandanayake, R. Iguchi and S. Shinkai, *J. Am. Chem. Soc.*, 1995, **117**, 8982-8987.

72. T. D. James, K. R. A. S. Sandanayake and S. Shinkai, *Angewandte Chemie International Edition in English*, 1994, **33**, 2207-2209.

73. Y.-J. Huang, W.-J. Ouyang, X. Wu, Z. Li, J. S. Fossey, T. D. James and Y.-B. Jiang, *J. Am. Chem. Soc.*, 2013, **135**, 1700-1703.

74. L. N. Neupane, S. Y. Han and K.-H. Lee, *Chem. Commun.*, 2014, **50**, 5854-5857.

75. S. Franzen, W. Ni and B. Wang, *The Journal of Physical Chemistry B*, 2003, **107**, 12942-12948.

76. X. Sun, T. D. James and E. V. Anslyn, *J. Am. Chem. Soc.*, 2018, **140**, 2348-2354.

77. A. Resendez and S. V. Malhotra, *Sci. Rep.*, 2019, **9**, 6651.

78. N. Wellington, S. Macklai and P. Britz-McKibbin, *Chemistry – A European Journal*, 2019, **25**, 15277-15280.

79. T. Xiao, F. Wang, Y. Chen, X. Yang, T. Wei, C. Liu, S. Chen, Z. Xu, J. Yoon and X. Chen, *Dyes Pigm.*, 2019, **163**, 227-231.

80. L. Zhang, X. A. Liu, K. D. Gillis and T. E. Glass, *Angew. Chem. Int. Ed.*, 2019, **58**, 7611-7614.

81. M. J. Deetz and B. D. Smith, *Tetrahedron Lett.*, 1998, **39**, 6841-6844.

82. D. R. Cary, C. B. Darrow, S. M. Lane, T. A. Peyser, J. H. Satcher, W. P. Van Antwerp, A. J. Nelson and J. G. Reynolds, *Sens. Actuators B: Chem.*, 2002, **87**, 25-32.

83. D. R. Cary, N. P. Zaitseva, K. Gray, K. E. O'Day, C. B. Darrow, S. M. Lane, T. A. Peyser, J. H. Satcher, W. P. Van Antwerp, A. J. Nelson and J. G. Reynolds, *Inorg. Chem.*, 2002, **41**, 1662-1669.

84. H.-W. Liu, W. H.-T. Law, L. C.-C. Lee, J. C.-W. Lau and K. K.-W. Lo, *Chem. Asian J.*, 2017, **12**, 1545-1556.

85. S. Gamsey, J. T. Suri, R. A. Wessling and B. Singaram, *Langmuir*, 2006, **22**, 9067-9074.

86. D. Bruen, C. Delaney, D. Diamond and L. Florea, *ACS Appl. Mater. Interfaces*, 2018, **10**, 38431-38437.

87. E. V. Lampard, A. C. Sedgwick, T. Sombuttan, G. T. Williams, B. Wannalerse, A. T. A. Jenkins, S. D. Bull and T. D. James, *ChemistryOpen*, 2018, **7**, 266-268.

88. T. Kawanishi, M. A. Romey, P. C. Zhu, M. Z. Holody and S. Shinkai, *J. Fluoresc.*, 2004, **14**, 499-512.

89. W. Fudickar and T. Linker, *Chem. Commun.*, 2008, DOI: 10.1039/B719637G, 1771-1773.

90. H. Shibata, Y. J. Heo, T. Okitsu, Y. Matsunaga, T. Kawanishi and S. Takeuchi, *Proc. Natl. Acad. Sci.*, 2010, **107**, 17894.

91. S. Xu, A. C. Sedgwick, S. A. Elfeky, W. Chen, A. S. Jones, G. T. Williams, A. T. A. Jenkins, S. D. Bull, J. S. Fossey and T. D. James, *Front. Chem. Sci. Eng.*, 2019, DOI: 10.1007/s11705-019-1812-5.

92. O. Alévêque and E. Levillain, in *Luminescence in Electrochemistry: Applications in Analytical Chemistry, Physics and Biology*, eds. F. Miomandre and P. Audebert, Springer International Publishing, Cham, 2017, DOI: 10.1007/978-3-319-49137-0_1, pp. 1-19.

93. S. H. Kim, H. S. Choi, J. Kim, S. J. Lee, D. T. Quang and J. S. Kim, *Org. Lett.*, 2010, **12**, 560-563.

94. H. Yang, Z. Zhou, K. Huang, M. Yu, F. Li, T. Yi and C. Huang, *Org. Lett.*, 2007, **9**, 4729-4732.

95. P. Anzenbacher, M. A. Palacios, K. Jursíková and M. Marquez, *Org. Lett.*, 2005, **7**, 5027-5030.

96. J. Xu, Y. Zhang, L. Li, Q. Kong, L. Zhang, S. Ge and J. Yu, *ACS Appl. Mater. Interfaces*, 2018, **10**, 3431-3440.

97. X. Hu, Y. Xu, X. Cui, W. Li, X. Huang, Z. Li, J. Shi and X. Zou, *Microchimica Acta*, 2020, **187**, 83.

98. A. Mars, M. Hamami, L. Bechnak, D. Patra and N. Raouafi, *Anal. Chim. Acta*, 2018, **1036**, 141-146.

99. X. Sun, B. M. Chapin, P. Metola, B. Collins, B. Wang, T. D. James and E. V. Anslyn, *Nat. Chem.*, 2019, **11**, 768-778.

100. L. Iannazzo, E. Benedetti, M. Catala, M. Etheve-Quelquejeu, C. Tisné and L. Micouin, *Org. Biomol. Chem.*, 2015, **13**, 8817-8821.

101. K. Tsukagoshi and S. Shinkai, *J. Org. Chem.*, 1991, **56**, 4089-4091.

102. K. Kondo, Y. Shiomi, M. Saisho, T. Harada and S. Shinkai, *Tetrahedron*, 1992, **48**, 8239-8252.

103. P. Ashokkumar, J. Bell, M. Buurman and K. Rurack, *Sens. Actuators B: Chem.*, 2018, **256**, 609-615.

104. Y. J. Heo, H. Shibata, T. Okitsu, T. Kawanishi and S. Takeuchi, *Proc. Natl. Acad. Sci.*, 2011, **108**, 13399.

105. H.-C. Wang, H. Zhou, B. Chen, P. M. Mendes, J. S. Fossey, T. D. James and Y.-T. Long, *Analyst*, 2013, **138**, 7146-7151.

106. D. S. Beaudoin and S. O. Obare, *Tetrahedron Lett.*, 2008, **49**, 6054-6057.

107. A. F. Henwood and E. Zysman-Colman, *Chem. Commun.*, 2017, **53**, 807-826.

108. S. E. Laird and C. F. Hogan, *Iridium(III) in Optoelectronic and Photonics Applications*, 2017, DOI: doi:10.1002/9781119007166.ch8, 359-414.

109. P. D. Beer, *Chem. Commun.*, 1996, DOI: 10.1039/CC9960000689, 689-696.

110. M. K. Nazeeruddin, D. Di Censo, R. Humphry-Baker and M. Grätzel, *Adv. Funct. Mater.*, 2006, **16**, 189-194.

111. H. Lin, M. E. Cinar and M. Schmittel, *Dalton Trans.*, 2010, **39**, 5130-5138.

112. D. Han, M. Qian, H. Gao, B. Wang, H. Qi and C. Zhang, *Anal. Chim. Acta*, 2019, **1074**, 98-107.

113. D.-L. Ma, S. Lin, W. Wang, C. Yang and C.-H. Leung, *Chem. Sci.*, 2017, **8**, 878-889.

114. K. K.-W. Lo, S. P.-Y. Li and K. Y. Zhang, *New J. Chem.*, 2011, **35**, 265-287.

115. K. K.-W. Lo and K. Y. Zhang, *RSC Advances*, 2012, **2**, 12069-12083.

116. K. K.-W. Lo and K. K.-S. Tso, *Inorganic Chemistry Frontiers*, 2015, **2**, 510-524.

117. S. J. Adams, A. J. Carrod, L. A. Rochford, M. Walker and Z. Pikramenou, *ChemistrySelect*, 2018, **3**, 3251-3257.

118. S. M. King, S. Claire, R. I. Teixeira, A. N. Dosumu, A. J. Carrod, H. Dehghani, M. J. Hannon, A. D. Ward, R. Bicknell, S. W. Botchway, N. J. Hodges and Z. Pikramenou, *J. Am. Chem. Soc.*, 2018, **140**, 10242-10249.

119. T. Leermann, F. R. Leroux and F. Colobert, *Org. Lett.*, 2011, **13**, 4479-4481.

120. Y. Ohsawa, S. Sprouse, K. A. King, M. K. DeArmond, K. W. Hanck and R. J. Watts, *J. Phys. Chem.*, 1987, **91**, 1047-1054.

121. T. Ishiyama, M. Murata and N. Miyaura, *J. Org. Chem.*, 1995, **60**, 7508-7510.

122. G. Kaupp, M. R. Naimi-Jamal and V. Stepanenko, *Chemistry – A European Journal*, 2003, **9**, 4156-4161.

123. L. Wang, C. Dai, S. K. Burroughs, S. L. Wang and B. Wang, *Chemistry – A European Journal*, 2013, **19**, 7587-7594.

124. K. K.-W. Lo, J. S.-W. Chan, L.-H. Lui and C.-K. Chung, *Organometallics*, 2004, **23**, 3108-3116.

125. R. D. Costa, E. Ortí, D. Tordera, A. Pertegás, H. J. Bolink, S. Graber, C. E. Housecroft, L. Sachno, M. Neuburger and E. C. Constable, *Advanced Energy Materials*, 2011, **1**, 282-290.

126. S. Ladouceur, D. Fortin and E. Zysman-Colman, *Inorg. Chem.*, 2011, **50**, 11514-11526.

127. S. Ladouceur and E. Zysman-Colman, *Eur. J. Inorg. Chem.*, 2013, **2013**, 2985-3007.

128. K. Hasan, A. K. Bansal, I. D. W. Samuel, C. Roldán-Carmona, H. J. Bolink and E. Zysman-Colman, *Sci. Rep.*, 2015, **5**, 12325.

129. K. K.-W. Lo, P.-K. Lee and J. S.-Y. Lau, *Organometallics*, 2008, **27**, 2998-3006.

130. L. Hua-Wei, K. Y. Zhang, W. H.-T. Law and K. K.-W. Lo, *Organometallics*, 2010, **29**, 3474-3476.

131. A. Juris, V. Balzani, F. Barigelletti, S. Campagna, P. Belser and A. von Zelewsky, *Coord. Chem. Rev.*, 1988, **84**, 85-277.

132. S. Serroni, A. Juris, S. Campagna, M. Venturi, G. Denti and V. Balzani, *J. Am. Chem. Soc.*, 1994, **116**, 9086-9091.

133. J. H. van Diemen, J. G. Haasnoot, R. Hage, E. Müller and J. Reedijk, *Inorg. Chim. Acta*, 1991, **181**, 245-251.

134. M. G. Colombo, A. Hauser and H. U. Güdel, in *Electronic and Vibronic Spectra of Transition Metal Complexes I*, ed. H. Yersin, Springer Berlin Heidelberg, Berlin, Heidelberg, 1994, DOI: 10.1007/3-540-58155-3_5, pp. 143-171.

135. C. Hansch, A. Leo and R. W. Taft, *Chem. Rev.*, 1991, **91**, 165-195.

136. A. F. Henwood, A. K. Bansal, D. B. Cordes, A. M. Z. Slawin, I. D. W. Samuel and E. Zysman-Colman, *J. Mater. Chem. C*, 2016, **4**, 3726-3737.

137. L. K. C. De La Cruz, S. L. Benoit, Z. Pan, B. Yu, R. J. Maier, X. Ji and B. Wang, *Org. Lett.*, 2018, **20**, 897-900.

138. R. Badugu, J. R. Lakowicz and C. D. Geddes, *J. Fluoresc.*, 2004, **14**, 693-703.

139. G. H.S, R. M. Melavanki, N. D, B. P and R. A. Kusanur, *J. Mol. Liq.*, 2017, **227**, 37-43.

140. E. Pomarico, M. Silatani, F. Messina, O. Braem, A. Cannizzo, E. Barranoff, J. H. Klein, C. Lambert and M. Chergui, *The Journal of Physical Chemistry C*, 2016, **120**, 16459-16469.

141. S. Tschierlei, A. Neubauer, N. Rockstroh, M. Karnahl, P. Schwarzbach, H. Junge, M. Beller and S. Lochbrunner, *PCCP*, 2016, **18**, 10682-10687.

142. R. Bevernaegie, L. Marcélis, A. Moreno-Betancourt, B. Laramée-Milette, G. S. Hanan, F. Loiseau, M. Sliwa and B. Elias, *PCCP*, 2018, **20**, 27256-27260.

143. Y. Shiomi, M. Saisho, K. Tsukagoshi and S. Shinkai, *J. Chem. Soc., Perkin Trans. 1*, 1993, DOI: 10.1039/P19930002111, 2111-2117.

144. A. L. Chibac, V. Melinte, T. Buruiana and E. C. Buruiana, *Sens. Actuators B: Chem.*, 2017, **253**, 987-998.

145. B. Vilozny, A. Schiller, R. A. Wessling and B. Singaram, *J. Mater. Chem.*, 2011, **21**, 7589-7595.

146. P. Thordarson, *Chem. Soc. Rev.*, 2011, **40**, 1305-1323.

147. M. P. Williamson, *Prog. Nucl. Magn. Reson. Spectrosc.*, 2013, **73**, 1-16.

148. K. Hirose, *J. Incl. Phenom. Macrocycl. Chem.*, 2001, **39**, 193-209.

149. W. J. Ramsay and H. Bayley, *Angew. Chem. Int. Ed.*, 2018, **57**, 2841-2845.

150. N. Arakawa, K. Nagao, R. Murakami, Y. Sumida, H. Arakawa, F. Inagaki and H. Ohmiya, *Bull. Chem. Soc. Jpn.*, 2020, **93**, 576-580.

151. B. P. Kovatchev, D. J. Cox, L. A. Gonder-Frederick and W. Clarke, *Diabetes Care*, 1997, **20**, 1655-1658.

152. B. P. Kovatchev, E. Otto, D. Cox, L. Gonder-Frederick and W. Clarke, *Diabetes Care*, 2006, **29**, 2433-2438.

153. R. S. Mazze, H. Shamoon, R. Pasmantier, D. Lucido, J. Murphy, K. Hartmann, V. Kuykendall and W. Lopatin, *The American Journal of Medicine*, 1984, **77**, 211-217.

154. D. Williams, T. D. Lee, N. Dinh and M. K. Young, *Rapid Commun. Mass Spectrom.*, 2000, **14**, 1530-1537.

155. Y. Yu, K.-S. Ko, C. J. Zea and N. L. Pohl, *Org. Lett.*, 2004, **6**, 2031-2033.

156. M. Kurogochi, M. Mizuno and A. Matsuda, *ChemistrySelect*, 2018, **3**, 8193-8198.

157. S. L. Yeste, M. E. Powell, S. D. Bull and T. D. James, *J. Org. Chem.*, 2009, **74**, 427-430.

158. H. C. Beachell and D. W. Beistel, *Inorg. Chem.*, 1964, **3**, 1028-1032.

159. M. Rivlin, J. Horev, I. Tsarfaty and G. Navon, *Sci. Rep.*, 2013, **3**, 3045.

160. A. Fatangare, C. Paetz, H. Saluz and A. Svatoš, *Frontiers in Plant Science*, 2015, **6**.

161. W. Miao, in *Handbook of Electrochemistry*, ed. C. G. Zoski, Elsevier, Amsterdam, 2007, DOI: https://doi.org/10.1016/B978-044451958-0.50026-4, pp. 541-590.

162. R. J. Forster, P. Bertoncello and T. E. Keyes, *Annual Review of Analytical Chemistry*, 2009, **2**, 359-385.

163. K. Chen and M. Schmittel, *Analyst*, 2013, **138**, 6742-6745.

164. T. Kim and J.-I. Hong, *ACS Omega*, 2019, **4**, 12616-12625.

165. Q. Li, Y. Guan and Y. Zhang, *Sens. Actuators B: Chem.*, 2018, **272**, 243-251.

166. V. L. Alexeev, S. Das, D. N. Finegold and S. A. Asher, *Clin. Chem.*, 2004, **50**, 2353.

167. X. Wang, Q. Li, Y. Guan and Y. Zhang, *Materials Today Chemistry*, 2016, **1-2**, 7-14.

168. A. K. Yetisen, N. Jiang, A. Fallahi, Y. Montelongo, G. U. Ruiz-Esparza, A. Tamayol, Y. S. Zhang, I. Mahmood, S.-A. Yang, K. S. Kim, H. Butt, A. Khademhosseini and S.-H. Yun, *Adv. Mater.*, 2017, **29**, 1606380.

169. T. Zhang, G.-Q. Liu, W.-H. Leong, C.-F. Liu, M.-H. Kwok, T. Ngai, R.-B. Liu and Q. Li, *Nature Communications*, 2018, **9**, 3188.

170. M.-L. Ho, J.-C. Wang, T.-Y. Wang, C.-Y. Lin, J. F. Zhu, Y.-A. Chen and T.-C. Chen, *Sens. Actuators B: Chem.*, 2014, **190**, 479-485.

171. W. F. March, A. Mueller and P. Herbrechtsmeier, *Diabetes Technol. Ther.*, 2004, **6**, 782-789.

172. A. M. Smith, M. C. Mancini and S. Nie, *Nat. Nanotechnol.*, 2009, **4**, 710-711.

173. T. Kawasaki, H. Akanuma and T. Yamanouchi, *Diabetes Care*, 2002, **25**, 353-357.

3 Sensing of Environmentally Harmful Fluorosurfactant *via* Luminescent Lifetime Augmentation of a Cyclometalated Ir(III) Complex in Solution and Immobilised on Gold.

3.1 Introduction

3.1.1 General remarks on surfaces, SAMs and their patterning

Surfaces consisting of an inert support coated with metals or metal oxides (herein referred to as the substrate) represent an exploitable opportunity to construct devices, based upon properties of adsorbed molecules. The properties of adsorbed molecules can differ drastically from the same molecule in the bulk solution, with free-energy, reactivity, and structure all liable to change upon surface adsorption.[1]

It is known that adventitious adsorption of organic material will occur spontaneously onto the metal surface, owing to the often-favourable reduction in the free energy of the interface between substrate and the ambient environment.[1] This however does not often provide a chemically or physically well-controlled coating or bring to bear a useful device.

To govern the adorned properties and reproducibly coat a substrate one may employ a molecule that will form a self-assembled monolayer (SAM). Self-assembled monolayers on substrates may be defined as assemblies formed from the coating of a solid from the adsorbate in solution or gas phase.[2] Schematic representation of a SAM is shown in Figure 3.1, along with labelled common constituents.

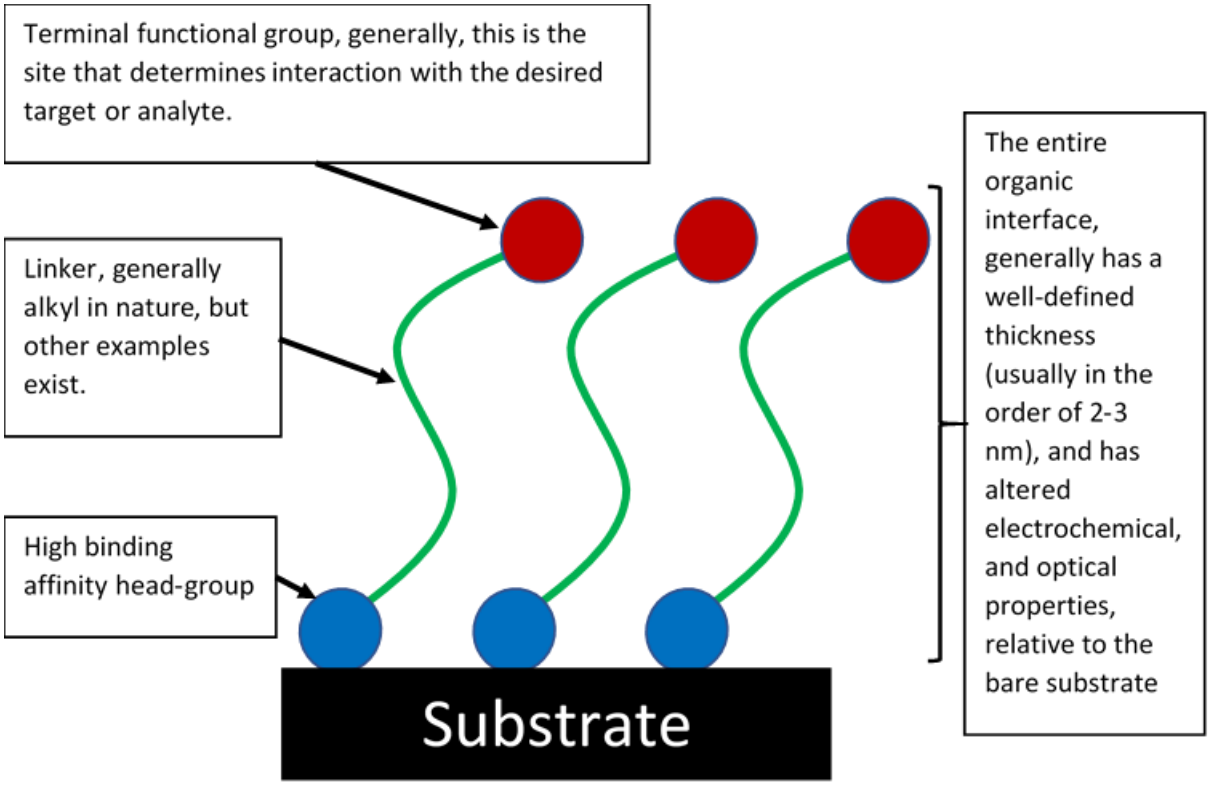


Figure 3.1: Graphical representation of the structure of an ideal organic SAM with each component labelled.

It can be seen from Figure 3.1 that a chemical functionality is present in the SAM forming molecule to facilitate covalent binding. The binding occurs with high affinity for the chosen substrate and varied functionality can be introduced into the self -assembling molecule to increase affinity for a specific substrate type.[2, 3] Understanding of the conformation, structure and binding modes of many surface-bound complexes to a variety of metals and metal-oxides has been investigated; researchers have and continue to use surface-active groups such as thiols,[4-7] amines,[8, 9] phosphonates,[10, 11] and carboxylic acids,[12-14] when forming SAMs.

Often the applications of the SAM are considered when developing the system. The use of SAMs has been described across a broad spectrum of scientific disciplines. SAMs as corrosion protective coatings,[15, 16] friction prevention films,[17] and stiction reduction coating in microelectrochemical systems have all been detailed.[18]

SAMs have also been used in functional device fabrication, with sensors and biosensors commonly utilizing monolayer coatings.[19-23] Further to this, metal nanoparticle stability and resistance to aggregation is determined by the surface coating, often applied by adsorption onto the surface from a solution containing adsorbate.[24, 25]

Alkanethiolate coated gold surfaces have been used to efficiently probe biomolecular interactions. The design of the surfaces often relies on creation of hydrophobic islands on the surface by addition of alkanethiolates in specific areas.[26] Deliberately patterned SAMs are therefore clearly of advantage. One can realise the creation of patterned SAMs by many methods.

One method is microcontact printing of the adsorbate,[27, 28] wherein the pattern is created by first coating a flexible elastomeric stamp manufactured with a desired micropattern, and subsequently mechanically pressing the stamp against the substrate.[29] This approach is shown schematically in Figure 3.2.

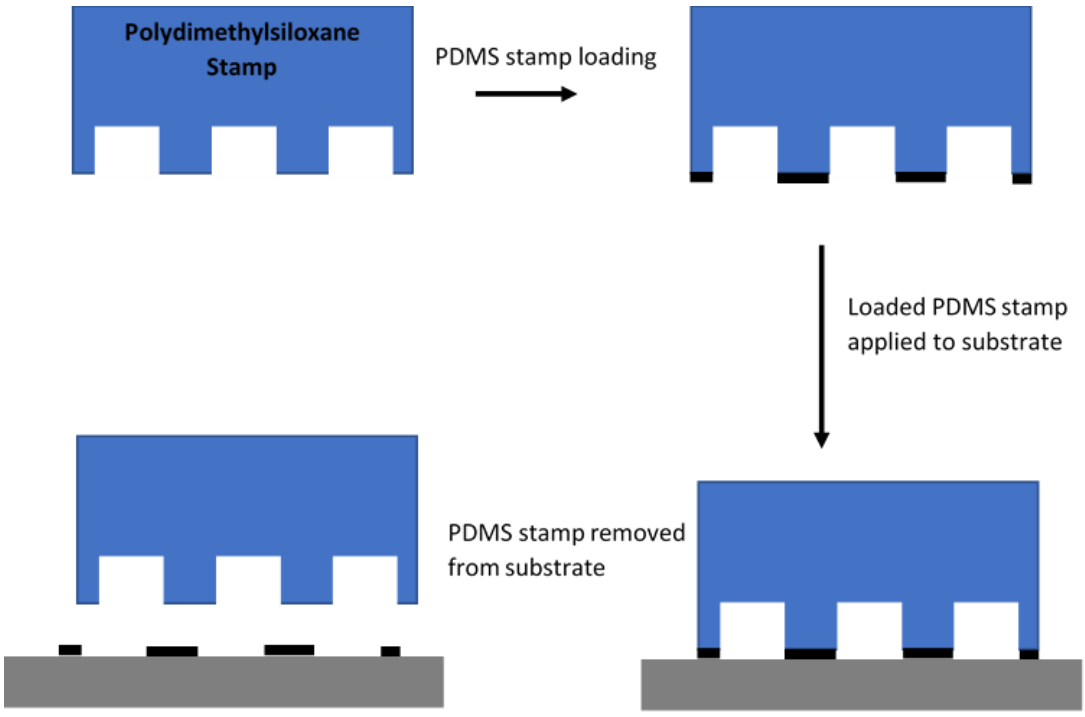


Figure 3.2: Schematic displaying the process of PDMS stamping of a SAM onto a substrate

A second method relies on coating specifically to a lithographically patterned substrate. This lithographic patterning may be achieved by high powered laser in a variety of substrate types.[30-32] With islands created in the substrate itself, the SAM forming molecules will bind specifically to these islands and not at the points where the metal or metal oxide of the substrate has been damaged/removed by lithography.[33, 34] This approach is shown in Figure 3.3.

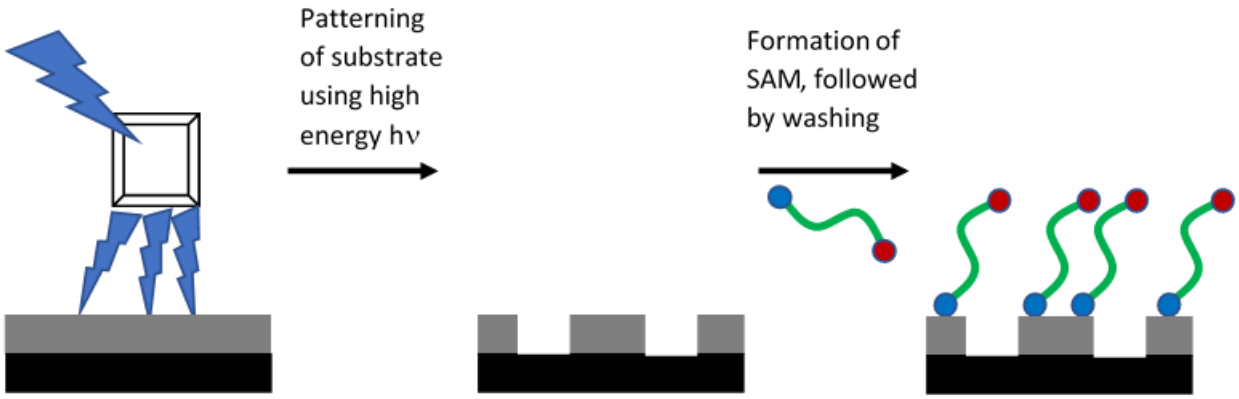


Figure 3.3: Surface patterning process by laser ablation, the dark square represents either a photomask or focussing lens intended to split the beam to create the desired pattern. Blue bolts indicate high energy photons.

The third method is reliant on photo-activation in which the surface-active molecule is patterned across the entirety of the substrate, to form a complete monolayer. In this method however, the bound molecule is in an inert form, protected by a photo-labile group, which upon light irradiation at a specific wavelength will convert to an active functional group.[35] One may utilise a photomask to allow specific irradiation of the desired areas on the substrate. This approach has been used to allow for re-usable sensors.[36] Sensor manufacture using this method is shown in Figure 3.4.

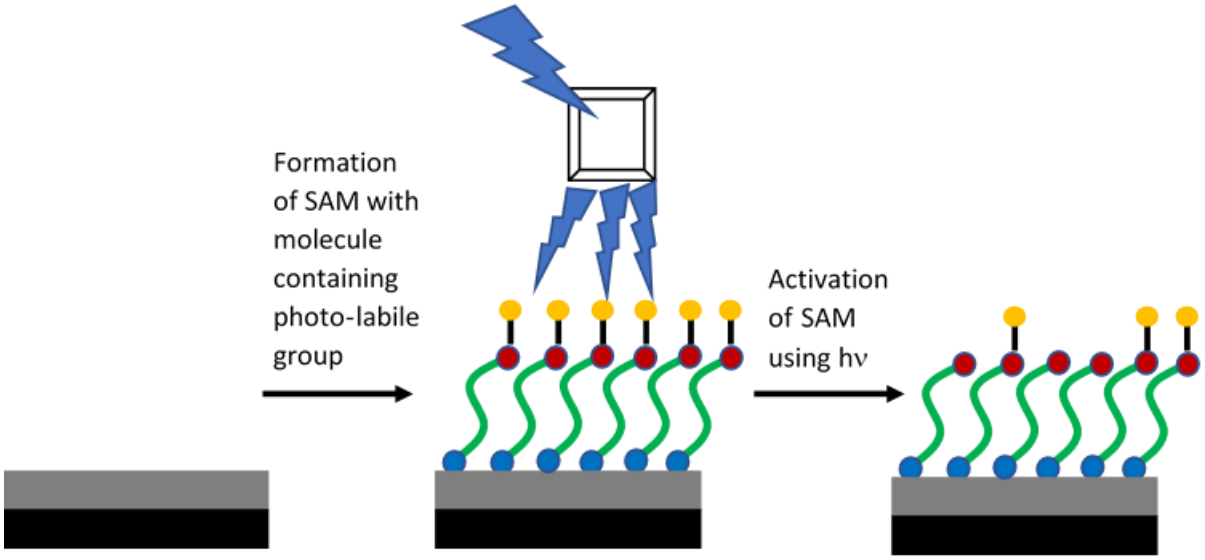


Figure 3.4: Photoactivation method of SAM patterning. The blue bolts are representative of photons, whilst the orange circles represent a photocleavable protecting group, removed after irradiation

3.1.2 Organic and mixed organic/inorganic SAMs as sensors by fluorescence

As discussed in section 1.1, chemosensors can be used as tools in detection of small molecules through a variety of methods. However, the design of optical sensors is of particular note, with fluorescence spectroscopy one of the more popular techniques utilised, owing to the high sensitivity of this technique.[19]

This section details a subset of examples found in the literature, to demonstrate the application of organic fluorophore based SAMs in optical sensing of small molecules.

An early example of fluorescent sensing utilizing a SAM was presented by Krauss *et al.*, wherein the authors utilise an oligonucleotide that has been functionalized at the 5‘ end with a thiol, and at the 3‘ end with tetramethylrhodamine.[37] The immobilised thiolated oligonucleodide forms a hairpin, which orientates the fluorophore towards the gold surface, which was previously demonstrated to be an efficient fluorescence quencher.[38, 39] Emission of the fluorophore was selectively monitored on a CCD camera. The emission intensity was

measured upon immersion in solutions with increasing concentrations of a complementary DNA strand. After complete hybridisation of the hairpin DNA, the gold chips displayed a ~24 fold emission intensity increase (see Figure 3.5 for a schematic of the working principle). This is reasoned to be due to the elimination of quenching effects on the rhodamine from the gold surface, via extension of the DNA such that the fluorophore is at a much-increased distance. The specificity of the sensor was good, with hybridization of a certain DNA oligonucleotide giving a luminescence increase of 94.2-fold and 7.8-fold for perfectly matched and singly mismatched complementary DNA respectively. The reusability of the chips was also favourable with four hybridisation/dehybridisation cycles (performed in 90 ^{o}C water as to denature the DNA) possible whilst maintaining the ability to discriminate between pre and post-hybridisation.

A similar example was later published with cy5 as the fluorophore, the authors of this later paper also characterised the DNA binding event by SPR spectroscopy.[40]

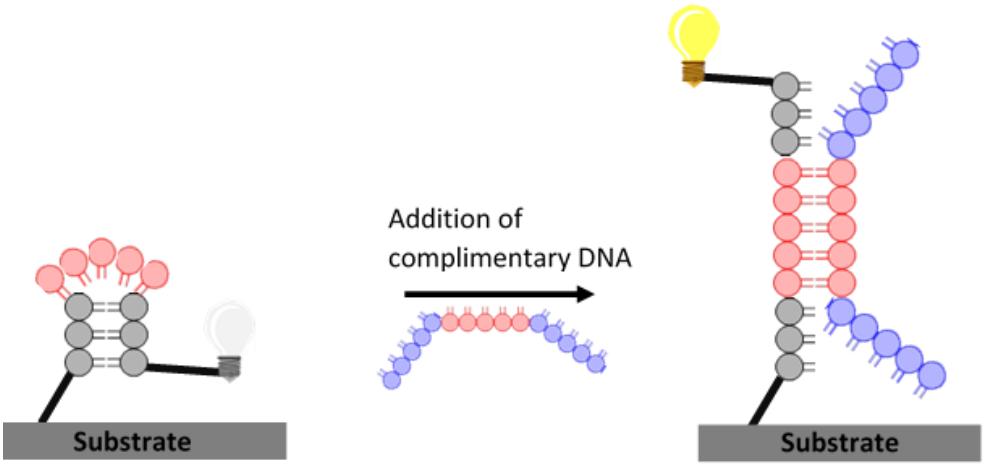
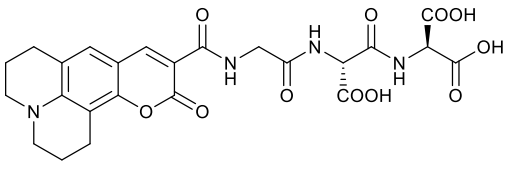


Figure 3.5: Working principle of devices based on a SAM of DNA on a substrate, DNA bases are represented by balls, and the fluorophore represented by a lightbulb. DNA is folded upon itself resulting in a short distance and quenching of the fluorophore emission, upon addition of complimentary DNA strands the system allows for detection and reporting by "light up" effects of the fluorophore

Yu *et al.* recently investigated the concept of SAM luminescence increase through DNA hybridisation (shown in Figure 3.5), and investigated the quenching effects observed with gold, glass and polycarbonate surfaces.[41] All three surfaces have been previously investigated as

materials for sensor platforms in biorecognition.[42-44] The authors of the paper demonstrate that the DNA hybridisation technique can be applied to all three substrate types and that, although formation of DNA hairpins on rougher surfaces is more limited, it can be achieved through correct modification of the DNA spacers.

In 2014 Prins *et al.* described a nanoparticle system, coated with an organic SAM for fluorescence sensing based upon displacement.[45] The monolayer was formed by sulfur attachment to gold nanoparticles with diameter of roughly 2 nm, with the monolayer consisting of hydrophobic C9-thiols terminating with a 1,4,7-triazacyclononane into which Zn^{2+} were coordinated. The group had previously characterised these particles.[46] A dye molecule **M1** (see Figure 3.6) previously synthesised in the group,[47] was found to have an affinity to the monolayer/AuNP's, although could be readily displaced by phosphate competitors. With the dye in proximity to the AuNP limited fluorescence was observed, due to quenching effects. The displacement of the dye could therefore be monitored by fluorescence spectroscopy. The authors added increasing concentrations of Hg^{2+} ions to an aqueous solution containing both thymidine diphosphate, and the Au nanoparticles coated with dye and the thiol monolayer. Upon each addition of the Hg^{2+} ions, thymine-Hg sandwich complexes are formed, as shown in other research.[48] The formation of these sandwich complexes promotes adhesion to the monolayer and allows for the displacement of the dye molecule into solution and therefore a linear increase of fluorescence intensity with Hg^{2+} concentration.



M1

Figure 3.6: Protonated form of the dye molecule used by Prins *et al.* in the solution based sensing assay for Hg^{2+} ions with gold nanoparticles with a SAM coating

Krull *et al*. described the immobilisation of upconverting nanoparticles (UCNPs) of yttrium and ytterbium on glass slides, to form a SAM. The nanoparticles were fabricated such that they were coated with a phosphoryl linked ethylamine group. The coating of the UCNPs allows for a monolayer formation, through the specific reaction of the amine groups on the UCNPs with the activated glass surface, which is coated with glutaraldehyde capped 3-aminopropyltrimethoxysilane groups. Once the monolayer had formed the nanoparticles were reacted with thrombin specific aptamer. This in effect created a luminescent monolayer, which is responsive to thrombin. Monolayer coated glass surfaces were immersed in thrombin containing buffered solution, after which thrombin aptamer coated quantum dots were added to the solution and the surfaces removed and washed. The adherence of a sequence of UCNP-thrombin aptamer-thrombi-thrombin aptamer-QD is now complete, and formation of an upconverting NP and QD system is formed, this is observed by monitoring emission at λ_{em} = 614 nm, with λ_{exc} = 980 nm. The platform then offers an excellent diagnostic device using organic/inorganic hybrids.[49]

In a later paper a trimethoxysilane modified rhodamine dye **M2** (Figure 3.7) is used to form a monolayer on silica coated UCNPs.[50] Rhodamine derivatives have been well studied for their ability to chelate metal cations which in turn alters their photophysical properties,[51] here the rhodamine shows strongly increased absorbance upon increasing the concentration of Hg^{2+}. This leads to increasing energy transfer from the upconverting nanoparticles to the rhodamine dye, and if one measures the intensity ratio of the UCNP emission to the emission of the rhodamine, one can observe ratiometric luminescence changes. This organic monolayer is a good example of SAMs usefulness to sensing.

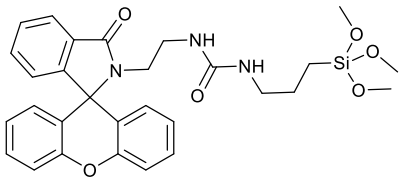


Figure 3.7: Rhodamine-type dye used to form a monolayer on silica coated nanoparticles, the dye absorbance is sensitive to Hg^{2+} concentration and as such can be used as a fluorescence reporter for the ion through emission intensity, arising from increased energy transfer from UCNPs

3.1.3 SAMs of Ru(II) and Ir(III) transition metal complexes

Organometallic molecules of Ru(II) were realised as ideal candidates for creating luminescent devices based on SAMs. The advantageous photophysical and electrochemical properties of these molecules could be incorporated into devices if the proper chemical modifications are made to efficiently bind and coat the surface. Redox active Os(II) and Ru(II) metal complexes bound to gold were explored for their electrochemical properties.[8, 52, 53] However, it was not until later that efficient luminescence of Ru(II) complex SAMs would be described. Early challenges in the creation of such devices were due to the limitations in the signal, reasoned to be due to quenching of the luminescence by the metal surface.[54-58] Our group has recently investigated the distance dependent luminescence of ruthenium(II) complexes immobilised on an Au nanoparticle, and found that increasing the distance between the Ru(II) polypyridyl core and gold support will increase luminescence signal, as the quenching of the excited state decreases.[59]

This section will detail some of the more recent examples of luminescent Ru(II) SAMs on a variety of substrates, to give a broad overview of the possibilities prescribed by use of these metal complexes in place of their organic counterparts. The section will also detail some iridium(III) complexes that are beginning to become more prevalent in the literature.

3.1.3.1 **Ru(II) SAM coated nanoparticles**

In 2011, Gunnlaugsson *et al.* described gold nanoparticle systems coated with a monolayer of luminescent Ru(II) complexes.[60] The luminescent complexes are linked to the nanoparticle through the alkane thiol of the phenanthroline ligand of each complex **M3-M5** shown in Figure 3.8. Upon excitation of a solution of ruthenium appended gold nanoparticles in 0.01 M PBS at pH 7.4, red emission was observed at 610, 605 and 635 nm for NP's appended with **M3-M5** respectively. The DNA binding affinity of each nanoparticle system was assessed and binding constants in the order of 10^7 M^{-1} were calculated for each of the coated systems. Cellular uptake studies reveal that there is a good localisation of these NP's in the nucleus and the cytoplasm. The luminescent nature of the nanoparticles allows for imaging agents based upon conjugated SAMs of Ru(II) on nanocarriers.

Later studies have been carried out using a very similar methodology, wherein reported Ru(II) complexes were used to form a SAM on silver nanoparticles (**M3** and **M4**, see Figure 3.8 for structure). UV-Vis spectroscopy of the SAM coated nanoparticles in 0.01 M PBS revealed a band at 400-470 nm, consistent with the ^{1}MLCT of complex **M3** and **M4** in solution. The emissive nanoparticles were evaluated for their subcellular localisation by confocal microscopy and mainly found in the lysosomes. The authors suggest that the nanoparticles could be used as novel theranostic agents.[61]

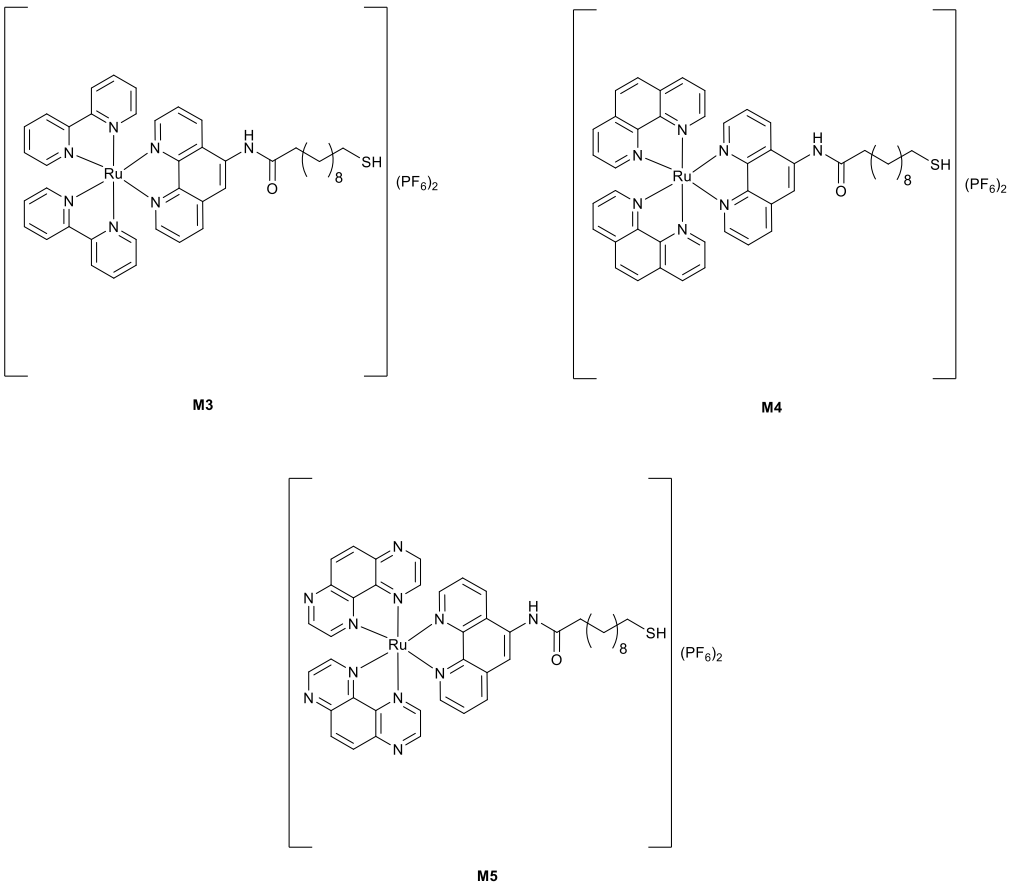


Figure 3.8: Structures of Ru(II) complexes **M3**-**M5** used by Gunnlaugsson *et al.* as SAM forming agents for AuNPs. Coated AuNPs were in turn used as DNA binding probes, utilising the luminescent signal of the ruthenium complexes to report the binding event.

The removal of ruthenium SAMs from gold nanoparticles was probed by Yam *et al.*,[62] lipoic acid functionalised ruthenium(II) and rhenium(I) complexes **M6** and **M7** (Figure 3.9) were linked to gold nanoparticles through the breaking of the disulfide unit of the lipoic acid. The resulting transition metal-nanoparticle conjugates are only weakly luminescent with luminescent QY's of 0.5 and 0.1 % for **M6** and **M7** respectively. This is relative to 5 % and 1 % in solution which suggests 90 % quenching by the nanoparticle in both cases. The ester linkage in both the Ru(II) and Re(I) complexes can be cleaved with an esterase (Figure 3.9), the emission intensity of solutions of functionalised gold nanoparticles containing esterase were monitored as a function of time. Hydrolysis of the ester over time led to increasing luminescent signal from the solutions, which led the authors to believe that there is a possibility of drug delivery and esterase sensing provided by these nanoparticle systems.

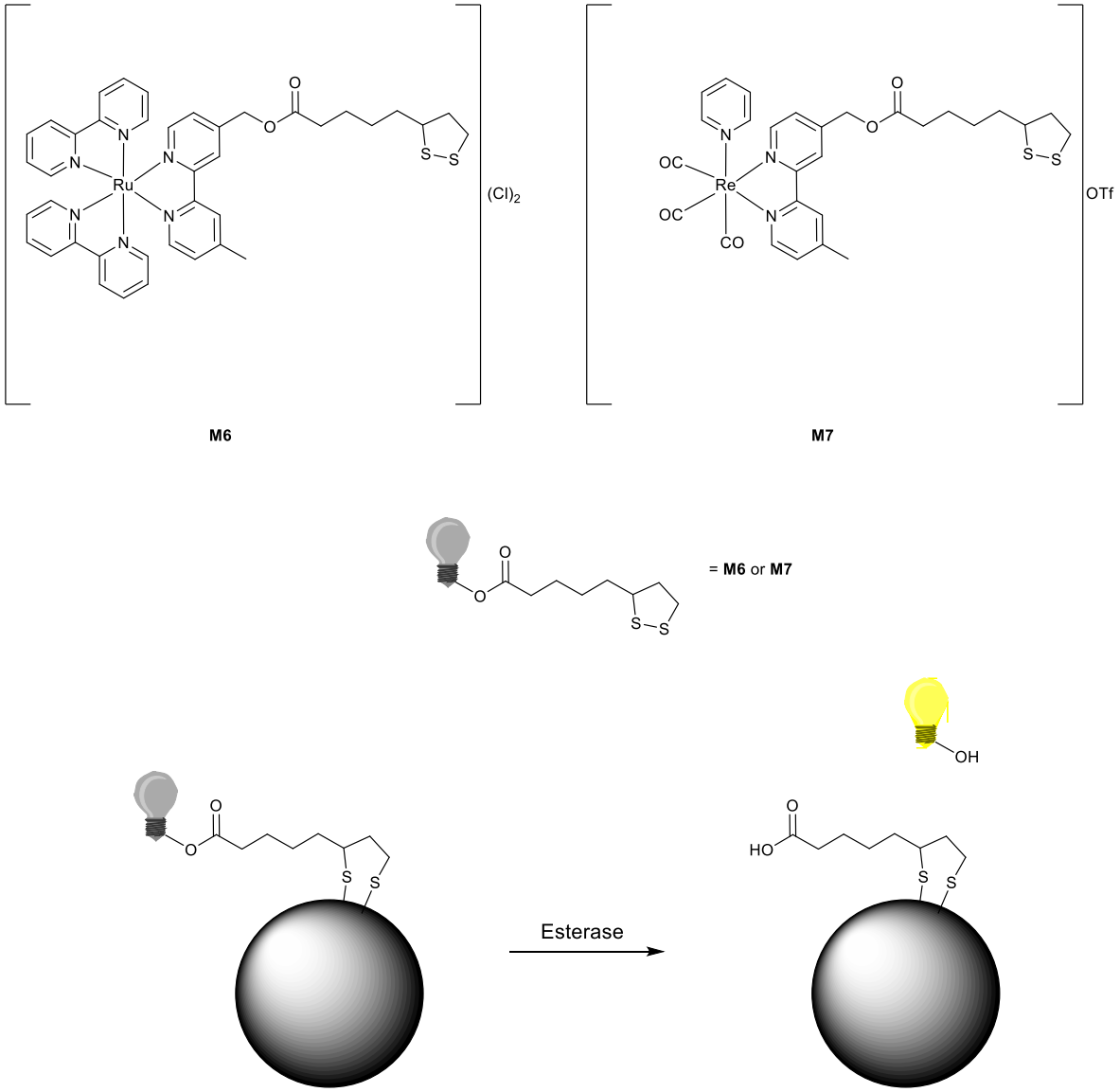


Figure 3.9: Ru(II) and Re(I) complexes **M5** and **M6** used by Yam *et al.* to form SAMs on gold nanoparticles. A schematic of the working principle behind esterase mediated cleavage is also shown. The colour of the lightbulb represents emission intensity of the lumiphore, grey is low intensity whilst yellow is higher

Spray pyrolysis allows the formation of high purity mesoporous silica nanoparticles with a highly ordered pore structure and spherical morphology,[63] and has been used as a method to create highly fluorescent silica nanoparticles.[64] Ribeiro *et al.* use spray pyrolysis to create mesoporous silica nanoparticles, and functionalise these nanoparticles with silylated Ru(II) complexes **M8** and **M9** (Figure 3.10).[65] The metal complexes were synthesised in accordance with existing protocols.[66] IR and luminescence spectroscopy were used to characterise the hybrid nanoparticle-metal complex materials. In the IR spectrum C=C, and C=N bonds as well

as C-H vibrations were observed, although peaks characteristic of covalent binding could not be observed due to the large background from the silica matrix. Luminescence spectra of the ruthenium(II) complex doped nanoparticles reveal emission spectra with emission maxima at λ_{em} = 630 nm. The authors compare this with the emission spectra of **M8** and **M9** in ethanolic solution in which λ_{em} = 716 and 745 nm respectively. The authors explain the large blue shift in emission as arising from the rigidochromic effect which was previously observed for transition metal complexes in sol-gels.[67]

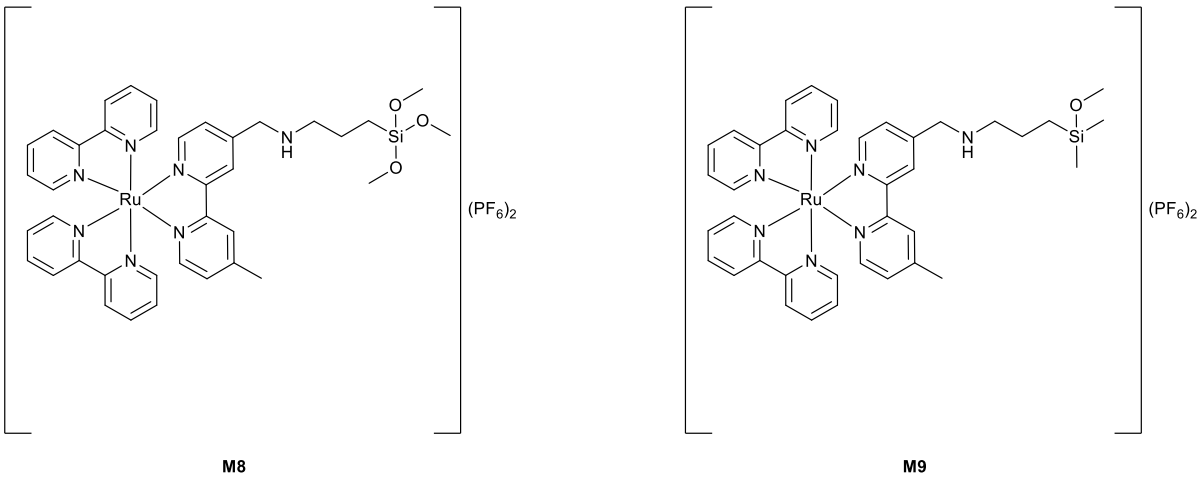
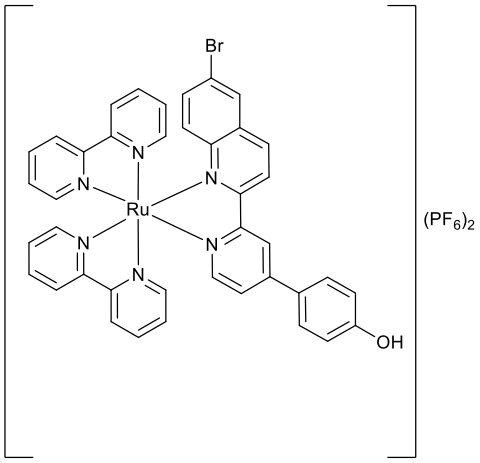


Figure 3.10: Ribeiro *et al.* synthesised both **M8** and **M9** as complexes to immobilise in mesopourous silica nanoparticles, monolayers would be formed by adhesion of the methoxysilane groups on the 2,2'-bipyridine ligand

3.1.3.2 **Ru(II) SAM modified planar substrates**

Gulino *et al.*, constructed a CO sensor from a ruthenium(II) complex SAM on silica.[68] Silica substrates were primed with trichloro[4-(chloromethyl)phenyl]silane molecules, and the Ruthenium complex **M10** (Figure 3.11) with the reactive hydroxyl group was added. This provided a monolayer covering of the surface, which was stable, proved by XPS studies in which deliberate removal by mechanical means was found to be extremely difficult. After XPS confirmed the presence of the Ru(II) complex, UV-Visible spectroscopy probed the changes in charge transfer states, although only a small 7 nm shift was observed for the ^{1}MLCT band, retaining its structure. Highly structured emission was observed across the range of 600-850

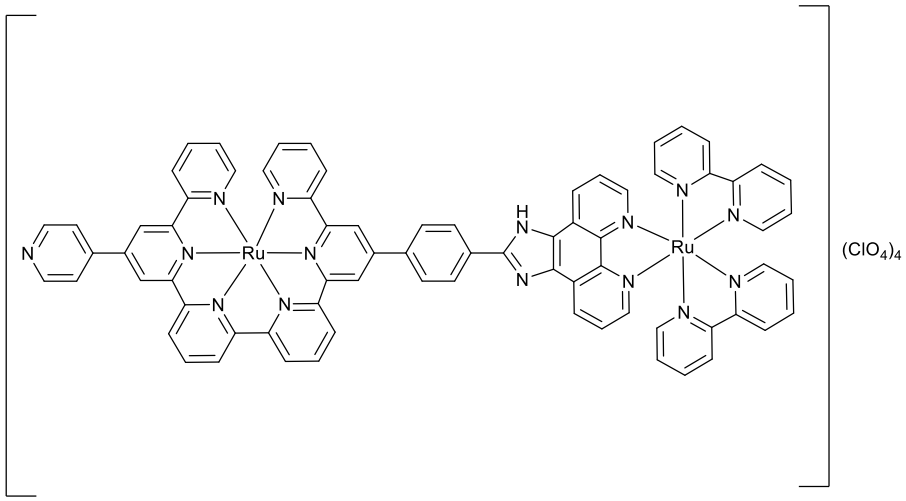
nm (λ_{exc} = 488 nm) which is atypical for ^{3}MLCT emission and likely means emission arises from ligand centred states. The emission intensity of the surface was monitored at λ = 680 nm with increasing concentrations of CO in the cuvette (0-200 ppm). Stern-Volmer fitting revealed a linear relationship between the decrease in intensity and the concentration of CO in the cuvette.



M10

Figure 3.11: Complex **M10** which used by Gulino *et al.* to fabricate CO sensing monolayers at silica surfaces

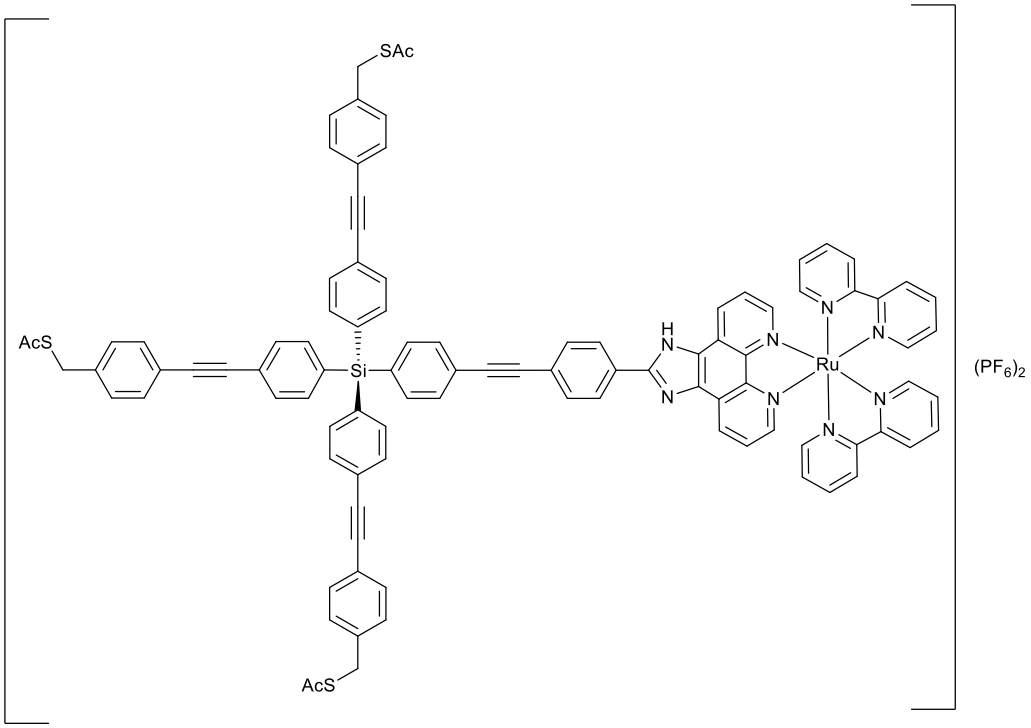
Later, the same group used a similar approach to build electro-switchable read-write device on ITO slides using complex **M11** (Figure 3.12).[69] The absorbance of the bimetallic layers could be modulated by controlling the potential applied to the surface. The final device was found to be stable and switchable across a large number of redox cycles and provides a number of discrete states which allow for creation of ternary memory units.



M11

Figure 3.12: To construct electro-switchable devices, the complex **M11** was synthesised by Gulino *et al.* redox cycles of this complex when immobilised on ITO allows for voltage dependent absorption

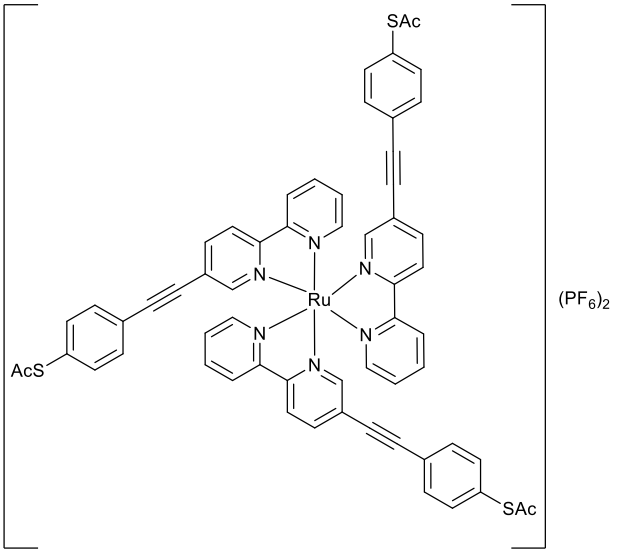
In 2011, De Cola *et al.* synthesised and investigated the photophysical properties of a tripodal ruthenium(II) complex bearing thiacetyl groups (**M12**, Figure 3.13).[70] The thioacetyl bearing complex was then anchored to a gold substrate. Monolayer formation was achieved by immersion of the gold slide in ethanolic solutions of **M12** containing hydrazine, with SAM formation confirmed by AFM. The Ru(II) complex forms islands with a height of ~3nm, this island effect is commonly observed for metal complex thiolates on gold.[71, 72] The photophysical properties of the monolayer formed on gold were investigated and compared to those in acetonitrile solution. Ru(II) monolayers emit at 619 nm whilst in acetonitrile solution the emission is observed at 609 nm. The red shift of 10 nm in emission is reasoned to be due to the electron withdrawing effect of the gold on the phenanthroline ligand, on which the LUMO is localised. The lifetime of the monolayer on gold is short, at 8 ns, and this is reasoned to be due to electron and/or energy transfer to the gold surface.



M12

Figure 3.13: Structure of the tripodal Ru(II) complex designed by De Cola *et al.* for the fabrication of SAMs on planar gold surfaces

Following the previously mentioned paper, Mayor *et al.* synthesised novel bipyridine complex **M13** (Figure 3.14). The group recognised that there will be a notable difference in the coordination characteristics of the facial vs the meridial isomer of a ruthenium bidentate complex in which each 2,2'-bipyridine is individually thiolated, owing to the spatial arrangement of the thiol groups.[73] The isomers were isolated and the arrangement of all thiol groups on one face in the *fac*- isomer confirmed by single crystal x-ray diffraction experiments. The deposition of the *fac*- isomer was investigated by STM and highly ordered structure of dimers was observed which contrasts with the groups previous deposition of tripodal lanthanide complexes.[74]

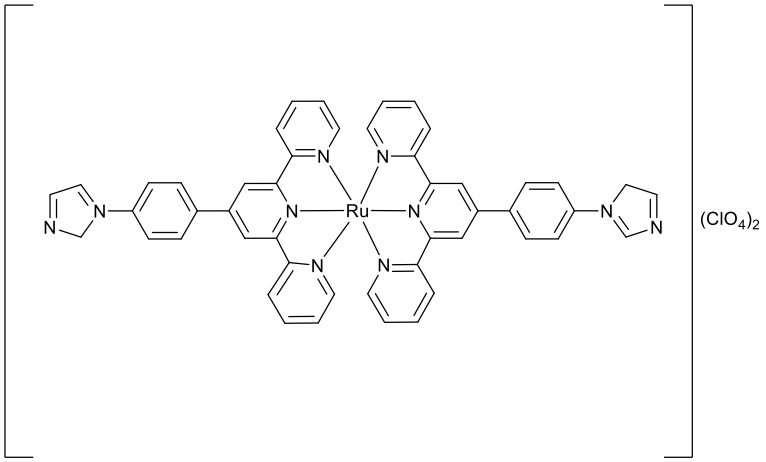


M13

Figure 3.14: Ruthenium complex synthesised and subsequently separated into *mer*- and *fac*- isomers, this isomerism was reasoned to be a factor in creating well ordered monolayers on gold surfaces

In an attempt to improve upon the spectroelectrochemical properties of previously reported monolayers of Ru(II) and Fe(II) terpyridine complexes.[71, 75] Wang *et al.*, report bis-terpyridyl Ru(II) complex **M14** (Figure 3.15), synthesised for the purposes of creating an ITO electrode.[76] A monolayer of **M14** was formed using a similar technique to that of Gulino *et al.*, in which conductive ITO substrates were silanized using 3-chloropropyltriethoxysilane. The silanized substrates were immersed in acetonitrile-DMF (5:1) solutions containing **M14**. UV-Vis spectra of the Ru(II) complex were collected in aqueous solution and immobilised on the surface. The bands in aqueous solution appear at 312 and 490 nm, when immobilised shifts of 4 and 9 nm are observed, to give a spectrum with absorption maxima at 316 and 499 nm. The authors also note the presence of a Ru(II)/Ru(III) redox couple on the ITO surface, at an $E_{1/2}$ of +1.349 V (vs SCE). The surface concentration was derived by both UV-Vis and CV studies, with concentrations found of 5.53×10^{-11} mol cm^{-2} and 1.64×10^{-11} mol cm^{-2} by each technique respectively. The discrepancy in the value can be explained due to the assumption that the molar absorption coefficient is equal in solution and in the film, significant differences have

been observed previously in Ru(II) Langmuir-Blodgett films.[77] Finally, the authors investigated the photocurrent generation, and found a maximum incident monochromatic photon-to-current conversion efficiency of 1.8% at 500 nm.



M14

Figure 3.15: Ruthenium complex synthesised by Wang et al. for the purposes of creating a photovoltaic ITO electrode.

In 2019, Bonacin and Toledo used a self-assembled monolayer of ruthenium complex to be used as an electrochemical sensor for dopamine.[78] The authors first formed a monolayer of 4-mercaptopyridine on a bare gold electrode, which was then immersed in a solution of $[Ru(H_4dcbpy)Cl_2]$ which led in turn to the formation of a Ru(II) complex monolayer on gold. The ruthenium coated electrode was assessed for its ability to facilitate the electrooxidation of the dopamine at the electrode, and the results compared with the bare gold electrode. A limit of detection for dopamine of 9.5 μM was found for the bare gold electrode, compared with 3.3 μM for the electrode with a ruthenium monolayer, proving the ability of the Ru(II) monolayer to aid in electrochemical dopamine sensing.

Lagrost *et al*. proposed a ruthenium-lanthanide mixed 4d and 4f bimetallic complexes for monolayer formation (**M15**-**M17**, Figure 3.16).[79] The self-assembled monolayers were formed on gold plates and gold electrodes, the thiol group bound covalently to the gold surface after in situ deprotection of the thioacetate with NH_4OH. The contact angle of the surfaces was

measured and an increase from 60° measured for bare gold, to 67°, 76°, and 77° for **M15** to **M17** respectively. Each monolayer was assessed for thickness through ellipsometry, with a monolayer thickness of ~3 nm for each complex. IR spectra confirmed the identity of the monolayer forming complex, with characteristic vibrations of the acetylide group observed at around 2040 cm^{-1}. Cyclic voltammetry of the monolayers was performed and the oxidation potential of ruthenium(II) complex **M15** found at 0.49 V. Upon addition of lanthanide complexes of Eu and Yb (forming **M16** and **M17**) to the SAMs the oxidation shifts by 30 mV, to 0.52 V. This shift demonstrates the SAMs ability to monitor lanthanide binding by electrochemical means at a surface. Luminescence spectroscopy was attempted but the authors did not observe sufficient signal, reasoned as quenching *via* energy transfer to the gold surface.

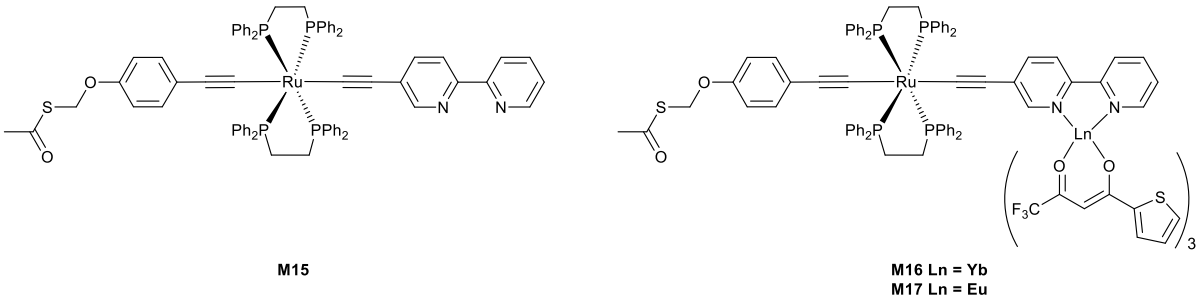
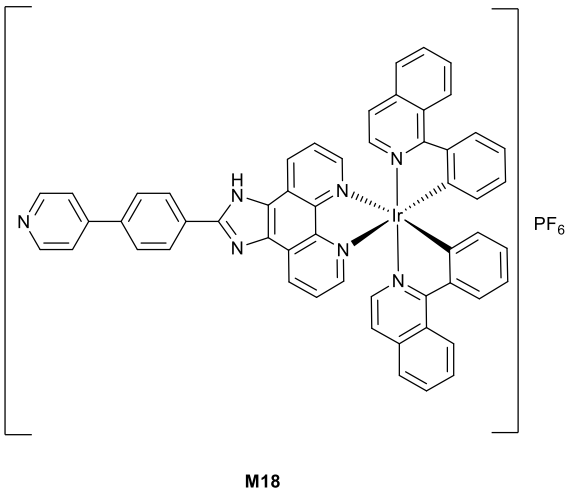


Figure 3.16: 2,2'-bipyridine containing4d and mixed 4d-4f metal centres for construction of electro-active SAMs, synthesised by Lagrost *et al.*

3.1.3.3 **Ir(III) SAM coated nanoparticles**

Mayer *et al*. described the use of iridium(III) complex **M18** (Figure 3.17) as SAM forming agent on Ag and Au nanoparticles.[80] The capping of the Ag and Au nanoparticles occurs through covalent binding to the NP surface through the 4-substituted pyridine moiety on the ancillary ligand, with the authors adapting previously described methods,[81] to estimate binding of around 15 complexes per AuNP. The coated nanoparticles are around 5 nm in diameter with polydispersity of < 0.5 nm as assessed by TEM. After synthesis, the photophysics of the iridium(III) complex free in solution and bound to nanoparticles was assessed in DCM solutions. The absorption spectra reveal bands at 288 and 333 nm in solution. On Ag these

bands appear at 292, and 336 nm. In Au only the 293 nm peak is visible above the SPR band which is observed at 516 nm. Emission spectra collected in deaerated DCM reveal emission maxima of λ_{em} = ~ 630 nm for **M18** in solution and as a SAM on Au and Ag nanoparticles. The complex displays a quasi-reversible CV spectrum oxidising at ca. + 0.7 V vs FC in acetonitrile. This behaviour allows the study of the electrofluorochromism, the phenomena of switching between luminescent and non-luminescent forms of the complex based upon altering of the oxidation state of the metal centre. In this study, the electrofluorochromism is only investigated in solution, but large decreases are observed in the luminescence intensity when the compound is oxidised to the Ir(IV) form, and recovery of luminescence observed when reduced back into the original Ir(III) complex.



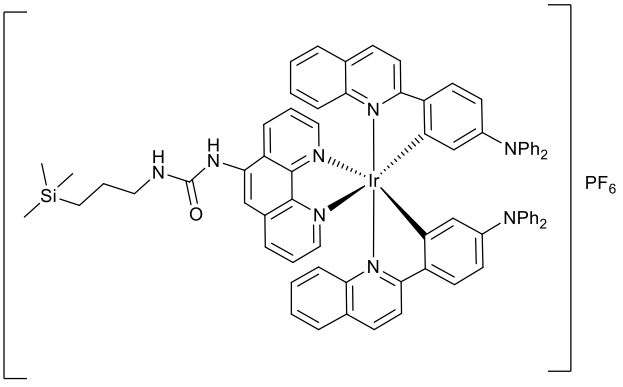
M18

Figure 3.17: Iridium(III) complex synthesised by Mayer *et al.,* to investigate electrofluorochromism

Further to the study of Mayer *et al.,* the group of Miomandre *et al.,* investigated the electrofluorochromism of both the **M18** complex and of the AuNP system coated with **M18**. This study therefore allows investigation of the effect of the Au surface charge on the electrofluorochromism. The authors note that with increasing redox potential the luminescence intensity lowers proportionally in the range 0.9-2.0 V. This effect is not observed in coated AuNPs, wherein only very small effects are observed through oxidation potentials 0.9-1.9 V with a large effect observed upon reaching 2.0 V. This finding suggests that whilst the oxidation

potential of Ir(III) complexes on gold nanoparticles with high surface charge may not be significantly shifted,[82] the charge of the nanoparticles may hinder the electrofluorochromism process.[83]

A tetraethylorthosilicate capped iridium(III) complex (**M19**, Figure 3.18) is used by Huang *et al.* to form a monolayer on upconverting silica coated nanoparticles.[84] The nanoparticles show emission peaks in the same region as the iridium complex absorption (λ_{em} = 477 nm). The authors estimate the FRET efficiency of the $^1G_4 \rightarrow {}^3H_6$ transition to the iridium complex to be 32 %, based upon the lifetime of the nanoparticle coated system. Luminescence spectra of the iridium complex were taken at differing concentrations of oxygen, and a Stern-Volmer plot was obtained which confirmed that the nanoparticles could be used to ratiometrically track oxygen content through their emission lifetime/intensity. The nanoparticles were non-toxic in cell studies and the authors used PLIM studies in live cells to give a luminescent readout of oxygen content.

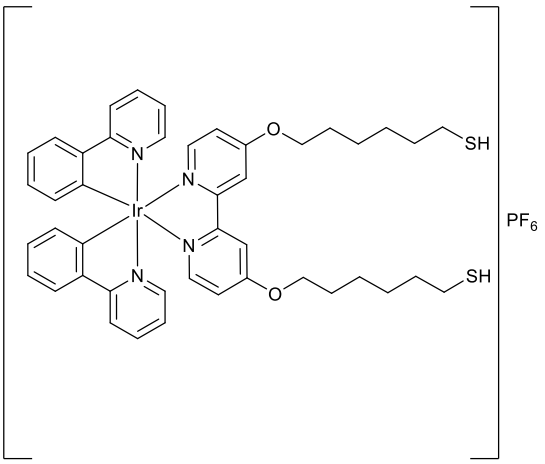


M19

Figure 3.18: Reported structure for **M19**, given by Huang *et al.* with phenylquinoline type ligands allowing for oxygen-sensing properties and the aliphatic linker for attachment to UCNPs

Monodisperse iridium(III) complex coated nanoparticles were reported by Pikramenou *et al.* in 2017. Covalent attachment of iridium complexes through a bipyridine appended-thiol linker (**M20**, structure shown in Figure 3.19) was confirmed through zeta potential experiments, which measure the potential difference between the dispersion medium and the stationary layer

attached to the particle. The zeta potential shows a shift from -50 to -35 mV on addition of the Ir(III) complex indicating a change in the stationary layer composition to a more positive charge. ICP-MS was used to calculate complexes per nanoparticle, found as 23000 complexes per nanoparticle. The nanoparticles were emissive, with λ_{em} = 570 nm, which allows for the nanoparticles to be used to track blood flow through luminescence. Mouse studies of the nanoparticles confirm good organ clearance , and the study highlights the utility of luminescent Ir(III) monolayers in nanomaterials.[85]



M20

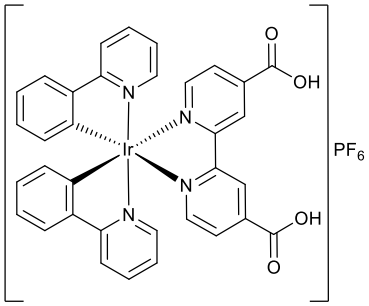
Figure 3.19: Ir(III) complex synthesised by Pikramenou *et al.*. Gold nanoparticles coated with **M20** can be used to track bloodflow with confocal microscopy, utilising the luminescent signal arising from the Ir core. Image

3.1.3.4 **Ir(III) SAM modified planar substrates**

Several methods of coating planar samples with luminescent layers of iridium(III) complexes have been previously described, such as spin coating,[86, 87] Langmuir-Blodgett films,[77, 88] and ink-jet printing.[89] There are still limited examples that exist of self-assembled monolayers formed on substrates.

One of the largest areas in which self-assembly is used to construct a functional surface is for solar cell applications. Several examples exist where titania or conductive ITO samples have been functionalised with iridium(III) complexes.[90-94] In brief, solar cell applications rely on excitation of the irdium complex followed by an electron injection into the TiO_2 layer from the

excited state. Recently a group found three-time constants associated with the electron injection process of **M21** (Figure 3.20) on TiO_2 and ascribed one of these to the triplet state of the bpy ligand. The study suggests then that somewhat matching photophysical processes can still occur in immobilised iridium(III) complexes.[94]



M21

Figure 3.20: Structure of **M21** that was immobilised on TiO_2 layers to investigate electron injection properties, one process was assigned to the bpy triplet state, the others continue to be investigated

For gold surfaces, De Cola *et al.* described both an iridium(III) and an osmium(II) complex (**M22** and **M23** respectively, Figure 3.21) bearing a tripodal ligand capped with thioacetate ligands.[95] Only SAMs of Os(II) are described and studied, but it is expected that the same trends will be observed in Ir(III). The monolayers were characterised by AFM, in which the 3 nm height of the monolayer matched the expected height of the molecule. Coverage was estimated from electrochemistry and a value of $4.5x10^{-11}$ mol cm^{-2} was found, which is around 1 order of magnitude smaller than that of alkane thiols. This fits however, knowing that both the steric bulk of the molecule, and the surface coverage of the anchoring group are much higher. Whilst the authors attempted to take luminescence spectra, they were unable due to the large amount of energy/electron transfer inherent in the system. The authors investigated the electron transfer rate, which is significantly faster than in other studies and concluded this is due to the highly conjugated nature of the surface bound ligand. This study may suggest therefore that to provide highly luminescent gold surfaces one may be best to avoid conjugation close to the surface.

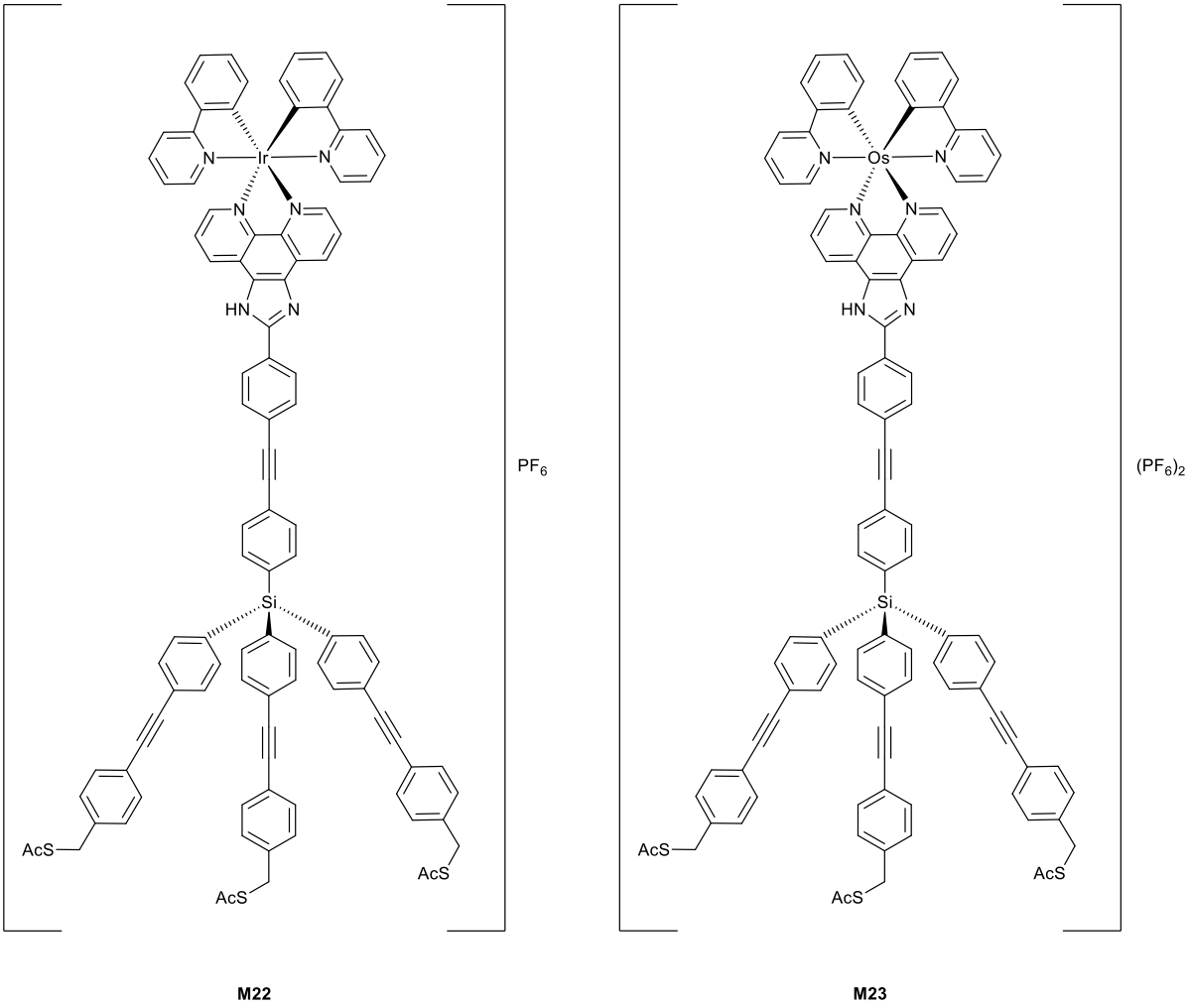


Figure 3.21: De Cola *et al.*, describe the use of these luminescent transition metal complexes in the formation of SAMs on gold substrates. The surface anchored Os(II) complex shows interesting electronic properties but very poor emission intensity

More recently Pikramenou *et al.* have worked with gold substrates for luminescent sensing based on the emission of a surface bound Ir(III) complex **M24** (Figure 3.22).[96] The metal complex bears a ligand with sufficient length to avoid quenching effects from the gold, and luminescent spectra may be obtained from the gold surfaces directly. Emission of the immobilised Ir(III) complex is observed at 530 nm with a luminescent lifetime of 130 ns. Upon immersion of the gold slides in aqueous BSA solutions, the lifetime increases to 170 ns. This increase in luminescent lifetime is characteristic of a reduction in the luminescent quenching pathways of the iridium, likely arising from exclusion of oxygen by the adsorbed BSA. The hydrophobicity-based interaction of the iridium with BSA was further proved in solution by CD spectra, in which the iridium complex induces a change in the secondary structure. Overall

the paper provides a useful foundation for the construction of luminescent gold surfaces functionalised with Ir(III) complexes for the purpose of sensing.

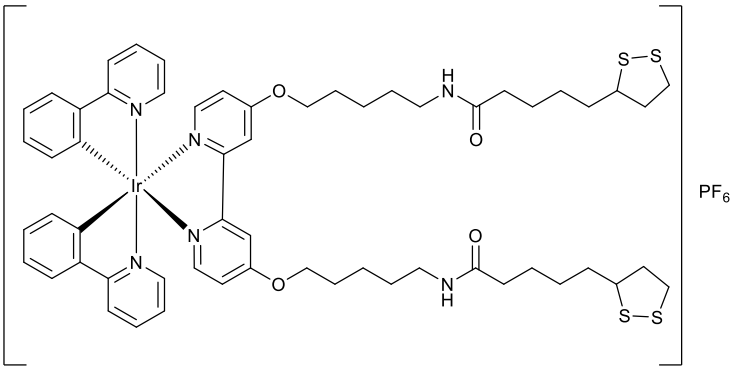


Figure 3.22: Complex synthesised by Pikramenou *et al.*, for SAM based detection of BSA on gold substrates, utilising the luminescent lifetime of the Ir(III) complex

In a later paper by the same group, the aforementioned surfaces were co-coated with fluorosurfactants to increase the binding through increasing overall hydrophobicity, and lower non-specific interactions with the gold. The paper concludes that addition of surfactants increases the luminescence lifetime of the Ir(III) coated surfaces, almost universally, and that the choice of surfactants should be carefully made in order to optimise the albumin binding event.[97]

3.1.4 General comments on perfluorooctanoic acid toxicity and monitoring

Perfluoroalkyl substances (PFAS) are small alkane molecules in which every hydrogen atom bound directly to the carbon backbone is replaced by a fluorine atom (Figure 3.23 shows the molecule perfluorooctanoic acid (PFOA) to demonstrate a perfluorinated compound). The substances were used in a variety of applications. Medicines, fire-retardants, adhesives, and surfactants have all been formulated with components including perfluoroalkyl substances.[98] The fluorine-carbon bond is notoriously strong,[99, 100] and resistant to even harsh chemical treatment, such as heating in sulfuric acid.

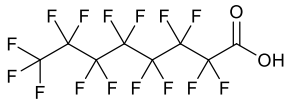


Figure 3.23: Structure of perfluorooctanoic acid, a derivative of octanoic acid, wherein each hydrogen atom on the carbon backbone has been replaced with a fluorine atom

Unfortunately, after this widespread popularity and the resistance to degradation inherent in these compounds, their environmental distribution is now ubiquitous.[101, 102] Persistence of the fluorosurfactant presence then seems inevitable, and detectable concentrations in human and animal tissues are frequently being recorded.[103] Exposure is possible from groundwater, drinking water, flora and forna;[104-107] with environmental levels recorded likely to have been building for several years.

The affinity of PFOA is high for the serum, kidneys, and liver in mammalian species. Many studies have focussed on the toxicity of several PFAS; summarising their findings briefly, one can conclude that these compounds are carcinogenic,[108] hepatotoxic,[109] immunotoxic,[110] and likely harmful to the development of mammalian young.[111]

Despite indications of toxicity, international guidelines for PFAS content in drinking water have not been drafted. Nations often determine their own regulations.[112] Developing nations such as China and India have at the time of writing still not set health advisory limits. More developed nations such as the UK, USA, and Australia have set drinking water values. Some representative guideline values for select nations can be found in Tables 3.1 and 3.2 below. Testing in these countries is frequently carried out by relevant water authorities; however independent peer reviewed studies on sources of water are often available. Selected experimentally determined values for the countries with testing data have also been shown in Table 3.1 and 3.2.

Table 3.1: Guideline PFOA concentration values in drinking water provided by governments or responsible water boards of select nations

Agency	**Guideline value (ng L^{-1})**	**Source**
UK Drinking Water Inspectorate	PFOA< 300 PFOS< 300	[113, 114]
U.S. Environmental Protection Agency	PFOA+PFOS: 70	[115]
Australian National Health and Medical Research Council	PFOS+PFHxS: 70 PFOA: 560	[116]
Swedish National Food Agency	$PFAS_{11}$< 900 Action level: $PFAS_{11}$<90	[114, 117]

Table 3.2: Experimentally determined PFOA content in water samples collected from a variety of sources in a variety of countries. The values are in every case determined by HPLC methods as described above

Country	**Total (median)** **(ng L^{-1})**	**Site/Remarks**	**Source**
Korea	1.44-224 (11.9)	Tap water collected from WPPs (Nakdong River) in 2017	[118]
China	Hangzhou: 12.5–175.3 (82.9) Changshu: 56.0–155.4 (122.4) Suzhou: 11.2–109.9 (66.9)	64 tapwater samples collected from 17 cities (only select cities are shown) in 2015	[119]
	Influent: 2.6-66000 Effluent: 2.8-16000	Waste water samples from 12 waste water treatment plants in China	[120]
France	<7-93	110 treated water samples were collected from public water system in 2009	[121]
German	nd-42.7	Maximum concentration 26 tap water samples were collected from various households in Germany in 2012	[122]
Netherlands	35.947	Tap water were collected from UV university in 2010	[123]
USA	<1-1102 (19.5)	Maximum concentration Treated drinking water were collected from 25 DWTPs represented 24 states within the contiguous United States	[124]

Values in drinking water often do not exceed recommended values; however, monitoring is vitally important. Environmental PFAS monitoring is traditionally slow and requires specialist equipment. The testing is commonly carried out by LC-MS, in the case of most matrices, solid phase extraction can be used to concentrate samples and clean out unwanted interfering molecules.[125] The technique allows for high sensitivity, high selectivity and high reproducibility. Careful consideration must be given however in this methods to the analysis of branched vs. linear PFAS as they will show matching mass signals, and can on occasion co-elute.[126] One also must consider the disadvantages of this technology, that it is not portable, it has a relatively time-consuming detection period, and requires specialist training for operation.

In 2013 an electrochemical method was proposed for the detection of PFAS.[127] In which a membrane ion-selective electrode for $PFOS^-$ and PFO^- was constructed. Whilst this technology does offer advantages over the HPLC methods in that the technology is able to be used in-situ, the sample preparation is reduced, and it is cost efficient. Unfortunately, the sensitivity and specificity of this instrumentation does not reach the same levels as HPLC. LOD for the $PFOS^-$ and PFO^- is 2.3 nM (1.0 ppb) and 0.86 nM (0.43 ppb), respectively. As discussed briefly above, this is due to the bond strength and lack of electrochemical activity of the PFAS.

3.1.5 PFOA detection by fluorometric methods

The discussion above poses an interesting question, in whether the sensitivity of fluorometric methods can be applied to the detection of PFAS. The following section will detail examples of fluorimetric methods for the detection of PFAS. It should be noted that examples do also exist of optical detection by UV-Vis method too, however these will not be considered in detail as they do not rely on the more sensitive fluorescence technique.

Walekar *et al.* used quantum dots fabricated through hydrothermal one pot synthesis from selenomethionine as a fluorescent system.[128] The fluorescent quantum dots are emissive in the blue, with emission maxima ~440 nm. Upon addition of PFOA the fluorescence intensity from the quantum dots decreases, proportional decreases are observed with increasing concentrations of PFOA (Figure 3.24 shows the working principle). The authors report response in the 10-70 μM range with a limit of detection at 1.8 μM. This is around 1000-fold higher than the environmentally acceptable limits in even the more lenient countries.

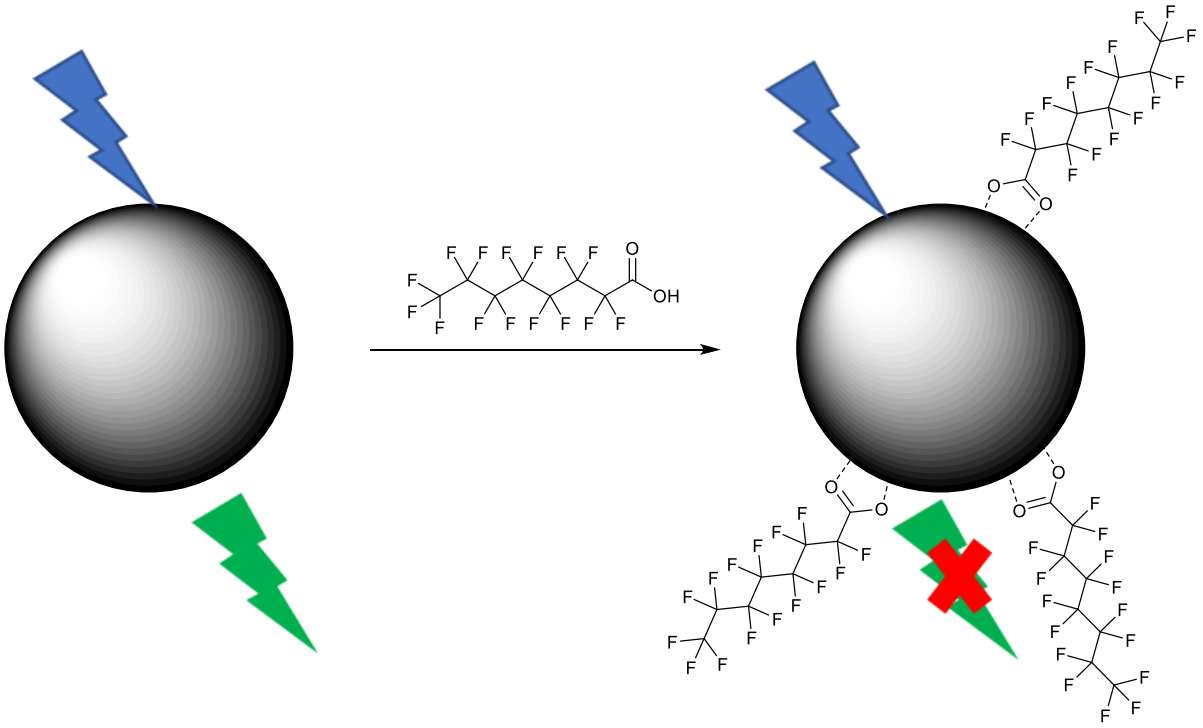


Figure 3.24: Working principle of the QDs utilised by Walekar *et al.*; increasing PFOA concentrations result in a decrease of the fluorescent signal arising from the QDs. Blue bolt signifies λ_{exc} = 350 nm, the green bolt λ_{em} = 440 nm

Tan *et al*. investigated the eosin Y dye as a potential hydrophobic sensor for PFOS.[129] The sensor is first mixed with polyethylenimine in pH 7.0 Britton–Robinson buffer (Figure 3.25 for structures). The resulting hydrophobic interaction quenches the fluorescence observed from the eosin. Addition of PFOS leads to dissociation of this bound complex and proportional fluorescence recovery is observed upon increasing concentrations of fluorosurfactant. The

method displays a limit of detection of 0.15 μM, improving upon other methods but still far short of measuring within currently detected levels in the environment.

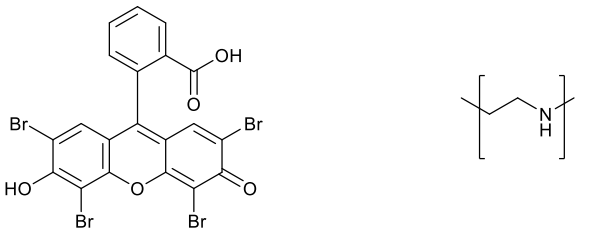


Figure 3.25: Structure of the eosin Y and the polyethylenimine used as a combined system to detect PFOA concentrations in aqueous solution through the fluorescence recovery of the eosin Y dye

Later the same group proposed the use of erythrosin B probe as a fluorescent complex when dissolved in buffer at pH 7.[130] The dye shows a hydrophobicity-based interaction with CTAB (Figure 3.26 for structures). At low CTAB concentrations the fluorescence is significantly quenched (>70 %), with higher concentrations giving no further quenching but a subsequent red-shift of 11 nm. Proportional fluorescence recovery is observed upon increasing concentrations of PFOA, with the method displaying a limit of detection of 11.8 nM, an improvement upon other methods and being just 4-fold higher than environmentally observed levels.

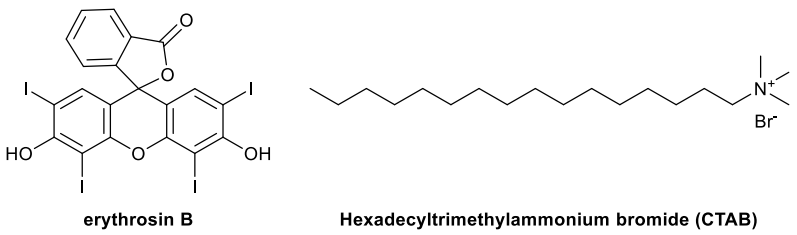


Figure 3.26: Tan *et al.* proposed the erythrosin B and CTAB combined system for aqueous detection of PFOA. The fluorescence recovery of the dye is measured across increasing concentrations of PFOA

Further examples of quantum dot based detection of PFOA was shown by Liu *et al.*[131] Interparticle distance is a determining factor in the fluorescence intensity of the quantum dots, so increasing/decreasing this distance should increase/decrease fluorescence intensity. In this study, fluorescence spectra of solution dispersed quantum dots upon sequential additions of

PFOA are taken in the range of 0.5 – 40 μM. It is thought that fluorine-fluorine interactions between PFOA molecules binding to the surface of nanoparticles drive the particles closer together (see Figure 3.27). This decrease in distance leads to significant quenching, and with further modification of the quantum dots the assay may be even more efficient.

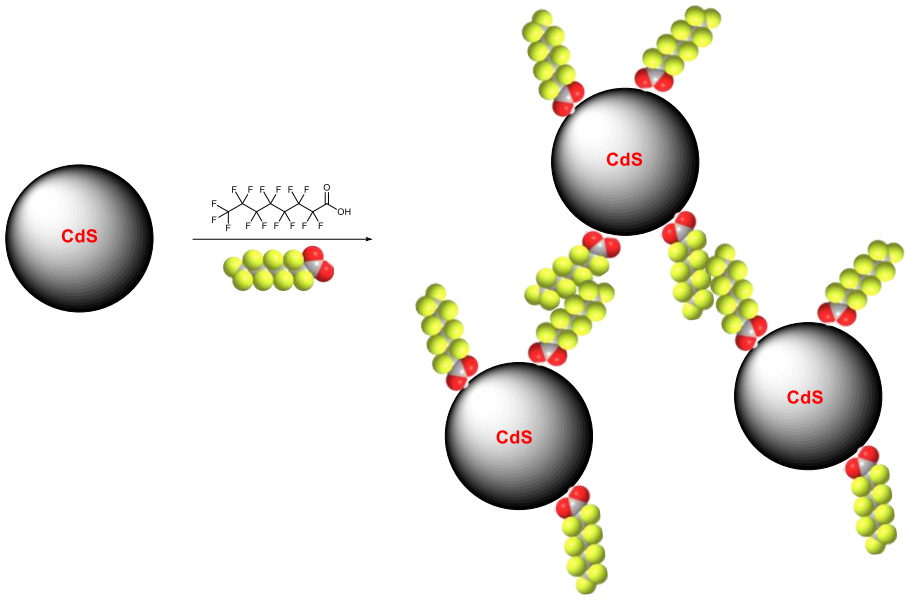


Figure 3.27: Cadmium sulfide quantum dots designed by Zhu et al. can be used as above to show aggregation induced quenching mediated by the concentration of PFOA in aqueous solution

Carbon nanodots were synthesised by Li *et al.*, from vitamin B1 and triethylamine.[132] These nanodots show good thermal, pH and UV stability, whilst displaying strong blue fluorescence (λ_{exc} = 370 nm, λ_{em} = 437 nm). The fluorescence may be enhanced through addition of PFOS to a solution of the nanodots; electrostatic interaction at the surface of the nanodot leads to binding and then aggregation (the working principle is the same as in Figure 3.27). Fluorescence enhancement is linear in the PFOS concentration range of 0.3 – 160 nM with a detection limit of 0.3 nM. This fluorescent probe therefore can show a fluorescence enhancement well within the PFOA concentration range found in environmental samples.

3.1.6 Our Aims

Development of fluorescent assays for perfluorooctanoic acid is an active area of study, many compounds developed for this role however rely on luminescence intensity measurements.[130-132] Facile detection of analytes by means of optical readout has long been a goal in chemistry. Modified gold surfaces, coated with iridium(III) complexes with a response to biomolecular recognition events have been previously developed by our group.[96] However further optimisation of these surface-active structures, with addition of a sensing moiety, is possible.[19, 133-136] Transition metal systems offer advantages including long lasting luminescent lifetimes and high photostability; however many studies have focussed on transition metal devices based upon electrochemical readout.[134, 137-142] Luminescence lifetime measurements of transition metal complexes can easily be used to probe the local environment and be used as a readout of binding events, as was previously shown by utilising Ir(III) complex coated nanoparticles to track microenvironments within cells using the luminescence lifetime of the Ir(III) complex.[143] A rapid screening luminescent transition metal-gold device would be advantageous in monitoring continuing environmental levels of PFOA, due to the portability, and accuracy of the fluorescence detection method.

In this work we introduce a small number of novel hydrophobic complexes, utilising alkylation of an aromatic phenylpyridine moiety with subsequent attachment to iridium metal centres. We describe the incorporation of these complexes into novel multimodal sensing devices. The work will also highlight structural, chemical and photophysical properties of the solution and surface bound iridium(III) complexes and their ability to detect PFOA.

3.2 Results and Discussion

3.2.1 Synthesis and characterisation of ligands and Ir(III) complexes

Two ligands based upon 2-phenylpyridine were synthesised in this work; the synthesis of both 2-(2-hexylphenyl)pyridine and 2-(2-dodecylphenyl)pyridine was carried out based upon previously reported methods.[144] The synthesis of these ligands subsequently allows for two iridium(III) dimers to be synthesised which in turn allows four complexes where either **bpySS** (previously reported by our group)[96] or 2,2'-bipyridine is used as the ancillary ligand. We name these complexes **IrC6bpySS**, **IrC12bpySS**, **IrC6bpy**, **IrC12bpy**. This section will summarise the synthesis and characterisation of both the **bpySS** ligand and the metal complexes. All steps in the synthesis of the **bpySS** ligand have been detailed in the experimental section. Figure 3.28 shows the full route to **bpySS**.

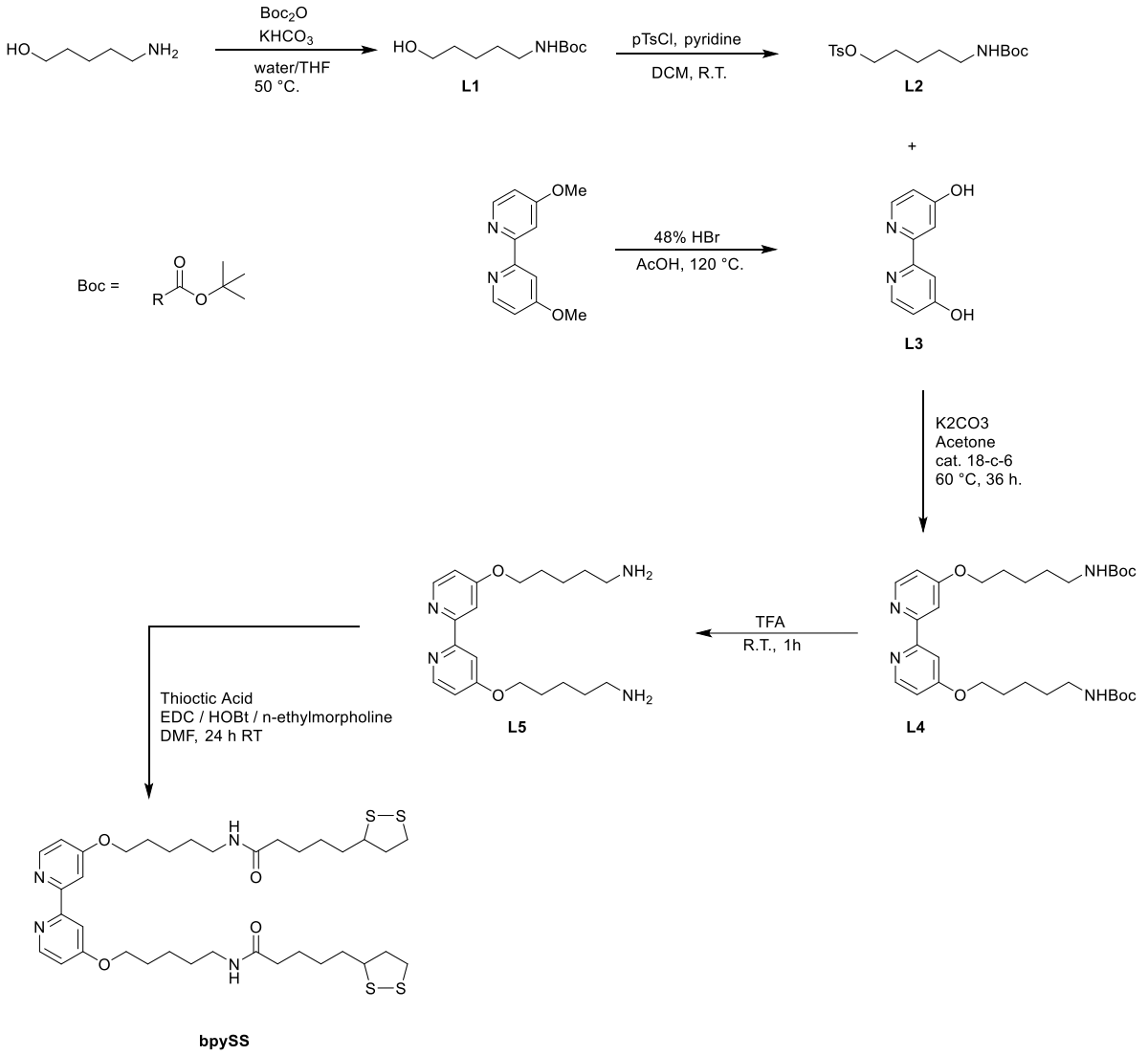


Figure 3.28: Multi step synthetic route from the starting material 5-amino-1-pentanol through to **bpySS**

In short, the synthesis of the ligand **bpySS** is achieved through protection of the amino group via a standard BOC protection, followed by increasing the lability of the alcohol by addition of the tosyl group. A Williamson ether coupling between the diol and the tosyl group is carried out, before deprotection of the BOC group is performed in TFA. The final step is an amide coupling with α-lipoic acid to yield the **bpySS** ligand. Characterisation of the product at each step was carried out by ^{1}H NMR and mass spectrometry. The data match that previously reported for all compounds,[96] and assignments of protons corroborated by 2D COSY spectra are given in the experimental section. NMR spectra for all products are given in the supplementary information.

The metal complexes were synthesised through a multi-step reaction. In which firstly the hydrophobic analogues of 2-phenylpyridine were synthesised through an alkylation reaction that relies on a ruthenium catalyst. This is followed by synthesis of two dimeric iridium complexes containing each cyclometalating ligand. The two dimers are then subsequently reacted with their ancillary ligand, either **bpySS** or 2,2'-bipyridine to form the four final iridium complexes. Figure 3.29 shows a general synthetic scheme for all Ir(III) complexes in this work with Figure 3.30 summarising the names and full structures of the complexes in this work.

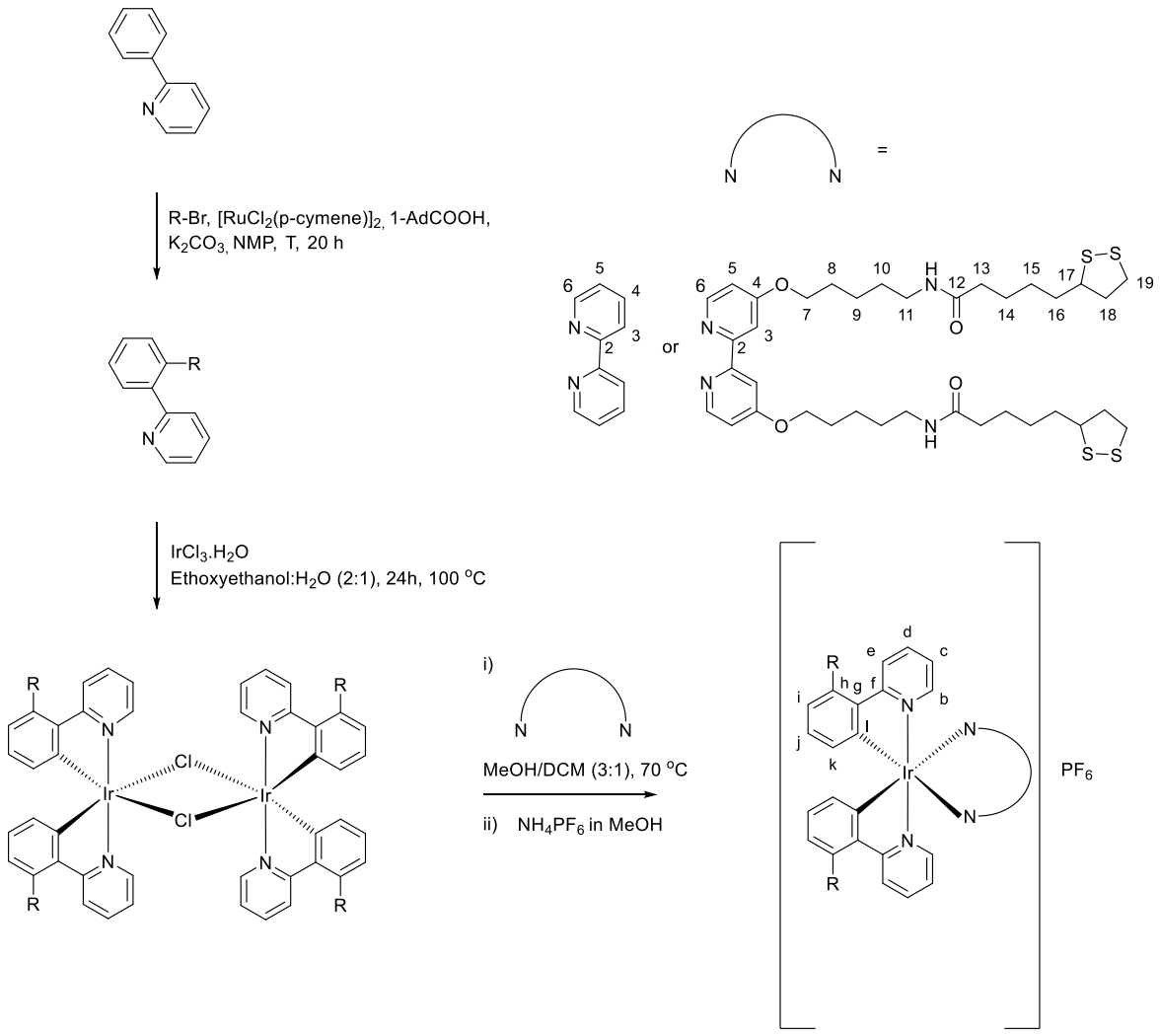


Figure 3.29: General synthetic scheme for all Ir(III) complexes in this work, the final structure is the general structure of the Ir(III) complexes synthesised in this work.

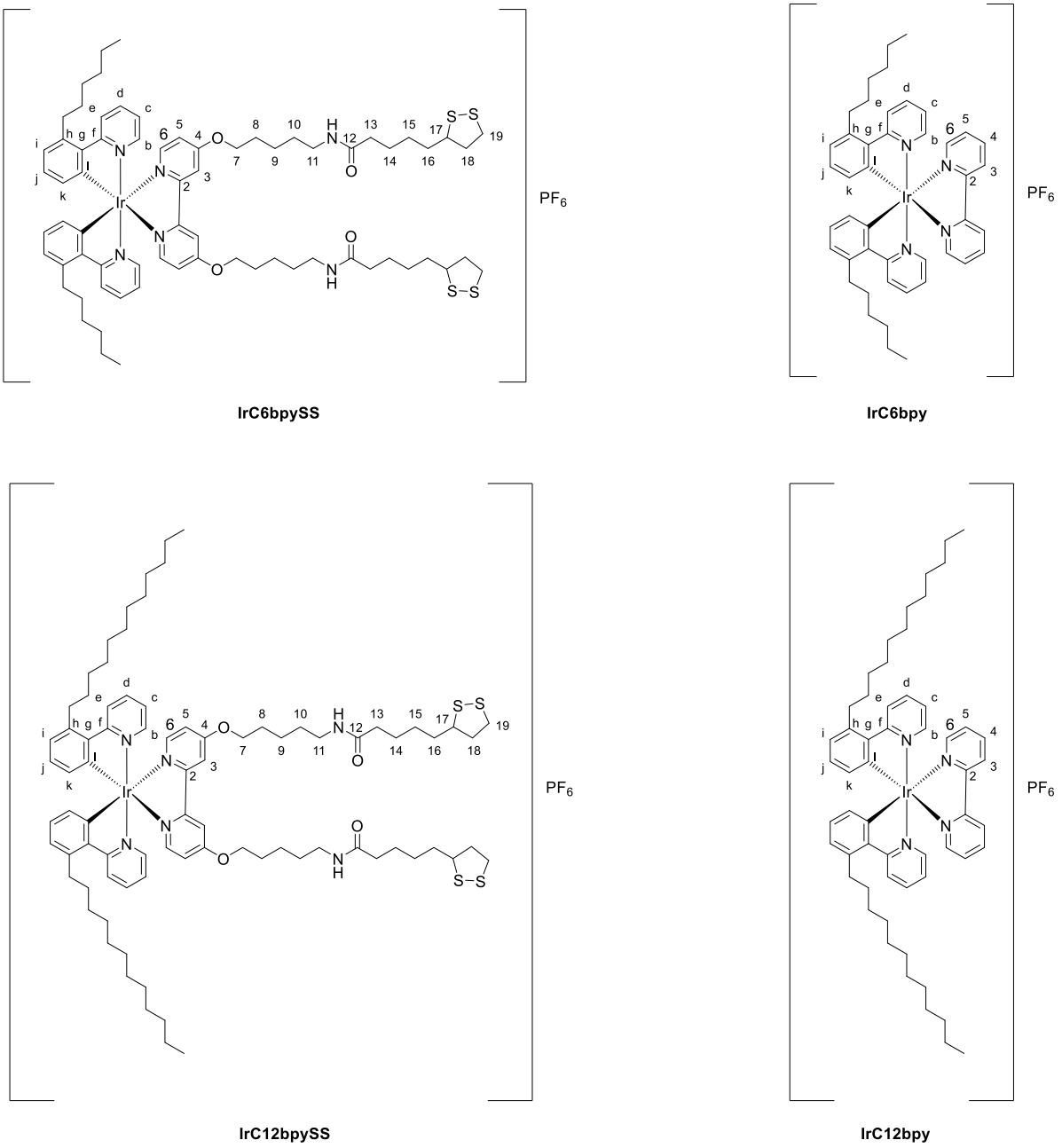
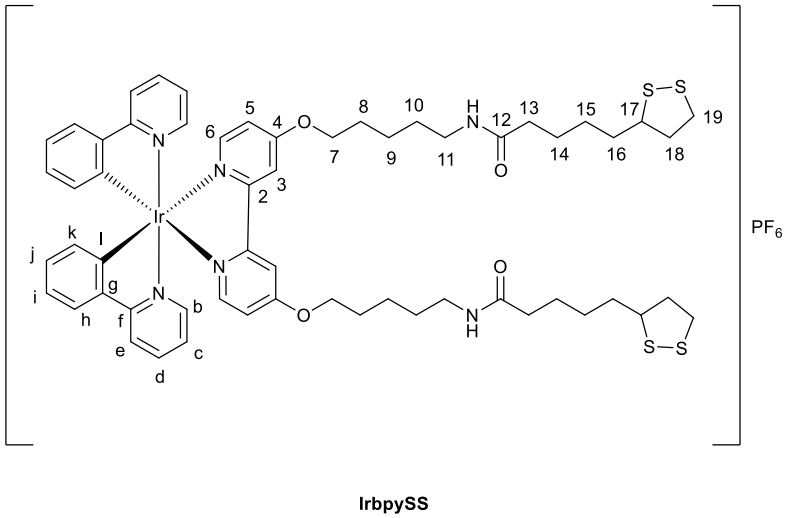


Figure 3.30: Structures of the novel Ir(III) complexes synthesised in this work (**IrC6bpySS**, **IrC12bpySS**, **IrC6bpy**, **IrC12bpy**).

The metal complexes were characterised by ^{1}H and ^{13}C NMR spectroscopy. Assignments were made by obtaining 2D COSY, HSQC, and HMBC spectra. Spectra taken for the metal complexes can be found in the SI. High-resolution mass spectrometry was also performed and good agreement between theoretical and observed masses is found. Elemental analysis is performed on both the **IrC6bpySS** and **IrC12bpySS** and the observed data agrees with that calculated for the metal complexes.

As they are run in the same solvent, NMR spectra obtained for the novel metal complexes may be directly compared against that taken for the previously described **IrbpySS**,[96] the structure of which is given below in Figure 3.31.



IrbpySS

Figure 3.31: Previously reported structure of **IrbpySS** with proton labelling shown, for comparison with metal complexes synthesised in this work.

Shifts and couplings observed for the aromatic and aliphatic protons in the ^{1}H spectra of the metal complexes are observed in broad agreement with previously reported data for **IrbpySS**,[96] and **IrC6bpySS**, however previous reports of **IrC6bpySS** complex did not include assignments of the signals observed in the ^{1}H spectrum,[143] the characterisation was also performed in a solvent not matching that reported for **IrbpySS** which makes a direct comparison difficult.

Differences from **IrbpySS** should be observed at protons i, j and possibly for k (Figure 3.31). In the **IrbpySS** both protons i and j are observed as triplet of doublets, as one might expect when proton i shows coupling to h, j and k. Proton j will show coupling to k, i and h. Based upon the new substitution pattern present in all metal complexes in this work, one would expect the observed coupling to be modified. Indeed, it can be observed from all NMR spectra of the metal complexes that the signal from proton i in every case becomes a double of doublets, and for j becomes a triplet as one would expect theoretically upon the absence of proton h. This

therefore confirms the substitution at the correct position, with the mass spectra of each complex confirming overall agreement with proposed formulae.

An extremely interesting observation in the NMR spectra is the shift observed of the H-3 proton from the observed shift in **IrbpySS** (8.29 ppm). Shifts of the H-3 proton in the **IrC6bpySS** and **IrC6bpy** complexes match well (8.75 and 8.84 ppm respectively). The shifts of the **IrC12bpySS** and **IrC12bpy** complexes match well (9.09 and 9.00 ppm respectively). It is interesting that sequential increases are observed in the downfield shift of this proton with carbon chain length. This result may warrant further investigation, as the opposite trend would be expected based solely on the inductive effects of the aliphatic chain.

3.2.2 Photophysical Properties of metal complexes in solution

The UV-Visible and steady state emission spectra of complexes all complexes were investigated in MeCN solution. Table 3.3 below summarises the photophysical properties observed in solution. Reported values for the IrbpySS complex are shown in the table for comparison.

UV-Visible absorption spectra reveal that all novel synthesised complexes display archetypal electronic transition features of Ir(III) cyclometallated complexes with good match between the reported **IrbpySS**, previously reported values for **IrC6bpySS**,[143] and the newly synthesised complexes (Figure 3.32 and Table 3.3).[145-147] For the Ir(III) complexes in CH_3CN there is a transition observed at 258 nm for **IrC6bpySS**, 254 nm for **IrC12bpySS** and at 260 nm for **IrC6bpy** and **IrC12bpy**, assigned to a ligand centred transitions of the aromatic phenylpyridine and bipyridine type ligands (^{1}LC, $\pi-\pi^*$), which is spin-allowed and gives rise to highly absorptive bands with $\varepsilon > 10000\ M^{-1}\ cm^{-1}$.[148-155]

Table 3.3: Summary of experimentally obtained photophysical data for Ir(III) complexes in MeCN. at 298 K λ_{exc} = 350 nm a) argon degassed 298 K λ_{exc} = 375 nm b) argon degassed 298 K λ_{exc} = 350 nm. Errors are estimated for emission wavelengths at ± 1 nm, emission lifetimes ± 10%, emission quantum yields ± 20%. ND = not determined

	Absorption	**Emission**	**τ/ns**		**φ/%**	
Complex	**λ_{max}/nm (ε / 10^4 M^{-1} cm^{-1})**	**λ_{em}/nm**	**Aerated**	**Deaerated[a]**	**Aerated**	**Dearated[b]**
IrbpySS	255 (5.0), 298sh (1.8), 337 (0.8)	580	25 (68%), 80 (32%)	35 (34%), 246 (66%)	0.5	3
IrC6bpySS	223 (4.2), 258sh (3.7), 298sh (1.7), 347 (0.7)	606	5 (7%), 58 (74%), 119 (19%)	6 (9%), 86 (43%), 214 (48%)	0.7	3
IrC12bpySS	224sh (5.8), 254sh (5.2), 298sh (2.4), 350 (0.9)	606	4 (1%), 68 (75%), 118 (24%)	6 (2%), 100 (28%), 256 (70%)	1	5
IrC6bpy	260 (4.0), 311 (2.2), 347 (0.9)	624	49 (100 %)	38 (1 %), 153 (99 %)	ND	ND
IrC12bpy	260 (3.5), 311 (1.9), 348 (0.7)	624	50 (100 %)	49 (3 %), 171 (97 %)	ND	ND

The absorption spectra also display less intense shoulders in the region 320 – 415 nm. These transitions are assigned as arising from ^{1}MLCT transitions (dπ(Ir)→π*(2,2'-bipyridine and phenylpyridine type ligand)) and are characteristically weaker than the ^{1}LC bands, with molar absorptivity in the range $3000 < \varepsilon < 10000$.[148-155]

Upon excitation all Ir(III) complexes in this study exhibit sub-microsecond luminescence with orange to red colour, exact wavelengths are recorded in Table 3.3 whilst emission spectra are displayed graphically below (Figure 3.32). **IrbpySS** displays emission at a reported maxima of 580 nm. The emission maxima for **IrC6bpySS** and **IrC12bpySS** are both found at 606 nm in CH_3CN. **IrC6bpy** and **IrC12bpy** display maxima at 624 nm in CH_3CN. It is unsurprising that the emission maxima is matching for complexes in each case, as there is very little difference in the inductive effect observed between hexyl and dodecyl substituents.[156]

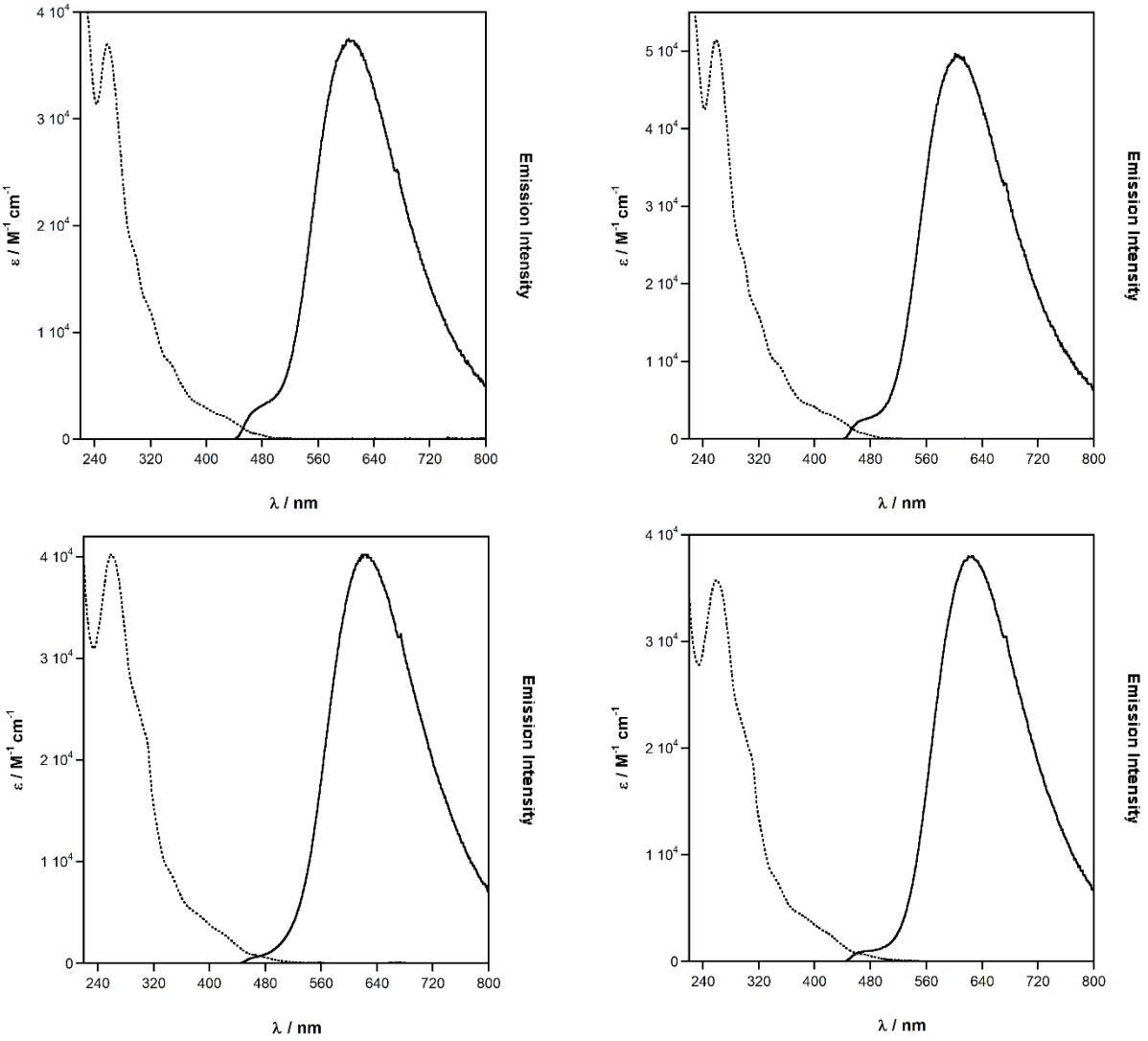


Figure 3.32: Electronic absorption spectra (dotted line) and emission spectra (solid line) of a) IrC6bpySS in CH_3CN, b) IrC12bpySS in CH_3CN, c) IrC6bpy in CH_3CN and d) IrC12bpy in CH_3CN. λ_{exc} = 350 nm for all spectra

The shifts in the emission maxima of the complexes from the **IrbpySS** can equally be justified using inductive or withdrawing effects of the substituents. A bathochromic shift of 26 nm is observed after addition of the alkyl substituents into **IrbpySS** (forming **IrC6bpySS** and **IrC12bpySS**) which can be attributed to the inductive effect of the alkyl substituents on the phenyl ring of the phenylpyridine ligands.[147] A further bathochromic shift of 18 nm is observed for the **IrC6bpy** and **IrC12bpy** complexes upon removal of the electron donating ether linkage found in the **bpySS** ligand.[147]

Luminescence lifetime measurements reveal a multi-component luminescence lifetime, likely due to some level of aggregation of the highly hydrophobic complex, leading to complex emission kinetics. The longest component of 0.21 μs for the **IrC6bpySS** and 0.26 μs for **IrC12bpySS** measured in degassed CH_3CN, compare well with the **IrbpySS** complex that has a longest component of 0.25 μs. The **Ir6bpy** and **IrC12bpy** have multicomponent lifetimes for the same reason, but the longest component is shorter, at 0.15 and 0.17 μs for **Ir6bpy** and **IrC12bpy** respectively. This compares favourably with reported values of 0.14 μs for the $Ir(ppy)_2bpy$ complex which is analogous but bears no alkyl chain.[86]

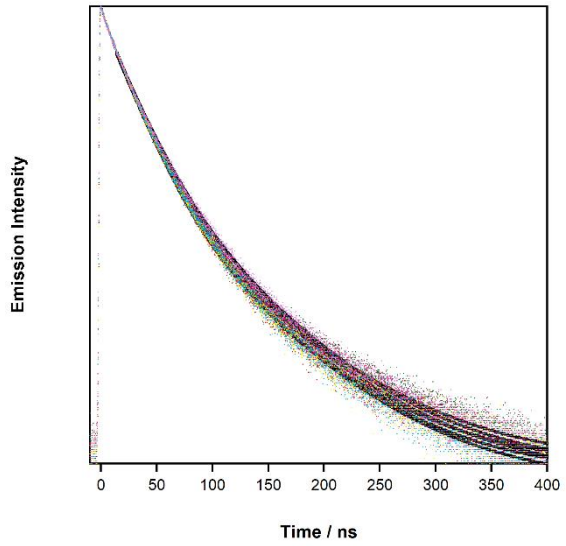
Quantum yields of the **IrC6bpySS** and **IrC12bpySS** in aerated CH_3CN are 0.7 and 1 % respectively, which are comparable to the quantum yield of **IrbpySS**. The quantum yields of the bpy containing complexes were not taken.

The **IrC6bpy** and **IrC12bpy** complexes were also studied at 77 K in glass of EtOH:MeOH (4:1). The emission spectra are given below in the supporting info. Blue shifts are observed in agreement with what would be expected for rigidochromism, however no structured bands are revealed. Resolution of differing emissive states was not expected, a lack of structure implying that the emitting state is largely MLCT in character with very little LC contribution, as has been described for the $Ir(ppy)_2bpy$ analogue.[151]

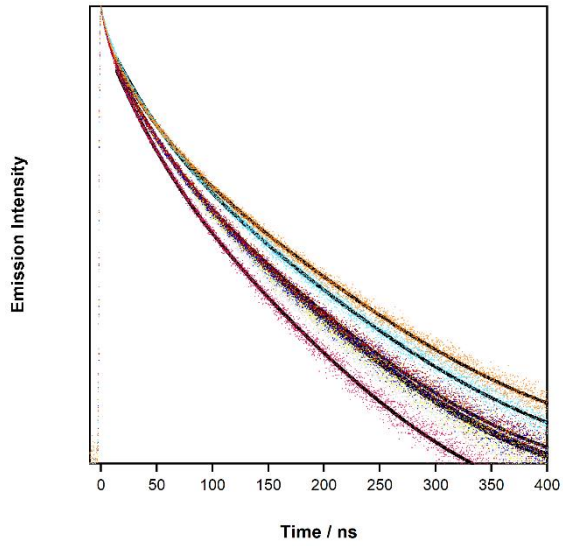
3.2.3 Sensing of fluorosurfactants in solution

To probe the affinity of all hydrophobic complexes to small analytes, solution phase luminescence studies were carried out to investigate the change in the luminescence properties with increasing analyte concentration. The analyte chosen was perfluorooctanoic acid (PFOA). The general structure and motivation for sensing of this analyte is covered in the introduction section.

Complexes **IrC6bpySS** and **IrC12bpySS** were dissolved in methanolic solutions (1:1, MeOH:H_2O) before adding aliquots of PFOA in the same solvent system. The luminescent lifetimes are fit biexponentially, and tabulated lifetime values at differing PFOA concentrations are shown in Figure 3.33 below. From the fits it is concluded that the longer alkyl chain in the **IrC12bpySS** allows for more efficient reporting of the interaction with fluorosurfactant, Luminescent lifetime increases from 74 to 93 ns upon each sequential addition of PFOA to a concentration of 0.24 μM, at the final concentration there is an increase of the luminescent lifetime above that of the ±10 % error. The **IrC6bpySS** complex does not follow the same trend and even at higher concentrations of above 20 μM no response is seen in the lifetime.



[PFOA] / mol L^{-1}	τ / ns
0	25 (62 %), 76 (38 %)
$2.39x10^{-8}$	25 (60 %), 81 (40 %)
$1.19x10^{-8}$	25 (60 %), 79 (40 %)
$1.94x10^{-5}$	25 (62 %), 76 (38 %)
$2.41x10^{-5}$	25 (62 %), 76 (38 %)
$1.06x10^{-4}$	25 (56 %), 76 (44 %)



[PFOA] / mol L^{-1}	τ / ns
0	25 (21 %), 74 (79 %)
$1.70x10^{-10}$	26 (26 %), 79 (74 %)
$2.39x10^{-8}$	26 (26 %), 83 (74 %)
$4.76x10^{-8}$	26 (26 %), 85 (74 %)
$1.19x10^{-7}$	26 (25 %), 86 (75 %)
$2.37x10^{-7}$	28 (24 %), 93 (76 %)

Figure 3.33: (left) luminescence lifetime decay plots for **IrC6bpySS** (5 μM in 1:1 MeOH:H_2O) with varying concentrations of PFOA, the table below displays the concentrations used and fit values with percentage contribution of each component. (right) luminescence lifetime decay plots for **IrC12bpySS** (5 μM in 1:1 MeOH:H_2O) at varying concentrations of PFOA, the table below displays concentrations used of PFOA and fit values with contribution of each component. The Y-axis is displayed logarithmically for clarity.

The response of the luminescence lifetime decay becomes significant (>10 % change) at 0.24 μM, a high concentration of PFOA compared to that regularly found in the environment (see

Table 3.1 and 3.2), and may be due to a subtle inhibition of triplet quenching through restricted oxygen diffusion in a surfactant containing system. As there is however a disparity between the two complexes we argue it is reasonable to assume that the affinity is due to the hydrophobicity as well as the unhindered access to the alkyl chains in solution. Responses were observed in the luminescence lifetime, with sensitivity similar to other reported fluorescence based assays, demonstrating the utility of this complex type in luminescence sensing applications.

Measurement of the wavelength shift is not expected to be as sensitive a measurement method, however from the polarity change upon addition of large excesses of surfactant, a hypsochromic shift in both complexes is observed (Figure 3.34). The blue shift if far less pronounced in the **IrC12bpySS** complex, which we reason to be due to the complex already having formed micelles in the solvent system, further investigation of the CMC for each complex could be carried out to test this reasoning.

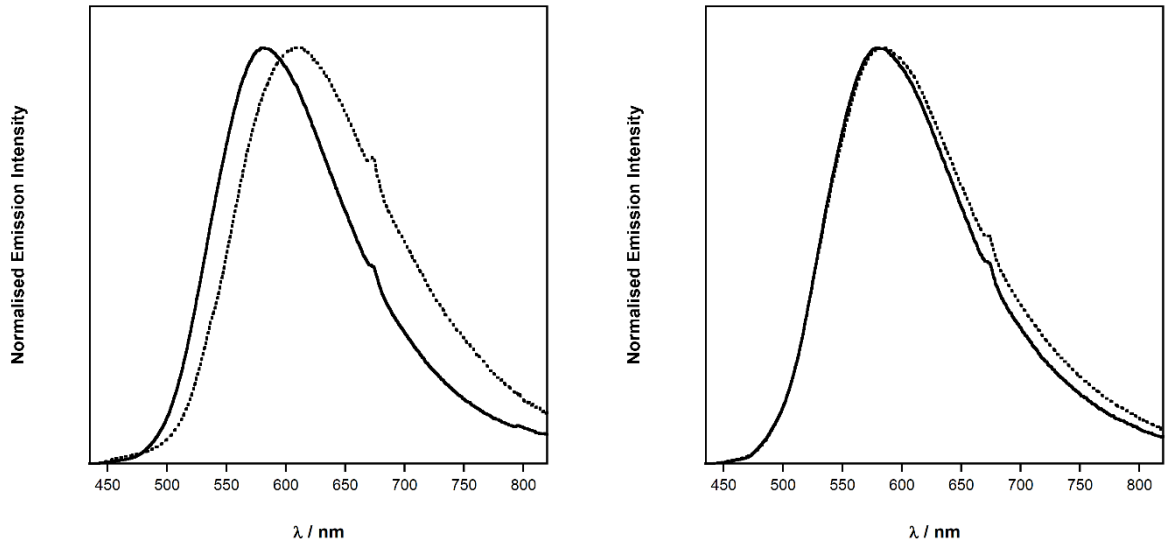


Figure 3.34: Emission spectra (5 μM in 1:1 MeOH:H_2O) of (left) **IrC6bpySS** and (right) **IrC12bpySS**, before (dashed line) and after (solid line) addition of 4 mM of PFOA.

The phenylpyridine ligand and the **bpySS** ligand of both **IrC6bpySS** and **IrC12bpySS** contain non-aromatic chains, meaning there was some room to question whether the dodecyl chain of **IrC12bpySS** is entirely responsible for the increased PFOA affinity observed over

IrC6bpySS. Therefore we investigated the effect of surfactant addition on the luminescence lifetime decay of **IrC6bpy** and **IrC12bpy** complexes which contain no **bpySS** ligand by performing an identical titration experiment. A similar trend as above was observed in that the increase of the lifetime in the dodecyl containing complex (**IrC12bpy**) was significant, whereas no significant change was observed in the hexyl containing derivative (**IrC6bpy**) (See Supporting Information).

To assess whether non-covalent binding between the PFOA and the metal complexes had occurred, ^{19}F experiments were attempted in MeOH-d_4 and D_2O, in which PFOA was mixed with **IrC6bpy** and **IrC12bpy**. The spectra obtained can be found in the NMR section of the supporting information. All spectra are referenced to the shift of the -CF_3 fluorine signal of the bare fluorosurfactant in the solvent system. Shifts are observed for every peak, which is indicative of an inclusion complex formed between the iridium(III) compounds and the PFOA.[157, 158]

3.2.4 Immobilisation of IrC6bpySS and IrC12bpySS on planar and patterned surfaces

To investigate the immobilisation and subsequent properties of monolayers formed by the thiolated Ir(III) complexes on gold surfaces; atomic force microscopy (AFM), x-ray photoelectron spectroscopy (XPS), and contact angle measurements were employed.

Briefly, surfaces for AFM, contact angle and XPS measurements were immersed for 16 h after cleaning, before being washed and dried under nitrogen for immediate use (per supporting information).

XPS provides direct chemical information about the sample through emission of an electron after irradiation with an X-ray photon. The emitted electrons have discrete kinetic energies that

differ based upon element and environment of such an element. These are known as electron lines and can provide extremely useful characterisation data especially in the solid state.[159] Penetration of the X-ray photons and the ability of the electrons to "escape" the surface is limited and the technique is therefore best suited to analysing thin monolayers.[160]

In this study, XPS confirms the presence of the metal complexes on the surface and the XPS spectra of the Ir 4f and S 2p regions are shown in Figure 3.35. The Ir 4f orbitals show both high and low spin-orbit states in complex **IrC6bpySS** and **IrC12bpySS** with the peak for Ir $4f_{7/2}$ appearing at 62.2 eV and that of Ir $4f_{5/2}$ at 65.2 eV. In the case of complex **IrC6bpySS**, the sulfur $2p_{3/2}$ peaks are observed at 161.7 and 163.8 eV assigned to the gold bound to thiol (55%) and disulphide (45%) species respectively.[161, 162] For complex **IrC12bpySS**, peaks are observed ad 161.7 and 163.7 again assigned to gold bound thiol (26%) and disulphide (45%) species; the remaining sulphur exists as oxidised sulfonate (29%). The oxidised sulfonate species may be converted to bound thiols by increasing the immersion time.[163] Although the presence of the disulfide species would seem to suggest unbound Ir(III) complexes, it is difficult to fully measure as the Ir(III) complexes contain two disulfide bridges, the remaining disulphide signal may arise from the binding modality not being equal for every complex. Some Ir(III) complexes may bind only through one thiol capped leg, whereas others may bind having broken both disulfide bridges. It is equally possible some complexes may be unbound, or bound through interactions between alkyl chains. The presence of unbound species is unlikely as the complexes are washed to remove non-specificly bound Ir(III) complex (see experimental).

Peaks in agreement with the proposed structures of **IrC6bpySS** and **IrC12bpySS** (e.g. the characteristic signal of the carbonyl group) are observed in the C 1s, N 1s, O 1s regions for both complexes providing indirect structural information (supporting information).

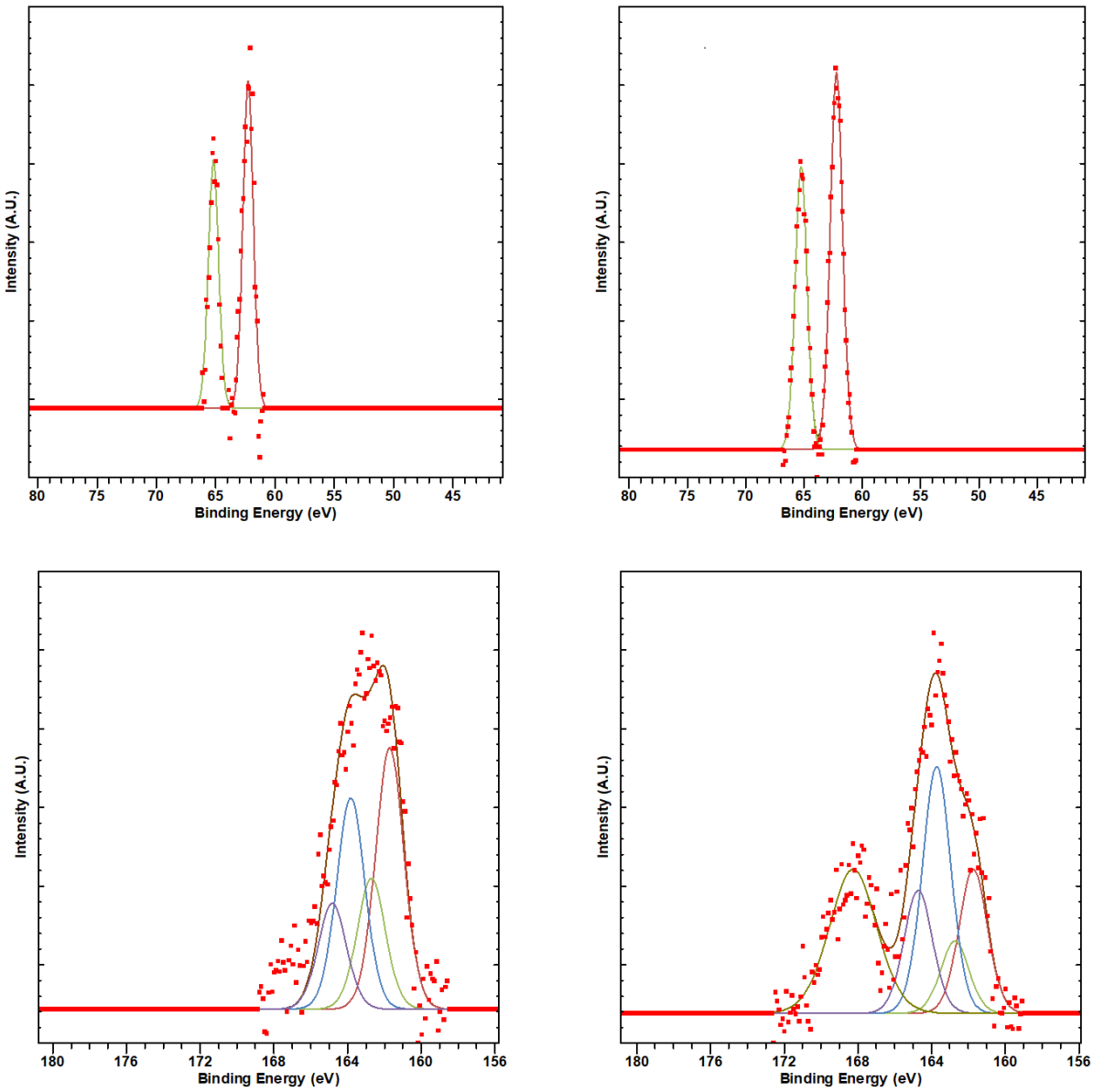


Figure 3.35: (a and b) XPS spectra taken of the Ir 4f region with dotted lines denoting the experimental data, and the solid lines the component fitting; brown peaks denote Ir $4f_{7/2}$ and green denote Ir $4f_{5/2}$ (c and d) XPS spectra with dotted experimental data and solid fitted data of the S 2p region where brown and blue lines represent the bound thiol regions and the green and purple lines represent disulfide.

AFM images were taken of gold surfaces coated with **IrbpySS** and **IrC6bpySS** to provide information on the spatial arrangement of the Ir(III) complexes on the gold surface (Figure 3.36). The images reveal that the complexes form islands on the surface, as observed for similar metal complexes. RMS roughness (R_q) values were calculated at 1.18 nm, whilst an island height of 1.78 nm was measured. This data fits well with that previously reported by

ellipsometry and AFM.[96, 97] The same parameters were measured for **IrC6bpySS** revealing an R_q of 2.42 nm and an island height of 3.90 nm. One would not expect such a large increase in island height from the alkyl chains alone, this may suggest formation of a self-assembled multilayer structure through aggregation of the alkyl regions, consistent with the disulphide species observed in the XPS. Induced by weak, non-covalent interactions of the alkyl regions, this effect is well detailed in the preparation of alkanethiol surfaces.[164]

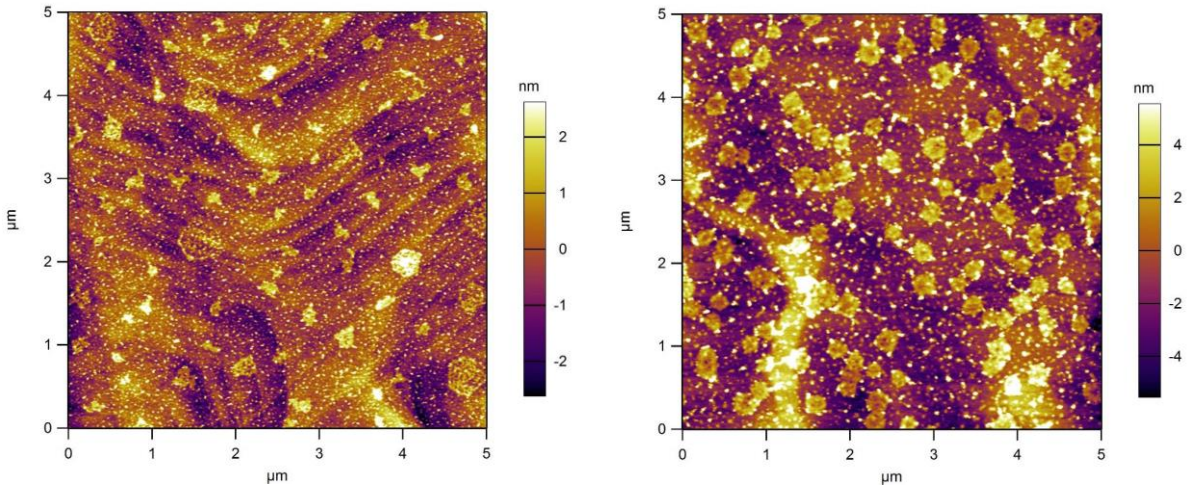


Figure 3.36: AFM images with scale bar of (left) Au on mica after immersion in a solution of **IrbpySS**, (right) Au on mica after immersion in a solution of **IrC6bpySS**

After successful surface coating was confirmed by both XPS and AFM, the hydrophobic properties of the transition metal-gold surfaces were investigated. Contact angle measurements were taken, via a static drop method and representative images of this testing are shown in Figure 3.37. Clean gold is used as a control and the contact angle agrees with previously reported values.[165] Larger angles between the water droplet edge and surface indicate increased hydrophobicity of the coating, the images then confirm that the surfaces become increasingly hydrophobic with longer alkyl chains. Average contact angle increases in the order: clean Au (59.6º) < **IrbpySS** coated Au (66.5º) < **IrC6bpySS** coated Au (73.8º) < **IrC12bpySS** coated Au (88.7º).

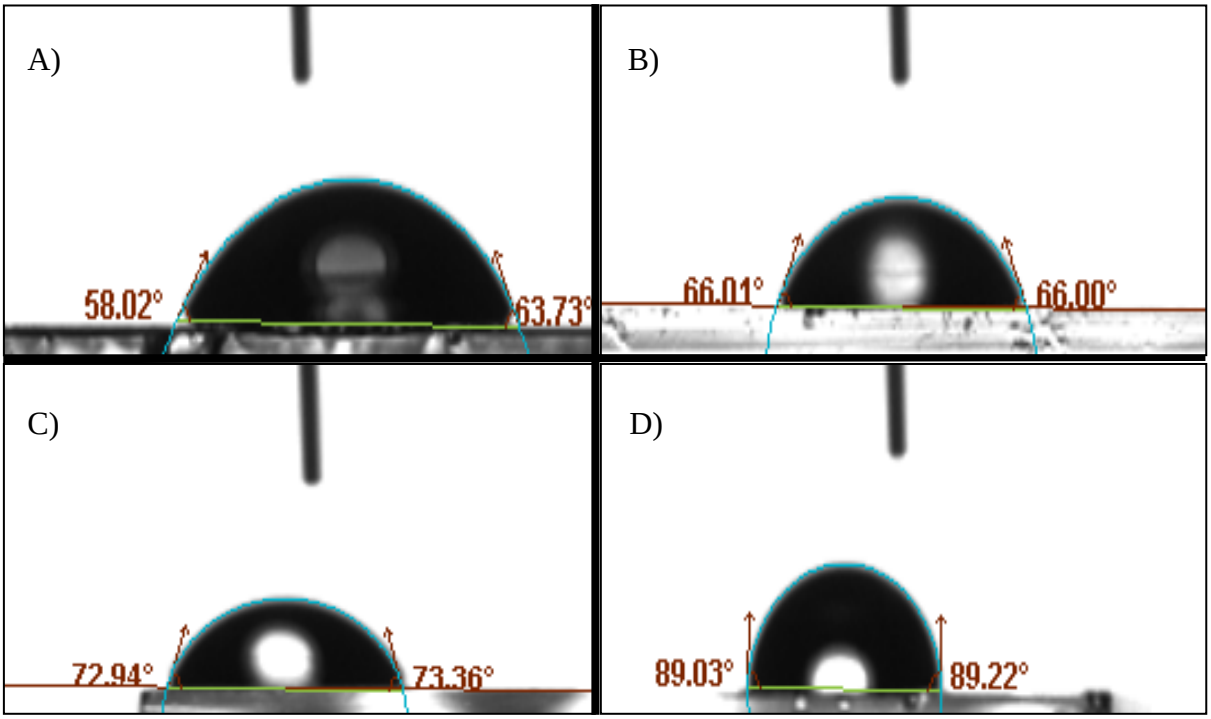


Figure 3.37: Representative images of coated surfaces with water droplet contact angle displayed. Images taken are of A) bare gold slide; B) gold slide coated with **IrbpySS**; C) gold slide coated with **IrC6bpySS**; D) gold slide coated with **IrC12bpySS**

All measurements in conjunction therefore allow us to conclude that we have in fact coated gold surfaces with iridium complexes, at least some of the complexes are covalently bound, showing architectures typical of transition metal-gold conjugates on the surface, and the surfaces are hydrophobic.

3.2.5 Photoluminescence properties of Ir(III) complexes immobilised on Au surfaces

Emission spectra for the complexes bound to gold reveal that the surfaces display large blue shifts of 42 and 22 nm (λ_{em} = 564 and 584 nm), for **IrC6bpySS** and **IrC12bpySS** respectively against the acetonitrile solutions of the complexes (Figures 3.38).

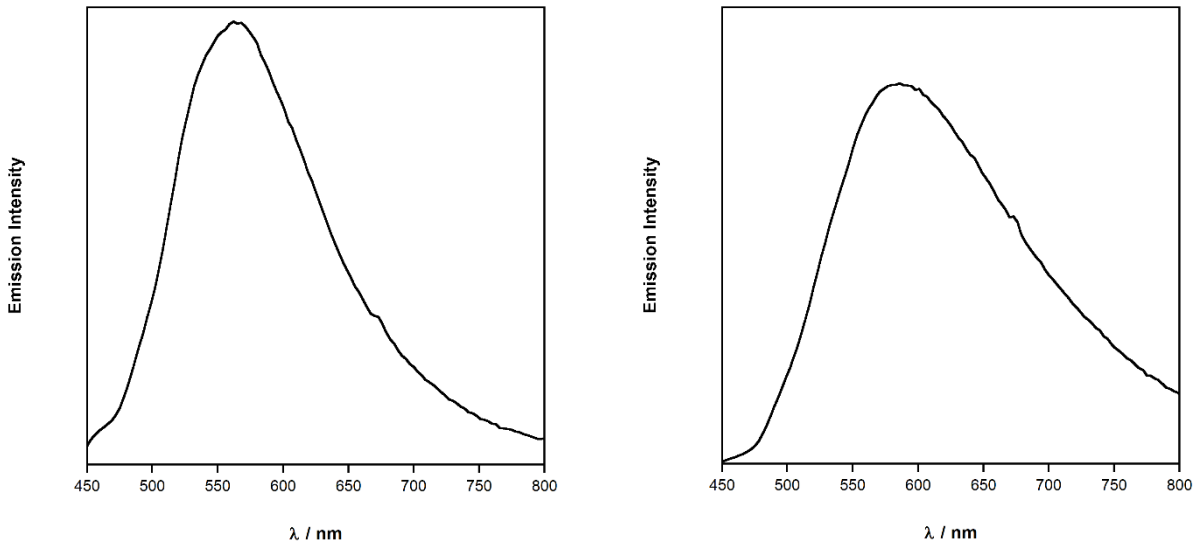


Figure 3.38: Emission spectra (λ_{exc} = 350 nm) of gold surfaces coated with (left) **IrC6bpySS** and (right) **IrC12bpySS**

Luminescent lifetime measurements of the complexes alone on the surfaces (Table 3.4, **IrC6bpySS.Au** and **IrC12bpySS.Au**) reveal similarly complicated lifetimes as observed in aerated acentonitrile solution, again due to the aggregation and scattering from the gold surface. The longest component still matches well **IrC6bpySS** = 120 ns, **IrC12bpySS** = 110 ns.

Knowing that these complexes are luminescence active at the surface we used confocal microscopy to further confirm the binding specificity of the metal complexes to gold. Confocal microscopy images (Figure 3.39 and 3.40) show that both complexes are immobilised specifically on gold, as luminescence of the iridium complex is observed consistent with the Au location observed in the bright field images. We suggest that it is possible to synthesise a highly patterned device for sensing, wherein lithography is used to create the pattern.

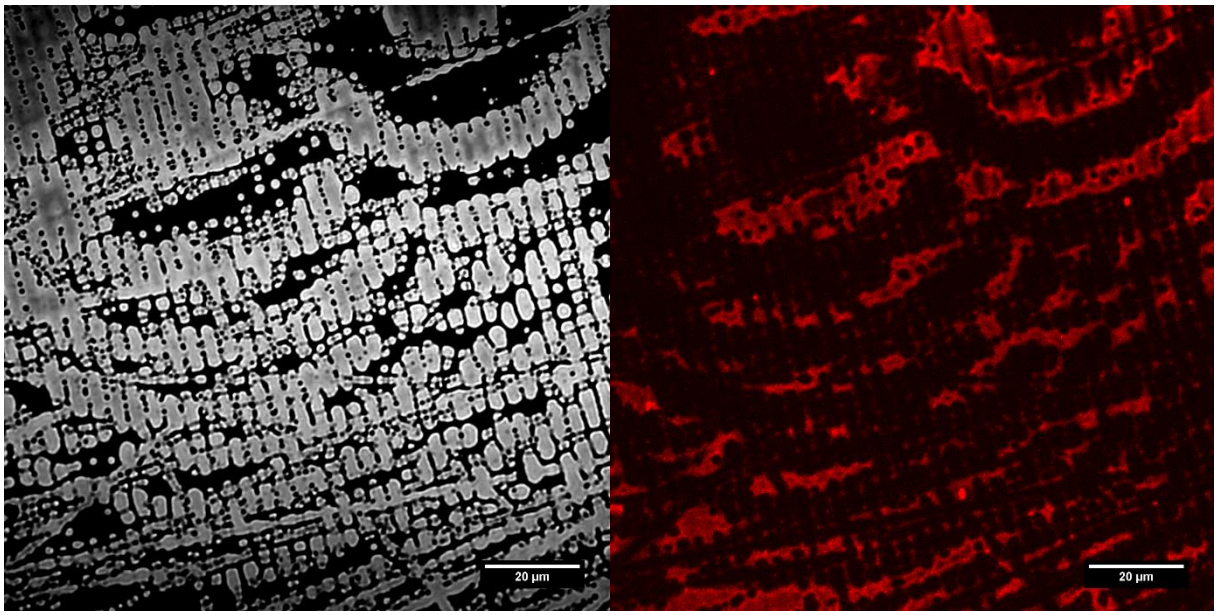


Figure 3.39: Micropatterned Au surface coated with **IrC12bpySS**. Bright-field (left) and iridium(III) fluorescence (right, red false colour applied).

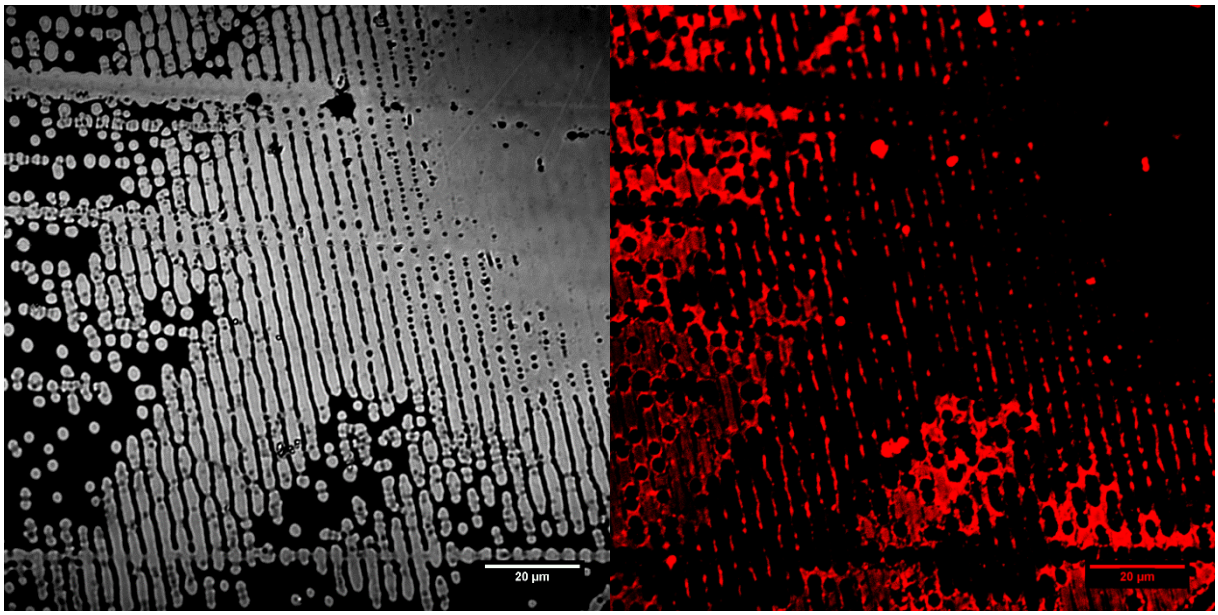


Figure 3.40: Micropatterned Au surface coated with **IrC6bpySS**. Bright-field (left) and iridium(III) fluorescence (right, red false colour applied).

3.2.6 Sensing of PFOA using Ir(III) complex coated gold surfaces

With binding in solution demonstrated by all complexes, and the fabrication and photophysics of Ir(III) coated gold substrates confirmed, **IrC6bpySS** and **IrC12bpySS** immobilised on the gold surfaces were tested as potential system for surfactant recognition, the working principle of this system is demonstrated graphically in Figure 3.41.

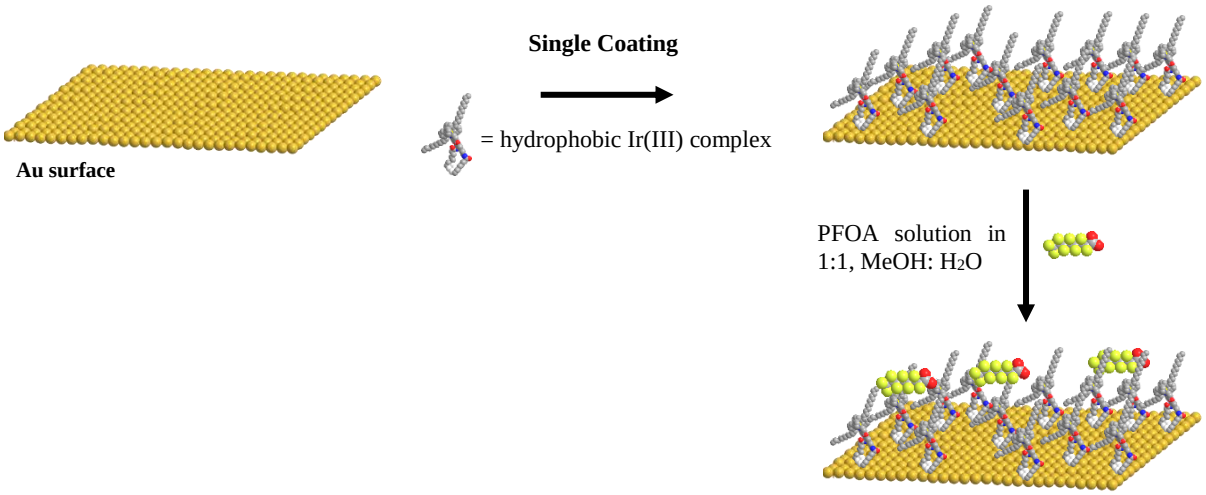


Figure 3.41: Working principle for the encapsulation of the PFOA molecule on the Ir(III) containing devices, which are formed by immobilisation of **IrC6bpySS** or **IrC12bpySS** on a gold substrate

Gold surfaces were prepared as for XPS studies and the surfaces used without any further modification, the subsequent devices are denoted as **IrC6bpySS.Au** and **IrC12bpySS.Au**. These surfaces were immersed in 1:1, MeOH:H_2O solutions containing PFOA. The devices only show reasonable affinity to PFOA at high concentrations (6 mM) when immersed for 1 h, with enhancements of 29 and 28 % in luminescent lifetime for **IrC6bpySS.Au** and **IrC12bpySS.Au** respectively (Table 3.4). In addition to a lifetime augmentation an emission maxima shift is observed for both **IrC6bpySS.Au** and **IrC12bpySS.Au** with a respective emission maximum observed at 558 and 563 nm as observed in Figure 3.42 (compared to 564 and 584 nm respectively, Figure 3.38). The signals are broad and suggest the presence of more than 1 emitting species. The change in local environment upon surfactant immobilisation leads

to the blue shift and increased lifetime, as is seen in solution, which we have mentioned could also possibly be oxygen exclusion.

Table 3.4: Luminescent lifetime decay values measured for the Ir(III) complex based devices, with solvent of immersion and goodness of fit values

Sample	τ / ns	χ^2
IrC6bpySS.Au	19(16 %), 119 (84%)	1.03
IrC6bpySS.Au with 6mM PFOA in MeOH/H_2O	13 (7 %), 154 (93 %)	1.04
IrC12bpySS.Au	27 (23 %), 112 (77 %)	1.02
IrC12bpySS.Au with 6 mM PFOA in MeOH/H_2O	20 (12 %), 143 (88%)	1.08
IrC12bpySS.Au with 6 mM PFOA in DCM	42 (27 %), 273 (73 %)	1.12

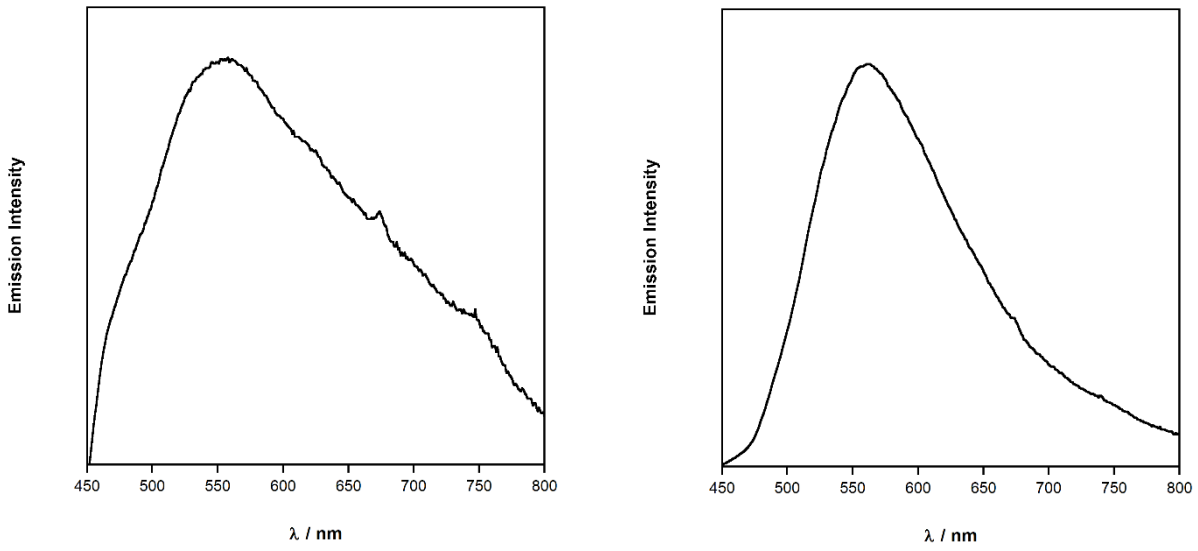


Figure 3.42: Emission spectra (λ_{exc} = 350 nm) of gold surfaces coated with (left) **IrC6bpySS** and (right) **IrC12bpySS** after immersion in methanolic solutions of PFOA (6 mM in 1:1, MeOH:H_2O) for 1 hour

Whilst a MeOH/H_2O solution is more representative of the conditions in which the fluorosurfactant would present, enhancement of the luminescent lifetime should be larger in less polar hydrophobic solutions. The enhancement of lifetime is indeed greater with a 145 % increase in the luminescent lifetime (Table 3.4).

3.2.7 Sensing of PFOA using Ir(III) complex coated gold surfaces co-coated with Zonyl FSA

Previously our group has applied a fluorosurfactant co-coating technique to modify gold surfaces with transition metal reporters. Zonyl FSA was one such co-coating with an iridium(III) complex for use in biomolecular sensing.[97] The C-F---F-C fluorine interaction is known within the literature and shown to direct self-assembly in some structures, with Baker et al. reporting selective interactions with stabilising energy up to 30 kcal / mol.[166] To take advantage of these interactions in the immobilisation and subsequent sensing of PFOA, freshly prepared **IrC6bpySS.Au** and **IrC12bpySS.Au** devices were immersed in Zonyl FSA solutions according to the procedure described (supporting information) to form sensors **IrC6bpySS.Au.Z** and **IrC12bpySS.Au.Z**. Co-coated surfaces were immersed in water for the detection of PFOA as the affinity was predicted to be high, and water more representative of environmental samples. The working principle for PFOA detection, and structure of Zonyl FSA is detailed below in Figure 3.43.

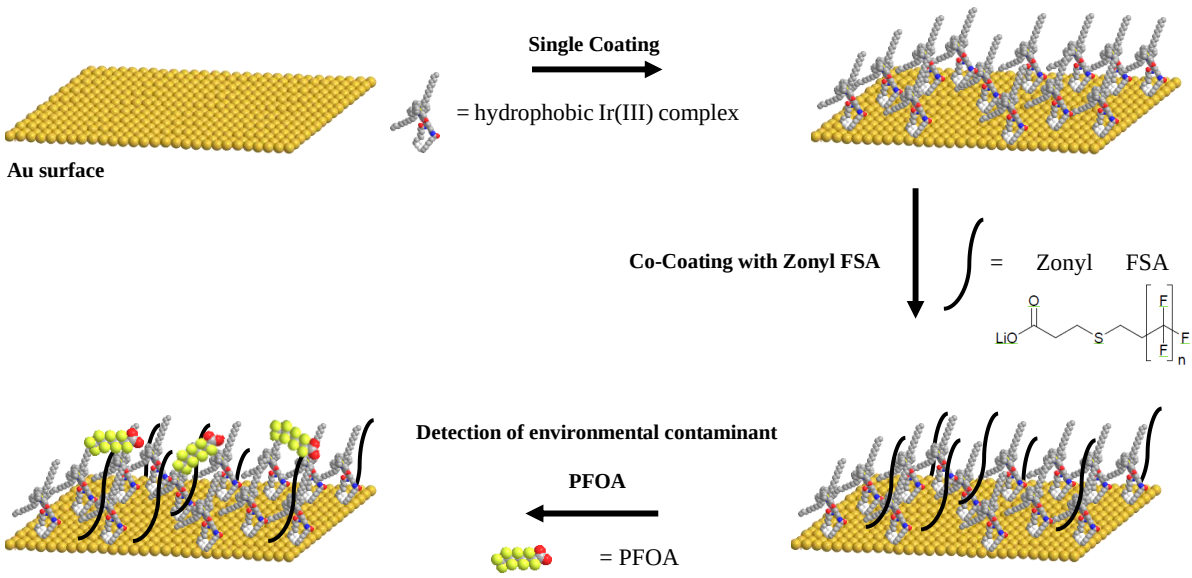


Figure 3.43: Principle of the co-coating of **IrC6bpySS.Au** and **IrC12bpySS.Au** with Zonyl FSA, and the subsequent sensing of the environmental contaminant PFOA with the created devices **IrC6bpySS.Au.Z** and **IrC12bpySS.Au.Z**

These co-coated surfaces show vastly different luminescent lifetimes, and affinity to PFOA far above that of the singularly coated gold surfaces. Detection is seen as low as 80 pM (Figure 3.44); which falls well within the environmental levels that have been reported in New Jersey drinking water of up to 0.24 nM.[104] Another study suggests a median value of 15 pM for PFOA concentration in the river water of Sweden.[107] This suggests the applicability of the sensor system in detecting relevant environmental concentrations of fluorosurfactants is good. It compares well with detection limits for the electrochemical detection technique proposed by Bühlmann *et al.*[127] (0.86 nM) but falls short of matching the capability of HPLC-MS.[125] However further work would be needed to prove that this method is robust under harsh environmental conditions such as water highly contaminated with several components.

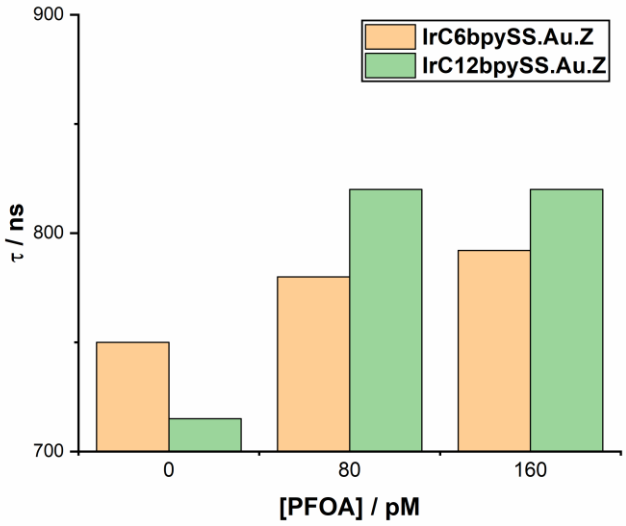


Figure 3.44: Bar chart showing average luminescent lifetime decay values of the devices **IrC6bpySS.Au.Z** and **IrC12bpySS.Au.Z** upon immersion in aqueous solutions with differing concentrations of fluorosurfactant. λ_{exc}=375 nm, λ_{em}= 600 nm.

3.2.8 Investigation of the Zonyl FSA mediated enhancement of PFOA detection

The Zonyl FSA fluorosurfactant clearly enhances the detection of PFOA, and to investigate the reason that this is the case, we used ^{19}F NMR. Zonyl FSA and PFOA were each run separately in 1:1 MeOH-d_4:D_2O, and a spectrum collected for a sample containing both Zonyl FSA and

PFOA in the same conditions. In Figure 3.45 below, it is seen that upon mixing the two fluorine containing compounds a significant shift of 3 ppm (120 to 117 ppm) occurs in the peak assigned to F2 of the PFOA (inset Figure 3.45) which is reported as an identifying feature of a formed inclusion complex.[158]

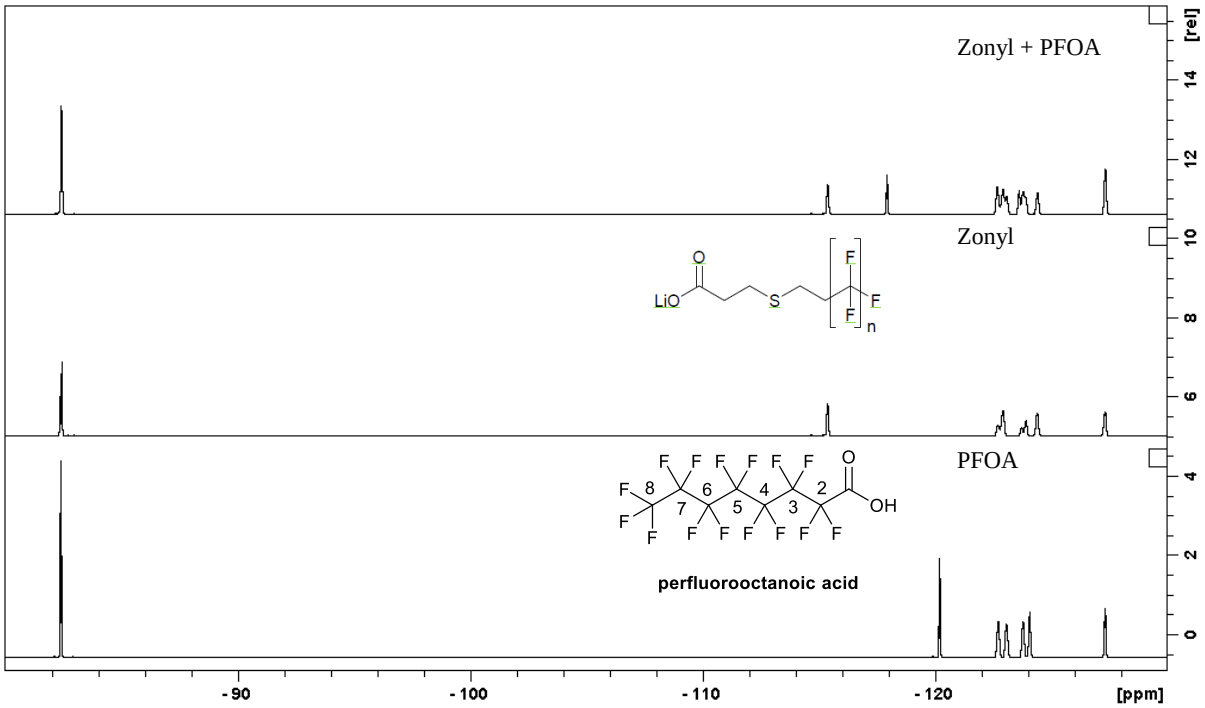


Figure 3.45: ^{19}F NMR of PFOA (bottom), Zonyl FSA (middle), and a mixture of PFOA and Zonyl FSA (top), in 1:1 MeOH-d_4:D_2O

3.2.9 Quantitative determination of the surface composition of IrC6bpySS.Au.Z and IrC12bpySS.Au.Z devices

Quantitative determination of the surface composition can be carried out using TOF-SIMS. This technique is a mass spectrometry technique, in which extremely high-resolution mass spectra can be obtained by fragmentation of molecules at the surface by an ion beam. The TOF-SIMS technique is often used to analyse surfaces, and is somewhat more surface sensitive than XPS giving information on the outermost 2 nm of the sample.[167] The technique is extremely advantageous due to its relatively quick sample analysis, and the sensitivity inherent to the analysis, down to the low ppm range. Unfortunately, the technique is only able to be used

qualitatively and is highly destructive, furthermore, samples with a large depth or roughness can be problematic to analyse.[168, 169]

In Figure 3.46 below, spectra collected from the TOF-SIMS experiments are displayed. A quantitative measure of the CF^+ ion concentration can be made from the intensity observed (Y-axis). Chip type 1 relates to the **IrbpySS.Au**, **IrC6bpySS.Au** and **IrC12bpySS.Au** devices; as these devices are not expected to contain any fluorocarbon material we expect no signal, and indeed the counts are within the intensity range consistent with trace contamination. The spectra collected for Chip type 2 are the same devices after immersion in high concentrations of PFOA in a consistent manner with the luminescence lifetime decay experiments performed in section 3.2.6. There is observation of a significant CF^+ signal in these samples. The order of the detection is somewhat surprising, with the highest immobilisation of PFOA seemingly afforded in the **IrbpySS** coated gold samples, followed by **IrC12bpySS** and **IrC6bpySS**. This observation is under continued investigation, and may suggest that the surface coverage of gold may be higher for the simpler **IrbpySS** complex. The final spectra shown in Figure 3.46 are those of Chip type 3 relating to the **IrbpySS.Au.Z**, **IrC6bpySS.Au.Z** and **IrC12bpySS.Au.Z** devices before immersion in PFOA. We observe that the highest CF^+ intensity is observed for the **IrC12bpySS** sample followed by **IrC6bpySS**, and then **IrbpySS** which clearly allows us to surmise that a hydrophobic interaction between the complexes and the Zonyl FSA allows for higher levels of immobilisation on the surface. The observation is further verified by measurement of the $C_2F_5^+$ ion signal, which has the same order in the measured signal intensity (Supplementary Information).

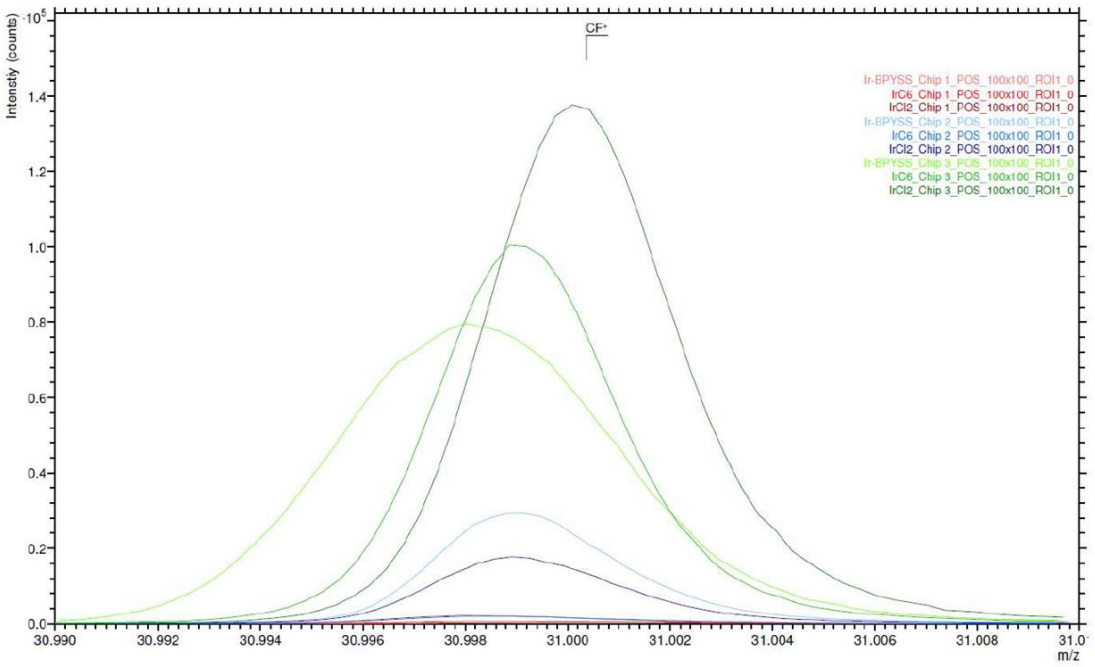


Figure 3.46: TOF-SIMS spectra of differing coated Au samples, the region analysed is typical of the CF^+ ion.

The **IrbpySS.Au.Z**, **IrC6bpySS.Au.Z** and **IrC12bpySS.Au.Z** samples were immersed in 6 mM solutions of PFOA in 1:1 MeOH:H_2O for 1 hour, and the resultant TOF-SIMS spectra were measured (Figure 3.47). The CF^+ spectra reveal an intensity order of **IrC6bpySS.Au.Z** < **IrbpySS.Au.Z** < **IrC12bpySS.Au.Z**. The trend however is somewhat difficult to relate to sensing capability, as the CF^+ signal cannot be deconvoluted for each type of fluorosurfactant, and only allows for the sum of both Zonyl FSA and PFOA on the surface.

It would seem however from the earlier NMR experiments confirming interaction with both the alkyl chain and Zonyl FSA with PFOA that the most advantageous surface for environmental sensing is **IrC12bpySS.Au.Z**.

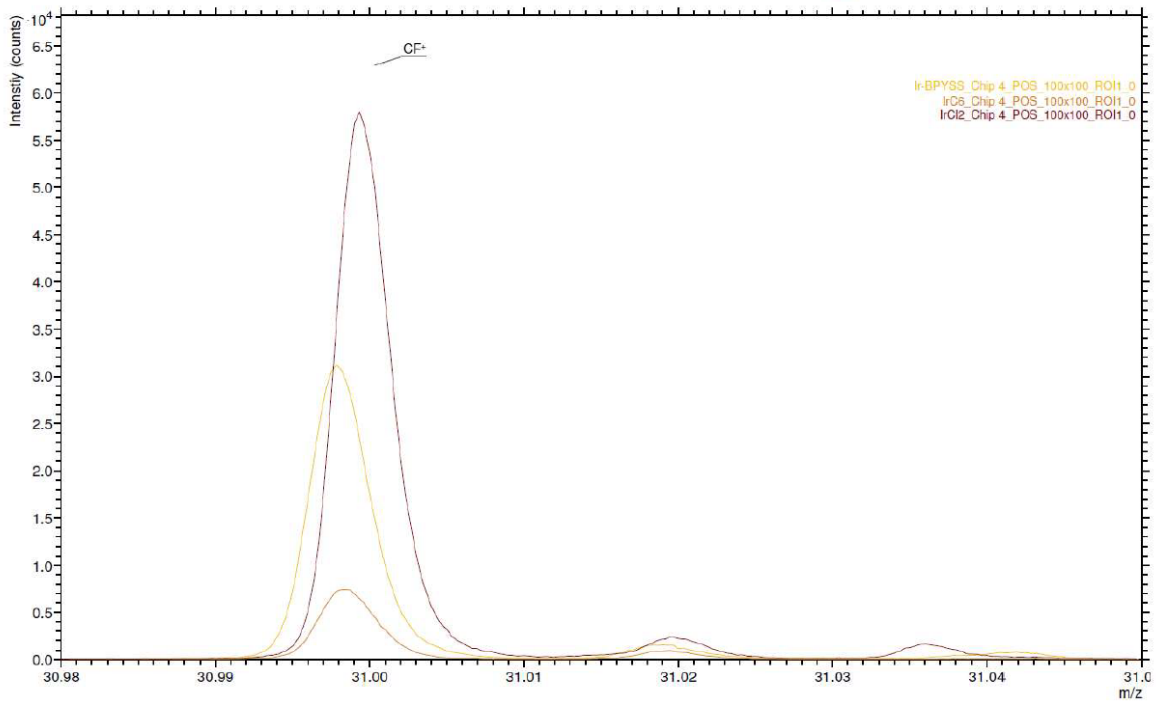


Figure 3.47: TOF-SIMS spectra of **IrbpySS.Au.Z**, **IrC6bpySS.Au.Z** and **IrC12bpySS.Au.Z** samples after immersion in 6mM PFOA solution (1:1, MeOH:H_2O), the region analysed is typical of the CF^+ ion.

3.3 Conclusions

In summary we have successfully synthesised a series of hydrophobic Ir(III) complexes (**IrC6bpy**, **IrC12bpy**, **IrC6bpySS**, and **IrC12bpySS**) for the detection of PFOA. We utilise the luminescent lifetime decay values of the transition metal complexes in solution as a readout for the interaction of the complex with PFOA. The interaction is also confirmed by ^{19}F NMR spectroscopy. Two sequential modifications to the initial solution based sensing system were made, firstly the bpySS containing Ir(III) complexes were immobilised on a gold surface, subsequently used as a solid device to detect PFOA. These devices are characterised by AFM and XPS, with their hydrophobicity measured by contact angle. The second modification, was the addition of Zonyl FSA as a co-coating to the Ir(III) complexes, forming the most efficient sensing platform herein. Zonyl FSA co-coated surfaces were able to detect environmental levels of PFOA down to 80 pM by augmentation of the luminescent lifetime decay value.

In order to explicitly demonstrate the effects of the sequential improvements we have made throughout this chapter to the sensing of PFOA with Ir(III) complexes, table 3.5 collates the lifetime data from the whole chapter. It can clearly be seen that the PFOA detection afforded by the **IrC12bpySS.Au.Z** is far superior in its sensitivity and luminescent lifetime. The surfaces allow a powerful tool for the portable and rapid analysis of PFOA concentrations in the environment, which compliments the current monitoring technologies.

Table 3.5 Summary of the luminescent lifetime decay values and percentage increases in those values measured for the Ir(III) complex based devices. The [PFOA] is given to reflect the sensitivity of the device.

Complex / Device	**τ of longest lifetime component before PFOA sensing / ns**	**[PFOA] / μM**	**τ increase on addition of [PFOA] / %**
IrC6bpySS in 1:1 MeOH:H_2O solution	76	106	0
IrC12bpySS in 1:1 MeOH:H_2O solution	74	0.24	26
IrC6bpySS.Au	119	6×10^{3}	29
IrC12bpySS.Au	143	6×10^{3}	28
IrC6bpySS.Au.Z	750	8×10^{-5}	6
IrC12bpySS.Au.Z	715	8×10^{-5}	16

Future work can take many forms, most pressingly a focus on assessing the device compatibility with collected environmental samples would be of use. Furthermore electrochemical analysis of the surfaces may in future be used to gain values for surface coverage, and electroluminescence measurements could be taken to screen the compounds for their usefulness in electroluminescent devices.

3.4 References

1. A. Adamson, *Physical chemistry of surfaces*, New York, NY (USA); John Wiley and Sons Inc., United States, 1990.
2. J. C. Love, L. A. Estroff, J. K. Kriebel, R. G. Nuzzo and G. M. Whitesides, *Chem. Rev.*, 2005, **105**, 1103-1170.
3. S. M. Barlow and R. Raval, *Surf. Sci. Rep.*, 2003, **50**, 201-341.
4. C. Vericat, M. E. Vela, G. Benitez, P. Carro and R. C. Salvarezza, *Chem. Soc. Rev.*, 2010, **39**, 1805-1834.
5. C. D. Bain, E. B. Troughton, Y. T. Tao, J. Evall, G. M. Whitesides and R. G. Nuzzo, *J. Am. Chem. Soc.*, 1989, **111**, 321-335.
6. P. E. Laibinis, G. M. Whitesides, D. L. Allara, Y. T. Tao, A. N. Parikh and R. G. Nuzzo, *J. Am. Chem. Soc.*, 1991, **113**, 7152-7167.
7. C. D. Bain and G. M. Whitesides, *Science*, 1988, **240**, 62.
8. R. J. Forster, E. Figgemeier, A. C. Lees, J. Hjelm and J. G. Vos, *Langmuir*, 2000, **16**, 7867-7870.
9. H. J. Himmel, M. Kaschke, P. Harder and C. Wöll, *Thin Solid Films*, 1996, **284-285**, 275-280.
10. R. Boissezon, J. Muller, V. Beaugeard, S. Monge and J.-J. Robin, *RSC Adv.*, 2014, **4**, 35690-35707.
11. G. Guerrero, J. G. Alauzun, M. Granier, D. Laurencin and P. H. Mutin, *Dalton Trans.*, 2013, **42**, 12569-12585.
12. S. Li, Y. Zheng, Z. Qi, X. Li and C. Chen, *Physics Procedia*, 2016, **85**, 41-46.
13. S. Alexander, L. Morrow, A. M. Lord, C. W. Dunnill and A. R. Barron, *Journal of Materials Chemistry A*, 2015, **3**, 10052-10059.
14. A. R. Barron, *Dalton Trans.*, 2014, **43**, 8127-8143.
15. C. M. Whelan, M. Kinsella, L. Carbonell, H. Meng Ho and K. Maex, *Microelectron. Eng.*, 2003, **70**, 551-557.
16. A. Khaskhoussi, L. Calabrese and E. Proverbio, *Applied Sciences*, 2020, **10**.
17. H. Xiang and K. Komvopoulos, *J. Appl. Phys.*, 2013, **113**, 224505.
18. U. Srinivasan, M. R. Houston, R. T. Howe and R. Maboudian, *Journal of Microelectromechanical Systems*, 1998, **7**, 252-260.
19. S. M. Borisov and O. S. Wolfbeis, *Chem. Rev.*, 2008, **108**, 423-461.
20. J. M. Costa-Fernández, R. Pereiro and A. Sanz-Medel, *TrAC, Trends Anal. Chem.*, 2006, **25**, 207-218.
21. M. I. J. Stich, S. Nagl, O. S. Wolfbeis, U. Henne and M. Schaeferling, *Adv. Funct. Mater.*, 2008, **18**, 1399-1406.
22. J. Homola and M. Piliarik, in *Surface Plasmon Resonance Based Sensors*, ed. J. Homola, Springer Berlin Heidelberg, Berlin, Heidelberg, 2006, DOI: 10.1007/5346_014, pp. 45-67.

23. T. M. Squires, R. J. Messinger and S. R. Manalis, *Nat. Biotechnol.*, 2008, **26**, 417-426.

24. S. Rana, A. Bajaj, R. Mout and V. M. Rotello, *Adv. Drug Del. Rev.*, 2012, **64**, 200-216.

25. H. M. Fahmy, A. M. Mosleh, A. A. Elghany, E. Shams-Eldin, E. S. Abu Serea, S. A. Ali and A. E. Shalan, *RSC Adv.*, 2019, **9**, 20118-20136.

26. J. T. Koepsel and W. L. Murphy, *ChemBioChem*, 2012, **13**, 1717-1724.

27. A. J. Khadpekar, M. Khan, A. Sose and A. Majumder, *Sci. Rep.*, 2019, **9**, 1024.

28. S. H. Lee, W.-Y. Rho, S. J. Park, J. Kim, O. S. Kwon and B.-H. Jun, *Sci. Rep.*, 2018, **8**, 16763.

29. S. Alom Ruiz and C. S. Chen, *Soft Matter*, 2007, **3**, 168-177.

30. T. Alqurashi, Y. Montelongo, P. Penchev, A. K. Yetisen, S. Dimov and H. Butt, *Nanoscale*, 2017, **9**, 13808-13819.

31. T. Alqurashi, P. Penchev, A. K. Yetisen, A. Sabouri, Rayan M. Ameen, S. Dimov and H. Butt, *RSC Adv.*, 2017, **7**, 18019-18023.

32. R. Ahmed and H. Butt, *ACS Photonics*, 2019, **6**, 1572-1580.

33. T. Kaneko, K. Sasakura, K. Furata, K. Oiwa, H. Shintaku, H. Kotera and R. Yokokawa, 2017.

34. B. Leuschel, A. Gwiazda, W. Heni, F. Diot, S.-Y. Yu, C. Bidaud, L. Vonna, A. Ponche, H. Haidara and O. Soppera, *Sci. Rep.*, 2018, **8**, 10444.

35. S. Singh-Gasson, R. D. Green, Y. Yue, C. Nelson, F. Blattner, M. R. Sussman and F. Cerrina, *Nat. Biotechnol.*, 1999, **17**, 974-978.

36. E. W. L. Chan, S. Park and M. N. Yousaf, *Angew. Chem. Int. Ed.*, 2008, **47**, 6267-6271.

37. H. Du, C. M. Strohsahl, J. Camera, B. L. Miller and T. D. Krauss, *J. Am. Chem. Soc.*, 2005, **127**, 7932-7940.

38. H. Du, M. D. Disney, B. L. Miller and T. D. Krauss, *J. Am. Chem. Soc.*, 2003, **125**, 4012-4013.

39. C. Fan, K. W. Plaxco and A. J. Heeger, *Proc. Natl. Acad. Sci.*, 2003, **100**, 9134.

40. Q. Su, D. Wesner, H. Schönherr and G. Nöll, *Langmuir*, 2014, **30**, 14360-14367.

41. J. He, X. Hu, X. Gao, C. Meng, Y. Li, X. Li, L. Fan and H.-Z. Yu, *Analyst*, 2020, **145**, 4522-4531.

42. G. Liu, Y. Wan, V. Gau, J. Zhang, L. Wang, S. Song and C. Fan, *J. Am. Chem. Soc.*, 2008, **130**, 6820-6825.

43. X. Yang, Q. Liu, D. Wen, M. Gao, D. Zhang, Q. Jin, J. Kong and J. Zhang, *Anal. Chim. Acta*, 2019, **1088**, 144-149.

44. X. Shi, X. Gao, L. Zhang, Y. Li, L. Fan and H.-Z. Yu, *Analyst*, 2015, **140**, 2608-2612.

45. S. Maiti, C. Pezzato, S. Garcia Martin and L. J. Prins, *J. Am. Chem. Soc.*, 2014, **136**, 11288-11291.

46. G. Pieters, A. Cazzolaro, R. Bonomi and L. J. Prins, *Chem. Commun.*, 2012, **48**, 1916-1918.

47. C. Pezzato, B. Lee, K. Severin and L. J. Prins, *Chem. Commun.*, 2013, **49**, 469-471.

48. A. Ono and H. Togashi, *Angew. Chem. Int. Ed.*, 2004, **43**, 4300-4302.

49. S. Doughan, Y. Han, U. Uddayasankar and U. J. Krull, *ACS Appl. Mater. Interfaces*, 2014, **6**, 14061-14068.

50. Y.-X. Wu, X.-B. Zhang, D.-L. Zhang, C.-C. Zhang, J.-B. Li, Y. Wu, Z.-L. Song, R.-Q. Yu and W. Tan, *Anal. Chem.*, 2016, **88**, 1639-1646.

51. N. Kumari, N. Dey and S. Bhattacharya, *Analyst*, 2014, **139**, 2370-2378.

52. M. Maskus and H. D. Abruña, *Langmuir*, 1996, **12**, 4455-4462.

53. E. Figgemeier, E. C. Constable, C. E. Housecroft and Y. C. Zimmermann, *Langmuir*, 2004, **20**, 9242-9248.

54. Y. S. Obeng and A. J. Bard, *Langmuir*, 1991, **7**, 195-201.

55. P. Bertoncello, E. T. Kefalas, Z. Pikramenou, P. R. Unwin and R. J. Forster, *The Journal of Physical Chemistry B*, 2006, **110**, 10063-10069.

56. M. J. J. Pereira Silva, P. Bertoncello, N. N. Daskalakis, N. Spencer, B. M. Kariuki, P. R. Unwin and Z. Pikramenou, *Supramol. Chem.*, 2007, **19**, 115-127.

57. K. W. Kittredge, M. A. Fox and J. K. Whitesell, *The Journal of Physical Chemistry B*, 2001, **105**, 10594-10599.

58. J. L. Shepherd, A. Kell, E. Chung, C. W. Sinclar, M. S. Workentin and D. Bizzotto, *J. Am. Chem. Soc.*, 2004, **126**, 8329-8335.

59. S. A. M. Osborne and Z. Pikramenou, *Faraday Discuss.*, 2015, **185**, 219-231.

60. R. B. P. Elmes, K. N. Orange, S. M. Cloonan, D. C. Williams and T. Gunnlaugsson, *J. Am. Chem. Soc.*, 2011, **133**, 15862-15865.

61. M. Wumaier, T.-M. Yao, X.-C. Hu, Z.-A. Hu and S. Shi, *Dalton Trans.*, 2019, **48**, 10393-10397.

62. F. C.-M. Leung, A. Y.-Y. Tam, V. K.-M. Au, M.-J. Li and V. W.-W. Yam, *ACS Appl. Mater. Interfaces*, 2014, **6**, 6644-6653.

63. J. M. A. Caiut, J. Dexpert-Ghys, Y. Kihn, M. Vérelst, H. Dexpert, S. J. L. Ribeiro and Y. Messaddeq, *Powder Technol.*, 2009, **190**, 95-98.

64. L. A. Rocha, J. M. A. Caiut, Y. Messaddeq, S. J. L. Ribeiro, M. A. U. Martines, J. d. C. Freiria, J. Dexpert-Ghys and M. Verelst, *Nanotechnology*, 2010, **21**, 155603.

65. R. M. Sábio, M. Gressier, J. M. A. Caiut, M.-J. Menu and S. J. L. Ribeiro, *Mater. Lett.*, 2016, **174**, 1-5.

66. S. Cousinié, L. Mauline, M. Gressier, S. R. Kandibanda, L. Datas, C. Reber and M.-J. Menu, *New J. Chem.*, 2012, **36**, 1355-1367.

67. K. Matsui and F. Momose, *Chem. Mater.*, 1997, **9**, 2588-2591.

68. F. Lupo, M. E. Fragalà, T. Gupta, A. Mamo, A. Aureliano, M. Bettinelli, A. Speghini and A. Gulino, *The Journal of Physical Chemistry C*, 2010, **114**, 13459-13464.

69. A. Kumar, M. Chhatwal, D. A. Cristaldi, S. K. Awasthi, R. D. Gupta and A. Gulino, *The Journal of Physical Chemistry C*, 2015, **119**, 5138-5145.

70. S. Ramachandra, K. C. Schuermann, F. Edafe, P. Belser, C. A. Nijhuis, W. F. Reus, G. M. Whitesides and L. De Cola, *Inorg. Chem.*, 2011, **50**, 1581-1591.

71. K. Terada, K. Kobayashi and M.-a. Haga, *Dalton Trans.*, 2008, DOI: 10.1039/B807526C, 4846-4854.

72. T.-Y. Dong, C. Huang, C.-P. Chen and M.-C. Lin, *J. Organomet. Chem.*, 2007, **692**, 5147-5155.

73. A. Schramm, C. Stroh, K. Dössel, M. Lukas, O. Fuhr, H. v. Löhneysen and M. Mayor, *Chem. Commun.*, 2013, **49**, 1076-1078.

74. A. Schramm, C. Stroh, K. Dössel, M. Lukas, M. Fischer, F. Schramm, O. Fuhr, H. v. Löhneysen and M. Mayor, *Eur. J. Inorg. Chem.*, 2013, **2013**, 70-79.

75. Y. Nishimori, K. Kanaizuka, M. Murata and H. Nishihara, *Chem. Asian J.*, 2007, **2**, 367-376.

76. H. Lin, Y.-C. Dai, X. Chen, Q.-Y. Huang and K.-Z. Wang, *Thin Solid Films*, 2013, **542**, 251-256.

77. L.-H. Gao, K.-Z. Wang, L. Cai, H.-X. Zhang, L.-P. Jin, C.-H. Huang and H.-J. Gao, *The Journal of Physical Chemistry B*, 2006, **110**, 7402-7408.

78. K. C. F. Toledo and J. A. Bonacin, *Inorg. Chem. Commun.*, 2019, **99**, 52-59.

79. A. Mulas, G. V. Dubacheva, H. Al Sabea, F. Miomandre, J.-F. Audibert, L. Norel, S. Rigaut and C. Lagrost, *Langmuir*, 2019, **35**, 13711-13717.

80. F. Miomandre, S. Stancheva, J.-F. Audibert, A. Brosseau, R. B. Pansu, M. Lepeltier and C. R. Mayer, *The Journal of Physical Chemistry C*, 2013, **117**, 12806-12814.

81. Y. Yu, M. Zhou and H. Cui, *J. Mater. Chem.*, 2011, **21**, 12622-12625.

82. C. R. Mayer, E. Dumas, F. Miomandre, R. Méallet-Renault, F. Warmont, J. Vigneron, R. Pansu, A. Etcheberry and F. Sécheresse, *New J. Chem.*, 2006, **30**, 1628-1637.

83. L. Guerret, J. F. Audibert, A. Debarre, M. Lepeltier, P. Haghi-Ashtiani, G. V. Dubacheva and F. Miomandre, *The Journal of Physical Chemistry C*, 2016, **120**, 2411-2418.

84. W. Lv, T. Yang, Q. Yu, Q. Zhao, K. Y. Zhang, H. Liang, S. Liu, F. Li and W. Huang, *Advanced Science*, 2015, **2**, 1500107.

85. N. J. Rogers, H. C. Jeffery, S. Claire, D. J. Lewis, G. Zikeli, N. J. Hodges, S. Egginton, G. B. Nash and Z. Pikramenou, *Nanomedicine*, 2017, **12**, 2725-2740.

86. R. D. Costa, E. Ortí, H. J. Bolink, S. Graber, S. Schaffner, M. Neuburger, C. E. Housecroft and E. C. Constable, *Adv. Funct. Mater.*, 2009, **19**, 3456-3463.

87. C. Li, W. Lu, X. Zhou, M. Pang and X. Luo, *Anal. Chem.*, 2018, **90**, 14239-14246.

88. R. Ozaki, T. Yamada, S. Yudate, K. Kadowaki and H. Sato, *Jpn. J. Appl. Phys.*, 2017, **57**, 03EG03.

89. E. Tekin, E. Holder, V. Marin, B.-J. de Gans and U. S. Schubert, *Macromol. Rapid Commun.*, 2005, **26**, 293-297.

90. C. Hierlinger, H. V. Flint, D. B. Cordes, A. M. Z. Slawin, E. A. Gibson, D. Jacquemin, V. Guerchais and E. Zysman-Colman, *Polyhedron*, 2018, **140**, 109-115.

91. E. I. Mayo, K. Kilsa, T. Tirrell, P. I. Djurovich, A. Tamayo, M. E. Thompson, N. S. Lewis and H. B. Gray, *Photochemical & Photobiological Sciences*, 2006, **5**, 871-873.

92. Y. Shinpuku, F. Inui, M. Nakai and Y. Nakabayashi, *J. Photochem. Photobiol. A: Chem.*, 2011, **222**, 203-209.

93. A. Sinopoli, C. J. Wood, E. A. Gibson and P. I. P. Elliott, *Inorg. Chim. Acta*, 2017, **457**, 81-89.

94. S. Tschierlei, A. Neubauer, N. Rockstroh, M. Karnahl, P. Schwarzbach, H. Junge, M. Beller and S. Lochbrunner, *PCCP*, 2016, **18**, 10682-10687.

95. R. Srinidhi, P. Federico, E. Fabio, C. S. Klaus, A. N. Christian, B. Peter, F. R. William, M. W. George and C. Luisa De, *Pure Appl. Chem.*, 2011, **83**, 779-799.

96. S. J. Adams, D. J. Lewis, J. A. Preece and Z. Pikramenou, *ACS Appl. Mater. Interfaces*, 2014, **6**, 11598-11608.

97. S. J. Adams, A. J. Carrod, L. A. Rochford, M. Walker and Z. Pikramenou, *ChemistrySelect*, 2018, **3**, 3251-3257.

98. R. C. Buck, J. Franklin, U. Berger, J. M. Conder, I. T. Cousins, P. de Voogt, A. A. Jensen, K. Kannan, S. A. Mabury and S. P. J. van Leeuwen, *Integr. Environ. Assess. Manage.*, 2011, **7**, 513-541.

99. B. C. Saunders, *Ciba Foundation Symposium 2 - Carbon-Fluorine Compounds; Chemistry, Biochemistry and Biological Activities*, 1972, DOI: doi:10.1002/9780470719855.ch2, 9-32.

100. D. F. McMillen and D. M. Golden, *Annu. Rev. Phys. Chem.*, 1982, **33**, 493-532.

101. R. Jaffe and R. A. Hites, *Environ. Sci. Technol.*, 1985, **19**, 736-740.

102. B. D. Key, R. D. Howell and C. S. Criddle, *Environ. Sci. Technol.*, 1997, **31**, 2445-2454.

103. G. W. Olsen, in *Toxicological Effects of Perfluoroalkyl and Polyfluoroalkyl Substances*, ed. J. C. DeWitt, Springer International Publishing, Cham, 2015, DOI: 10.1007/978-3-319-15518-0_4, pp. 77-125.

104. G. B. Post, J. B. Louis, R. L. Lippincott and N. A. Procopio, *Environ. Sci. Technol.*, 2013, **47**, 13266-13275.

105. G. B. Post, P. D. Cohn and K. R. Cooper, *Environ. Res.*, 2012, **116**, 93-117.

106. X. C. Hu, D. Q. Andrews, A. B. Lindstrom, T. A. Bruton, L. A. Schaider, P. Grandjean, R. Lohmann, C. C. Carignan, A. Blum, S. A. Balan, C. P. Higgins and E. M. Sunderland, *Environmental Science & Technology Letters*, 2016, **3**, 344-350.

107. L. Gobelius, J. Hedlund, W. Dürig, R. Tröger, K. Lilja, K. Wiberg and L. Ahrens, *Environ. Sci. Technol.*, 2018, **52**, 4340-4349.

108. G. L. Kennedy and J. M. Symons, in *Toxicological Effects of Perfluoroalkyl and Polyfluoroalkyl Substances*, ed. J. C. DeWitt, Springer International Publishing, Cham, 2015, DOI: 10.1007/978-3-319-15518-0_12, pp. 265-304.

109. K. Kannan, *Environmental Chemistry*, 2011, **8**, 333-338.

110. D. E. Keil, in *Toxicological Effects of Perfluoroalkyl and Polyfluoroalkyl Substances*, ed. J. C. DeWitt, Springer International Publishing, Cham, 2015, DOI: 10.1007/978-3-319-15518-0_10, pp. 239-248.

111. B. D. Abbott, in *Toxicological Effects of Perfluoroalkyl and Polyfluoroalkyl Substances*, ed. J. C. DeWitt, Springer International Publishing, Cham, 2015, DOI: 10.1007/978-3-319-15518-0_8, pp. 203-218.

112. A. Cordner, V. Y. De La Rosa, L. A. Schaider, R. A. Rudel, L. Richter and P. Brown, *J. Expo. Sci. Environ. Epidemiol.*, 2019, **29**, 157-171.

113. Clare Atkinson, Simon Blake, Tom Hall, Rakesh Kanda and P. Rumsby, *Survey Of The Prevalence Of Perfluorooctane Sulphonate (Pfos), Perfluorooctanoic Acid (Pfoa) And Related Compounds In Drinking Water And Their Sources*, 2008.

114. DEPA, *Perfluoroalkylated substances: PFOA, PFOS and PFOSA. Evaluation of health hazards and proposal of a health based quality criterion for drinking water, soil and ground water*, The Danish Environmental Protection Agency Strandgade 29 1401 Copenhagen K Denmark, www.mst.dk/english, 2015.

115. EPA, Lifetime health advisories and health effects support documents for perfluorooctanoic acid and perfluorooctane sulfonate, https://www.epa.gov/ground-water-and-drinking-water/supporting-documents-drinking-water-health-advisories-pfoa-and-pfos).

116. NHMRC, *NRMMC (2011) Australian Drinking Water Guidelines Paper 6 National Water Quality Management Strategy.*, National Health and Medical Research Council, National Resource Management Ministerial Council,

Commonwealth of Australia, Canberra, 2018.

117. Swedish Food Agency, PFAS in drinking water and fish-risk management, https://www.livsmedelsverket.se/en/food-and-content/oonskade-amnen/miljogifter/pfas-in-drinking-water-fish-risk-management#Action%20levels).

118. H. Park, G. Choo, H. Kim and J. E. Oh, *Sci Total Environ*, 2018, **634**, 1505-1512.

119. K. Y. Tan, G. H. Lu, H. T. Piao, S. Chen, X. C. Jiao, N. Gai, E. Yamazaki, N. Yamashita, J. Pan and Y. L. Yang, *Bull Environ Contam Toxicol*, 2017, **99**, 224-231.

120. H. Chen, C. Zhang, J. Han, Y. Yu and P. Zhang, *Environ Pollut*, 2012, **170**, 26-31.

121. V. Boiteux, X. Dauchy, C. Rosin and J. F. Munoz, *Arch Environ Contam Toxicol*, 2012, **63**, 1-12.

122. V. Gellrich, H. Brunn and T. Stahl, *J Environ Sci Health A Tox Hazard Subst Environ Eng*, 2013, **48**, 129-135.

123. S. Ullah, T. Alsberg and U. Berger, *J Chromatogr A*, 2011, **1218**, 6388-6395.

124. J. S. Boone, C. Vigo, T. Boone, C. Byrne, J. Ferrario, R. Benson, J. Donohue, J. E. Simmons, D. W. Kolpin, E. T. Furlong and S. T. Glassmeyer, *Sci Total Environ*, 2019, **653**, 359-369.

125. *Anal. Chem.*, 2007, **79**, 3966-3973.

126. U. Berger, M. A. Kaiser, A. Kärrman, J. L. Barber and S. P. J. van Leeuwen, *Anal. Bioanal. Chem.*, 2011, **400**, 1625-1635.

127. L. D. Chen, C.-Z. Lai, L. P. Granda, M. A. Fierke, D. Mandal, A. Stein, J. A. Gladysz and P. Bühlmann, *Anal. Chem.*, 2013, **85**, 7471-7477.

128. L. S. Walekar, M. Zheng, L. Zheng and M. Long, *Microchim. Acta*, 2019, **186**, 278.

129. J. Liang, X. Deng and K. Tan, *Spectrochimica Acta Part A: Molecular and Biomolecular Spectroscopy*, 2015, **150**, 772-777.

130. Z. Cheng, L. Du, P. Zhu, Q. Chen and K. Tan, *Spectrochimica Acta Part A: Molecular and Biomolecular Spectroscopy*, 2018, **201**, 281-287.

131. Q. Liu, A. Huang, N. Wang, G. Zheng and L. Zhu, *J. Lumin.*, 2015, **161**, 374-381.

132. L. Lin, S. Zhou, H. Guo, Y. Chen, S. Lin, L. Yan, K. Li and J. Li, *Microchim. Acta*, 2019, **186**, 380.

133. J. Wang, H. Wu and L. Angnes, *Anal. Chem.*, 1993, **65**, 1893-1896.

134. M. A. McRipley and R. A. Linsenmeier, *J. Electroanal. Chem.*, 1996, **414**, 235-246.

135. D. A. Cristaldi, I. Fragala, A. Pappalardo, R. M. Toscano, F. P. Ballistreri, G. A. Tomaselli and A. Gulino, *J. Mater. Chem.*, 2012, **22**, 675-683.

136. Z.-B. Zheng, S.-Y. Kang, Y. Zhao, N. Zhang, X. Yi and K.-Z. Wang, *Sens. Actuators B: Chem.*, 2015, **221**, 614-624.

137. R. Y. Lai, M. Chiba, N. Kitamura and A. J. Bard, *Anal. Chem.*, 2002, **74**, 551-553.

138. A. D. Shukla, A. Das and M. E. van der Boom, *Angew. Chem. Int. Ed.*, 2005, **44**, 3237-3240.

139. Y. C. Anthony D'Aléoa René M. Williams, Vijay M. Iyerb, Peter Belserb Frank Vergeerc, Virginia Ruizd, Patrick R. Unwin, and Luisa De Cola, *TOICJ*, 2007, **1**, 26-36.

140. S. Zanarini, E. Rampazzo, D. Bich, R. Canteri, L. Della Ciana, M. Marcaccio, E. Marzocchi, M. Montalti, C. Panciatichi, C. Pederzolli, F. Paolucci, L. Prodi and L. Vanzetti, *The Journal of Physical Chemistry C*, 2008, **112**, 2949-2957.

141. S. Bozorgzadeh, B. Haghighi and L. Gorton, *Electrochim. Acta*, 2015, **164**, 211-217.

142. I. Bist, B. Song, I. M. Mosa, T. E. Keyes, A. Martin, R. J. Forster and J. F. Rusling, *ACS Sensors*, 2016, **1**, 272-278.

143. S. M. King, S. Claire, R. I. Teixeira, A. N. Dosumu, A. J. Carrod, H. Dehghani, M. J. Hannon, A. D. Ward, R. Bicknell, S. W. Botchway, N. J. Hodges and Z. Pikramenou, *J. Am. Chem. Soc.*, 2018, **140**, 10242-10249.

144. L. Ackermann, P. Novák, R. Vicente and N. Hofmann, *Angew. Chem. Int. Ed.*, 2009, **48**, 6045-6048.

145. S. Ladouceur, D. Fortin and E. Zysman-Colman, *Inorg. Chem.*, 2011, **50**, 11514-11526.

146. K. Hasan, A. K. Bansal, I. D. W. Samuel, C. Roldán-Carmona, H. J. Bolink and E. Zysman-Colman, *Sci. Rep.*, 2015, **5**, 12325.

147. A. F. Henwood and E. Zysman-Colman, *Chem. Commun.*, 2017, **53**, 807-826.

148. K. K.-W. Lo, J. S.-W. Chan, L.-H. Lui and C.-K. Chung, *Organometallics*, 2004, **23**, 3108-3116.

149. K. K.-W. Lo, P.-K. Lee and J. S.-Y. Lau, *Organometallics*, 2008, **27**, 2998-3006.

150. L. Hua-Wei, K. Y. Zhang, W. H.-T. Law and K. K.-W. Lo, *Organometallics*, 2010, **29**, 3474-3476.

151. Y. Ohsawa, S. Sprouse, K. A. King, M. K. DeArmond, K. W. Hanck and R. J. Watts, *J. Phys. Chem.*, 1987, **91**, 1047-1054.

152. A. Juris, V. Balzani, F. Barigelletti, S. Campagna, P. Belser and A. von Zelewsky, *Coord. Chem. Rev.*, 1988, **84**, 85-277.

153. S. Serroni, A. Juris, S. Campagna, M. Venturi, G. Denti and V. Balzani, *J. Am. Chem. Soc.*, 1994, **116**, 9086-9091.

154. J. H. van Diemen, J. G. Haasnoot, R. Hage, E. Müller and J. Reedijk, *Inorg. Chim. Acta*, 1991, **181**, 245-251.

155. M. G. Colombo, A. Hauser and H. U. Güdel, in *Electronic and Vibronic Spectra of Transition Metal Complexes I*, ed. H. Yersin, Springer Berlin Heidelberg, Berlin, Heidelberg, 1994, DOI: 10.1007/3-540-58155-3_5, pp. 143-171.

156. R. Tandon, T. A. Nigst and H. Zipse, *Eur. J. Org. Chem.*, 2013, **2013**, 5423-5430.

157. C. Ning, H. Ma, C. M. Pedersen, H. Chang, Y. Wang and Y. Qiao, *J. Mol. Liq.*, 2019, **283**, 45-50.

158. H. Omorodion, M. Palenzuela, M. Ruether, B. Twamley, J. A. Platts and R. J. Baker, *New J. Chem.*, 2018, **42**, 7956-7968.

159. J. M. Hollander and W. L. Jolly, *Acc. Chem. Res.*, 1970, **3**, 193-200.

160. A. G. Shard, in *Characterization of Nanoparticles*, eds. V.-D. Hodoroaba, W. E. S. Unger and A. G. Shard, Elsevier, 2020, DOI: https://doi.org/10.1016/B978-0-12-814182-3.00019-5, pp. 349-371.

161. T. M. Willey, A. L. Vance, C. Bostedt, T. van Buuren, R. W. Meulenberg, L. J. Terminello and C. S. Fadley, *Langmuir*, 2004, **20**, 4939-4944.

162. L. Pukenas, P. Prompinit, B. Nishitha, D. J. Tate, N. D. P. Singh, C. Wälti, S. D. Evans and R. J. Bushby, *ACS Appl. Mater. Interfaces*, 2017, **9**, 18388-18397.

163. Y. Dong, S. Abaci, C. Shannon and M. J. Bozack, *Langmuir*, 2003, **19**, 8922-8926.

164. J. C. Love, D. B. Wolfe, R. Haasch, M. L. Chabinyc, K. E. Paul, G. M. Whitesides and R. G. Nuzzo, *J. Am. Chem. Soc.*, 2003, **125**, 2597-2609.

165. K. W. Bewig and W. A. Zisman, *J. Phys. Chem.*, 1965, **69**, 4238-4242.

166. R. J. Baker, P. E. Colavita, D. M. Murphy, J. A. Platts and J. D. Wallis, *The Journal of Physical Chemistry A*, 2012, **116**, 1435-1444.

167. S. Ebnesajjad, in *Surface Treatment of Materials for Adhesive Bonding (Second Edition)*, ed. S. Ebnesajjad, William Andrew Publishing, Oxford, 2014, DOI: https://doi.org/10.1016/B978-0-323-26435-8.00004-6, pp. 39-75.

168. L. H. Yahia and L. K. Mireles, in *Characterization of Polymeric Biomaterials*, eds. M. C. Tanzi and S. Farè, Woodhead Publishing, 2017, DOI: https://doi.org/10.1016/B978-0-08-100737-2.00004-2, pp. 83-97.

169. K. Schaepe, H. Jungnickel, T. Heinrich, J. Tentschert, A. Luch and W. E. S. Unger, in *Characterization of Nanoparticles*, eds. V.-D. Hodoroaba, W. E. S. Unger and A. G. Shard, Elsevier, 2020, DOI: https://doi.org/10.1016/B978-0-12-814182-3.00025-0, pp. 481-509.

4 General conclusions and future work

Six cyclometalated Ir(III) complexes were successfully synthesised and fully characterised. The complexes were used in every case for detection based on an optical readout, due to the high sensitivity of the emission characteristics to local environmental changes. We probe detection of analytes using both the emission intensity and the luminescence lifetime of the Ir(III) complexes. Several advantages are afforded by using iridium transition metal complexes for optical detection; including the facile synthetic modification of the ligands surrounding the metal centre, high photostability, long-lived luminescence lifetime, and strong orange to red emission.

In the case of the synthesised Ir(III) complexes appended with boronic acid moieties, **Ir-4-BOH** and **Ir-3-BOH**, we have shown to have high affinities to saccharides at physiological pH in aqueous solutions in the order of 10^2 M^{-1}. The binding events are measurable through both photoluminescence spectroscopy and electrochemiluminescence studies. ^{11}B and ^{19}F NMR spectroscopies in conjunction with MALDI mass spectrometry were used to elucidate the structure of the bound complex. Functional materials constructed from hydrogels are reported, and the materials allow for a non-toxic, and stable wearable device. Looking forward, as we have shown that it is possible to sense saccharides using the advantageous photophysical and electrochemical properties of Ir(III) complexes, there are many opportunities that present themselves. One limitation of this work is the low luminescence quantum yield for the Ir(III) complex which may hinder use as a biological sensor at low concentrations, we propose that second generation iridium complexes could be synthesised, in which higher quantum yields would be sought. One particular strategy for this could be to use known higher quantum yield iridium complexes (see section 1.3.1, figure 1.4) and modify the ligands of these complexes using a similar substitution strategy used in the work detailed in this thesis an example of this

. Further to this, due to the success of our studies, it would be possible in future to construct multifunctional sensors, sensitive to saccharides and a further analyte concurrently. A common secondary condition associated with diabetes is haemochromatosis in which iron levels in a patients blood are elevated. Optical assays for metal ions have been reported using the absorbance intensity changes or emission intensity of rhodamine derivatives as a detection tool (see section 3.1.2, figure 3.7). Iridium complexes with rhodamine attached could be synthesised through the selective functionalisation of the ancillary bipyridyl ligand. This in turn would give rise to a multifunctional saccharide and iron sensors. Figure FW1.1 below gives some potential structures that would be of interest based on the two future avenues of investigation detailed above.

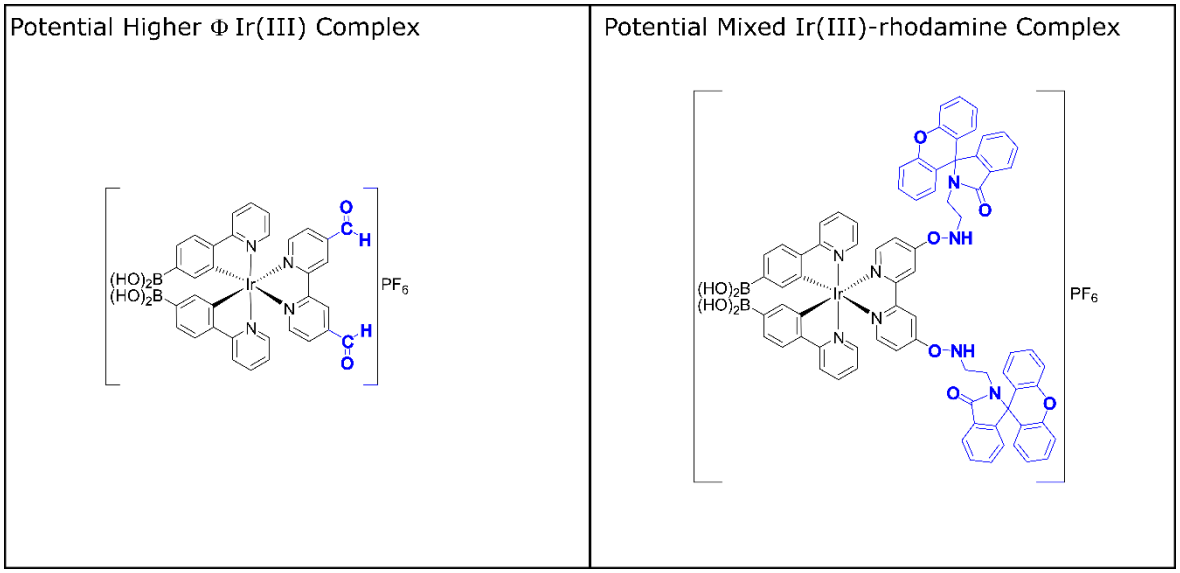


Figure FW1.1: Structures of the Ir(III) complexes suggested to be useful in taking the **Ir-4-BOH** structure and modifying to achieve certain goals. The image on the left is based upon the bipyridine ligand structure seen in Figure 1.4, and aims to increase quantum yield of the parent **Ir-4-BOH**. The image on the right pertains to a complex which culd potentially show Fe(III) and sugar sensing concurrently. Modifications to the original **Ir-4-BOH** complex are shown in blue.

In the third chapter of this thesis the synthesis and characterisation of a series of luminescent Ir(III) complexes with surface binding lipoic acid moieties are described, for the purpose of sensing PFOA. The complexes are bound to gold surfaces, anchored through the lipoic acid chain to create a luminescent gold-Ir(III) transition metal platform. We characterise the properties of these surfaces through AFM, XPS, contact angle and TOF-SIMS. After

fabrication of the devices we utilise the bound Ir(III) complex as a reporter for fluorosurfactant concentration, through measurement of the luminescence lifetime. High fluorosurfactant concentrations lead to observation of a longer luminescent lifetime. To increase the sensitivity of the surfaces, a known second fluorosurfactant Zonyl FSA is used to co-coat the surfaces with the Ir(III) complexes. We observe an augmentation of the luminescent lifetime when PFOA concentrations are comparable to that found in ground water samples from several countries. The fabricated devices could therefore provide a method with sufficient accuracy but significantly lower analysis times vs. traditional HPLC methods. It is important to consider the advantages of using this iridium complex over other reported fluorescent sensors for PFOA. Reported fluorescence sensors rely on changes in emission intensity, and are until now only reported in solution. Whilst the fluorescence quantum yield of the organic dyes used is larger, we provide an approach utilising gold surfaces as devices measuring luminescent lifetime, which is in the hundreds of ns, far greater than that of organic complexes. To continue this work, it would be important to collect and analyse environmental samples, this would test the robustness of the gold surface system in conditions more representative than can be wholly recreated in the laboratory. In the work described above for the sensing of saccharides we described a mechanism of dual-modality photo- and electrochemical sensing. This is likely to be useful if applied to the detection of PFOA, therefore an investigation of the PFOA sensing ability of Ir(III) complexes through electrochemical methods can be envisaged. Gold electrodes which the current bpySS ligand would readily attach to could be used to facilitate this new detection route. It would also be of interest to fluorinate the alkyl chain appended to the 2-phenylpyridine ligand of the Ir(III) complex. We believe, based on previously published computational studies that confirm fluorine-fluorine interactions can occur between perfluorinated alkyl molecules, a fluorinated iridium complex would lead to efficient capture of the PFOA through physisorption. Once this modification had been made it could be

incorporated into the surfaces for sensing in the same manner as the **IrC6bpySS** and **IrC12bpySS** compounds. Figure FW1.2 below details a potential novel fluorine containing Ir(III) complex **IrCF12bpySS** which could be used to simultaneously improve sensitivity to PFOA concentration, and to coat gold electrodes.

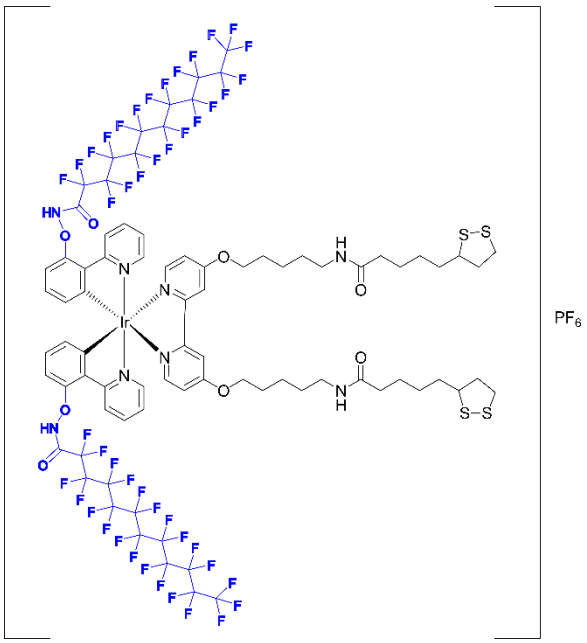


Figure FW1.2: Structure of the potential Ir(III) complex **IrCF12bpySS** which could act as a gold bound sensor for PFOA in a similar manner to the described **IrC12bpySS**. The addition of the perfluorinated alkyl chain (blue) may help to increase the affinity through fluorine-fluorine interactions.

The thesis demonstrates two different applications of iridium complexes for sensing, both in solution and immobilised on a gold support. All complexes can successfully report the detection of the analytes of interest through optical effects. The work demonstrates the high efficiency of these Ir(III) complexes in sensing, and these results provide a good starting point to tailor the applicability of the complexes to sensing outside of a laboratory setting.

5 Appendix

5.1 Experimental and Supplementary Information for Chapter 2: Photoluminescent and Electrochemical Sensing of Sugars at Physiological pH via an iridium(III) Complex Bearing Directly Boronated Ligands.

5.1.1 Experimental

5.1.1.1 Materials and methods

Starting materials and solvents were obtained from Sigma-Aldrich, Fluka, Fisher Scientific, or Acros Chemicals and used without any further purification. Flash column chromatography was performed using LC60A 40−63 μm silica gel (Merck) or activated, neutral Brockmann I grade alumina (Merck). All reactions were performed under an argon atmosphere unless stated otherwise.

^{1}H, ^{13}C and 2D NMR spectroscopy was carried out on a Bruker AVANCE NEO 400 NMR spectrometer (^{1}H: 400 MHz, ^{13}C: 101 MHz), ^{1}H and ^{13}C assignments were confirmed by COSY, HSQC and HMBC spectra. Electrospray mass spectrometry was carried out on a Waters Micromass Q-TOF, and MALDI mass spectrometry on a Bruker Flextreme MALDI-TOF. A suitable crystal was selected and a dataset for **ppy-4-BOH** was measured on an Agilent SuperNova diffractometer using an Atlas detector. The data collection was driven and processed and an absorption correction was applied using CrysAlisPro. The structure was solved using ShelXT and was refined by a full-matrix least-squares procedure on F^2 in ShelXL. Figures and reports were produced using OLEX2. All non-hydrogen atoms were refined with anisotropic displacement parameters. The hydrogen atoms bonded to O(1) and O(2) were located in the electron density and freely refined. All remaining hydrogen atoms were fixed as

riding models and the isotropic thermal parameters (U_{iso}) were based on the U_{eq} of the parent atoms.

UV−Visible spectra were collected using 1 cm path length polished quartz cuvettes on an Agilent Cary 60 spectrophotometer. Luminescence spectra for saccharide binding studies of **Ir-4-BOH** were carried out using a Photon Technology International luminescence spectrometer with a 150 W xenon arc lamp as the excitation source. Felix analysis software was used to record data, all spectra were corrected for Photomultiplier tube and instrument response. Luminescent spectra taken for saccharide binding studies of **Ir-3-BOH** were recorded on an Edinburgh Instruments FLS920 steady state and time-resolved spectrometer. The detection system used an incorporated R928 (visible) Hamamatsu photomultiplier tube. The emission monochromator is fitted with gratings blazed at 500 nm. F900 spectrometer analysis software was used to record the data, and all spectra were corrected for Photomultiplier and instrument response. Luminescent lifetimes of all complexes were recorded with an Edinburgh Instruments EPL-375 laser as an excitation source and fitted using Edinburgh Instruments FAST software with estimated error of ± 10%. Argon was used to degas samples by bubbling through the solution inside a cuvette fitted with a tight sealed septum for 15 min. Quantum yield measurements were taken using an integrating sphere attachment supplied by Edinburgh Instruments. Photoluminescence experiments for saccharide binding were carried out in 0.01 M aqueous PBS containing 2 % acetonitrile. Sugars were first added as a solution in PBS. 2.5 μL aliquots were added up to a concentration of 10 mM, after which saccharides were added as powders, to avoid dilution effects. The binding constants were determined according to equation in section 2.4.3. Samples for MALDI mass spectrometry were prepared by first making a saturated solution of iridium(III) complex in a 0.1 mL aqueous solution (1:1, MeCN:H_2O) and adding 1.8 mg (0.01 mol) of glucose. 5 mL of this solution was co spotted with a 0.1 M solution of 2,3-dihydroxybenzoic acid, onto the target plate.

Cyclic Voltammograms were recorded using a potentiostat workstation (CH Instrument model 760E) using a conventional three-electrode configuration cell. A glassy carbon electrode (IJ Cambria) of 3 mm diameter (area 0.07 cm2) was used as the working electrode and a platinum wire as a counter electrode. All potentials were quoted versus an Ag/AgCl reference electrode and all the measurements were recorded at room temperature. ECL measurements were performed using a Hamamatsu power supply photosensor module with an open window of 530 V coupled with the potentiostat. The ECL signal was acquired using a PMT and the optical fiber model supplied by Hamamatsu positioned perpendicularly to the GCE. CV and ECL curves were recorded at scan rate of 50 mV/s.

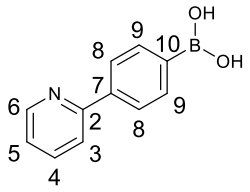
Hydrogel devices were fabricated using an AnalytikJena UVP CL-1000 crosslinker, programmed to 999,900 $\mu J/cm^2$ and irradiation time of 1 minute. A Thorlabs CPS450 (λ = 450 nm) laser was used as an excitation source, with energy of 3 J/cm^2 pulsed for 3 seconds. An Ocean Optics USB 2000 was used as the detector, with bifurcated fibre optical fibres. Measurements were taken in a cuvette with parallel clear sides in dark conditions. To reach the reported saccharide concentrations, 1 mL of PBS (0.01 M) was added to the cuvette and increasing amounts of monosaccharide were added as powders to reach the appropriate concentrations.

To investigate potential toxicity of the hydrogels to cells in the skin, primary adult human epidermal keratinocytes (Keratinocytes; ThermoFisher Scientific, cat no. C0055C), primary adult human epidermal melanocytes (lightly pigmented donor) (Melanocytes; ThermoFisher, cat no. C0245C) and primary adult human dermal fibroblasts (HDF; ThermoFisher, cat no. C0135C) were expanded in Epilife CF (ThermoFisher, Cat no. MEPICF500), human melanocyte growth supplement (ThermoFisher; Cat no. S0025) and DMEM supplemented with 10% FCS (ThermoFisher), respectively. Cells were used between passage 7-10 for all

experiments. The MTT assay was then used to assess toxicity of gels to human skin cells, as described by us previously (Badaway et al., 2018). Briefly, 5 × 103 cells of each population were plated in six-well plates (n = 5 wells/condition), covered with 2 mL of each respective growth medium, defined masses of gels were immersed into the culture medium and left in contact with cells for 72 h at 37 °C and 5% CO_2. After 72 h, supernatants were removed and cells were washed in PBS and the MTT assay was performed according to the manufacturer's instructions (R&D Systems, Watford, UK). The resulting absorbances were read at 570 nm and absorbance units calculated from triplicate readings after subtraction of blank wells (culture media only).

5.1.1.2 **Synthesis of ligands, Ir(III) complexes and hydrogels**

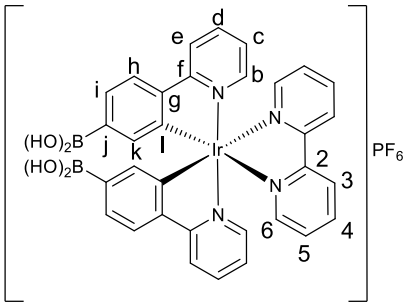
Synthesis of ppy-4-BOH



To a stirring mixture of Mg (610 mg, 25.0 mmol) and LiCl (25.0 mL, 0.5 M in THF, 15.5 mmol), diisobutylaluminium hydride (0.1 mL, 1 M in toluene, 0.1 mmol) was added, and the solution stirred for 5 min. After this time 2-(4-bromophenyl)pyridine (2.34 g, 10.0 mmol) was added at room temperature, and stirring continued for 1 h. The mixture was cooled to 0 ^{o}C and the trimethyl borate (2.09 mL, 20.0 mmol) was added and stirred for 5 min, before quenching with HCl (0.1 M, 5 mL). The reaction mixture was extracted with EtOAc (2 x 20 mL) and the organic layer was isolated and dried over Na_2SO_4 and the solvent evaporated *in vacuo* to give a crude solid that was recrystallised (CH_3CN:H_2O, 1:1) to yield a white crystalline solid. (1.68 g, 8.44 mmol, 84%) ^{1}H NMR (400 MHz, DMSO-d6) δ 8.68 (ddd, *J* = 4.8, 1.1, 0.9 Hz, 1H, H-6), 8.17 (m, 2H, B(OH)2), 8.05 (d, *J* = 8.2 Hz, 2H, H-8), 8.01 (dt, *J* = 8.0, 1.1 Hz, 1H, H-4), 7.97 – 7.89 (m, 3H, H-3, H-9), 7.39 (ddd, *J* = 8.0, 4.9, 1.2 Hz, 1H, H-5). ^{13}C NMR (101 MHz, DMSO-d6) δ

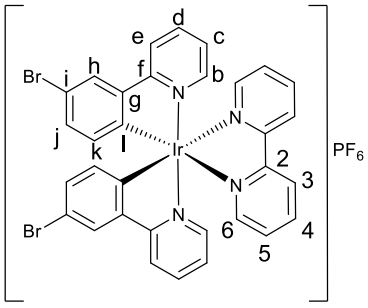
156.2 (C-7), 149.6 (C-6), 140.0 (C-2), 138.2 (C-3), 135.5 (C-10), 135.0 (C-9), 126.0 (C-8), 123.3 (C-5), 121.2 (C-4). m/z (ESI-TOF) 200.22 $[M+H]^+$

Synthesis of Ir-4-BOH



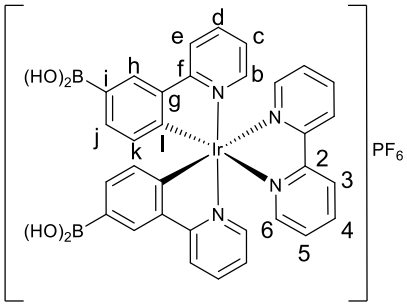
A solution of **ppy-4-BOH** (119 mg, 0.60 mmol) and $IrCl_3.H_2O$ (100 mg, 0.33 mmol), in 2-ethoxyethanol (20 mL) and H_2O (10 mL) was stirred at 100 ºC for 24 h, cooled, and the resulting precipitate was isolated by filtration. The precipitate was washed with H_2O (2 x 10 mL) and hexane (30 mL) to yield a crude iridium(III) chloro bridged dimer. The crude chloro bridged dimer (60 mg, 0.048 mmol) and 2,2'-bipyridine (16.52 mg, 0.106 mmol) were added to a round bottom flask before dry dichloromethane and methanol were added (1:3, 20 mL). The solution was heated to 60 ºC and stirring continued at this temperature for 6 h. The solution was filtered and the volume reduced *in vacuo* to 1 mL; 2 mL of methanol containing NH_4PF_6 (1 g, 6.1 mmol) was added and the product was columned (silica gel, 9:1, DCM:MeOH) before drying *in vacuo* to yield a yellow crystalline solid. (38 mg, 0.043 mmol, 43 %) ^{1}H (400 MHz, CD_3CN) ^{1}H NMR (400 MHz, CD_3CN) δ 8.51 (d, *J* = 8.1 Hz, 2H, H-3), 8.13 – 8.08 (m, 4H, H-4,e), 7.95 (ddd, *J* = 5.5, 1.7, 0.8 Hz, 2H, H-6), 7.86 (ddd, *J* = 8.2, 7.3, 1.5 Hz, 2H, H-d), 7.79 (d, *J* = 7.5 Hz, 2H, H-h), 7.62 (ddd, *J* = 5.9, 1.6, 0.8 Hz, 2H, H-b), 7.48 (ddd, *J* = 7.7, 5.5, 1.3 Hz, 2H, H-5), 7.40 (dd, *J* = 7.5, 1.2 Hz, 2H, H-i), 7.04 (ddd, *J* = 7.3, 5.9, 1.5 Hz, 2H, H-c), 6.71 (d, *J* = 1.2 Hz, 2H, H-k), 5.74 (s, 4H, BOH). λ_{max} (CH_3CN)/nm (ε/dm^3 mol^{-1} cm^{-1}) 261 (41200), 291 (27000), 307 (22200), 349 (7100), 415 (3400). *m/z* (ESI-TOF) $C_{32}H_{26}B_2N_4O_4Ir$ Calcd: 745.1768, Found: 745.1769, elemental analysis Calc (%). $C_{32}H_{26}B_2IrN_4O_4PF_6(NH_4PF_6)_{0.25}$: C, 41.32, H, 2.93, N, 6.40, Found: C, 40.94; H, 3.13; N, 6.53.

Synthesis of Ir-3-Br



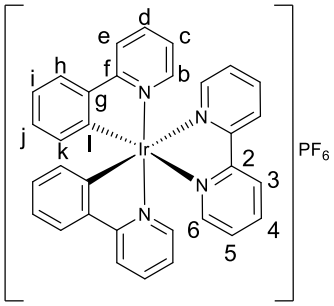
To 2-(3-bromophenyl)pyridine (500 mg, 2.1 mmol) and $IrCl_3.H_2O$ (250 mg, 0.8 mmol) was added 2-ethoxyethanol (20 mL) and water (10mL), the mixture was heated at 100 ^oC for 24 h, cooled and the resulting yellow precipitate filtered. The solid was washed with water and dried *in vacuo* to yield a yellow chloro-bridged dimer which was used without further purification (400 mg). The crude chloro bridged dimer (200 mg) was added to an argon flushed RBF containing 2,2'-bipyridine (45.1 mg, 0.29 mmol). Methanol (15mL) and DCM (5mL) were added and the mixture heated to 60 ^oC for 6 h, before cooling and reducing the volume to 2 mL. NH_4PF_6 in 2 mL of MeOH (1 g, 6.13 mmol) was added and the resulting precipitate filtered and washed with water (5 mL) and diethyl ether (10 mL). The solid was dried to yield Ir-3-Br as a yellow powder (180 mg, 0.19 mmol, 66%) ^{1}H NMR (400 MHz, DMSO-d_6) δ 8.90 (d, *J* = 8.0 Hz, 2H, H-3), 8.41 (dt, *J* = 8.0, 1.1 Hz, 2H, H-e), 8.30 (td, *J* = 8.0, 1.5 Hz, 2H, H-4), 8.17 (d, *J* = 2.1 Hz, 2H, H-h), 7.98 (td, *J* = 8.0, 1.0 Hz, 2H, H-d), 7.91 (dd, *J* = 5.4, 1.4 Hz, 2H, H-6), 7.72 (ddd, *J* = 7.9, 5.4, 1.3 Hz, 2H, H-5), 7.67 – 7.61 (dd, *J* = 5.8, 1.0 Hz, 2H, H-b), 7.21 (ddd, *J* = 7.6, 5.8, 1.1 Hz, 2H, H-c), 7.09 (dd, *J* = 8.1, 2.1 Hz, 2H, H-j), 6.08 (d, *J* = 8.1 Hz, 2H, H-k). ^{13}C NMR (101 MHz, DMSO-d_6) δ 165.61 (C-f), 155.73 (C-2), 150.55 (C-6), 149.63 (C-b), 149.02 (C-g), 146.85 (C-l), 140.36 (C-4), 139.67 (C-d), 133.44 (C-k), 133.15 (C-j), 129.37 (C-5), 128.02 (C-h), 125.58 (C-3), 125.29 (C-c), 121.33 (C-e), 116.23 (C-i). *m/z* (ESI-TOF) 815.10 $[M]^+$

Synthesis of Ir-3-BOH



DMSO (6 mL) containing **Ir-3-Br** (82 mg, 0.1 mmol) was added to $PdCl_2$(dppf) (22 mg, 0.03 mmol), KOAc (29.4 mg, 0.3 mmol), and Bis(pinacolato)diboron (27.9 mg, 0.1 mmol), and stirred at 80 °C for 18 h, the product was precipitated with H_2O (10 mL) and isolated by filtration. The precipitate was dissolved in MeOH (2 mL), and NH_4PF_6 (100 mg, 0.6 mmol) added, before evaporating to dryness and washing with H_2O (3mL). The product was re-dissolved in acetone (5 mL) and water (5 mL), and added to a RBF. To the aqueous solution was added $NaHCO_3$ (150 mg, 1.8 mmol), and the mixture stirred for 2 h at 40 ºC. The product was extracted by washing the aqueous layer with dichloromethane containing 1% TFA (2 x 10 mL). The organic layer was evaporated to dryness, re-dissolved in methanol (2 mL), NH_4PF_6 (100 mg, 0.6 mmol) was added and the resulting precipitate filtered and washed with water (5 mL) and diethyl ether (10 mL). The product was purified by neutral alumina TLC (96:4, DCM:MeOH), before drying in vacuo to yield **Ir-3-BOH** as a yellow powder (3 mg, 3.4 μmol, 3 %). ^{1}H NMR (300 MHz, DMSO-d_6) δ 8.91 (d, J = 8.0 Hz, 2H, H-3), 8.35 (s, 2H, H-h), 8.28 (t, J = 8.0 Hz, 2H, H-4), 8.20 (d, J = 8.1 Hz, 2H, H-e), 7.98 (t, J = 8.1 Hz, 2H, H-d), 7.91 (s, 4H, B(OH)2), 7.86 (d, J = 5.9 Hz, 2H H-6), 7.70 (t, J = 6.0 Hz, 2H, H-5), 7.62 (d, J = 5.9 Hz, 2H, H-b), 7.28 (d, J = 7.5 Hz, 2H, H-j), 7.17 (t, J = 6.0 Hz, 2H, H-c), 6.19 (d, J = 7.6 Hz, 2H, H-k). λ_{max} (CH_3CN)/nm (ε/dm^3 mol^{-1} cm^{-1}) 257(40700), 265(39700), 310(18200), 339sh(7600). *m/z* (ESI-TOF) 787.10 $[M+3Me-3H]^+$

Ir-ppy



This synthesis was adapted from Ohsawa *et al.*[15] $Ir(ppy)_2Cl$ (30 mg, 0.03 mmol) and 2,2'-bipyridine (10 mg, 0.06 mmol) were added to an argon flushed Schlenk flask containing DCM:MeOH (3:1, 20 mL) and the solution stirred at room temperature for 12 h. To the solution was added NH_4PF_6 (1 g in 2 mL MeOH), and the solution stirred at room temperature for 15 min, before reduction in volume to 3 mL. The solution was subjected to column chromatography (silica gel, DCM:MeOH, 97:3) to yield $Ir(ppy)_2bpy$ as yellow crystalline powder (32 mg, 0.04 mmol, 68 %) NMR data matches that previously reported.[125] ^1H (400 MHz, CD_3CN) δ 8.58 (d, *J* = 8.0, 2H, H-3), 8.13 (td, *J* = 8.0, 1.6 Hz, 2H, H-4), 8.06 (d, *J* = 7.9 Hz, 2H, H-e), 7.98 (ddd, *J* = 5.5, 1.6, 0.7 Hz, 2H, H-6), 7.83 (ddd, *J* = 8.1, 7.0, 1.6 Hz, 2H, H-d) 7.80 (dd, *J* = 7.7, 1.3 Hz, 2H, H-k), 7.60 (ddd, *J* = 5.8, 1.6, 0.7 Hz, 2H, H-b), 7.50 (ddd, *J* = 8.0, 5.4, 1.1 Hz, 2H, H-5), 7.09 – 6.99 (m, 4H, H-c, H-j), 6.91 (td, *J* = 7.5, 1.4 Hz, 2H, H-i), 6.28 (dd, *J* = 7.5, 0.8 Hz, 2H, H-h). ^{13}C NMR (101 MHz, CD_3CN) δ 168.3 (C-f), 156.8 (C-2), 151.5 (C-6), 151.3 (C-l), 150.1 (C-b), 145.0 (C-g), 140.3 (C-4), 139.5 (C-d), 132.4 (C-h), 131.3 (C-i), 129.3 (C-5), 125.8 (C-k), 125.7 (C-3), 124.4 (C-c), 123.5 (C-j), 120.8 (C-e). λ_{max} (CH_3CN)/nm (ε/dm^3 mol^{-1} cm^{-1}) 254(44800), 265 (43300), 310 sh(19800), 375 sh(5600), 410 sh(3300). *m/z* (ESI-TOF) 657.17 $[M]^+$.

Synthesis of Hydrogel

2-Hydroxyethyl methacrylate (900 mg, 6.9 mmol), di(ethyleneglycol) dimethacrylate (50 mg, 0.3 mmol), 2-hydroxy-2-methylpropiophenone (20 mg, 0.1 mmol) were added to 1mL of DMSO, to which was added 50 μL of a 3.5 mM (0.2 μmol) solution of **Ir-4-BOH** or **Ir-ppy** in DMSO. The solution was stirred for 5 mins and then placed under a UV-crosslinker for 1 minute. Once set, the gel was cut out of the mould and transferred to a 2-sided cuvette.

Derivation of quadratic binding formula

In a regular 1:1 host guest system where A represents the host, and B the guest:

$$K = \frac{[AB]}{[A][B]} \quad (1)$$

$$[A]=[A]_0-[AB] \quad (2)$$

$$[B]=[B]_t-[AB] \quad (3)$$

$[B]_t$ is used to donate B as this parameter is changing throughout the experiment. And therefore $[B]_t \neq [B]_0$

$$K= \frac{[AB]}{([A]_0-[AB])([B]_t-[AB])} \quad (4): (2) \text{ and } (3) \text{ into } (1)$$

$$K[A]_0[B]_t-(K[A]_0[AB]-K[B]_t[AB]-[AB])+K[AB]^2 = 0 \quad (5): \text{rearrange } (4)$$

If one were to solve for a quadratic equation: $x = \frac{-b \pm \sqrt{b^2-4ac}}{2a}$

$$[AB]= \frac{1}{2}\left([A]_0+[B]_t+ \frac{1}{K}\right) \pm \frac{1}{2}\sqrt{\left([A]_t+[B]_t+\frac{1}{K}\right)^2 - 4[A]_0[B]_t} \quad (6): (5) \text{ solved}$$

Molar fraction of A can be defined as $f_A = \frac{[A]}{[A]+[AB]}$ (7)

So $f_A = \frac{[A]_0 - [AB]}{[A]_0}$ (8): (2) into (7)

If the same steps are applied to mole fraction of [AB]

$f_{AB} = \frac{[AB]}{[A]_0}$ (9)

Since $I_{obs} = I_A f_A + I_{AB} f_{AB}$ (10)

$I_{obs} = I_A \frac{[A]_0 - [AB]}{[A]_0} + I_{AB} \frac{[AB]}{[A]_0}$ (11): (8) and (9) into (10)

$I_{obs} = I_A + (I_{AB} - I_A) \frac{[AB]}{[A]_0}$ (12): (11) Simplified

Since when equilibrium is reached $I_{AB} - I_A = \Delta I_{max}$ (13)

$I_{obs} = I_A + \Delta I_{max} \frac{[AB]}{[A]_0}$ (14)

$$I_{obs} - I_A = \Delta I_{max} \frac{[AB]}{[A]_0}$$ (15): (14) rearranged

Substitution into the equation (6) yields (16) below:

$$I_{obs} - I_A = \frac{\Delta I_{max}}{[A]_0}\left(\frac{1}{2}\left([A]_0 + [B]_t + \frac{1}{K}\right) \pm \frac{1}{2}\sqrt{\left([A]_0 + [B]_t + \frac{1}{K}\right)^2 - 4[A]_0[B]_t}\right)$$

When using Kaleidagraph one must use the syntax and create a binding curve based upon the following script.

y = m1/(2*[A]$_0$)*((m0+[A]$_0$+1/m2)-((m0+[A]$_0$+1/m2)^2 – 4*[A]$_0$*m0)^(1/2))

where:

y = $I_{obs} - I_A = \Delta I$

m1 = ΔI_{max}

m2 = K

m0 = $[B]_t$ (equal to amount added of guest)

5.1.2 Supplementary Information

NMR spectra

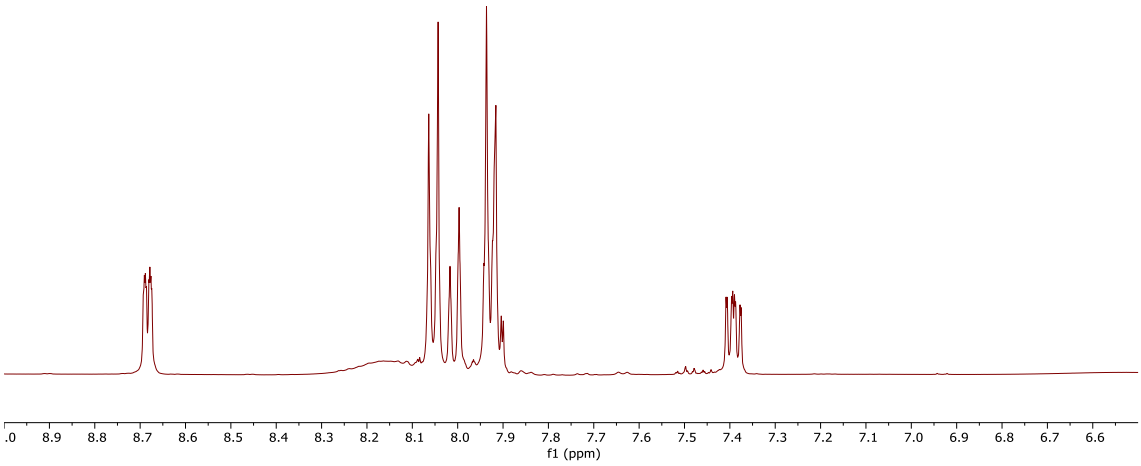


Figure S2.1: 400 MHz ^{1}H NMR of **ppy-4-BOH** in DMSO-d_6

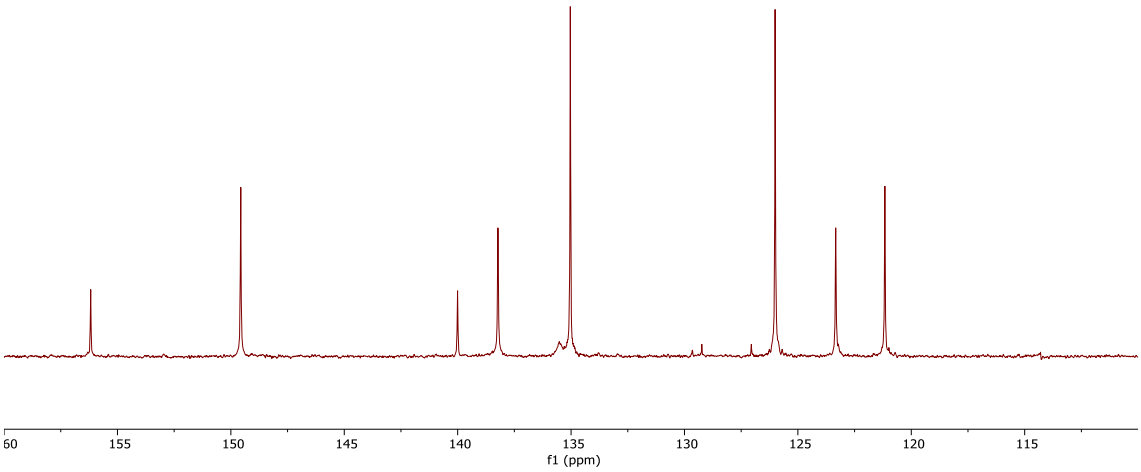


Figure S2.2: 101 MHz ^{13}C NMR of **ppy-4-BOH** in DMSO-d_6

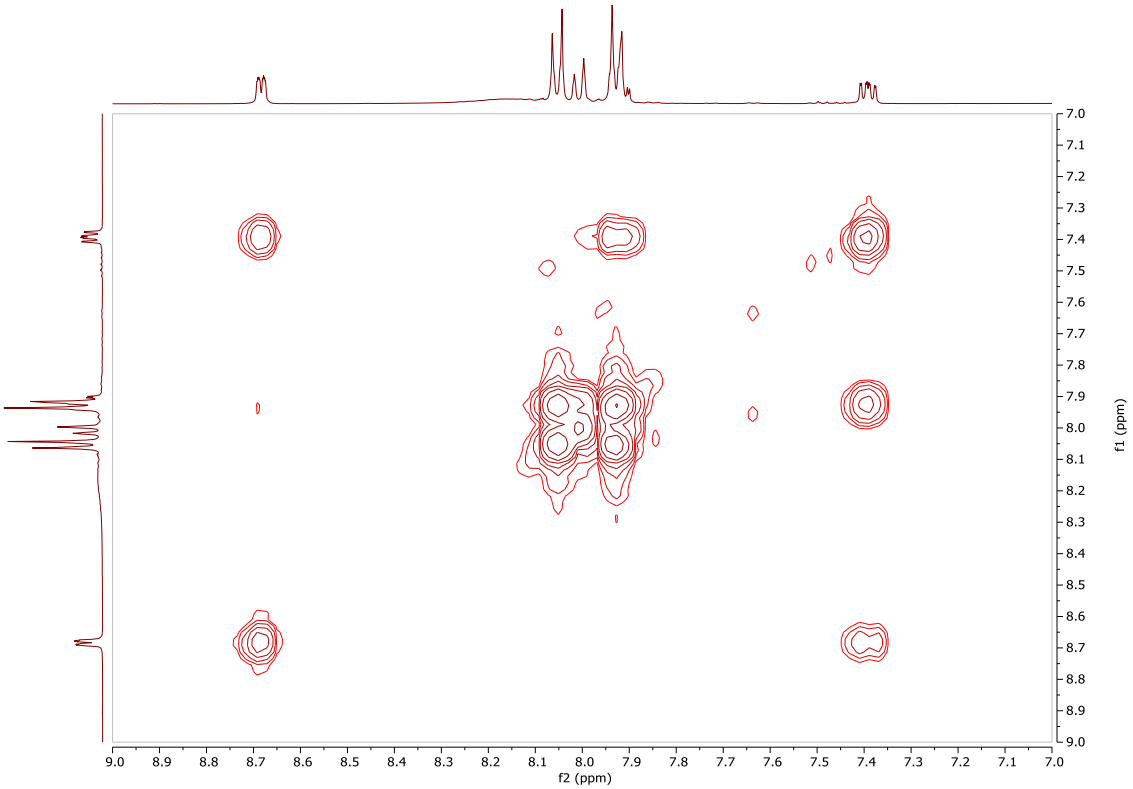


Figure S2.3: 2D COSY spectrum of **ppy-4-BOH** in DMSO-d_6

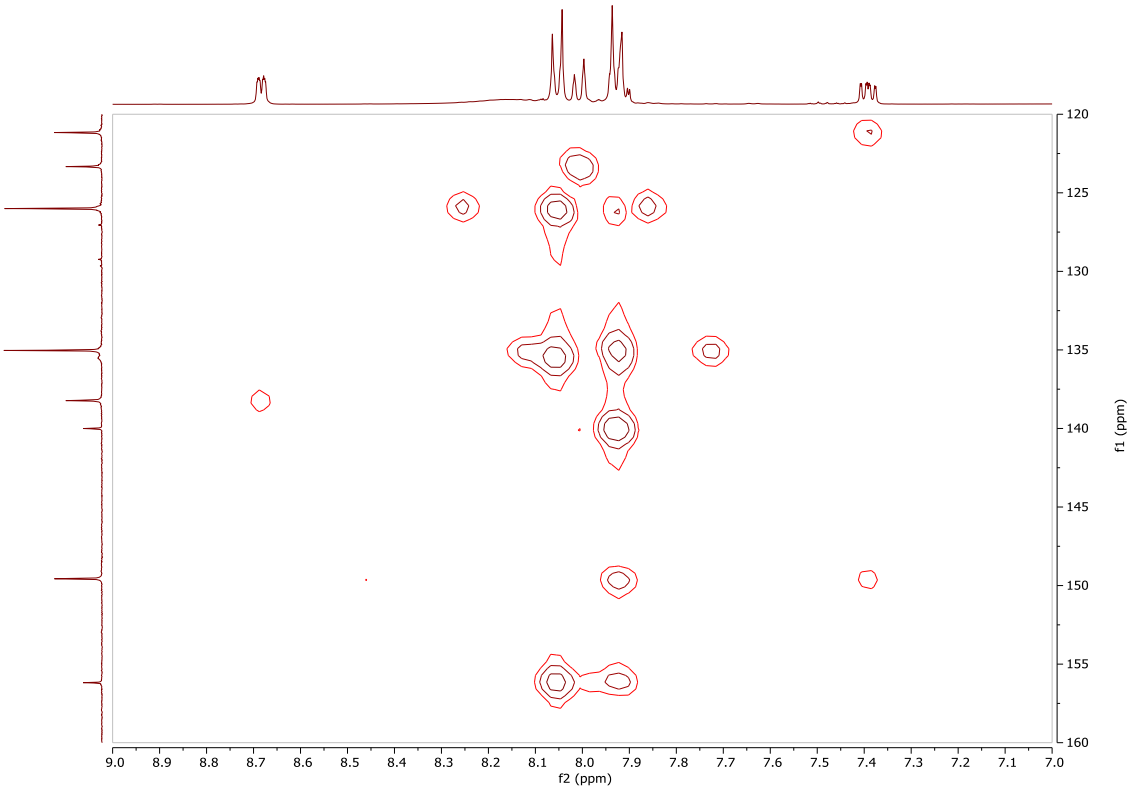


Figure S2.4: 2D ^{1}H-^{13}C HSQC spectrum of **ppy-4-BOH** in DMSO-d_6

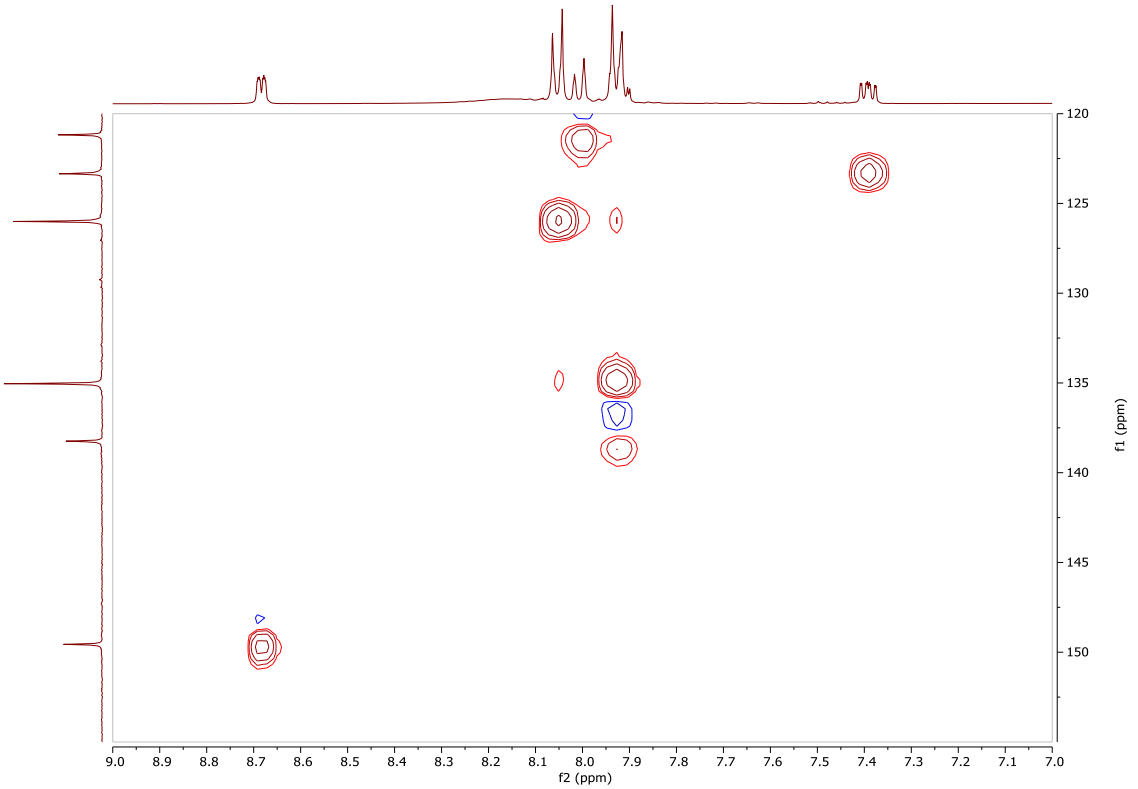


Figure S2.5: 2D ^{1}H-^{13}C HMBC NMR of **ppy-4-BOH** in DMSO-d_6

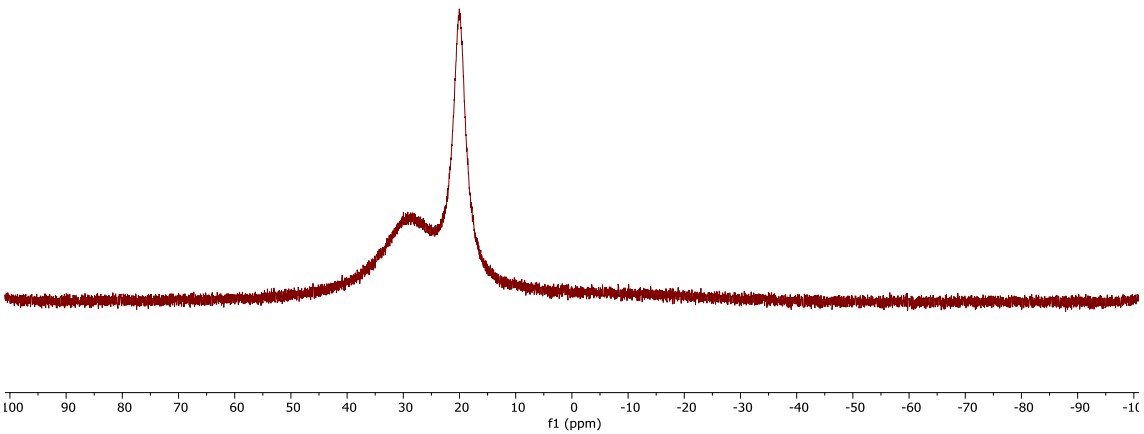


Figure S2.6: ^{11}B NMR spectrum of **ppy-4-BOH** in DMSO-d_6

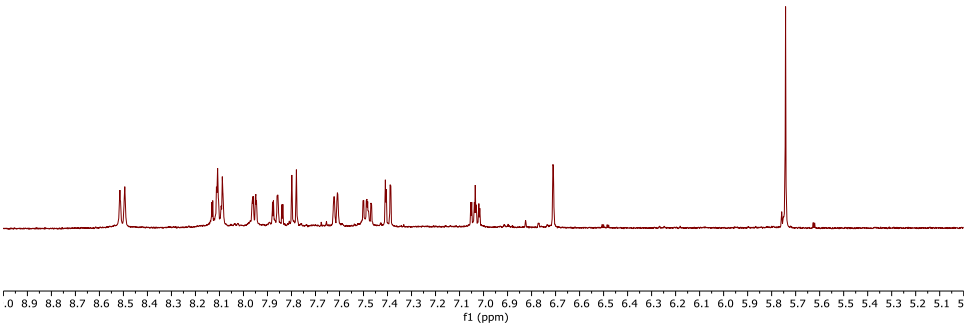


Figure S2.7: 400 MHz ^{1}H NMR of **Ir-4-BOH** in CD_3CN

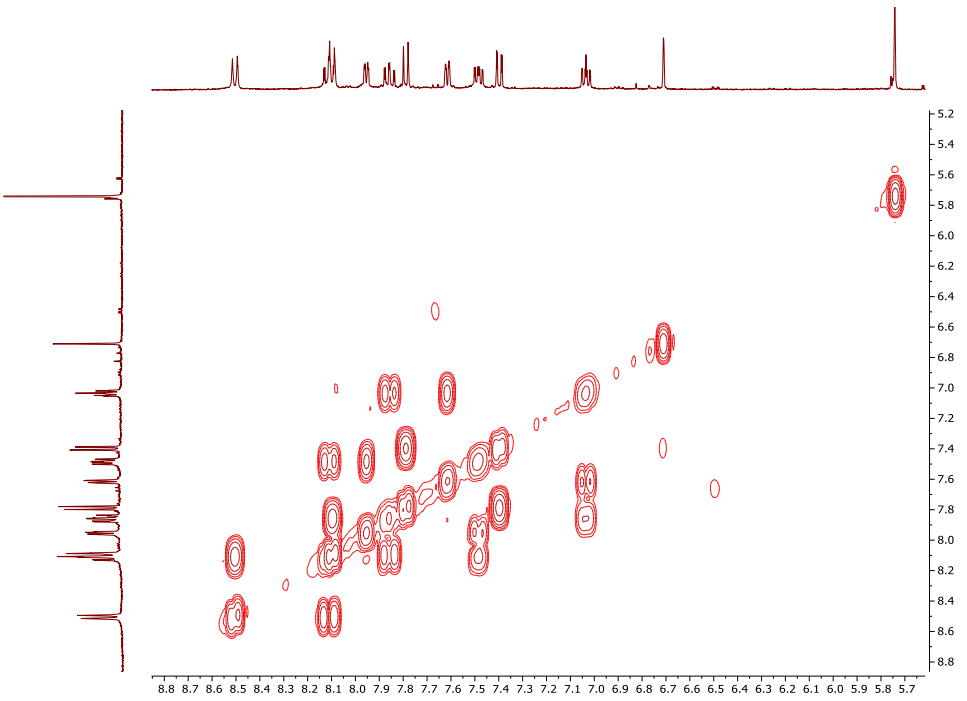


Figure S2.8: 2D COSY spectrum of **Ir-4-BOH** in CD_3CN

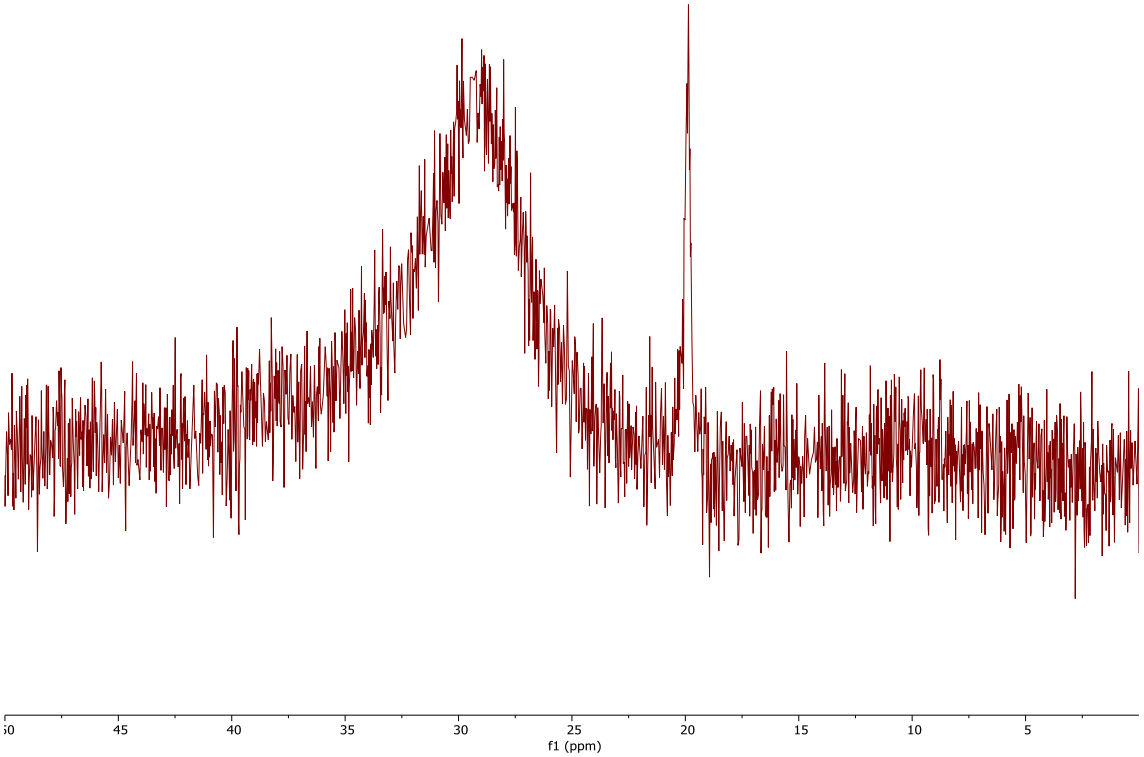


Figure S2.9: 128 MHz ^{11}B NMR of **Ir-4-BOH** in CD_3CN

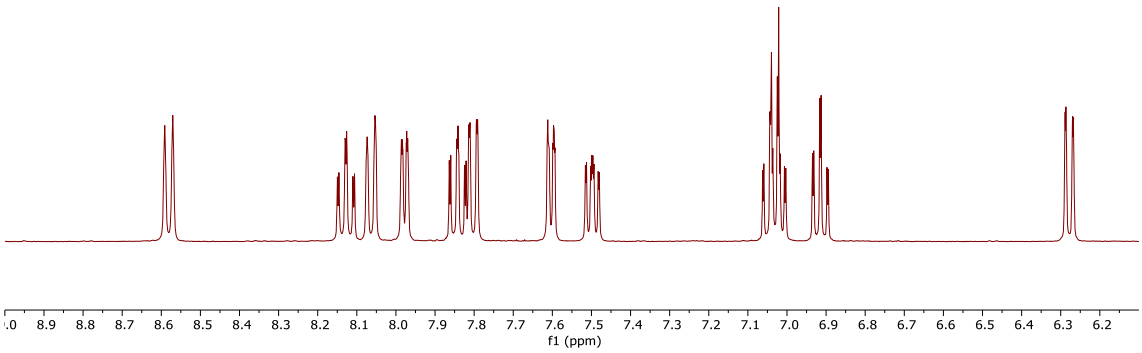


Figure S2.10: 400 MHz ^{1}H NMR of **Ir-ppy** in CD_3CN

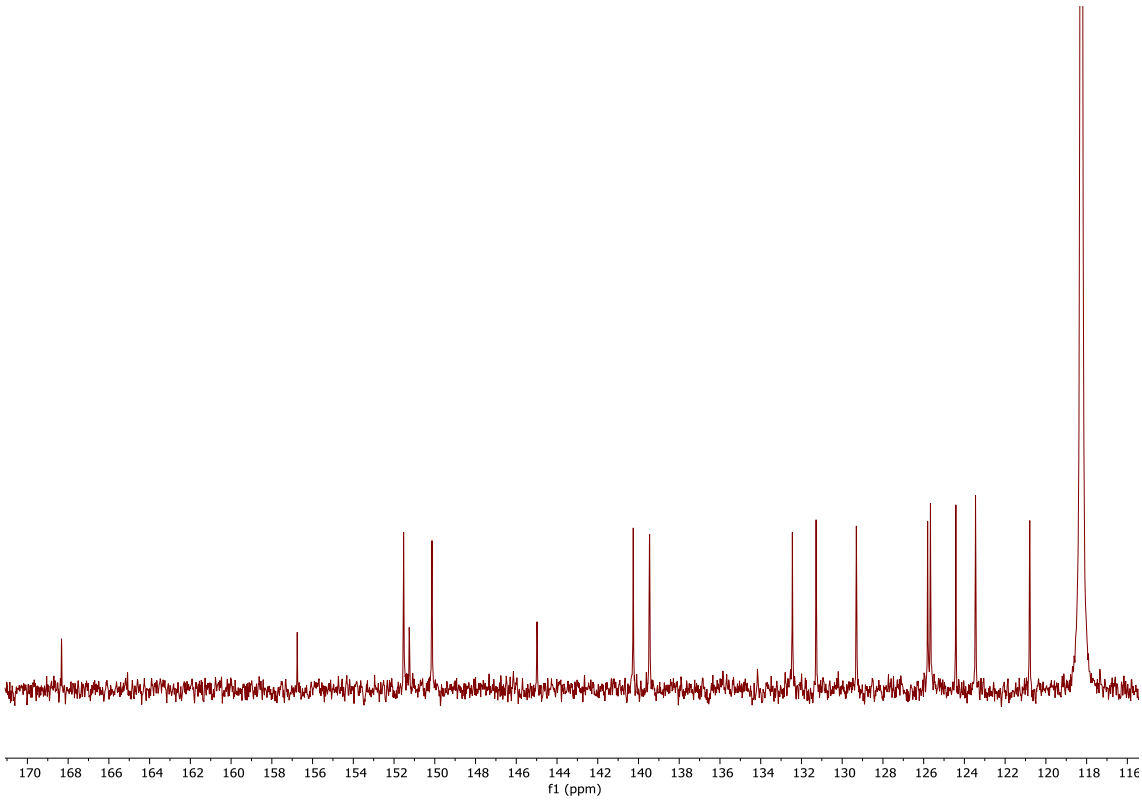


Figure S2.11: 101 MHz ^{13}C NMR of **Ir-ppy** in CD_3CN

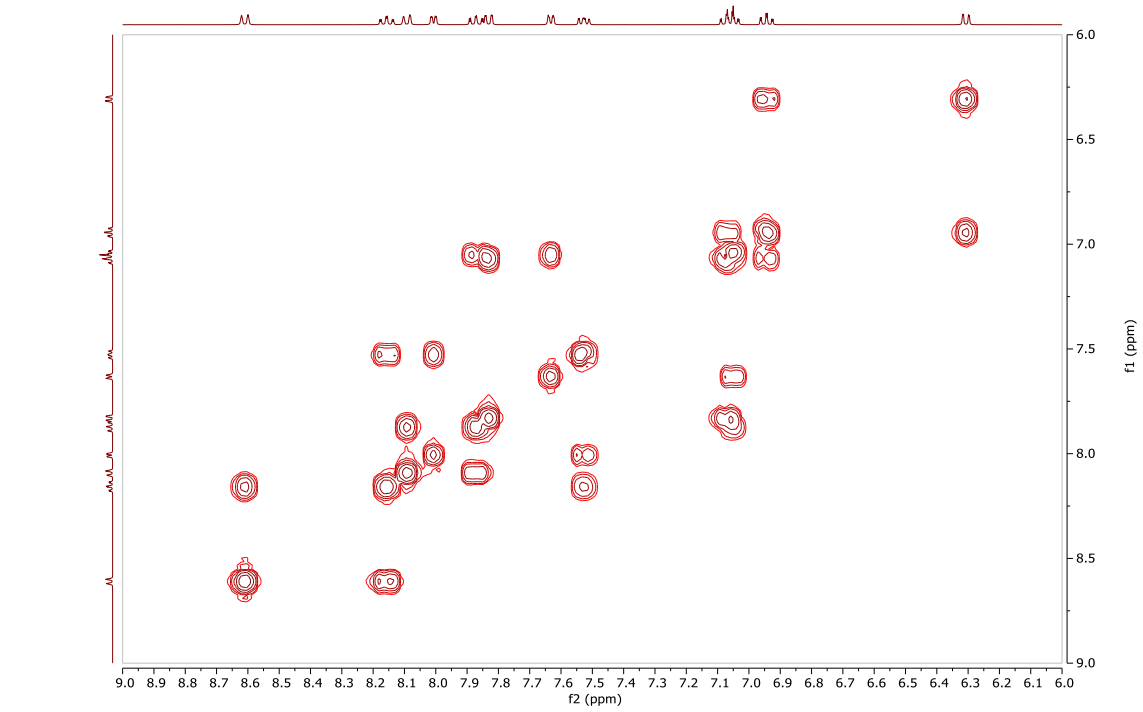


Figure S2.12: 2D ^{1}H COSY NMR of **Ir-ppy** in CD_3CN

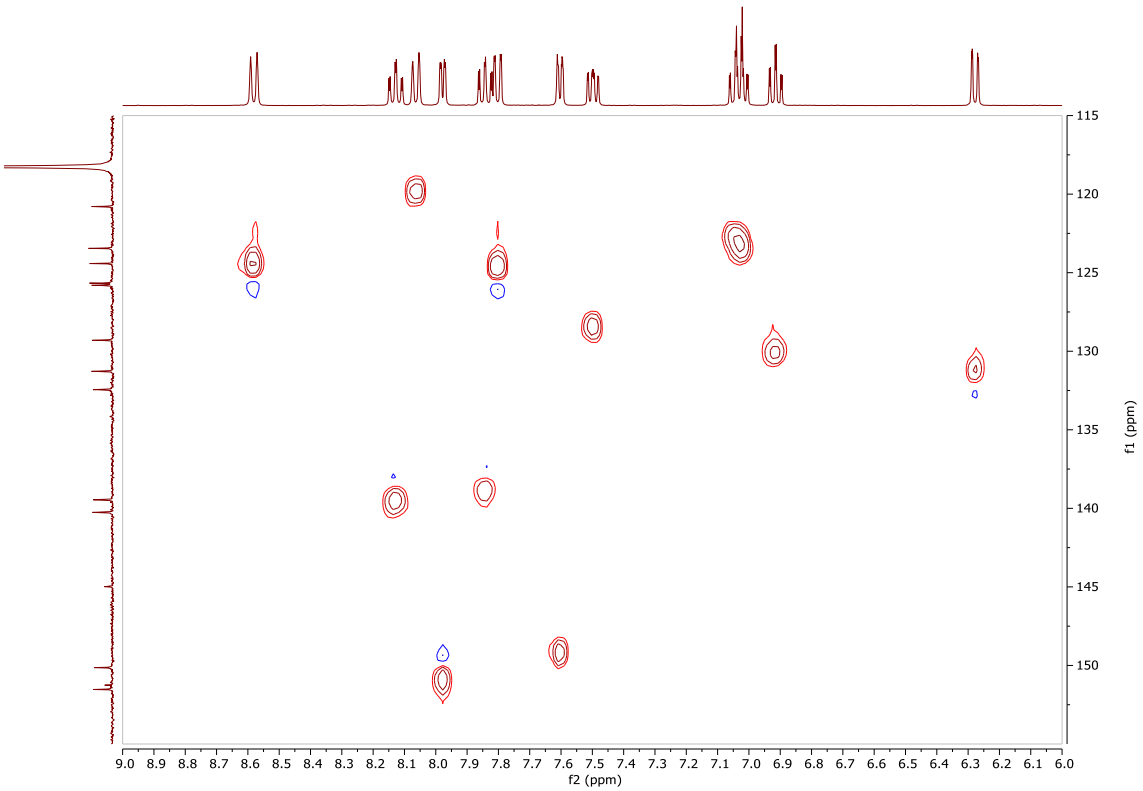


Figure S2.13: 2D ^{1}H-^{13}C HSQC NMR of **Ir-ppy** in CD_3CN

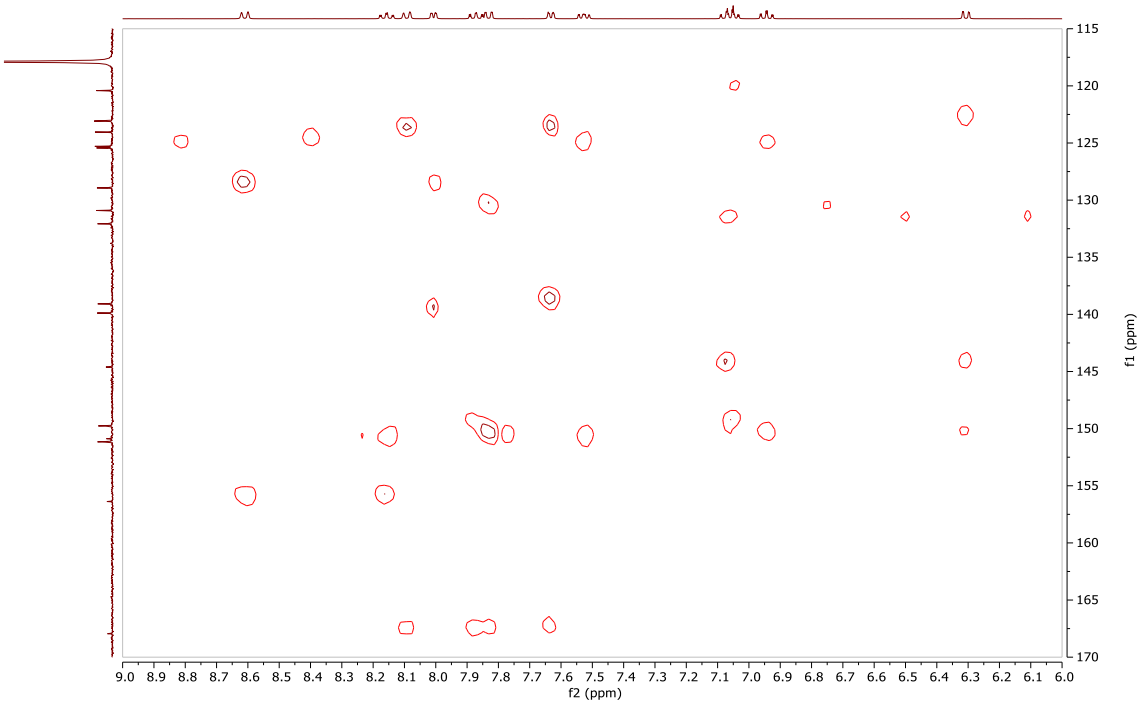


Figure S2.14: 2D ^{1}H-^{13}C HMBC NMR of **Ir-ppy** in CD_3CN

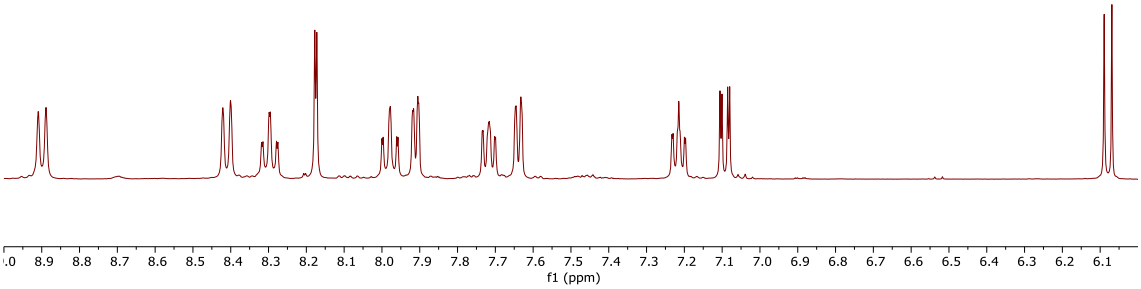


Figure S2.15: 400 MHz ^{1}H NMR of **Ir-3-Br** in DMSO-d_6

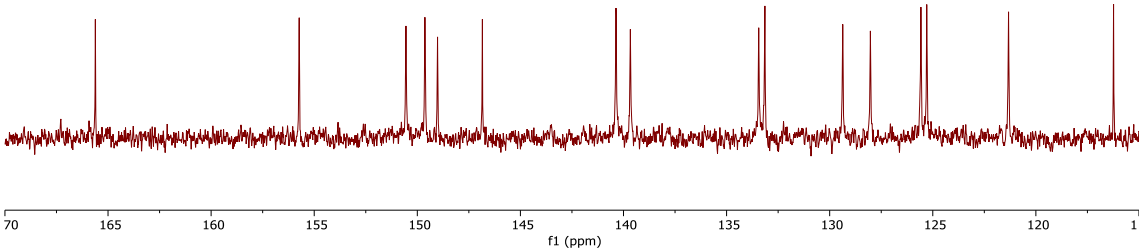


Figure S2.16: 101 MHz ^{13}C NMR of **Ir-3-Br** in DMSO-d_6

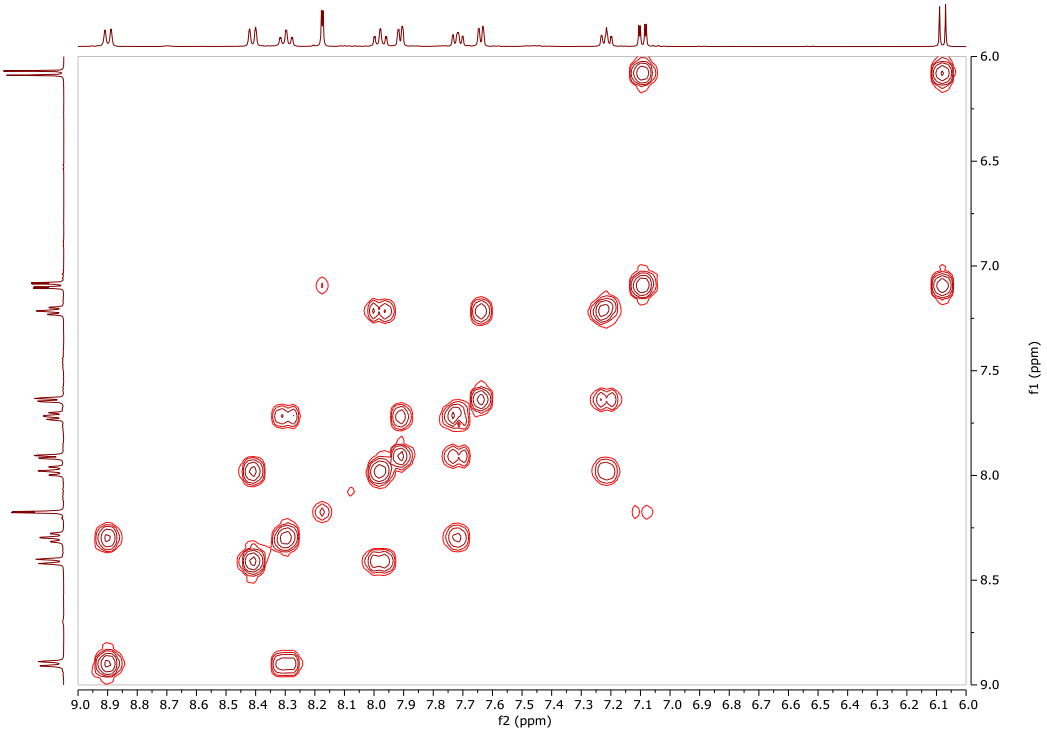


Figure S2.17: 2D COSY NMR of **Ir-3-Br** in DMSO-d_6

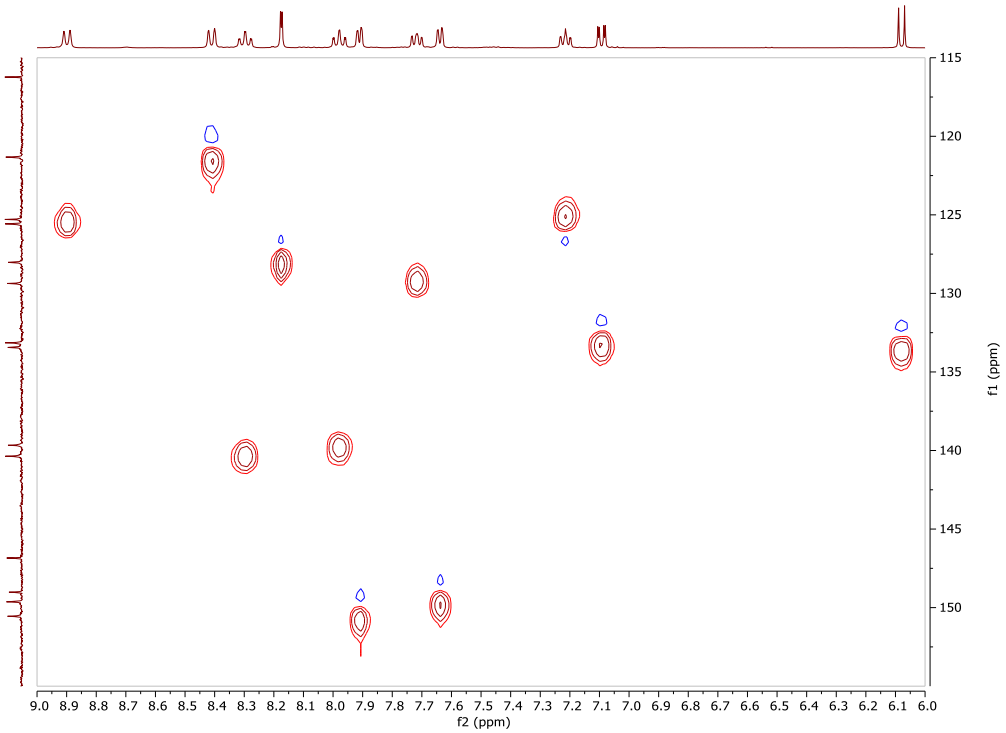


Figure S2.18: 2D ^{1}H-^{13}C HSQC NMR of **Ir-3-Br** in DMSO-d_6

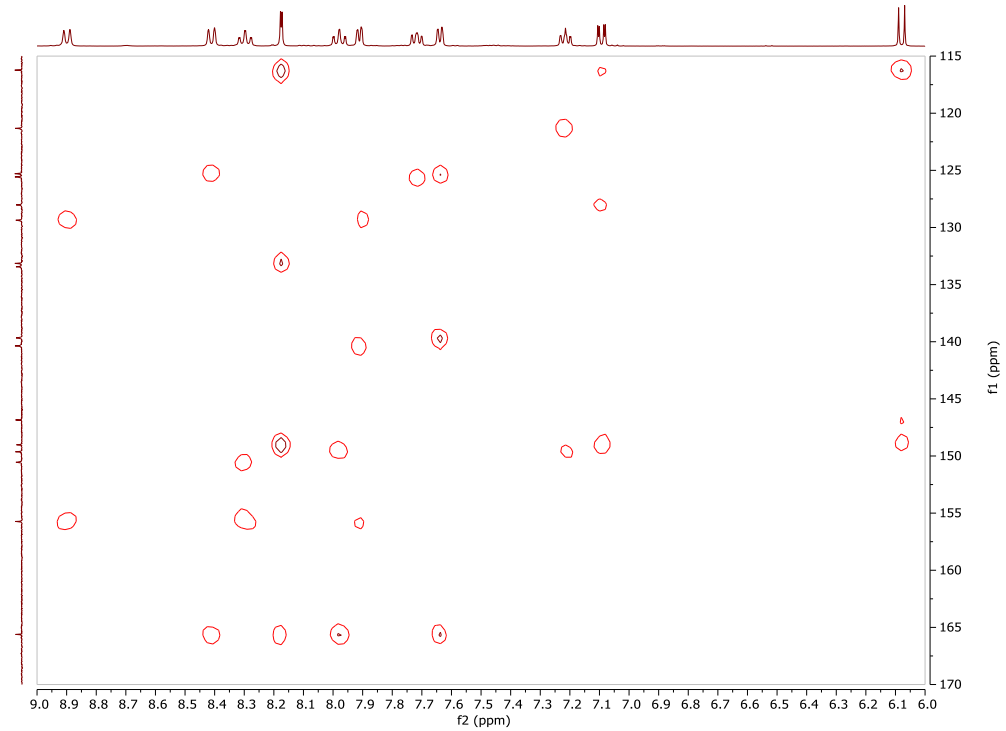


Figure S2.19: 2D ^{1}H-^{13}C HMBC NMR of **Ir-3-Br** in DMSO-d_6

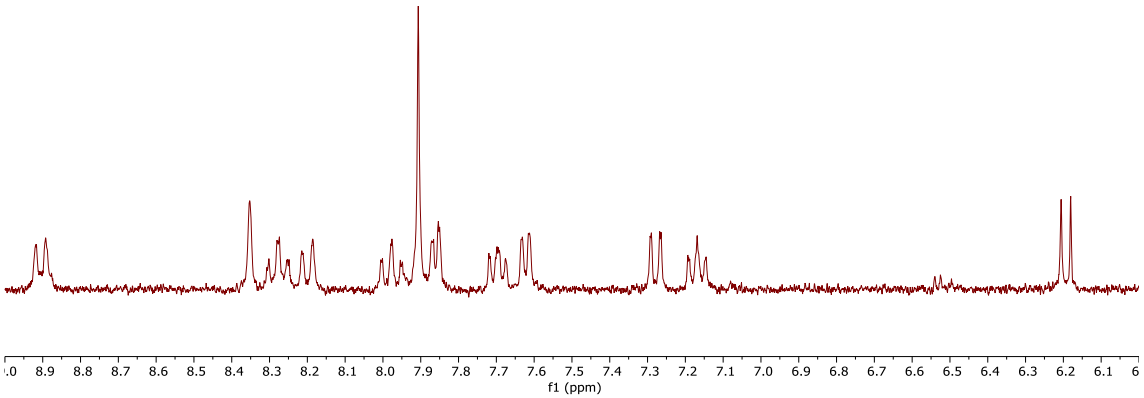


Figure S2.20: 300 MHz ^{1}H NMR of **Ir-3-BOH** in DMSO-d_6

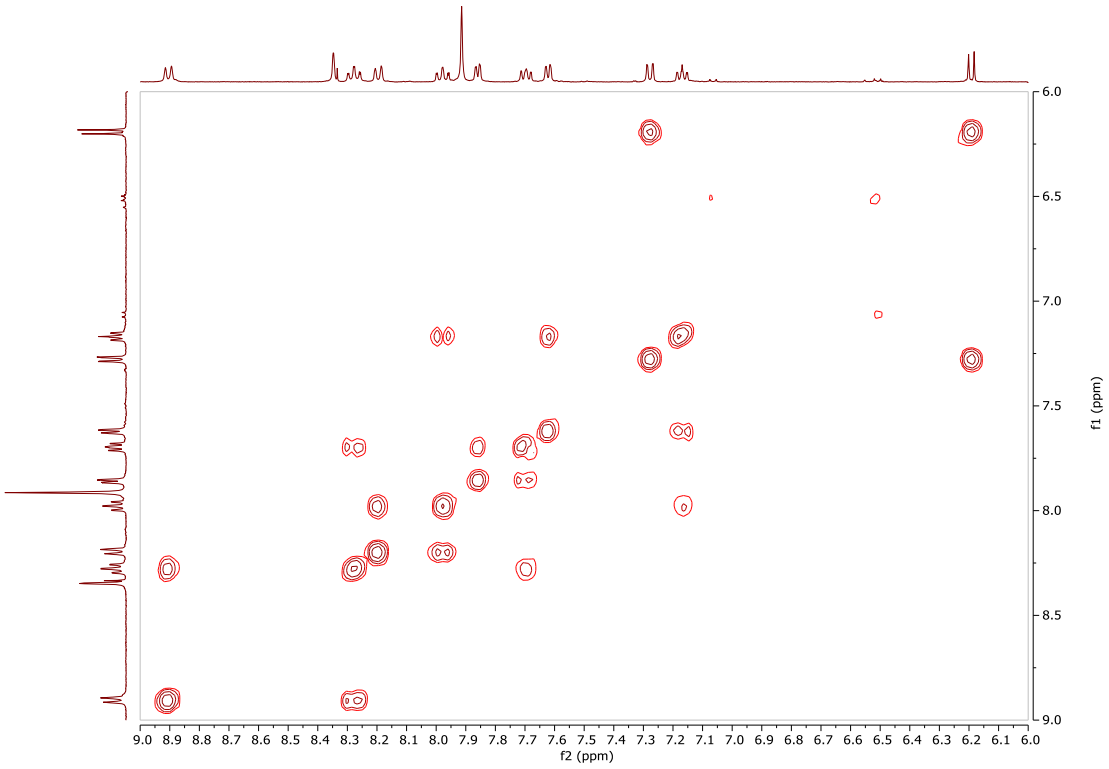


Figure S2.21: 2D COSY NMR of **Ir-3-BOH** in DMSO-d_6

Mass Spectra

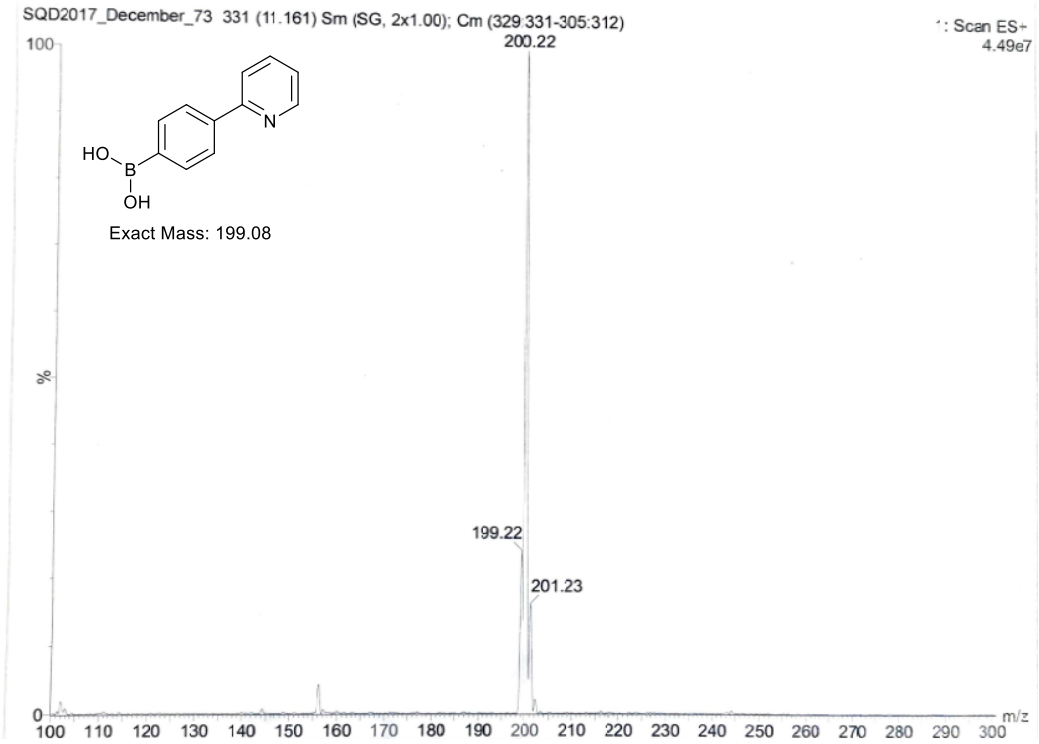


Figure S2.22: ESI-MS spectrum (positive mode) of **ppy-4-BOH** in MeOH

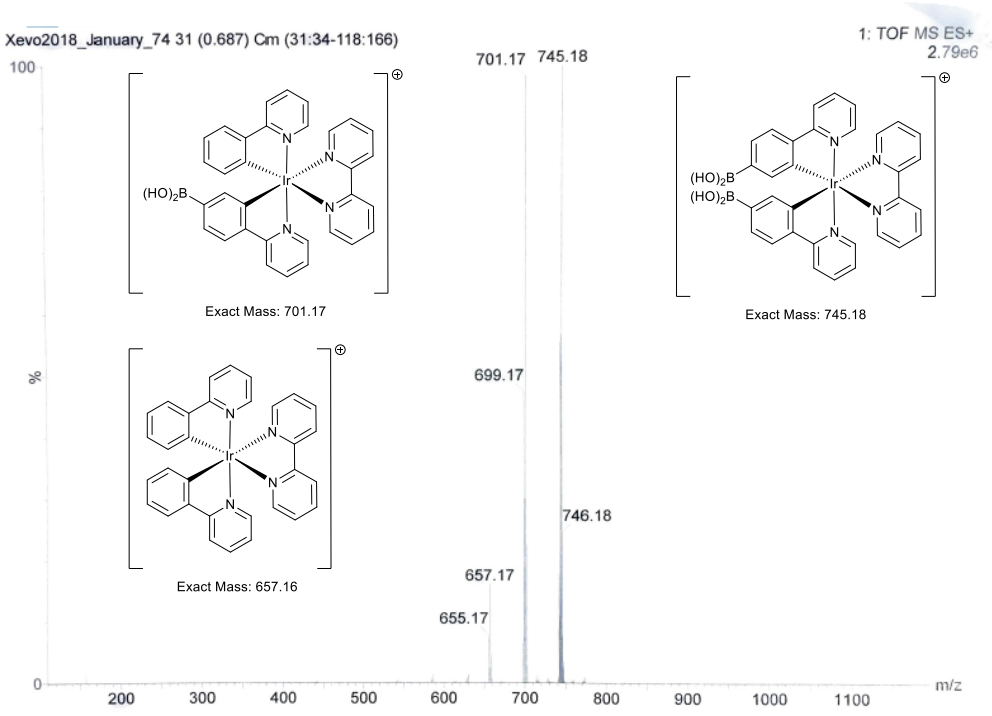


Figure S2.23: ESI-MS spectrum (positive mode) of **Ir-4-BOH** in MeCN with structures of all observed ionised species displayed with structures and masses.

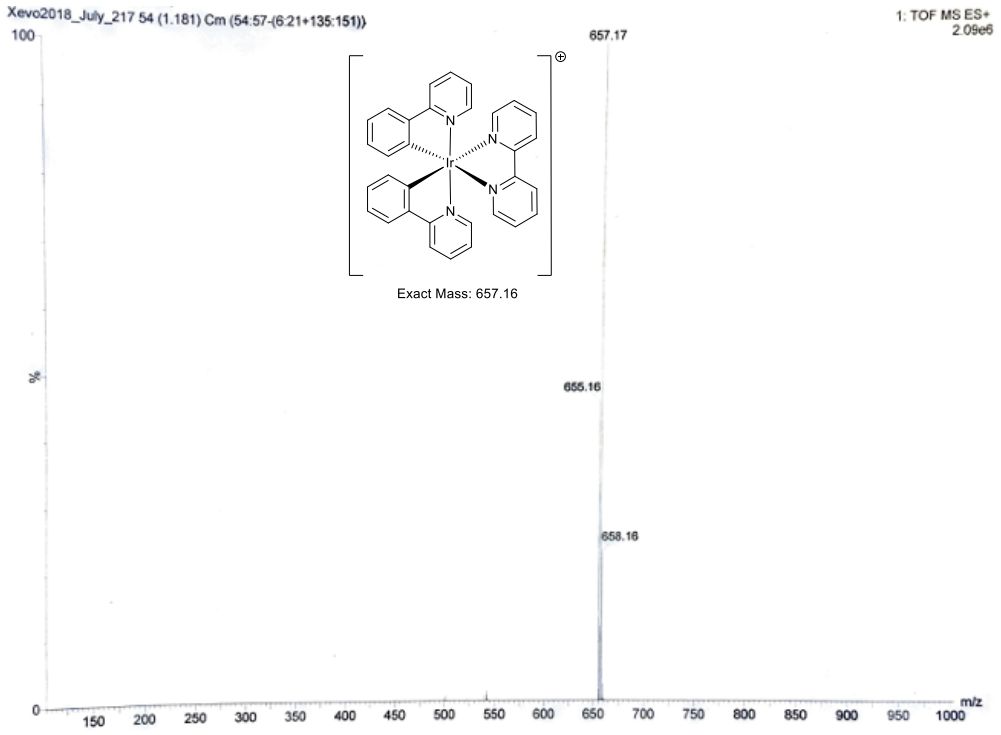


Figure S2.24: ESI-MS spectrum (positive mode) of **Ir-ppy** in MeCN with observed ionised species shown

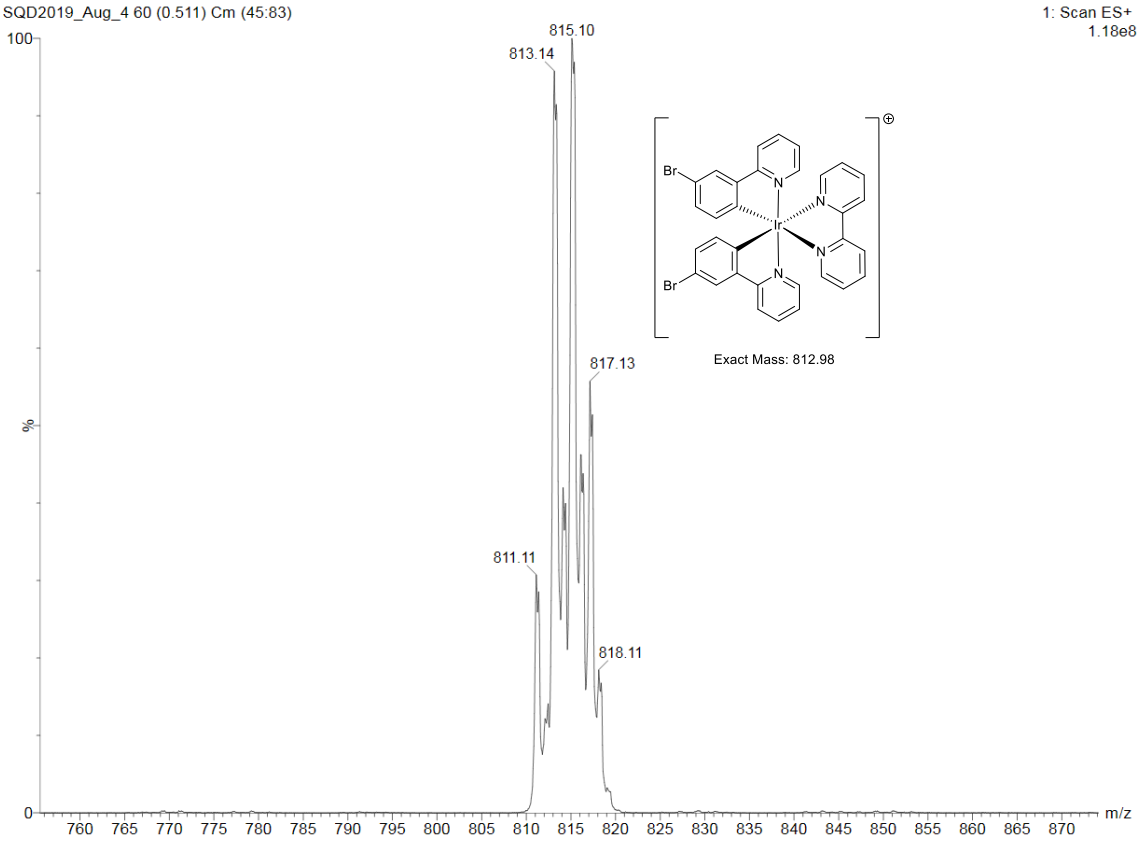


Figure S2.25: ESI-MS spectrum (positive mode) of **Ir-3-Br** in MeOH with observed ionised species shown

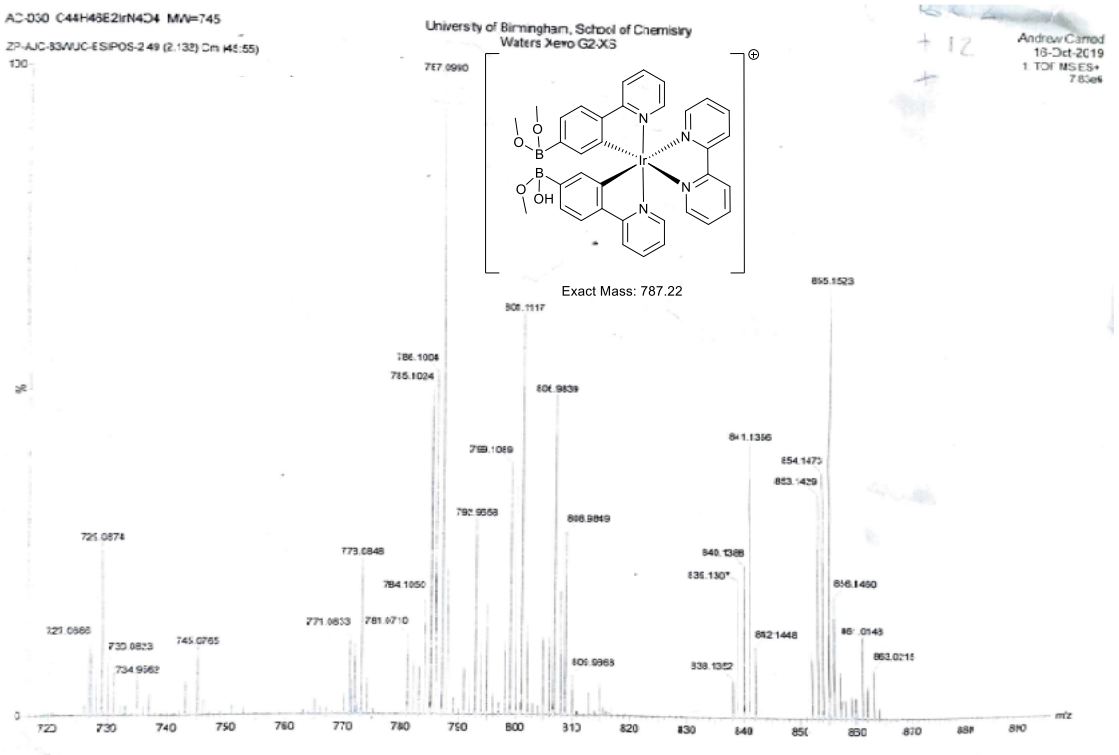


Figure S2.26: ESI-MS spectrum (positive mode) of **Ir-3-BOH** in MeCN with main ionised species shown

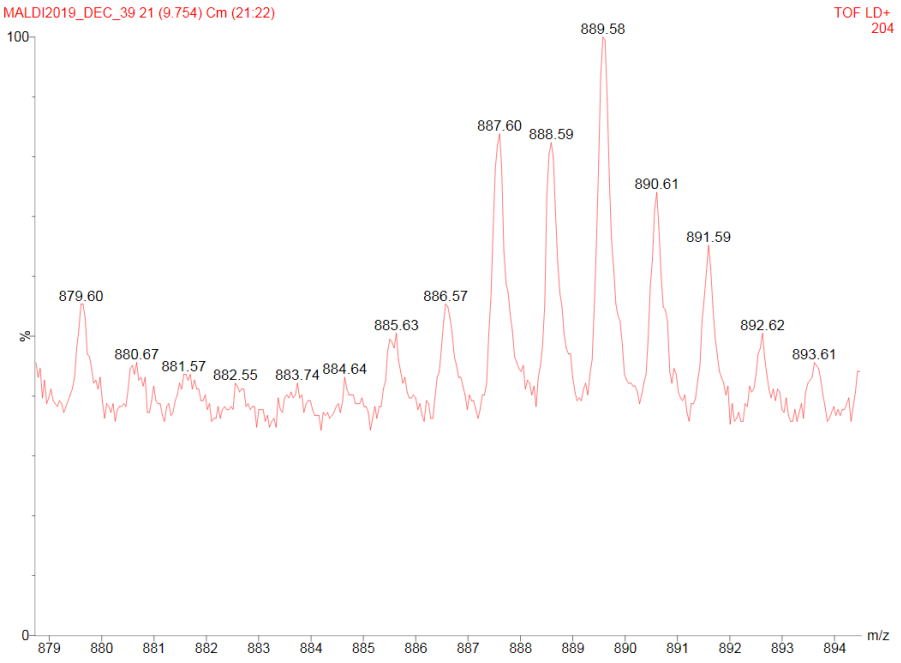


Figure S2.27: MALDI-TOF spectrum (positive mode) of a solution of **Ir-3-BOH** (4 μM) with glucose (50 mM)

5.2 Experimental and Supplementary Information for Chapter 3: Sensing of Environmentally Harmful Fluorosurfactant via Luminescent Lifetime Augmentation of a Cyclometalated Ir(III) Complex in Solution and Immobilised on Gold.

5.2.1 Experimental

5.2.1.1 Materials and Methods.

Starting materials were obtained from Sigma-Aldrich, Fluka, Fisher Scientific, or Acros Chemicals and used without any further purification. Gold slides (30 nm on silicon with 5 nm Ti priming layer) were purchased from Georg Albert PVD, Germany. Flash column chromatography was performed using LC60A 40−63 μm silica gel or activated, neutral, Brockmann I grade alumina. All reactions were performed under an argon atmosphere unless stated otherwise. 4,4′-Dihydroxy-2,2′-bipyridine was prepared by the method of Gorman *et al.*, bpySS was synthesised according to earlier procedures, and the synthesis of 2-(hexyl)-phenylpyridine and 2-(dodecyl)-phenylpyridine was based upon Ackermann et. al.[144]

^{1}H, ^{13}C and 2D NMR spectroscopy was carried out on a Bruker AVANCE NEO 400 NMR spectrometer (^{1}H: 400 MHz, ^{13}C: 101 MHz), ^{1}H and ^{13}C assignments were confirmed by COSY, HSQC and HMBC spectra. Electrospray mass spectrometry was carried out on a Waters Micromass Q-TOF. XPS studies were carried out at the EPSRC national facility at Harwell on a kratos Kα instrument.

UV−Visible spectra were collected using 1 cm path length polished quartz cuvettes on an Agilent Cary 50, 60, or 5000 spectrophotometer. Steady state emission spectra were recorded on an Edinburgh Instruments FLS920 steady state and time-resolved spectrometer fitted with an Olympus IX71 inverted microscope. The detection system used an incorporated R928

(visible) Hamamatsu photomultiplier tube. The emission monochromator is fitted with two interchangeable gratings blazed at 500 and 1200 nm. F900 spectrometer analysis software was used to record the data, and all spectra were corrected for PMT and instrument response. Luminescent lifetimes were recorded with an Edinburgh Instruments EPL-375 laser as an excitation source and fitted using Edinburgh Instruments FAST software with errors of ± 10%. Argon was used to degas samples by bubbling through the solution inside a cuvette fitted with a tight sealed septum for 15 min. Quantum yield measurements were taken using an integrating sphere attachment supplied by Edinburgh Instruments. Confocal microscopy images were collected on a Nikon A1R inverted microscope system with a laser line at 405 nm, a long pass emission filter was set at 550 nm to avoid detection of scattered light.

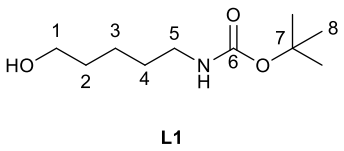
Gold slides were cleaned by UVO cleaner (1 h) before immersion in piranha solution for 10 min and subsequent washing and storage in ethanol until use. The surfaces were coated by immersion in a 0.5 mM solution of the relevant iridium(III) complex (MeCN:H_2O, 1:1) for 16 h. The solutions were removed, and the gold chip washed thoroughly in acetonitrile, dried in a stream of nitrogen and stored under a nitrogen atmosphere.

Patterned slides were synthesised in accordance to the methods previously published by Butt *et al.*[31]

Subsequent coatings of Zonyl were carried out by immersing the coated chips in methanolic solutions (H_2O:MeOH, 50:50) for 1 h. HPLC grade solvents were used for all surface experiments.

5.2.1.2 **Synthesis and characterisation**

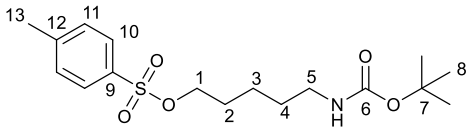
Synthesis of L1



L1

Potassium bicarbonate (14.17 g, 141.5 mmol) and 5-amino-1-pentanol (5.04 g, 48.8 mmol) were suspended in a biphasic mixture of H_2O:THF (1:1, 150 mL), the mixture was cooled to 0-5 ^oC and di-tert-butyl-dicarbonate (11.12 g, 51.0 mmol) was added dropwise over 15 minutes with stirring, maintaining a temperature below 10 ^oC. The resulting solution was allowed to stir for 24 hours at 50 ^oC. The organic layer was separated and the solvent removed in vacuo. To the resulting oil, H_2O:Et_2O (2:1, 150 mL) was added and the, the aqueous layer washed with Et_2O (2 x 50 mL). the combined organic layers were dried (Na_2SO_4) and the solvent removed in vacuo to yield N-(Boc)-5-amino-1-pentanol (**L1**) as a light yellow oil. (8.30 g, 40.8 mmol , 83.6 %) ^{1}H-NMR (400 MHz, $CDCl_3$): δ = 4.73 (s, 1H, NH), 3.60 (t, *J* = 6.5 Hz, 2H, H-1), 3.09 (q, *J* = 6.7 Hz, 2H, H-5), 1.60 - 1.44 (m, 4H, H-2,3,4) 1.42 (s, 9H H-8), 1.25 (s, 1H, OH). ^{13}C-NMR (100 MHz, CDCl3): δ = 156.2, 79.1, 62.4, 41.4, 40.4, 32.2, 29.8, 28.4, 22.9. MS (ESI^+) m/z: 226.1 $(M+Na)^+$

Synthesis of L2

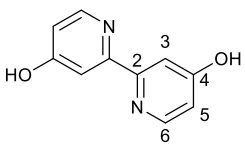


L2

A solution of **L1** (8.28 g, 40.7 mmol) and p-toluenesulfonylchloride (9.53 g, 50 mmol) in CH2Cl2 (50 mL) was stirred for 5 minutes before cooling to <5 ^oC. Pyridine was added dropwise over 15 minutes, and the solution allowed to stir for 24 hours at room temperature. To this solution H_2O:Et_2O (100 mL, 1:1) was added and the organic layer washed with $NaHCO_3$ (50 mL) and brine (50 mL), the organic layer was dried (Na_2SO_4) and the solvent removed in vacuo to yield a clear oil. This oil was triturated in n-hexane to give white powder **L2** that was filtered, washed with ice cold n-hexane and dried in air. (7.14 g,

20.0 mmol, 49.1%). ^{1}H-NMR (400 MHz, $CDCl_3$): δ = 7.80 (d, *J* =8.1 Hz, 2H, H-11), 7.54 (d, *J* =8.1 Hz, 2H, H-10), 4.51 (s, NH), 4.03 (t, *J* =6.4 Hz, 2H, H-1), 3.05 -3.12 (m, 2H, H-5) 2.47 (s, 3H, H-13), 1.67 (q, *J* =6.9, 2H, H-4), 1.45 (s, 9H, H-8), 1.40-1.32 (m, 4H, H-2,3). ^{13}C-NMR (100 MHz, CDCl3): δ = 156.4, 144.7, 140.8, 129.8, 127.9, 79.2, 70.3, 40.2, 29.4, 28.5, 28.4, 22.7, 21.6. MS (ESI^+) m/z: 380.2 $(M+Na)^+$

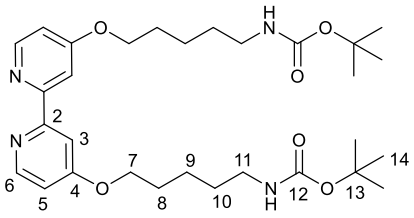
Synthesis of L3



L3

Based on methodology of Hong *et al*., to a solution of 4,4'-dimethoxy-2-2'-bipyridine (4.96 g, 23 mmol) in glacial acetic acid (250 mL) was added dropwise hydrobromic acid (48% w/v, 40mL, 357 mmol) to give a white suspension. The resulting suspension was heated under reflux in a N_2 atmosphere for 24 h. The resulting solution was evaporated in vacuum to give a cream solid. The resulting solid was dissolved in H_2O (300 mL) and neutralized with NH_3 (31%). The resulting solid was filtered in vacuum and washed with cold H_2O (3x 20mL). The solid was slightly dried in air, then dried at 70 ^{o}C in an oven for one hour to give a white solid (3.55g, 18.9 mmol, 82.0% yield). ^{1}H-NMR (400 MHz, 9:1, D_2O/NaOD): δ = 7.65 (d, *J* =5.9 Hz, 2H, H-6), 6.60 (d, *J* =2.5 Hz, 2H, H-3), 6.12 (dd, *J* =6.0, 2.5 Hz, 2H, H-5). MS (ESI^+) m/z: 189.1 $(M+H)^+$

Synthesis of L4

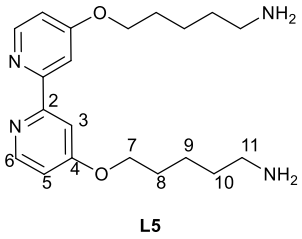


L4

K_2CO_3 (2.22 g, 15.8 mmol), **L2** (7.10 g, 19.9 mmol), and **L**3 (1.35 g, 7.2 mmol) were suspended in acetone (200 mL) and a catalytic amount of 18-crown-6 was added. The mixture was heated to 60 ^{o}C and stirred for 48h. The mixture was hot filtrated and the filtrate allowed to cool to room temperature. The precipitate was collected, washed with ice cold acetone (20 mL) and dried in vacuo to obtain a yellow solid. (0.98 g, 1.75 mmol, 24.3%) ^{1}H-NMR (400 MHz, $CDCl_3$): δ = 8.47 (d, *J* =5.6 Hz, 2H, H-6), 7.96 (d, *J* =2.5

Hz, 2H, H-3), 6.84 (dd, *J* = 5.7, 2.5 Hz), 4.59 (s, 2H, NH), 4.15 (t, *J* =6.4Hz, 4H, H-7), 3.18 (q, *J* =6.5 Hz, 4H, H-4), 1.87 (p, *J* = 6.6, 4H, H-5) 1.46-1.65 (m, 8H, H-6,7), 1.46 (s,18H, H-1). ^{13}C-NMR (100 MHz, $CDCl_3$): δ = 166.1, 157.9, 150.1, 111.3, 106.7, 67.8, 40.4, 29.8, 28.6, 28.4, 23.3. MS (ESI+) m/z: 559.3 $(M+H)^+$

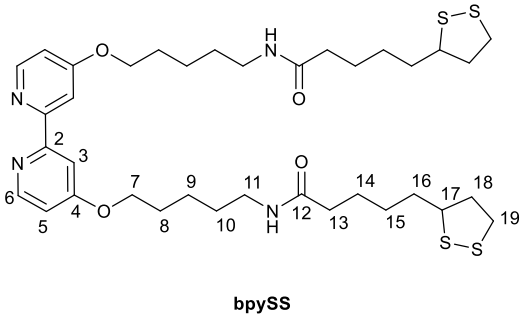
Synthesis of L5



L5

L4 (0.98 g, 1.75 mmol) was dissolved in trifluoroacetic acid (5 mL) and stirred for 1 hour. The solvent was removed *in vacuo* to produce a yellow oil, which was basified (pH ≈ 11) with 1M NaOH. To this was added 40mL of chloroform, and the aqueous layer extracted with chloroform (3 x 20 mL). The combined organic layers were collected and dried (Na_2SO_4) and the solvent removed *in vacuo* to yield a white powder. (0.36 g, 1.00 mmol, 57.4 %) ^{1}H-NMR (400 MHz, $CDCl_3$): δ = 8.48 (d, *J* =5.6 Hz, 2H, H-6), 7.97 (d, *J* =2.5 Hz, 2H, H-3), 6.84 (dd, *J* =5.7, 2.6 Hz, 2H, H-5), 4.16 (t, *J* =6.4 Hz, 4H, H-7), 2.78 – 2.73 (m, 4H, H-8), 1.87 (p, *J* =7.0 Hz, 4H, H-2), 1.55 (p, *J* =3.4 Hz, 8H, H-3,4), 1.34 (s, 4H, NH_2). ^{13}C-NMR (100 MHz, $CDCl_3$): δ = 166.13, 157.89, 150.11, 111.29, 106.70, 77.33, 77.02, 76.70, 67.91, 42.12, 33.47, 28.84, 23.34. m/z: 381.2 $(M+Na)^+$

Synthesis of bpySS

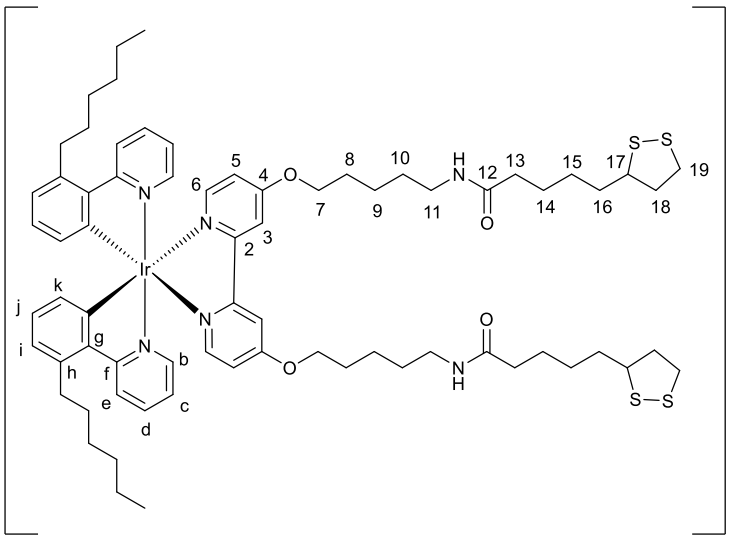


bpySS

1-Hydroxybenzotriazole hydrate (0.50 g, 3.7 mmol) and α-lipoic acid (0.46 g, 2.2 mmol), in dry DMF (10 mL) was cooled to 0-5 ºC, upon which 1-Ethyl-3-(3-dimethylaminopropyl)carbodiimide (EDC) (0.57 g, 3.7 mmol) was added dropwise and allowed to stir until full dissolution of EDC. The solution was warmed to room temperature, and a solution of N-ethylmorpholine (0.26 g, 2.3 mmol) and 4,4'-di-(5-amino-1-pentoxy)-2,2'-

bipyridine (0.36 g, 1.00 mmol) in dry DMF (10 mL) was added dropwise and the reaction stirred overnight. The resulting cream precipitate was filtered, washed with Diethyl-ether and dried in air to yield BpySS as a white powder (0.18 g, 0.24 mmol, 24%) ^{1}H-NMR (300 MHz, $CDCl_3$): δ = 8.39 (d, *J* =5.6 Hz, 2H, H-6), 7.87 (d, *J* =2.5 Hz, 2H, H-3), 6.75 (dd, *J* =5.7, 2.5 Hz, 2H, H-5), 5.41 (s, 2H, NH), 4.07 (t, *J* =6.3 Hz, 4H, H-7), 3.50 (dt, *J* =13.6, 6.5 Hz, 2H, H-17), 3.22 (q, *J* =6.5 Hz, 4H, H-11), 3.17 – 2.96 (m, 4H, H-19), 2.38 (dtd, *J* =13.0, 6.5, 5.4 Hz, 2H, H-18), 2.11 (t, *J* =7.4 Hz, 4H, H-13), 1.89-1.75(m, 6H, H-18', H-10) 1.63-1.57 (m, 8H, H-14, H-16), 1.51 – 1.30 (m, 12H, H-8, H-9, H-15). m/z: 757.3 $(M+Na)^+$

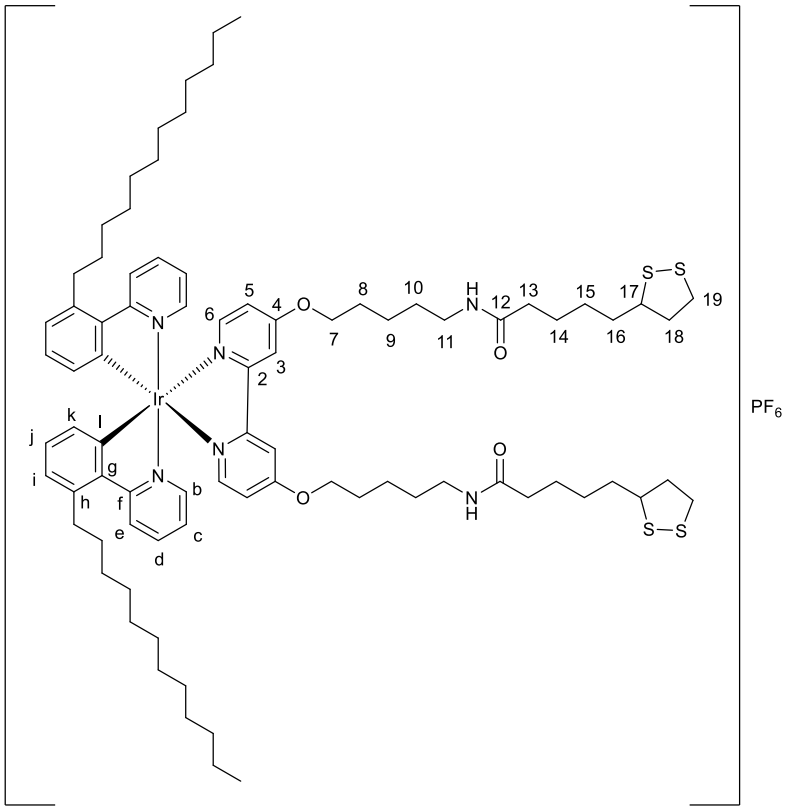
Synthesis of IrC6bpySS



A part of this procedure was adapted from Ackermann *et al.*[144] A suspension of $[RuCl_2(p\text{-cymene})_2]$ (30.8 mg, 0.05 mmol, 2.5 mol%), 1-$AdCO_2H$ (108.2 mg, 0.60 mmol, 30 mol%), K_2CO_3 (552 mg, 4.00 mmol), 2-phenylpyridine (310 mg, 2.00 mmol), and 1-bromo-hexane (990 mg, 6.00mmol) in NMP (15 mL) was stirred for 48h at 130 ºC. EtOAc (100 mL) and H_2O (100 mL) were added to the cold reaction mixture. The aqueous phase was extracted with EtOAc (4 x 50 mL). The combined organic layers were washed with H_2O (2 x 50 mL) and brine (2 x 50 mL). The remaining residue was purified by column chromatography on silica gel (n-hexane/EtOAc 4:1) to yield a yellow oil (0.28 g). This crude oil was used as collected and combined with $IrCl_3.H_2O$ (0.10 g, 0.33 mmol) in 2-ethoxyethanol (20 mL) and water (10 mL). The solution was stirred at reflux for 24 hours, cooled, and the resulting precipitate filtered. The precipitate was washed with

H_2O (2 x 10 mL) and hexane (30 mL) to yield a crude iridium(III) chloro bridged dimer Ir_2(ppy-C6)$_4Cl_2$. The dimer (40 mg, 0.03 mmol) and **bpySS** (50 mg, 0.11 mmol) were dissolved in MeOH/DCM (20 mL, 3/1, v/v) and heated at reflux for 4 hours. The solution was filtered and reduced in volume to 5 mL. NH_4PF_6 (48.9 mg, 3.00 mmol) in MeOH (2 mL) was added and stirred for 1 h. The solvent was removed, and the precipitate washed with H_2O (10 mL) then Hexane (5 mL). The resulting yellow solid was purified by alumina column chromatography with dichloromethane and methanol (16/1, v/v) to yield **IrC6bpySS** as a yellow solid (28 mg, 60%). Found: C, 55.6; H, 6.5; N, 5.5 Calc. $C_{70}H_{94}IrN_6O_4S_4PF_6.C_6H_{14}$: C, 55.8, H, 6.7 N 5.1 % λ_{max}(MeCN)/nm 223 (ε/dm^3 mol^{-1} cm^{-1} 42200), 258sh (37000), 298sh (17400), 347(7200). ν_{max}/cm^{-1} 3323 (NH), 2925 and 2855 (CH_2), 1608 (CO), 1557 (NH), 1428 (CC), 1336 and 1252 (C-N), 1022 (CO), 818 (CH), 555 (SS). ^{1}H (400 MHz, acetone-d_6) δ 8.75 (2 H, d, *J* = 2.6, H-3), 8.24 (2 H, d, *J* =8.6, H-b), 8.02 – 7.94 (4 H, m, H-c,e), 7.66 (2 H, d, *J* =6.3, H-6), 7.58 (1 H, s, NH), 7.19 – 7.07 (4 H, m, H-5,d), 6.85 (2 H, dd, *J* =7.5, 1.3, H-i), 6.73 (2 H, t, *J* =7.5, H-j), 6.12 (2 H, dd, *J* =7.6, 1.2, H-k), 4.42 (4 H, td, *J* =6.5, 2.9, H-7), 3.55 (2 H, dt, *J* =14.9, 5.9, H-17), 3.25 – 3.00 (12 H, m, H-10,11,19), 2.44 (2 H, dp, *J* =12.4, 6.2, 5.7, H-18'), 2.19 (4 H, t, *J* =7.4, H-13), 1.90 – 1.81 (6 H, m, H-18, CH_2), 1.71 (8 H, dd, *J* =11.9, 4.8, H-8, CH_2), 1.66 – 1.44 (15 H, m, H-9,14,15,16), 1.44 – 1.26 (12 H, m, CH_2), 0.93 – 0.75 (6 H, m, CH_3). ^{13}C (126 MHz, acetone-d_6) δ 172.9 (C-12), 168.5 (C-4), 168.5 (C-f), 158.7 (C-2), 155.0 (C-l), 151.5 (C-6), 150.6 (C-e), 142.7 (C-g), 142.6 (C-h), 138.9 (C-c), 130.6 (C-k), 130.3 (C-j), 126.8 (C-i), 124.3 (C-b), 123.8 (C-d), 115.8 (C-5), 112.9 (C-3), 71.0 (C-7), 57.3 (C-17), 41.0 (C-18), 39.2 (C-11), 39.1 (C-19), 36.5 (C-10), 35.4 (C-16), 32.5 (CH_2), 31.2 (C-8), 30.4 (CH_2), 30.2 (CH_2), 28.8 (CH_2), 26.3 (C-15), 23.7 (C-9), 23.3 (CH_2), 14.4 (CH_3). *m/z* (ESI-TOF) $C_{70}H_{94}IrN_6O_4S_4$ Calcd: 1401.5825 Found: 1401.5818

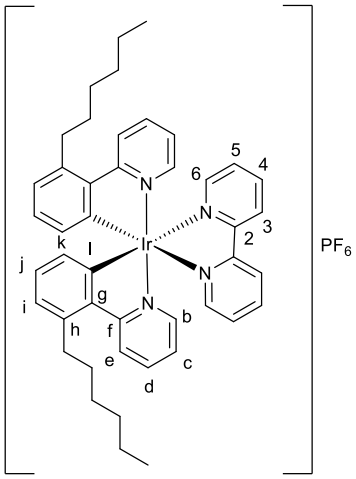
Synthesis of IrC12bpySS



A part of this procedure was adapted from Ackermann *et al.*[144] A suspension of $[RuCl_2(p\text{-cymene})_2]$ (30.8 mg, 0.05 mmol, 2.5 mol%), 1-$AdCO_2H$ (108.2 mg, 0.60 mmol, 30 mol%), K_2CO_3 (552 mg, 4.00 mmol), 2-phenylpyridine (310 mg, 2.00 mmol), and 1-bromo-dodecane (1.49 g, 6.00 mmol) in NMP (15 mL) was stirred for 48h at 130 ºC. EtOAc (100 mL) and H_2O (100 mL) were added to the cold reaction mixture. The aqueous phase was extracted with EtOAc (4 x 50 mL). The combined organic layers were washed with H_2O (2 x 50 mL) and brine (2 x 50 mL). The remaining residue was purified by column chromatography on silica gel (n-hexane/EtOAc 4:1) to yield a yellow oil (0.28 g). This crude oil was used as collected and combined with $IrCl_3.H_2O$ (0.10 g, 0.33 mmol) in 2-ethoxyethanol (20 mL) and water (10 mL). The solution was stirred at reflux for 24 hours, the solvent was removed in vacuo and the resulting residue triturated in ethanol to produce a crude chloro bridged dimer $Ir_2(ppy\text{-}C12)_4Cl_2$. The dimer (55 mg, 0.03 mmol) and bpySS (50 mg, 0.07 mmol) were dissolved in MeOH/DCM (20 mL, 3/1, v/v) and heated at reflux for 8 hours. The solution was filtered and reduced in volume to 5 mL. NH_4PF_6 (48.9 mg, 3.00 mmol) was added in MeOH (2 mL) and stirred for 1 h. The solvent was removed, and the precipitate washed with H_2O (10 mL). The resulting yellow solid was purified by alumina column chromatography

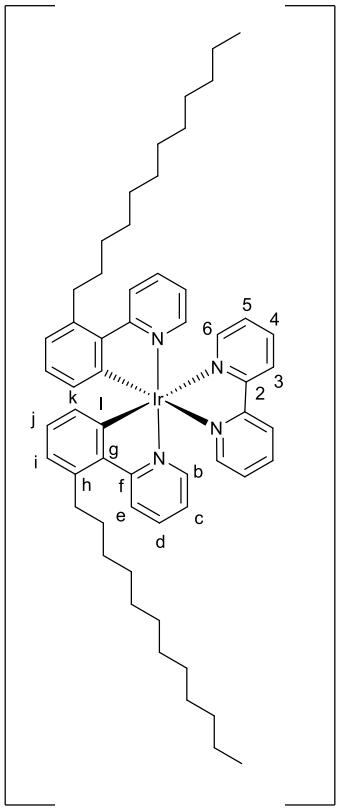
with dichloromethane and methanol (8/1, v/v), the solvent was removed yielding **IrC12bpySS** as a yellow solid (30 mg, 29 %) Found: C, 57.6; H, 7.2; N, 4.9. Calc.: C, 57.4; H, 6.9; N, 4.9%. λ_{max}(MeCN)/nm 224sh (ε/dm^3 mol^{-1} cm^{-1} 57600), 254sh (51800), 298sh (23500), 350 (9500). ν_{max}/cm^{-1} 3423 and 3327 (NH), 2923 and 2852 (CH_2), 1608 (CO), 1557 (NH), 1432 (CC) 1336 and 1256 (CN) 1019 (CO), 828 (CH), 556 (SS). ^{1}H (400 MHz, acetone-d_6) δ 9.09 (2 H, d, *J* = 2.6, H-3), 8.23 (2 H, d, *J* = 8.6, H-b), 8.00 – 7.91 (4 H, m, H-c,e), 7.63 (2 H, d, *J* = 6.4, H-6), 7.16 (2 H, dd, *J* = 7.5, 5.8, H-d), 7.06 (2 H, dd, *J* = 6.4, 2.4, H-5), 6.83 (2 H, dd, *J* = 7.5, 0.7, H-i), 6.72 (2 H, t, *J* = 7.5, H-j), 6.12 (2 H, dd, *J* = 6.8, 0.8, H-k), 4.63 – 4.47 (4 H, m, H-7), 3.56 – 3.47 (2 H, m, H-17), 3.22 – 2.98 (12 H, m, H-10,11,19), 2.41 (2 H, dq, *J* = 12.4, 6.2, H-18'), 2.23 (4 H, t, *J* = 7.3, H-13), 1.89 – 1.78 (6 H, m, H-18, CH_2), 1.78 – 1.64 (8 H, m, H-8, CH_2), 1.64 – 1.42 (16 H, m, H-9,14,15,16), 1.41 – 1.17 (36 H, m, CH_2), 0.87 (6 H, t, *J* = 7.0, 6.6, CH_3). ^{13}C (126 MHz, acetone-d_6) 172.9 (C-12), 168.6 (C-4), 168.5 (C-f), 158.9 (C-2), 155.2 (C-l), 151.1 (C-6), 150.5 (C-e), 142.6 (C-g), 142.6 (C-h), 138.8 (C-c), 130.6 (C-k), 130.2 (C-j), 126.8 (C-i), 124.3 (C-b), 123.9 (C-d), 116.4 (C-5), 113.0 (C-3), 71.5 (C-7), 57.4 (C-10), 41.0 (C-18), 39.2 (C-11), 39.0 (C-19), 36.5 (C-13), 36.5 (CH_2), 36.4 (CH_2), 35.4 (C-16), 32.7 (CH_2), 31.2 (CH_2), 30.4 (CH_2), 30.3 (CH_2), 30.3 (CH_2), 30.1 (CH_2), 29.5 (C-8), 28.8 (CH_2), 26.4 (C-15), 23.6 (C-9), 23.3 (CH_2), 14.4 (CH_3). *m/z* (ESI-TOF) $C_{82}H_{118}N_6O_4S_4Ir$ Calcd: 1569.7703 Found: 1569.7690

Synthesis of IrC6bpy



The crude dimer $Ir_2(ppy\text{-}C6)_4Cl_2$ (40 mg, 0.03 mmol) and 2,2'-bipyridine (10 mg, 0.06 mmol), were dissolved in MeOH/DCM (20 mL, 3/1, v/v) and heated to reflux for 6 hours. The solution was filtered and reduced in volume to 2 mL. NH_4PF_6 (48.9 mg, 3.00 mmol) was added in MeOH (2 mL) and stirred for 1 h. The solvent was removed, and the yellow solid purified by silica column chromatography, using DCM/MeOH as an eluent (9/1, v/v) the solvent was removed in vacuo to yield **IrC6bpy** as a yellow/orange solid. (20 mg, 0.02 mmol, 36 %) λ_{max}(MeCN)/nm 260sh (ε/dm^3 mol^{-1} cm^{-1} 35800), 311sh (19000), 348 (7400), 350 (9500). ^{1}H (400 MHz, acetone-d_6) δ 8.84 (d, *J* =8.2, 2H, H-3), 8.35 – 8.23 (m, 4H, H-4,b), 8.03 – 7.94 (m, 4H, H-c,d), 7.92 (ddd, *J* =5.8, 1.7, 0.7 Hz, 2H, H-6), 7.67 (ddd, *J* =7.7, 5.4, 1.2 Hz, 2H, H-5), 7.14 – 7.10 (m, *J* =7.2, 5.8, 1.3 Hz, 2H, H-e), 6.89 (dd, *J*= 7.5, 1.3 Hz, 2H, H-i), 6.77 (t, *J* =7.5 Hz, 2H, H-j), 6.13 (dd, *J* =7.5, 1.3 Hz, 2H, H-k), 3.21 – 3.02 (m, 4H, CH_2), 1.80 – 1.64 (m, 4H, CH_2), 1.54 – 1.43 (m, 4H, CH_2), 1.38 – 1.30 (m, 8H, CH_2), 0.93 – 0.82 (m, 6H, CH_3). ^{13}C (101 MHz, acetone-d_6) δ 168.4 (C-f), 156.8 (C-2), 154.0 (C-l), 151.2 (C-d), 150.7 (C-6), 142.8 (C-g), 142.5 (C-h), 140.5 (C-4), 139.2 (C-c), 130.5 (C-k), 130.4 (C-j), 129.3 (C-5), 127.2 (C-i), 125.7 (C-3), 124.6 (C-b)), 123.9 (C-e), 36.5 (CH_2), 32.5 (CH_2), 31.1 (CH_2), 23.3 (CH_2), 14.4 (CH_3). *m/z* (ESI-TOF) $C_{44}H_{48}N_4Ir$ Calcd: 825.3508 Found: 825.3510

Synthesis of IrC12bpy



The crude dimer $Ir_2(ppy\text{-}C12)_4Cl_2$ (40 mg, 0.02 mmol) and 2,2'-bipyridine (10 mg, 0.06 mmol), were dissolved in MeOH/DCM (20 mL, 3/1, v/v) and heated to reflux for 6 hours. The solution was filtered and reduced in volume to 2 mL. NH_4PF_6 (48.9 mg, 3.00 mmol) in MeOH (2 mL) was added and stirred for 1 h. The solvent was removed, and the yellow solid purified by silica column chromatography, using DCM/MeOH as an eluent (9/1, v/v) the solvent was removed in vacuo to yield **IrC12bpy** as a yellow/orange solid. (22 mg, 0.02 mmol, 42 %) λ_{max}(MeCN)/nm 260sh (ε/dm3 mol-1 cm-1 36000), 311sh (19100), 348 (7400). ^{1}H NMR (400 MHz, acetone-*d*$_6$) δ 9.00 (dt, *J* =8.3, 1.0 Hz, 2H, H-3), 8.37 – 8.16 (m, 4H, H-4,b), 8.06 – 7.83 (m, 6H, H-6,c,d), 7.64 (ddd, *J* =7.7, 5.4, 1.1 Hz, 2H, H-5), 7.12 (ddd, *J* =7.3, 5.8, 1.3 Hz, 2H, H-e), 6.87 (dd, *J* =7.5, 1.3 Hz, 2H, H-i), 6.76 (t, *J* =7.5 Hz, 2H, H-j), 6.13 (dd, *J* =7.5, 1.3 Hz, 2H, H-k), 3.65 – 3.55 (m, 4H, CH_2), 3.15 – 3.08 (m, 4H, CH_2), 1.81 – 1.65 (m, 6H, CH_2), 1.52 – 1.43 (m, 6H CH_2), 1.27 (s, 24H, CH_2), 0.91 – 0.80 (m, 6H, CH_3). ^{13}C (101 MHz, acetone-d_6) δ 168.3 (C-f), 156.8 (C-2), 154.1 (C-l), 151.0 (C-d), 150.7 (C-6), 142.8 (C-g), 142.5 (C-h), 140.6 (C-4), 139.1 (C-c), 130.5 (C-k), 130.4 (C-j), 129.2 (C-5), 127.1 (C-i), 126.2 (C-3), 124.5 (C-b), 124.0 (C-e), 68.1 (CH_2), 55.0 (CH_2), 49.7 (CH_2), 36.5 (CH_2), 32.6 (CH_2), 31.1 (CH_2), 23.3 (CH_2), 14.4 (CH_3). m/z (ESI-TOF) $C_{56}H_{72}N_4Ir$ Calcd: 993.5386 Found: 993.5385

5.2.2 Supplementary information

NMR Spectra

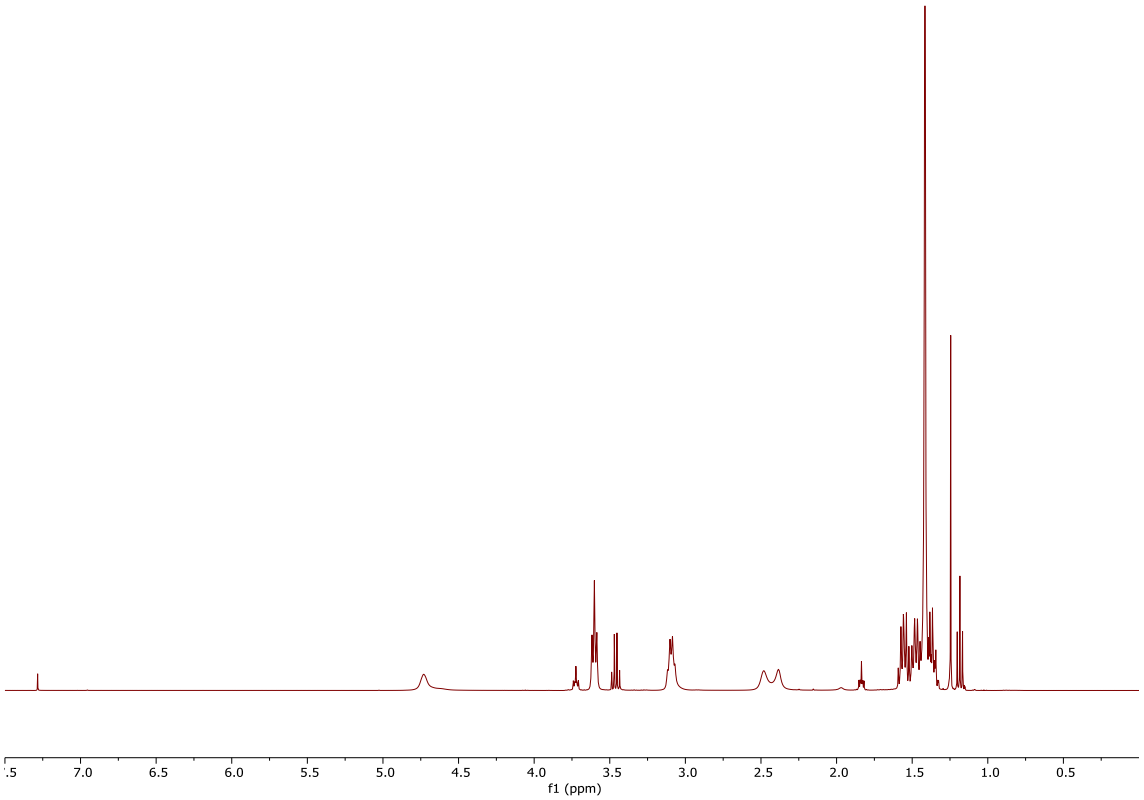


Figure S3.1: 400 MHz ^{1}H NMR of **L1** in $CDCl_3$

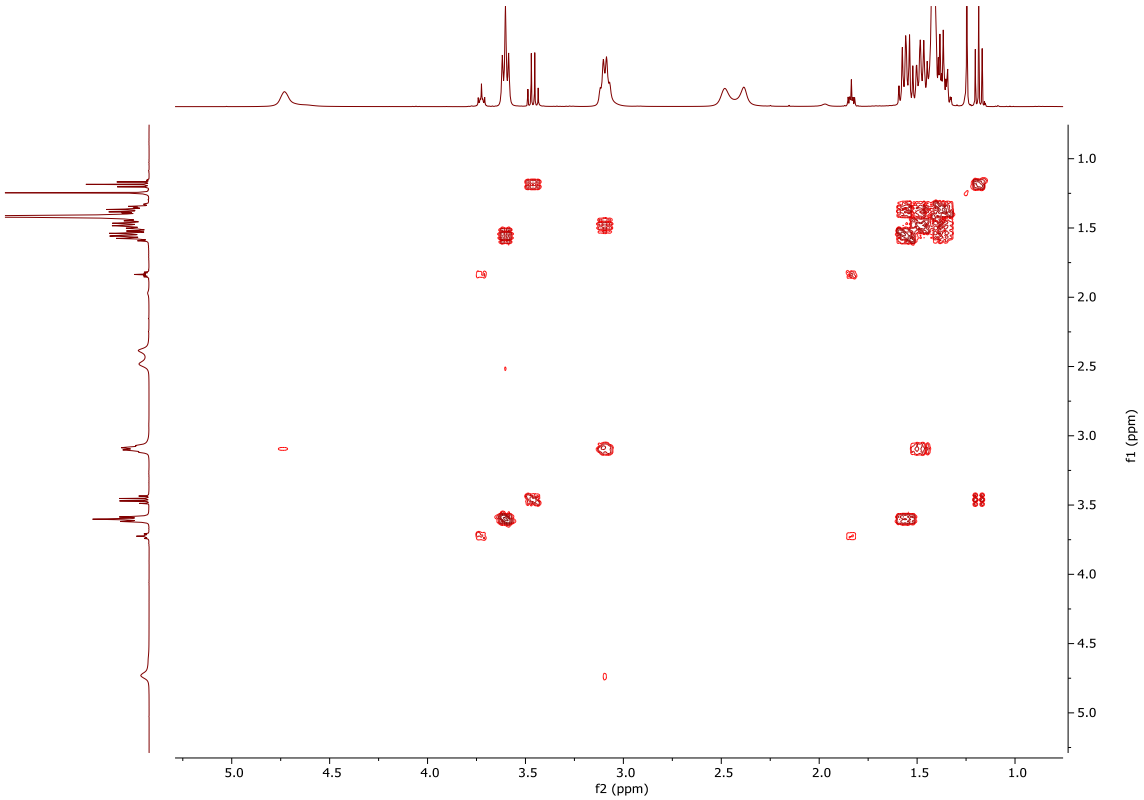


Figure S3.2: 2D COSY spectrum of **L1** in $CDCl_3$

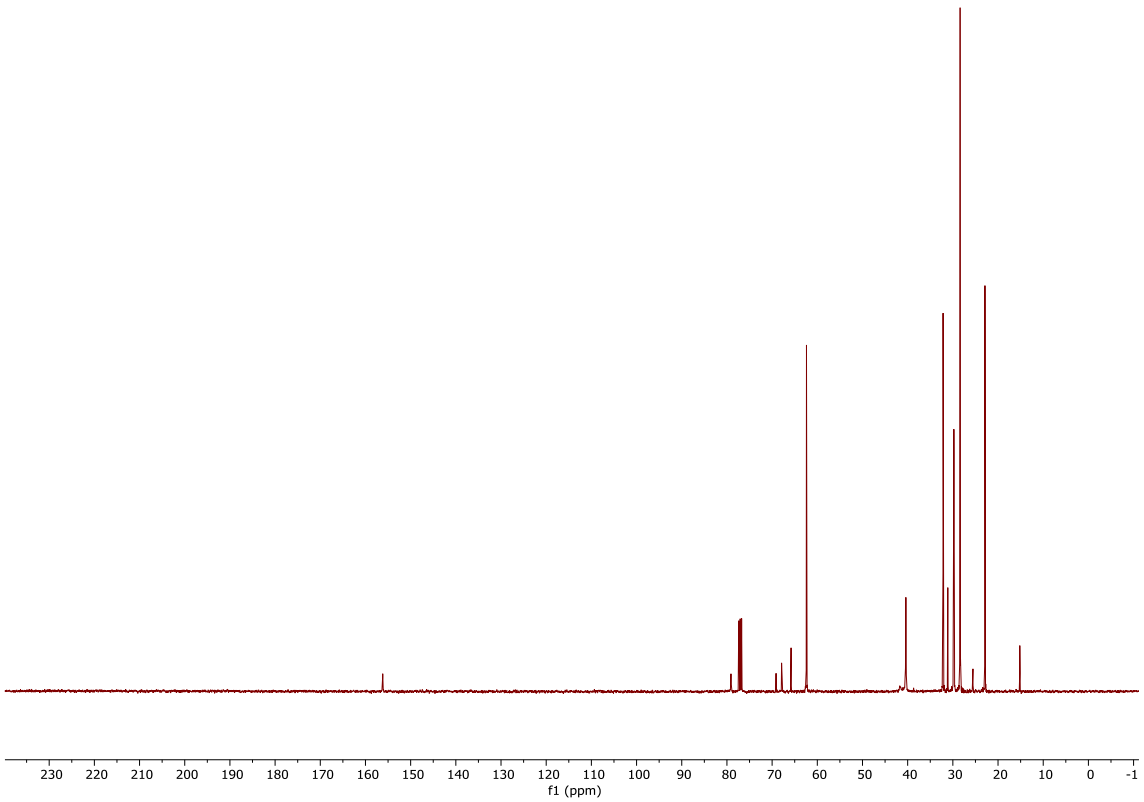


Figure S3.3: 101 MHz ^{13}C NMR of **L1** in $CDCl_3$

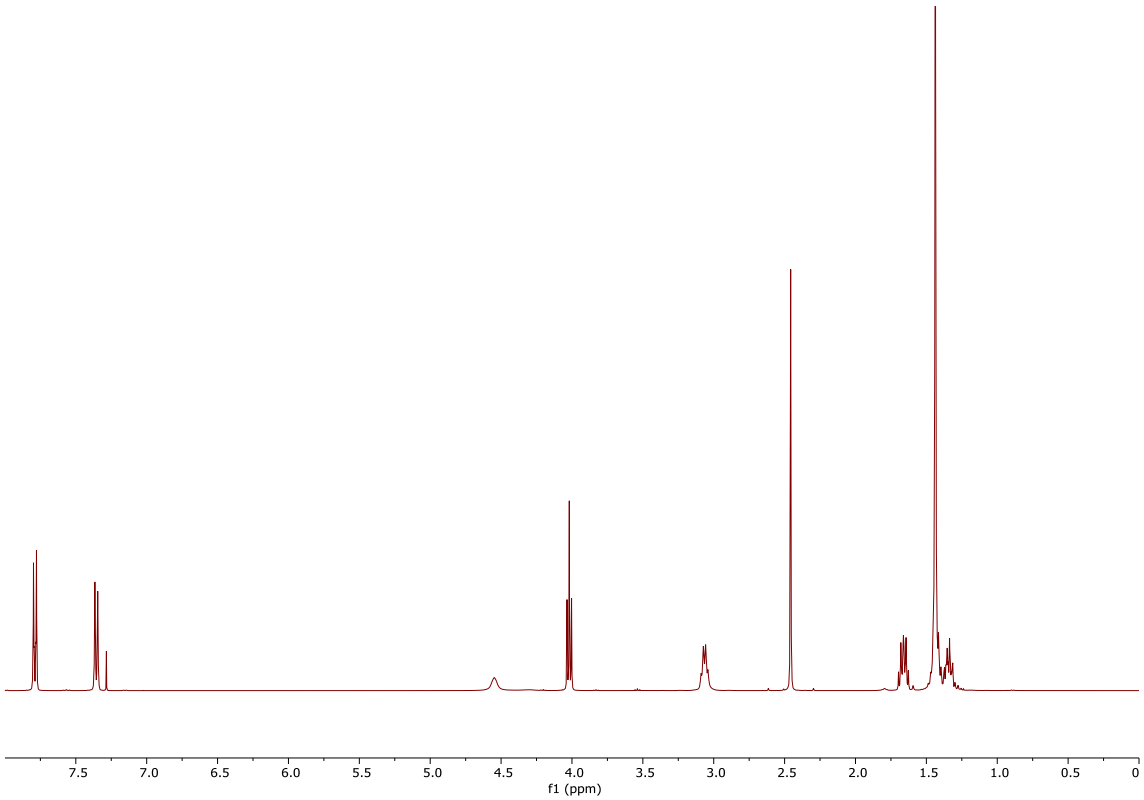


Figure S3.4: 400 MHz ^{1}H NMR of **L2** in $CDCl_3$

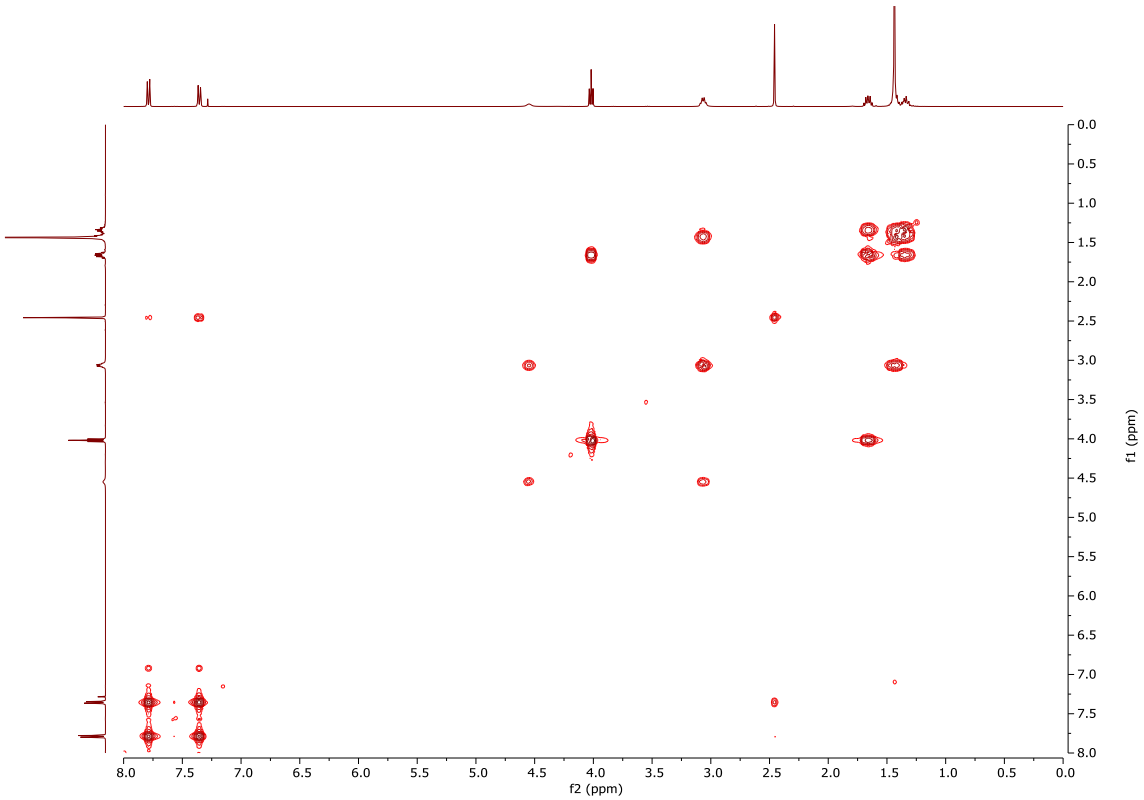


Figure S3.5: 2D COSY spectrum of **L2** in $CDCl_3$

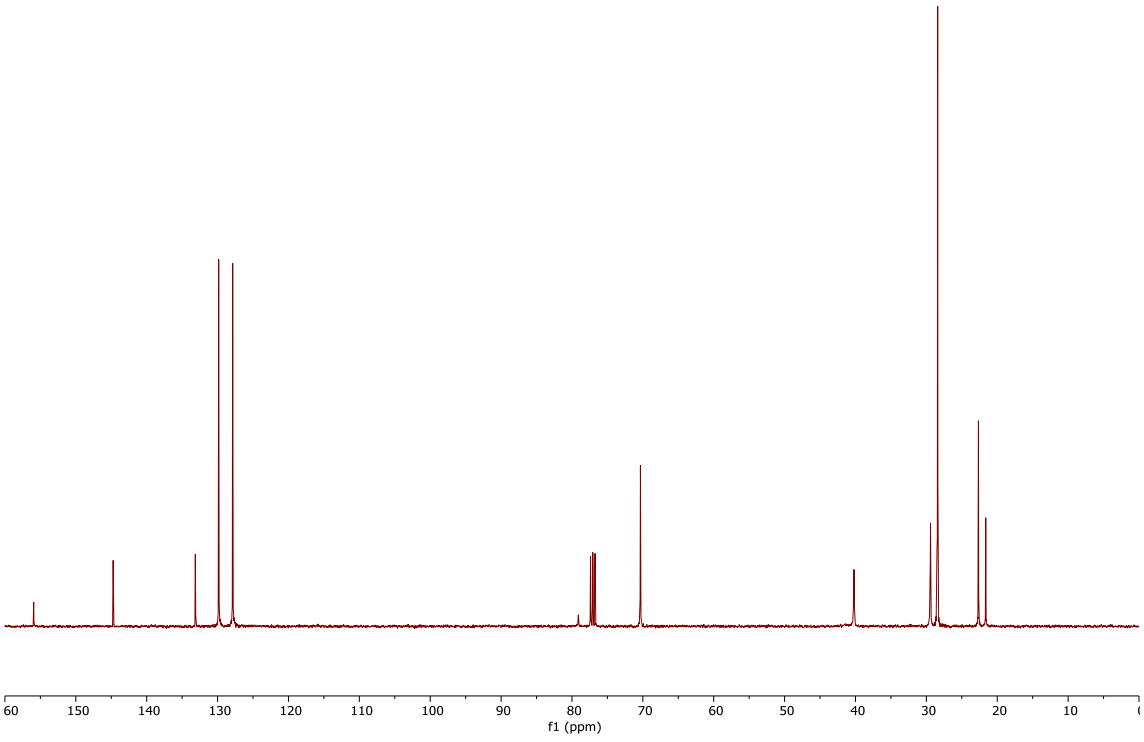


Figure S3.6: 101 MHz ^{13}C NMR of **L2** in $CDCl_3$

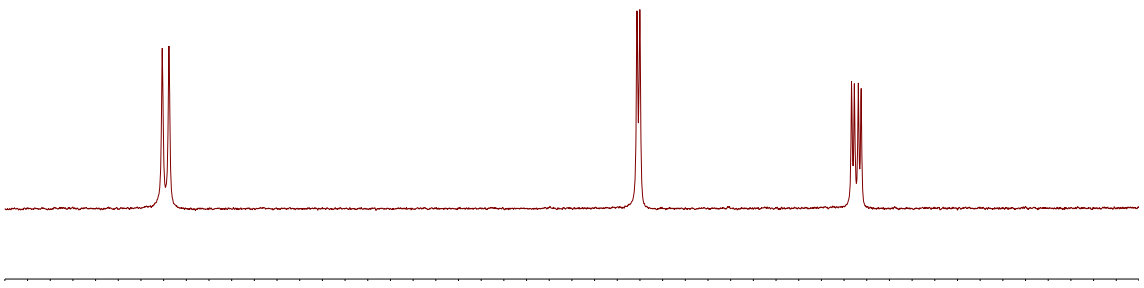


Figure S3.7: 400 MHz ^{1}H NMR of **L3** in D_2O:NaOD

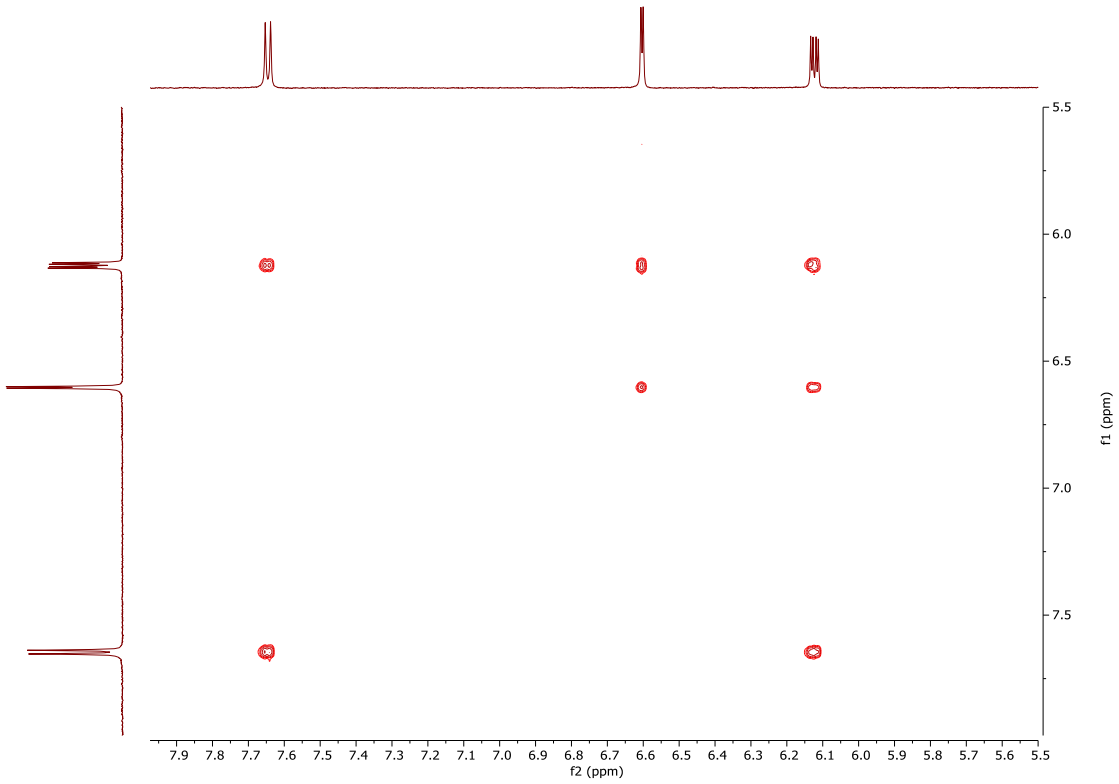


Figure S3.8: 2D COSY of **L3** in D_2O:NaOD

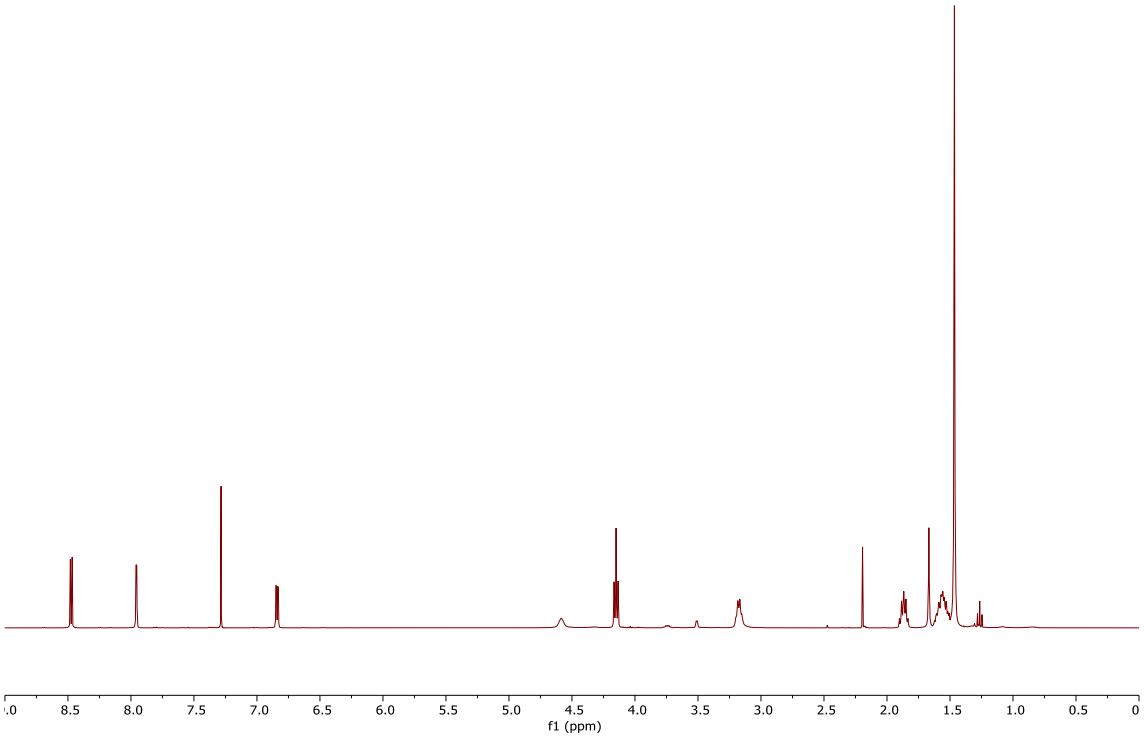


Figure S3.9: 400 MHz ^{1}H NMR of **L4** in $CDCl_3$

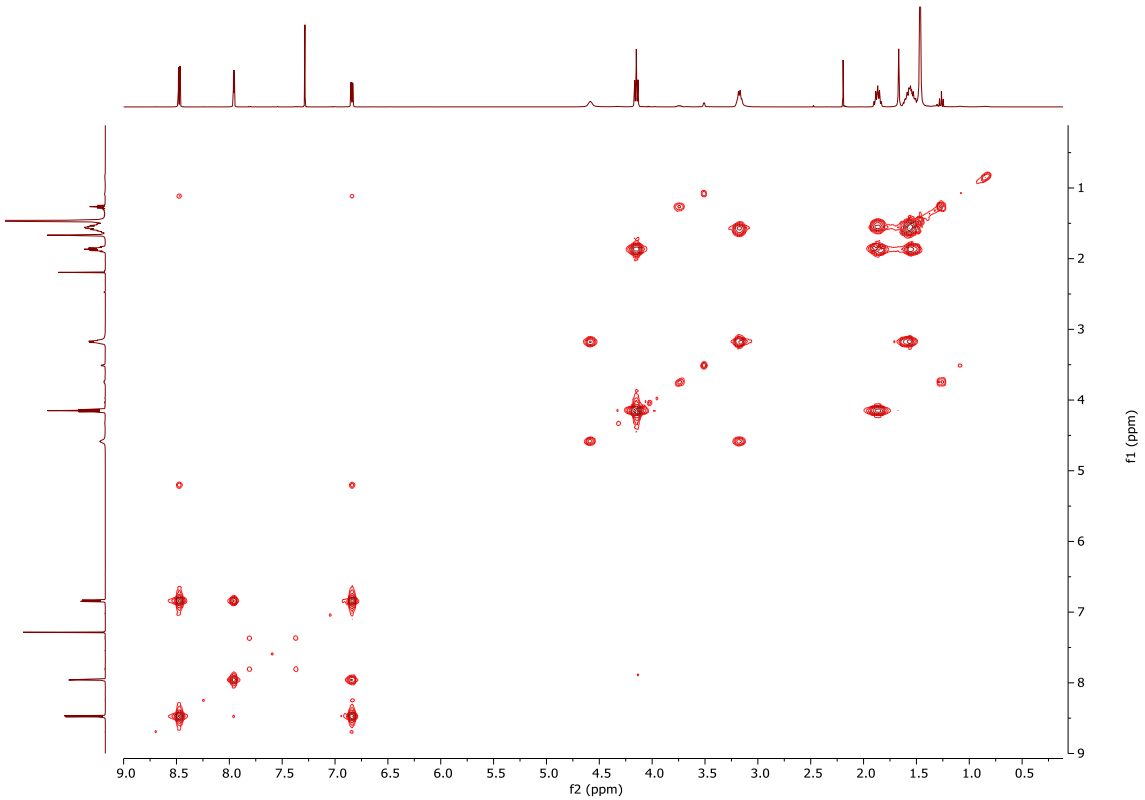


Figure S3.10: 2D COSY of **L4** in $CDCl_3$

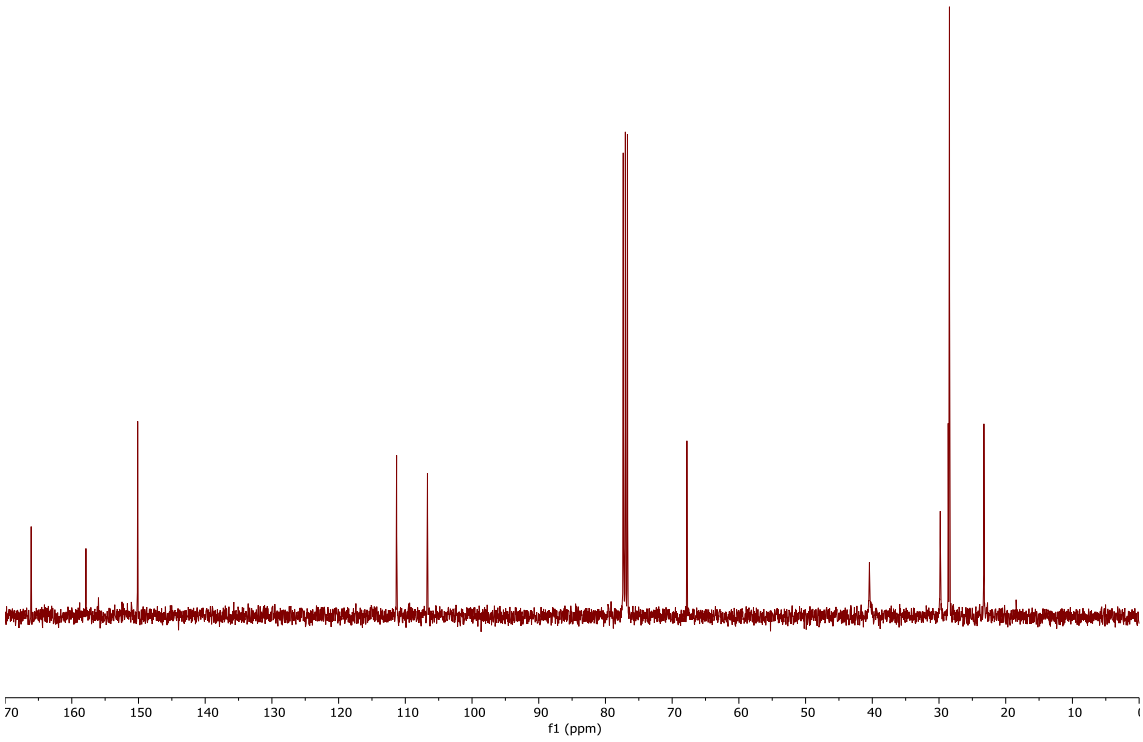


Figure S3.11: 101 MHz ^{13}C NMR of **L4** in $CDCl_3$

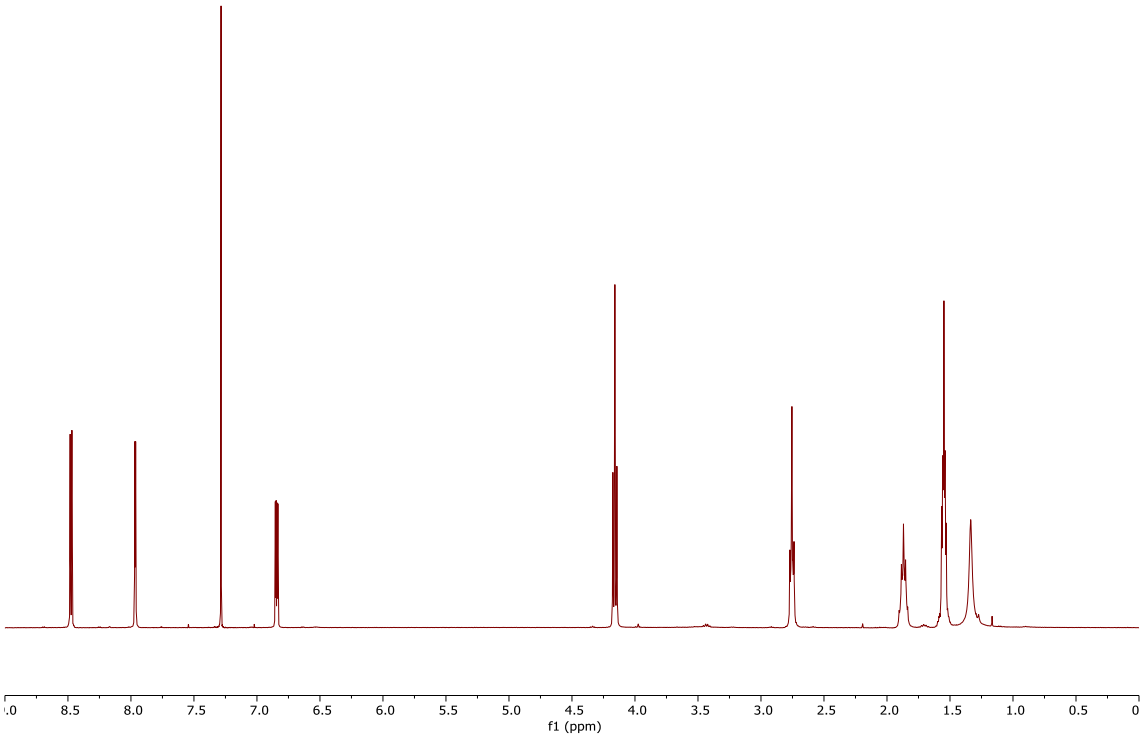


Figure S3.12: 400 MHz ^{1}H NMR of **L5** in $CDCl_3$

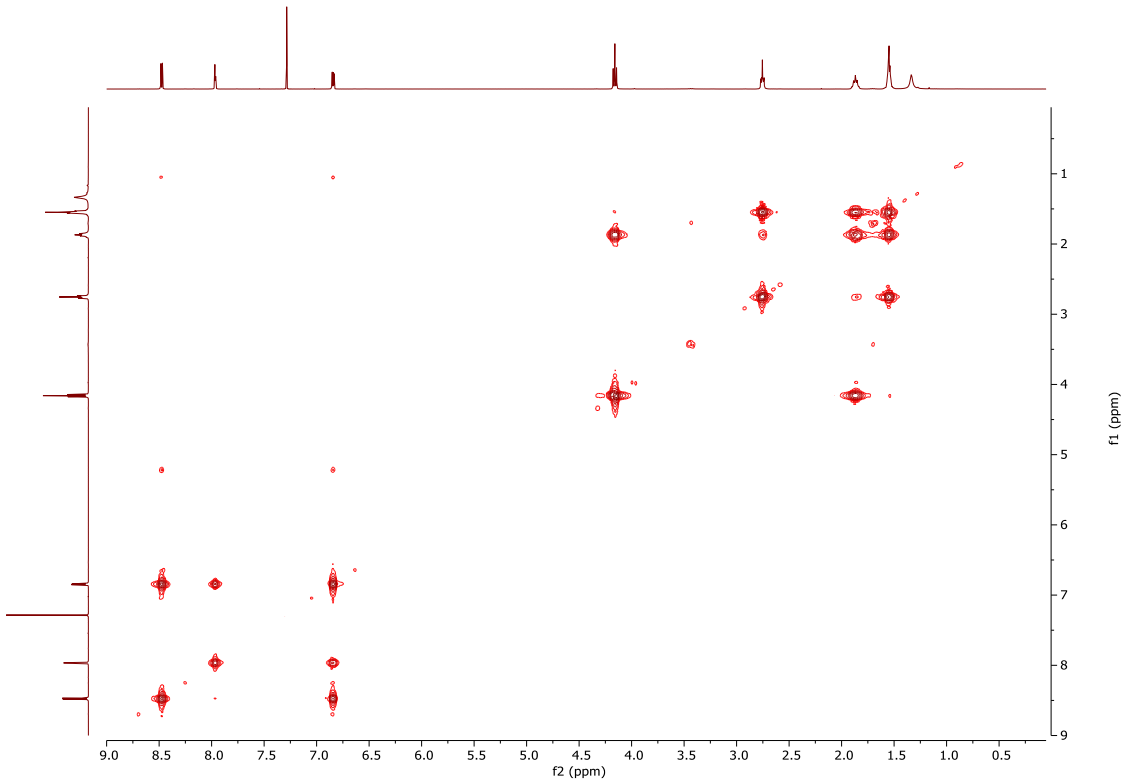


Figure S3.13: 2D COSY of **L5** in $CDCl_3$

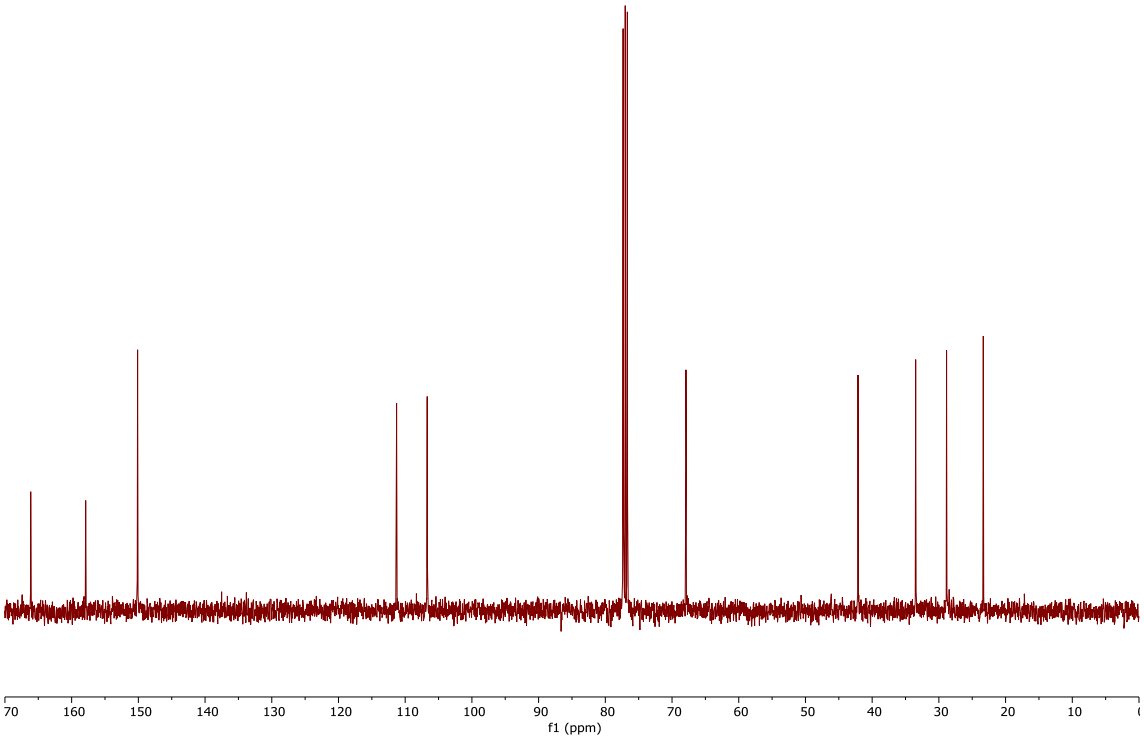


Figure S3.14: 400 MHz ^{13}C NMR of **L5** in $CDCl_3$

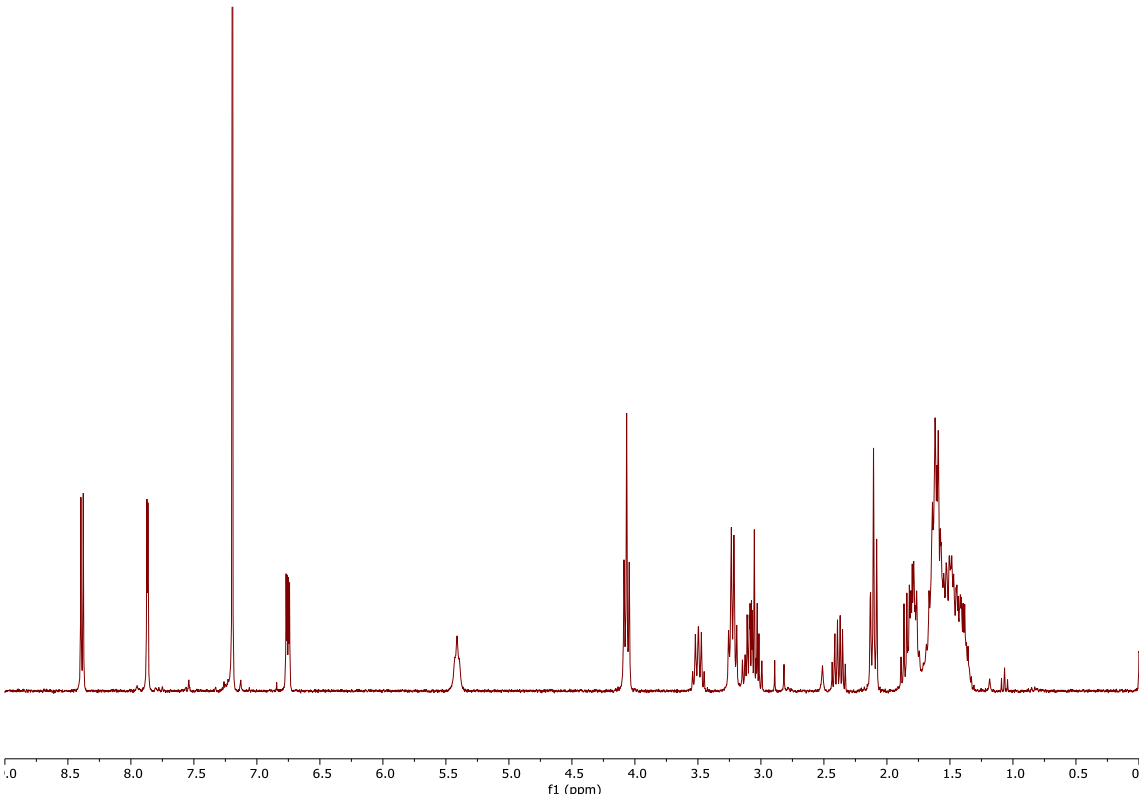


Figure S3.15: 400 MHz ^{1}H NMR of **bpySS** in $CDCl_3$

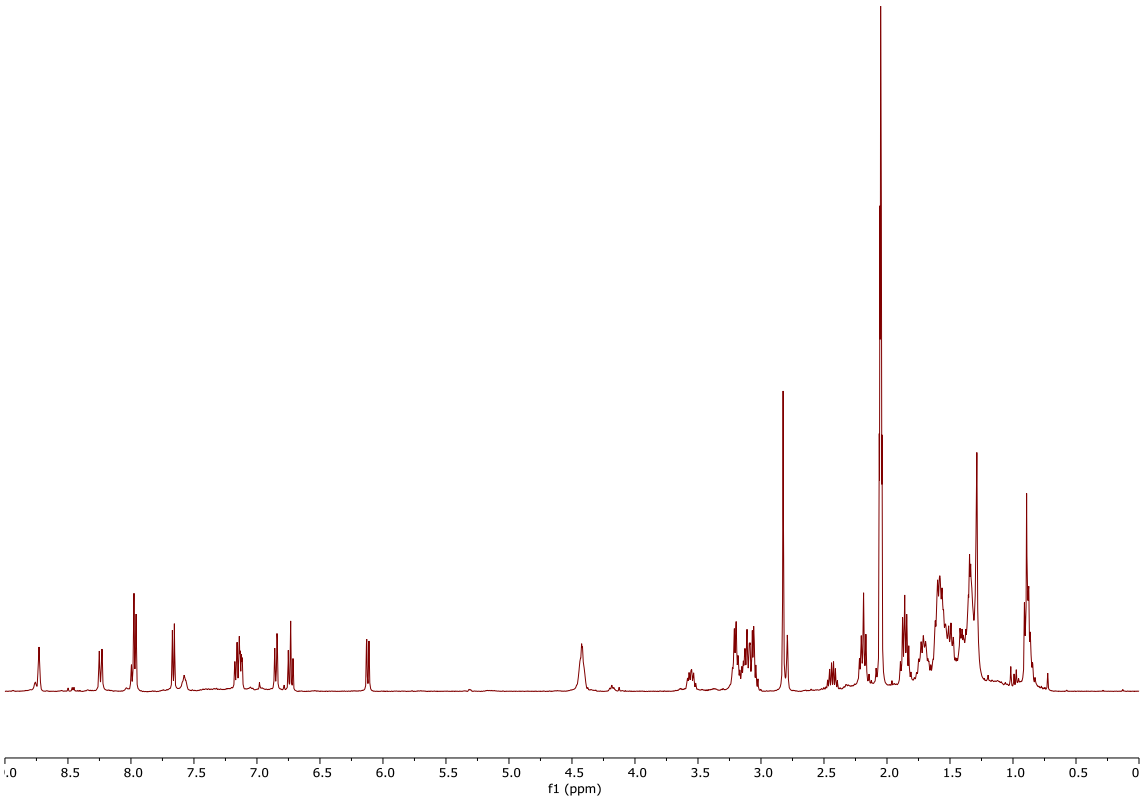


Figure S3.16: 400 MHz ^{1}H NMR of **IrC6bpySS** in acetone-d_6

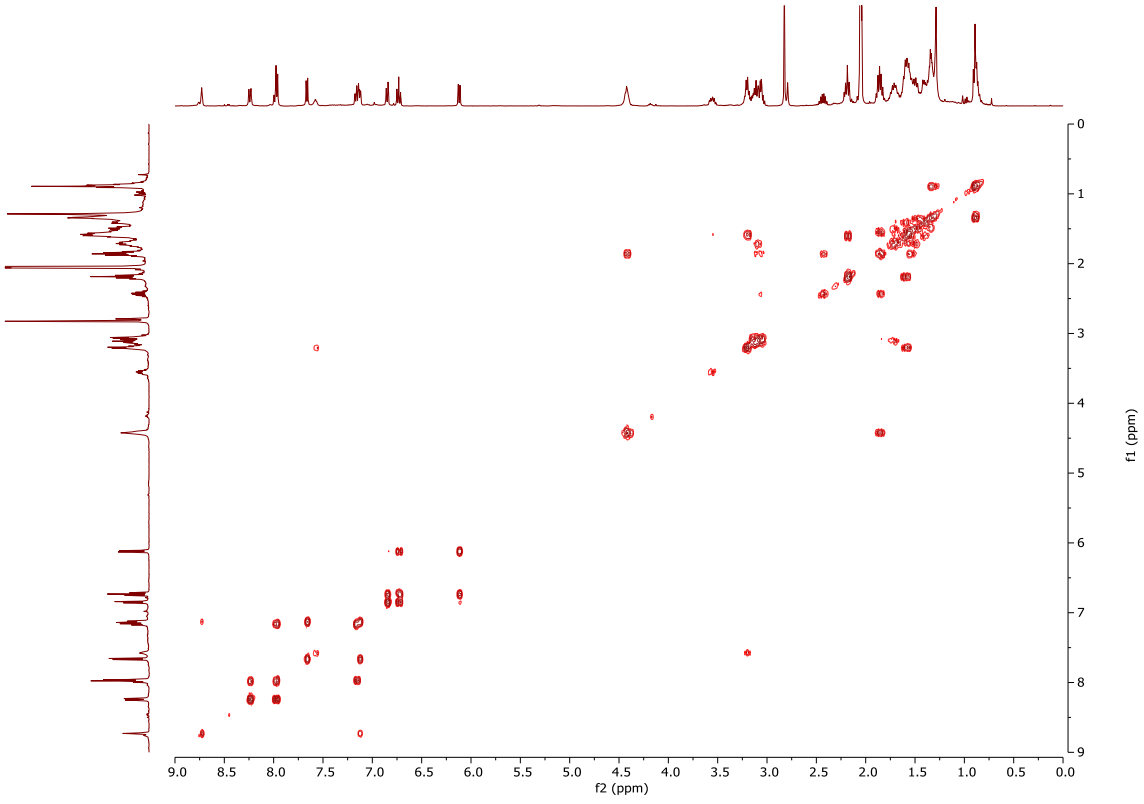


Figure S3.17: 2D COSY of **IrC6bpySS** in acetone-d_6

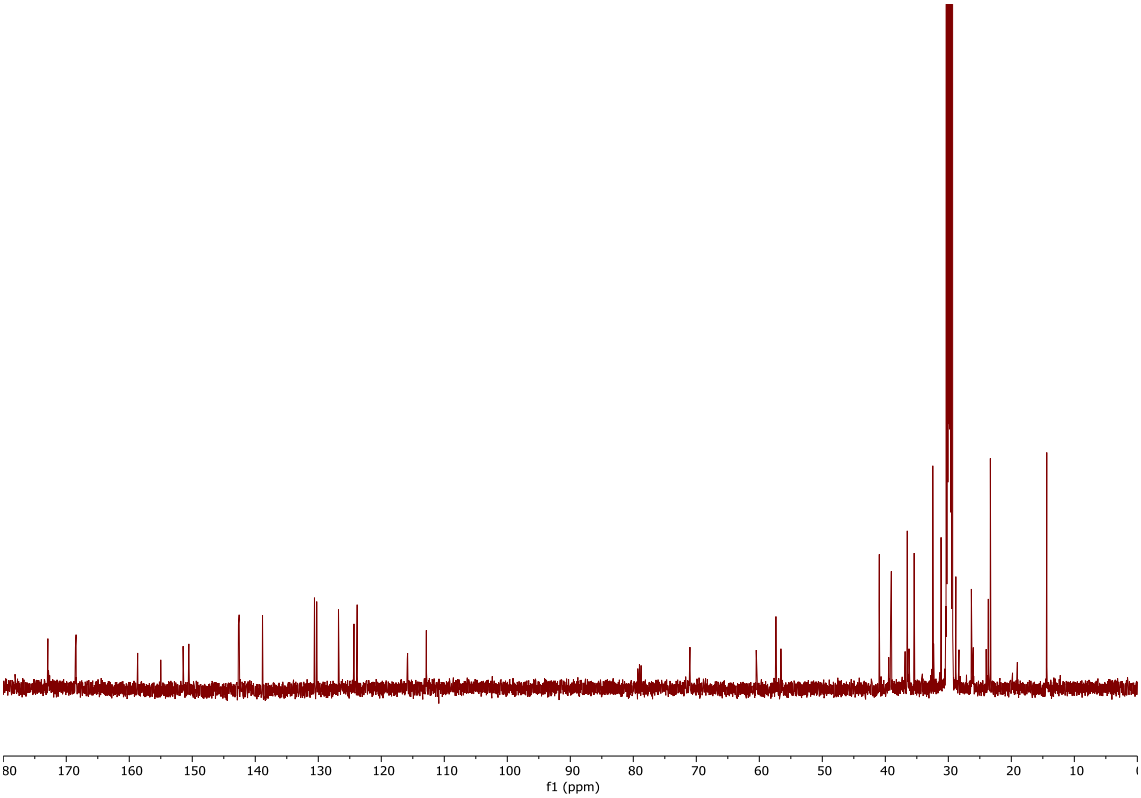


Figure S3.18: 101 MHz ^{13}C NMR of **IrC6bpySS** in acetone-d_6

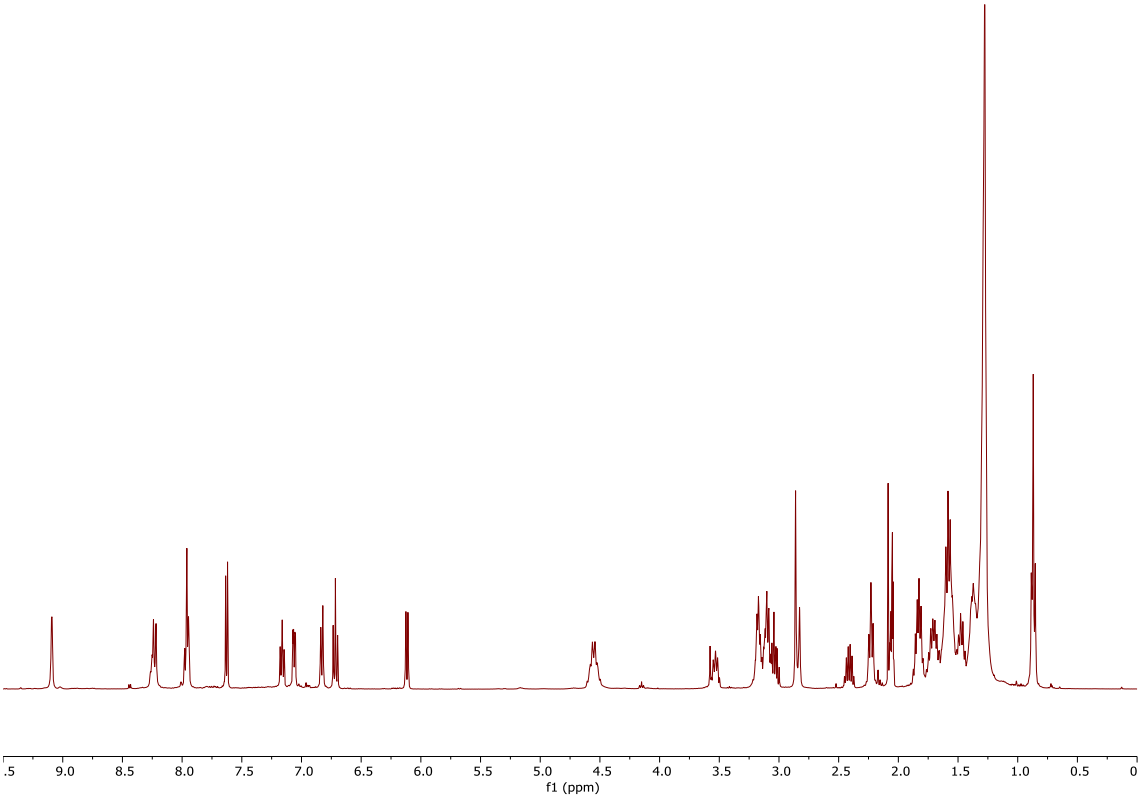


Figure S3.19: 400 MHz ^{1}H NMR of **IrC12bpySS** in acetone-d_6

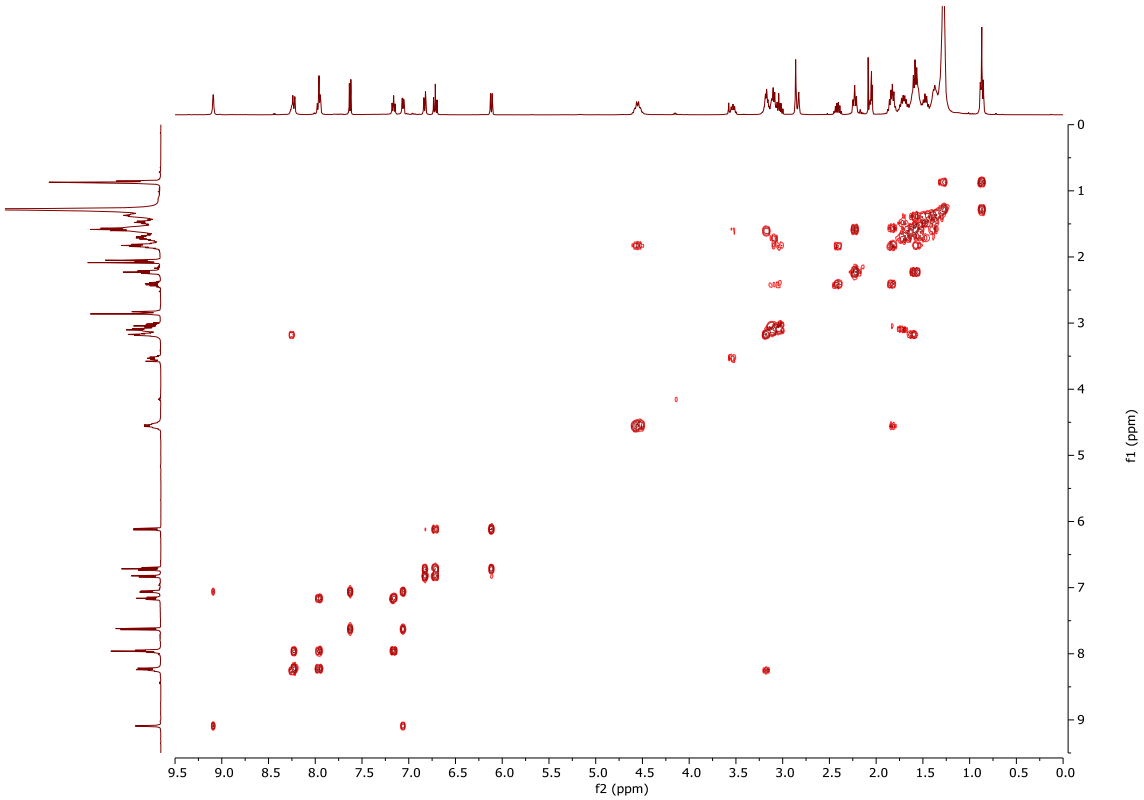


Figure S3.20: 2D COSY of **IrC12bpySS** in acetone-d_6

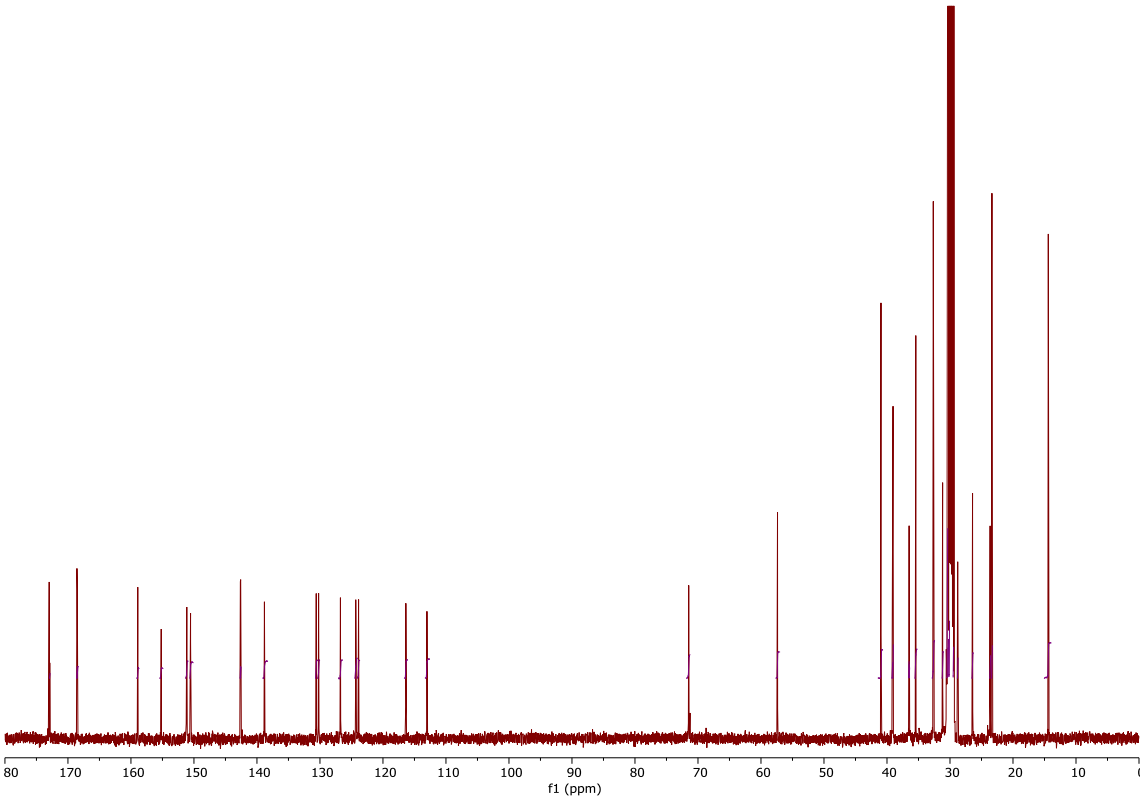


Figure S3.21: 101 MHz ^{13}C NMR of **IrC12bpySS** in acetone-d_6

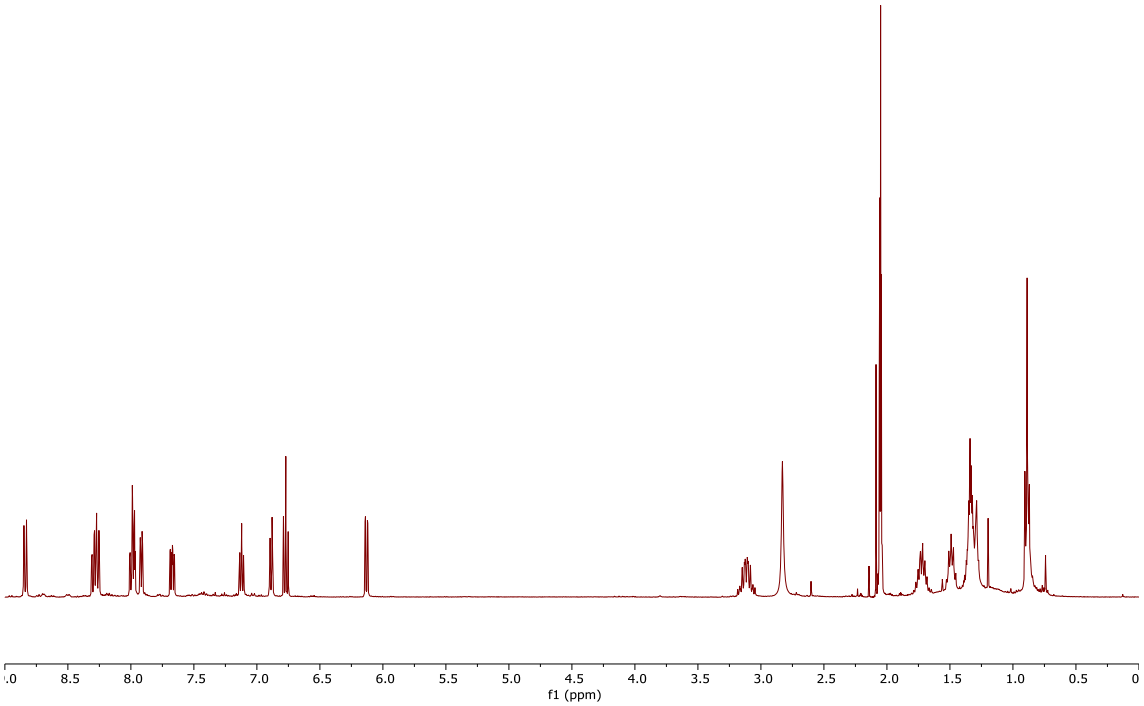


Figure S3.22: 400 MHz ^{1}H NMR of **IrC6bpy** in acetone-*d*$_6$

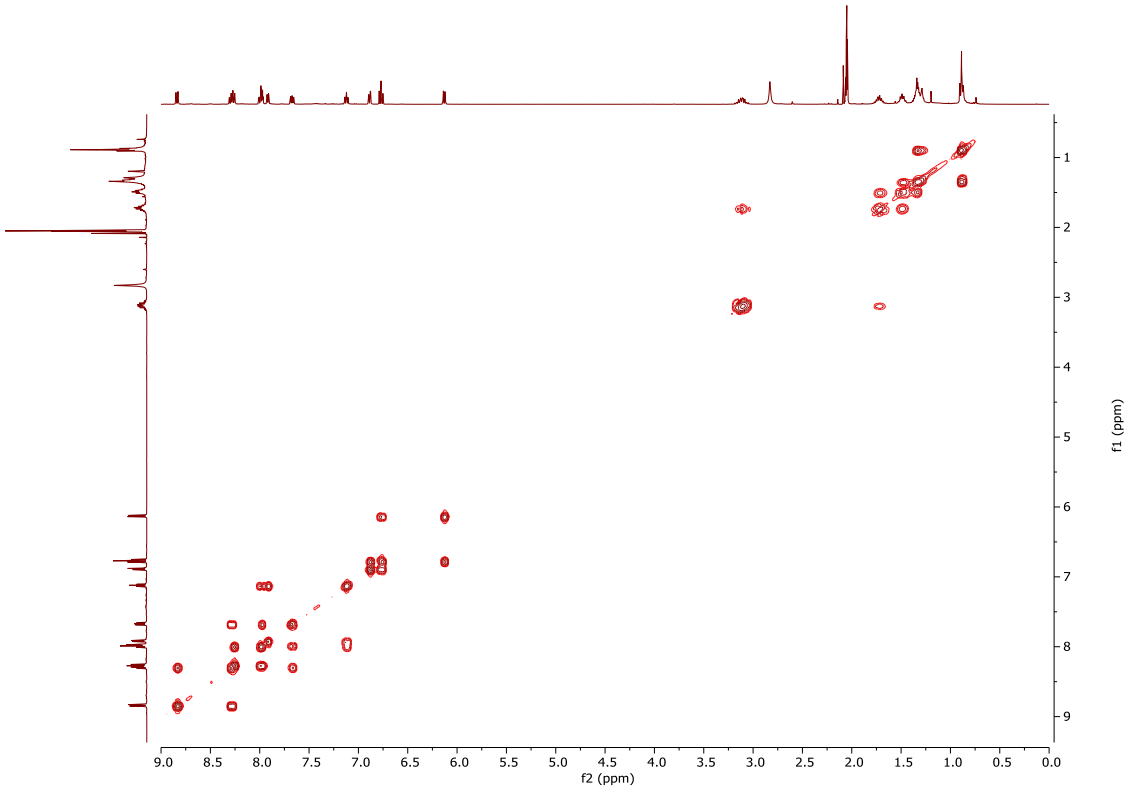


Figure S3.23: 2D COSY of **IrC6bpy** in acetone-*d*$_6$

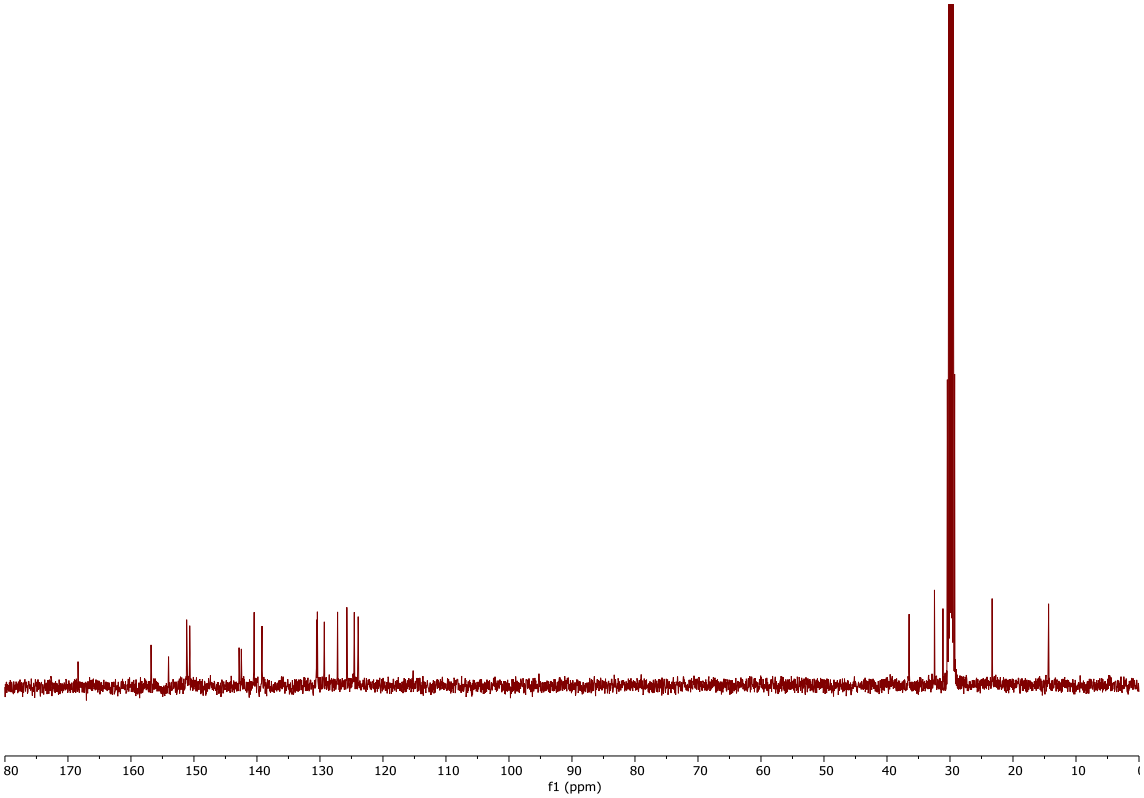


Figure S3.24: 101 MHz ^{13}C NMR of **IrC6bpy** in acetone-d_6

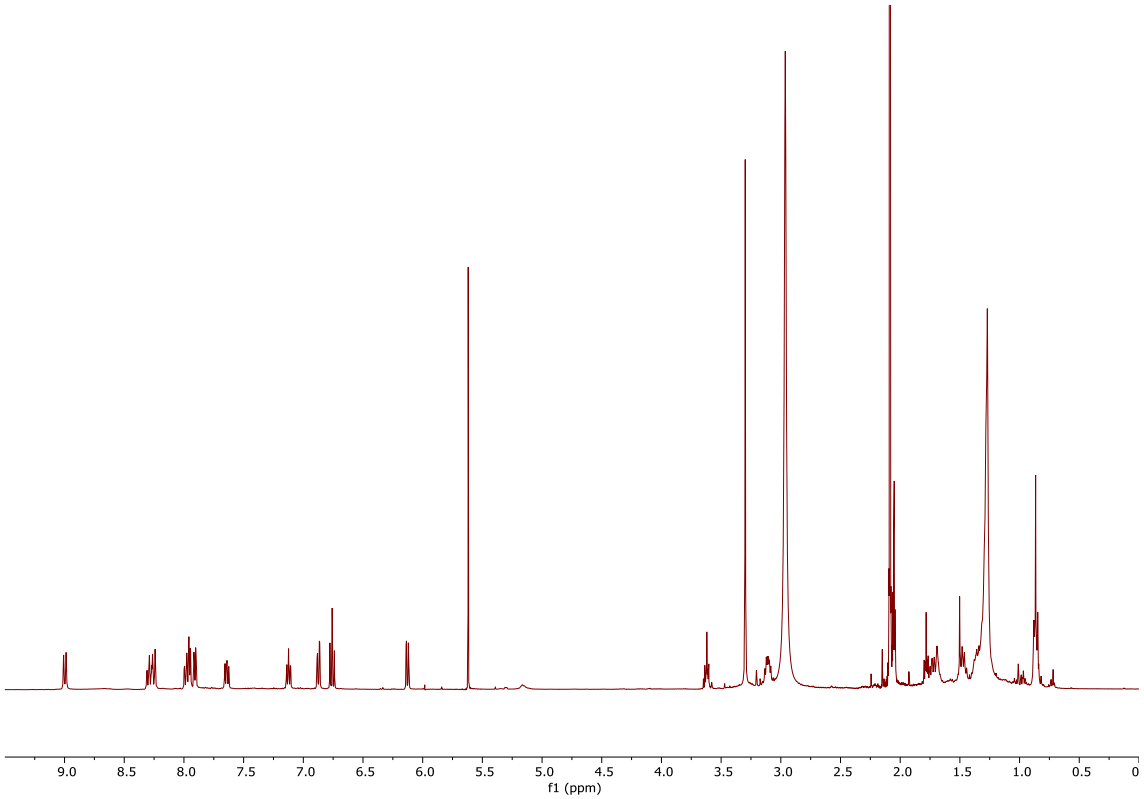


Figure S3.25: 400 MHz ^{1}H NMR of **IrC12bpy** in acetone-d_6

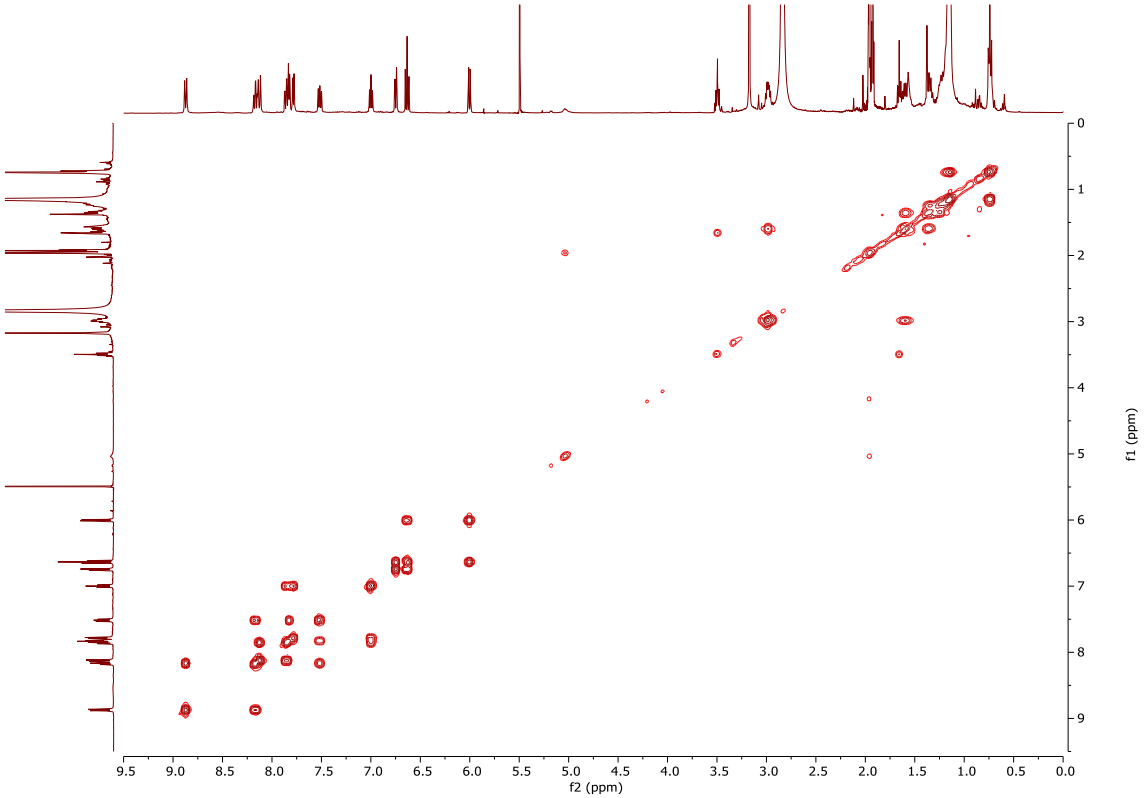


Figure S3.26: 2D COSY of **IrC12bpy** in acetone-d_6

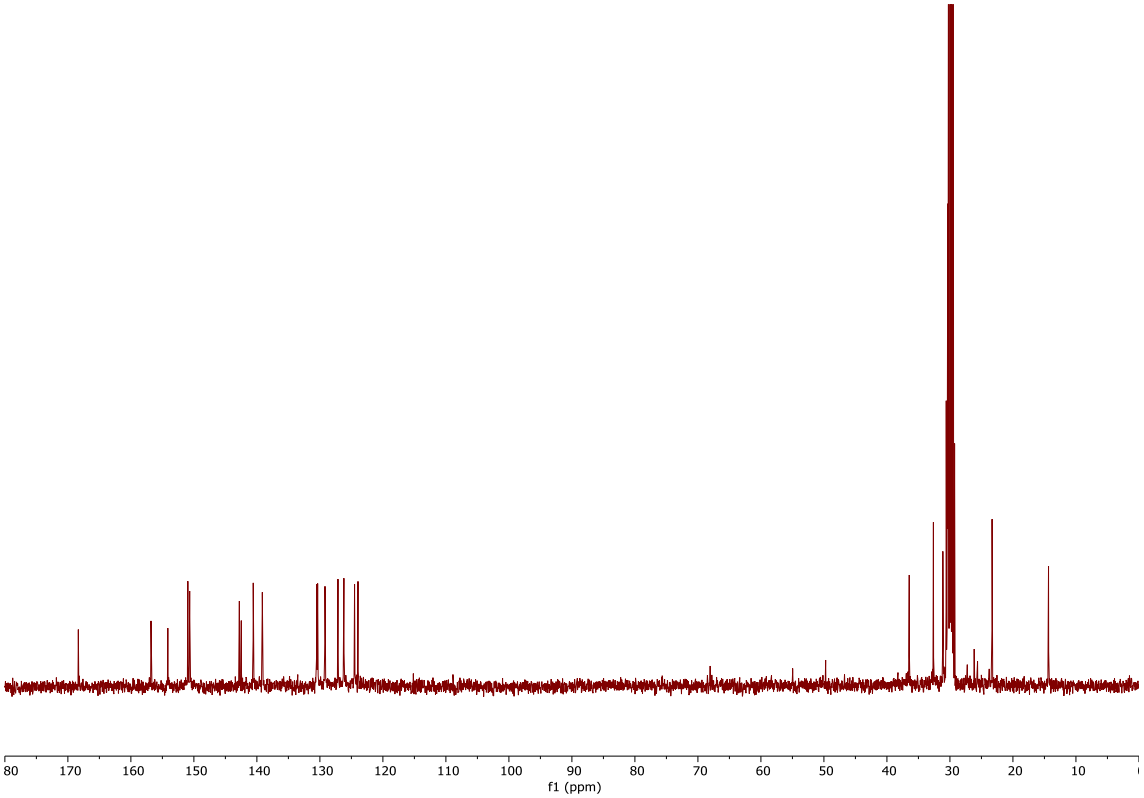


Figure S3.27: 101 MHz ^{13}C NMR of **IrC12bpy** in acetone-d_6

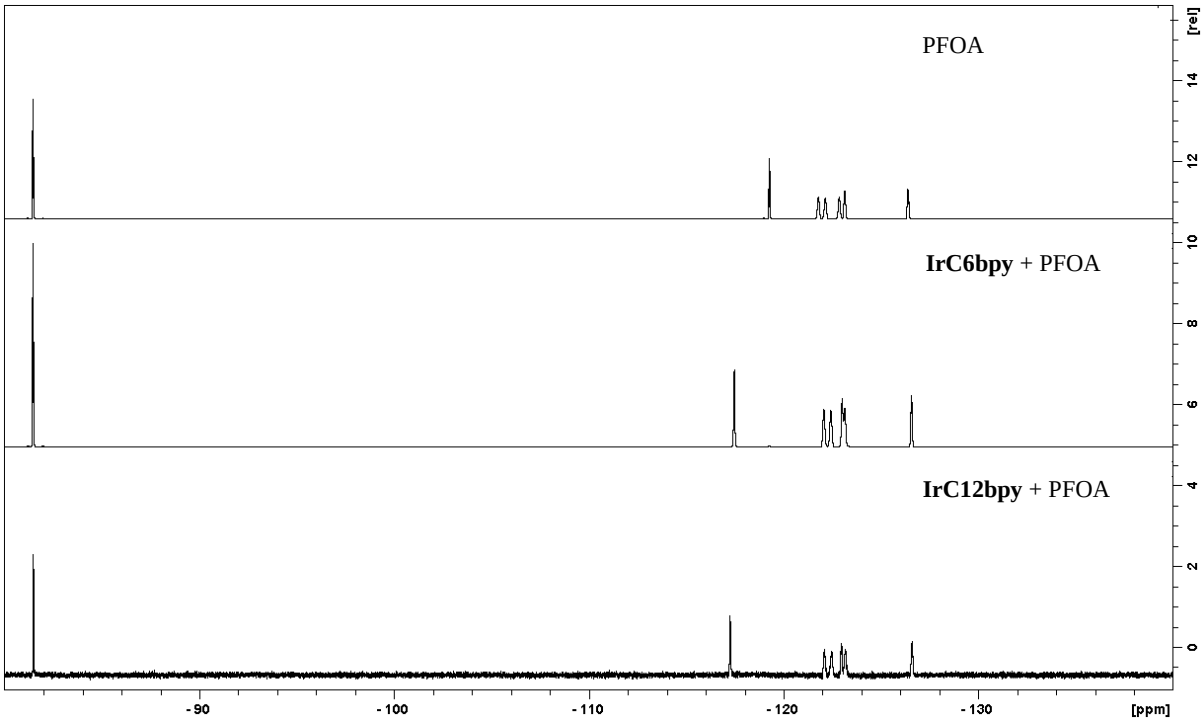


Figure S3.28: ^{19}F NMR of PFOA alone and with each metal complex. All spectra are taken in 1:1 MeOH-d_4:D_2O mixtures

Mass Spectra

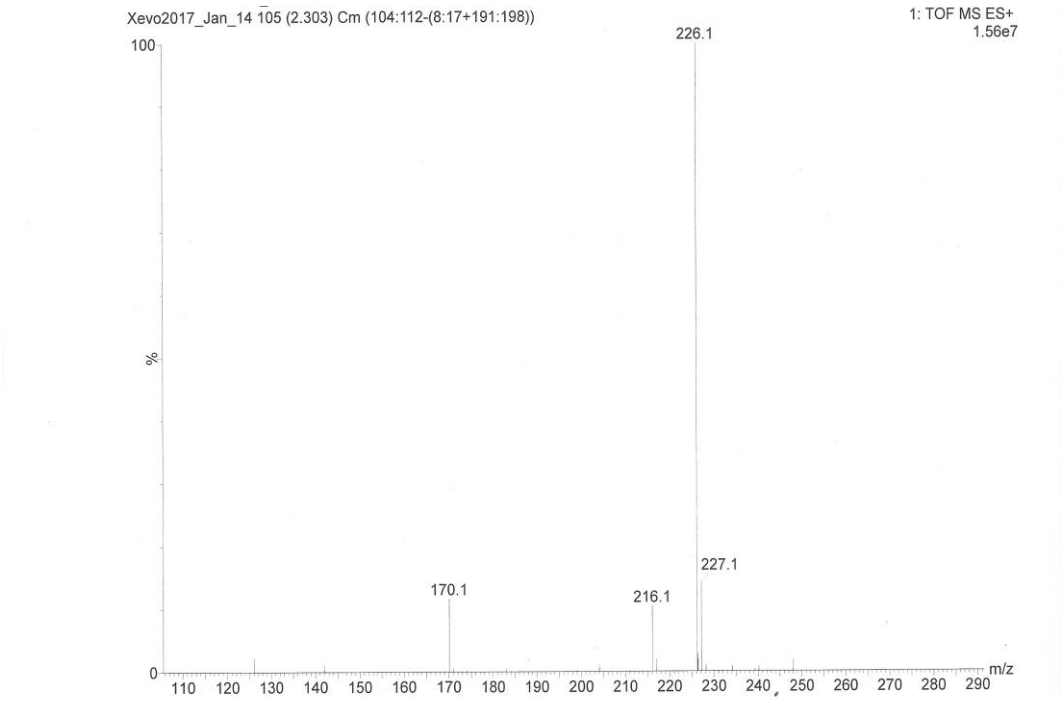


Figure S3.29: Mass spectrum of **L1**

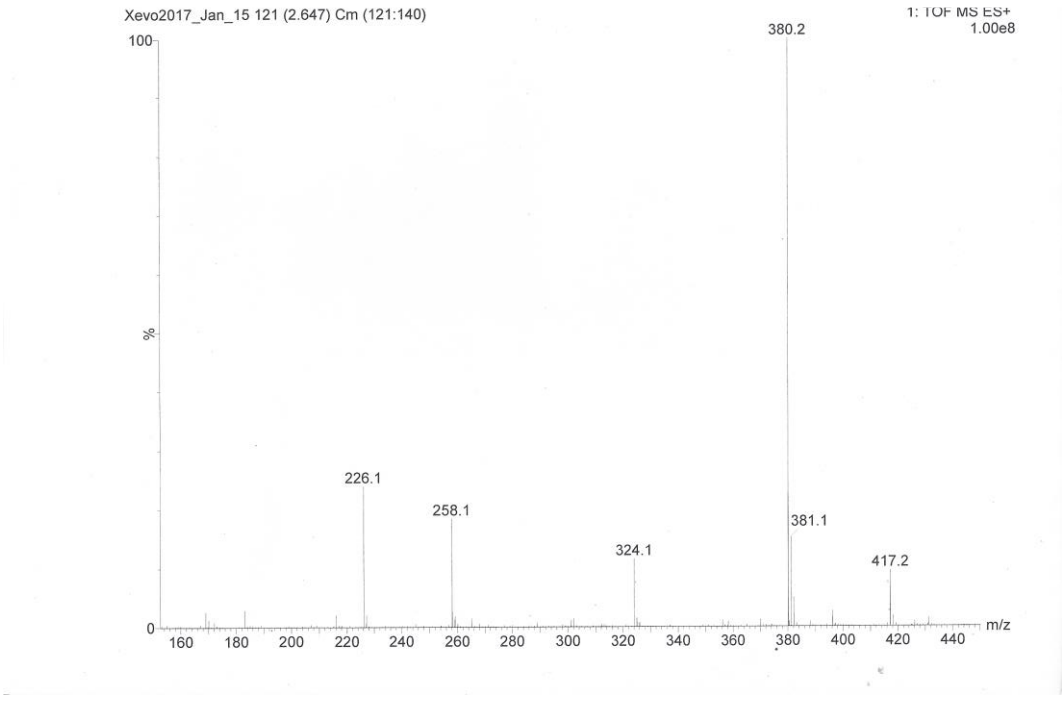


Figure S3.30: Mass spectrum of **L2**

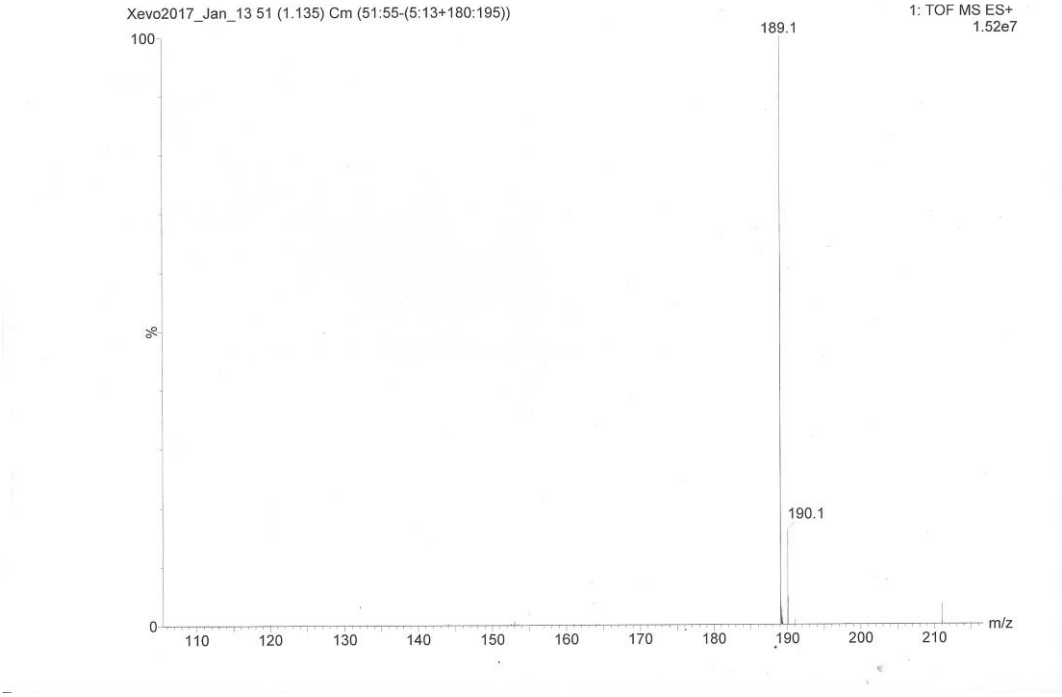


Figure S3.31: Mass spectrum of **L3**

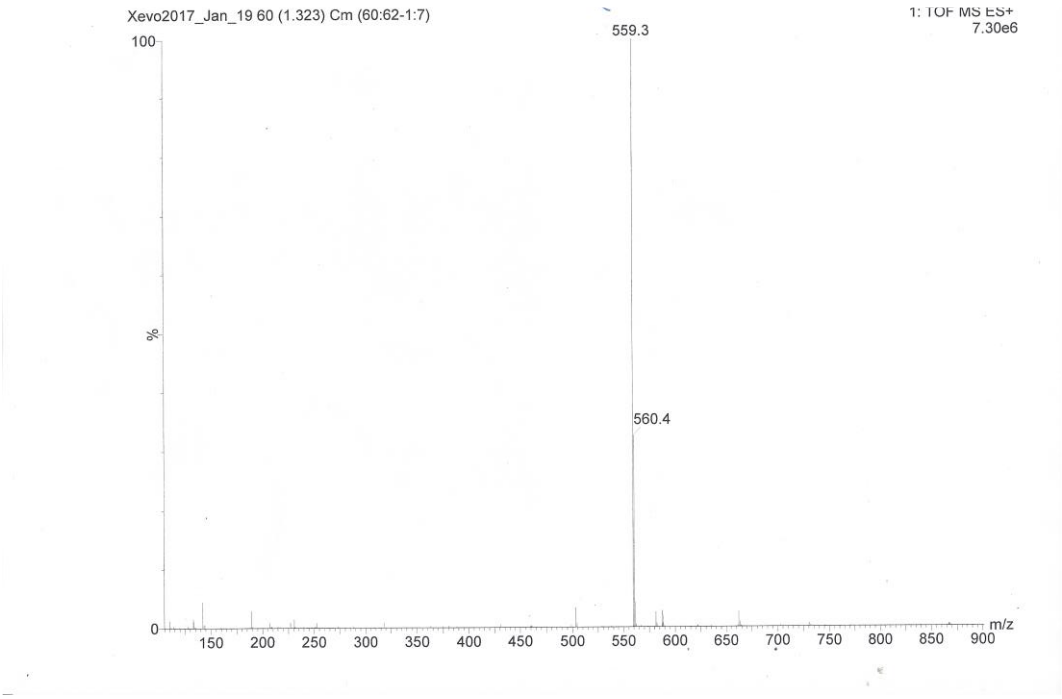


Figure S3.32: Mass spectrum of **L4**

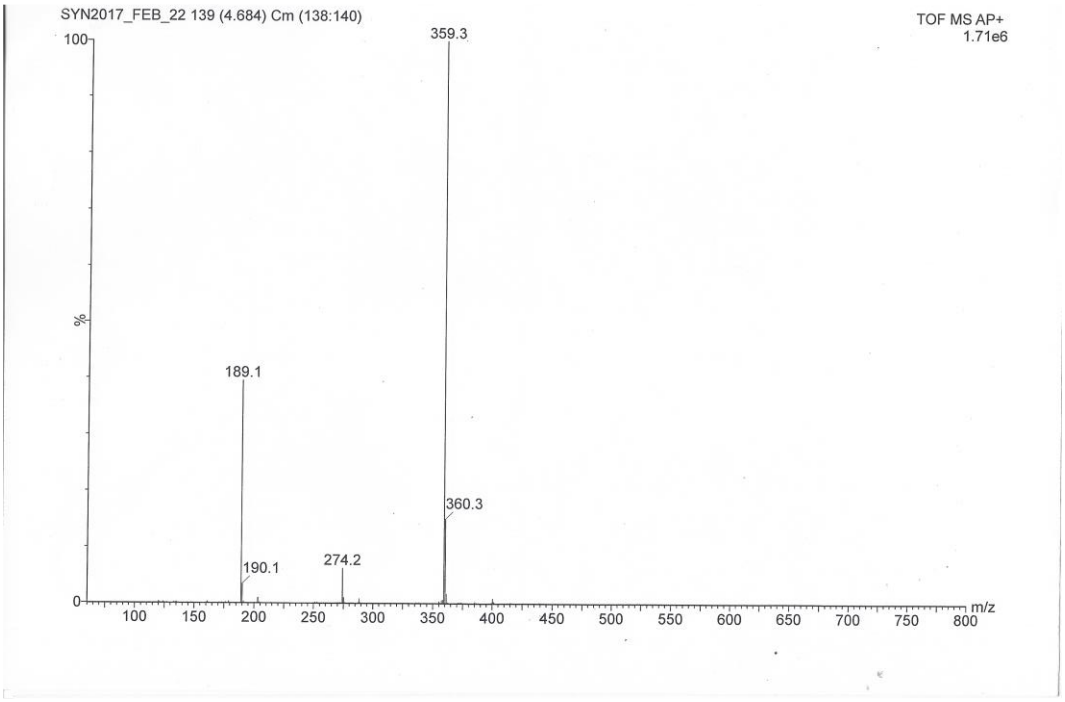


Figure S3.33: Mass spectrum of **L5**

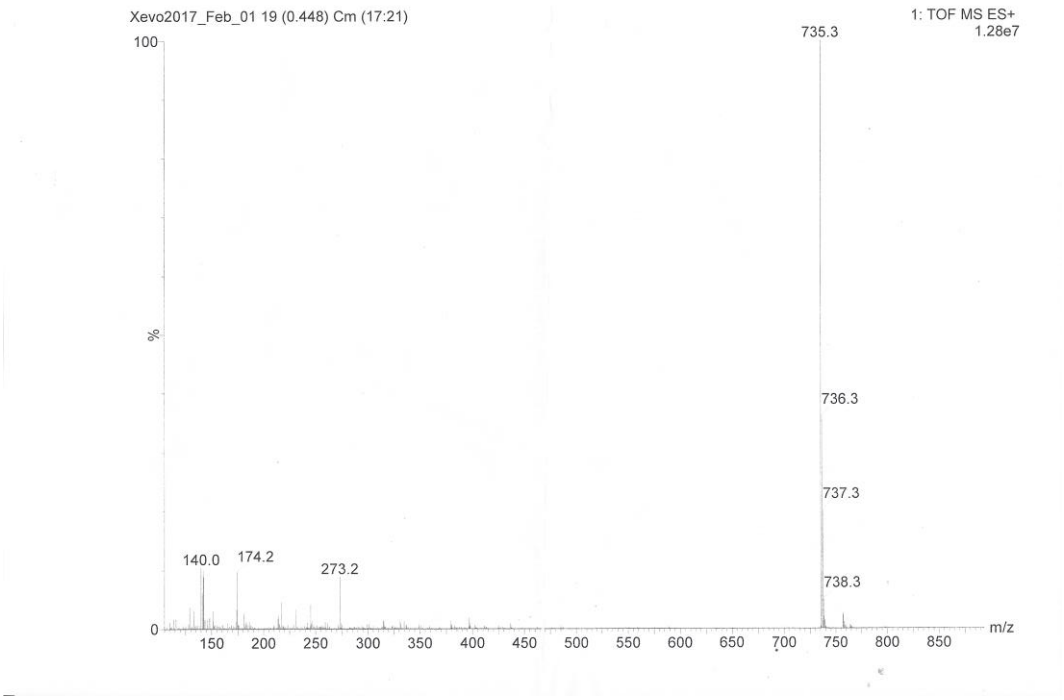


Figure S3.34: Mass spectrum of **bpySS**

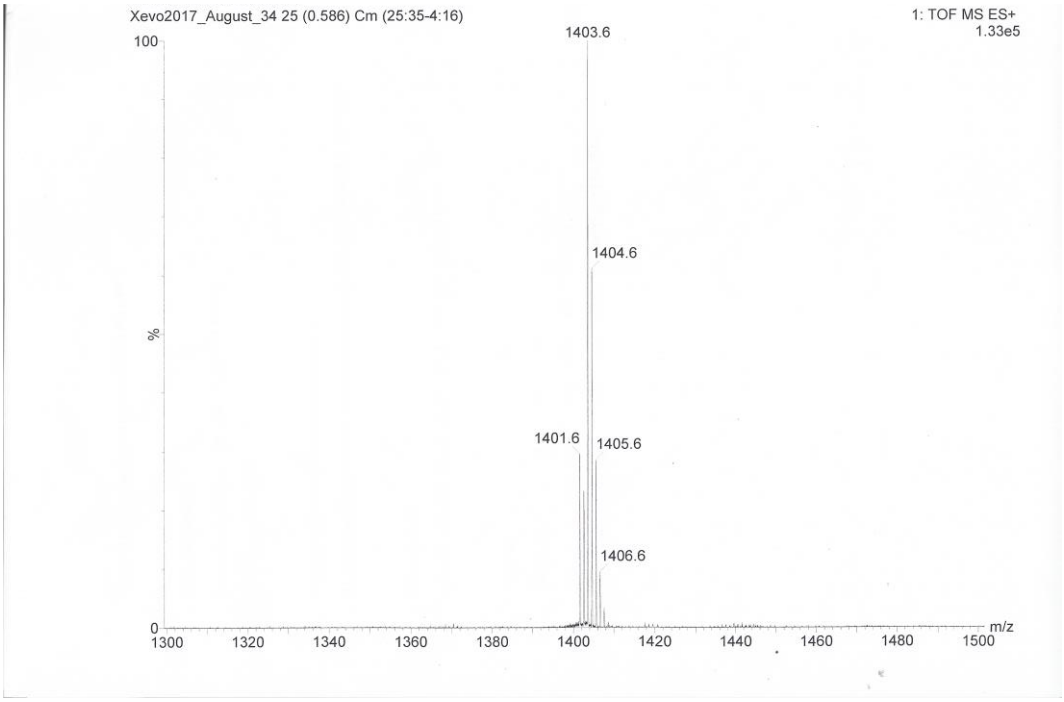


Figure S3.35: Mass spectrum of **IrC6bpySS**

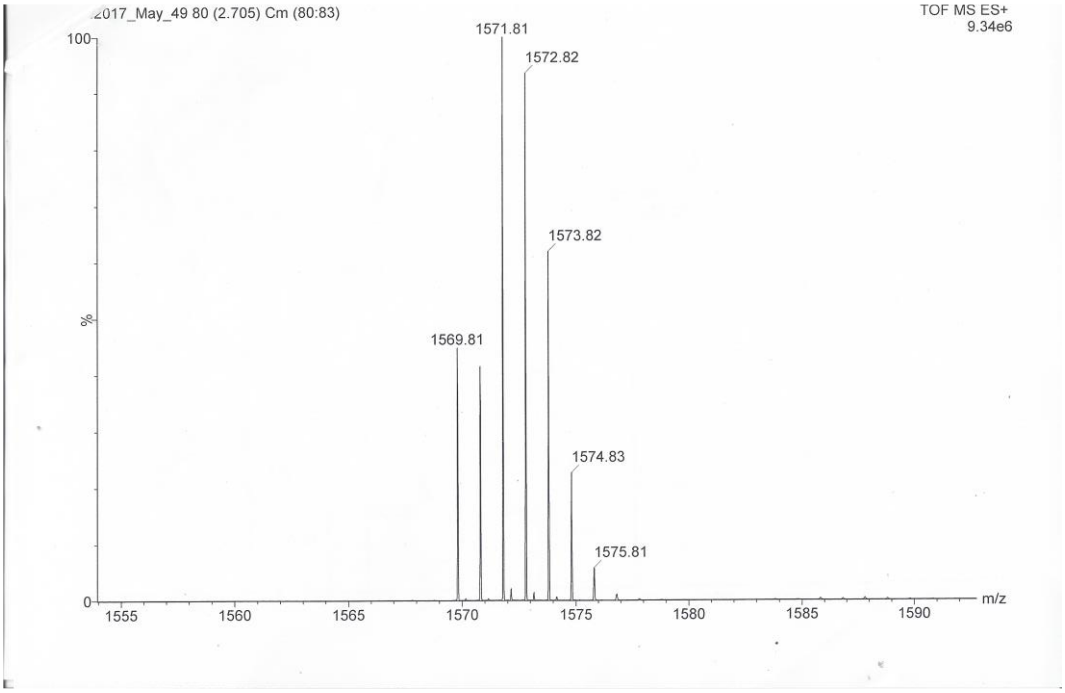


Figure S3.36: Mass spectrum of **IrC12bpySS**

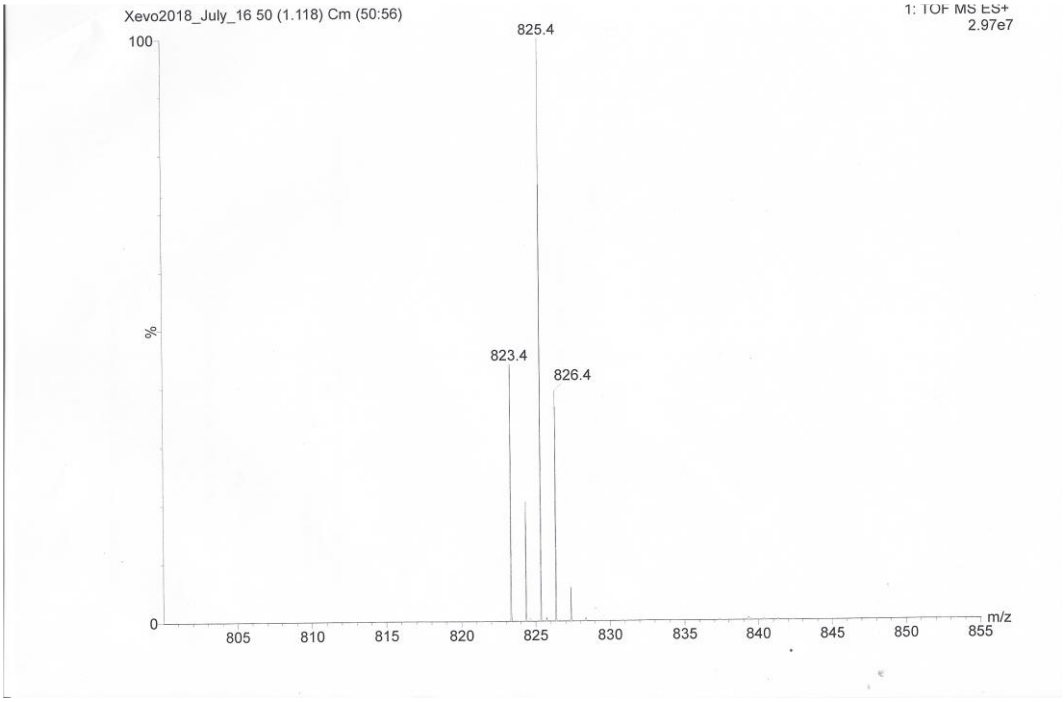


Figure S3.37: Mass spectrum of **IrC6bpy**

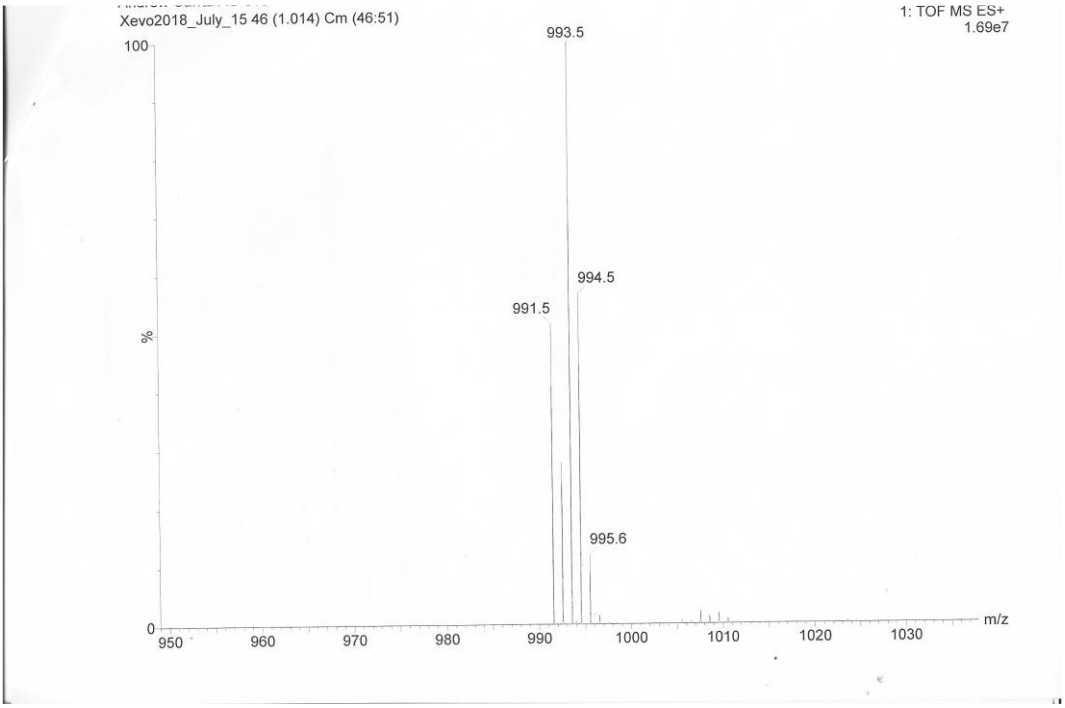


Figure S3.38: Mass spectrum of **IrC12bpy**

Luminescent lifetime decay curves

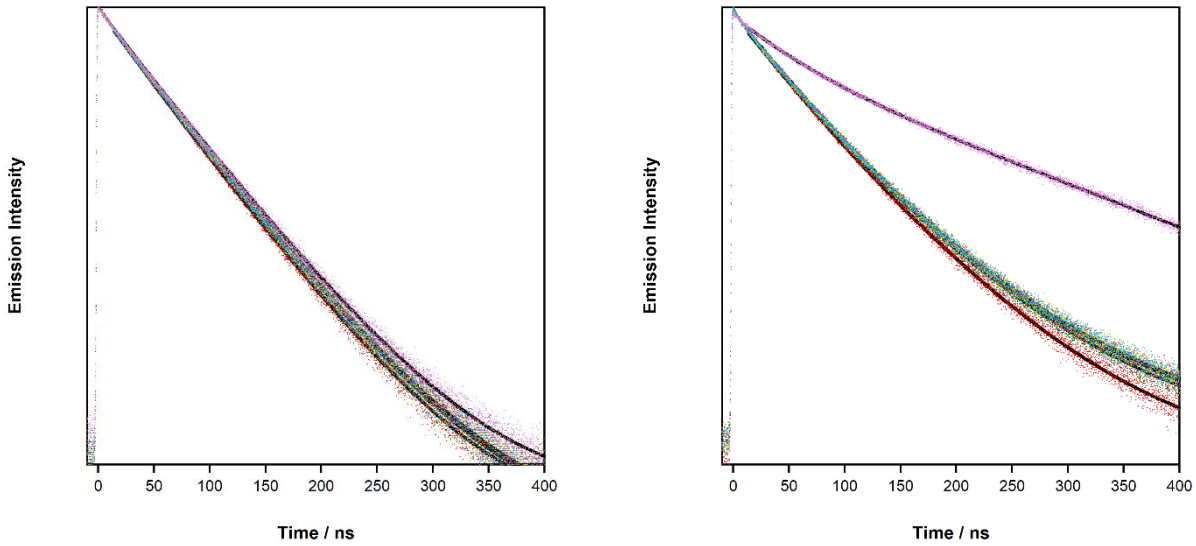


Figure S3.39: Luminescent lifetime decay curves of (left) IrC6bpy and (right) IrC12bpy in 1:1 MeOH:H_2O solutions with increasing concentrations of PFOA, concentrations of PFOA added for both complexes match those given for the **bpySS** analogues in Figure 3.32

XPS spectra

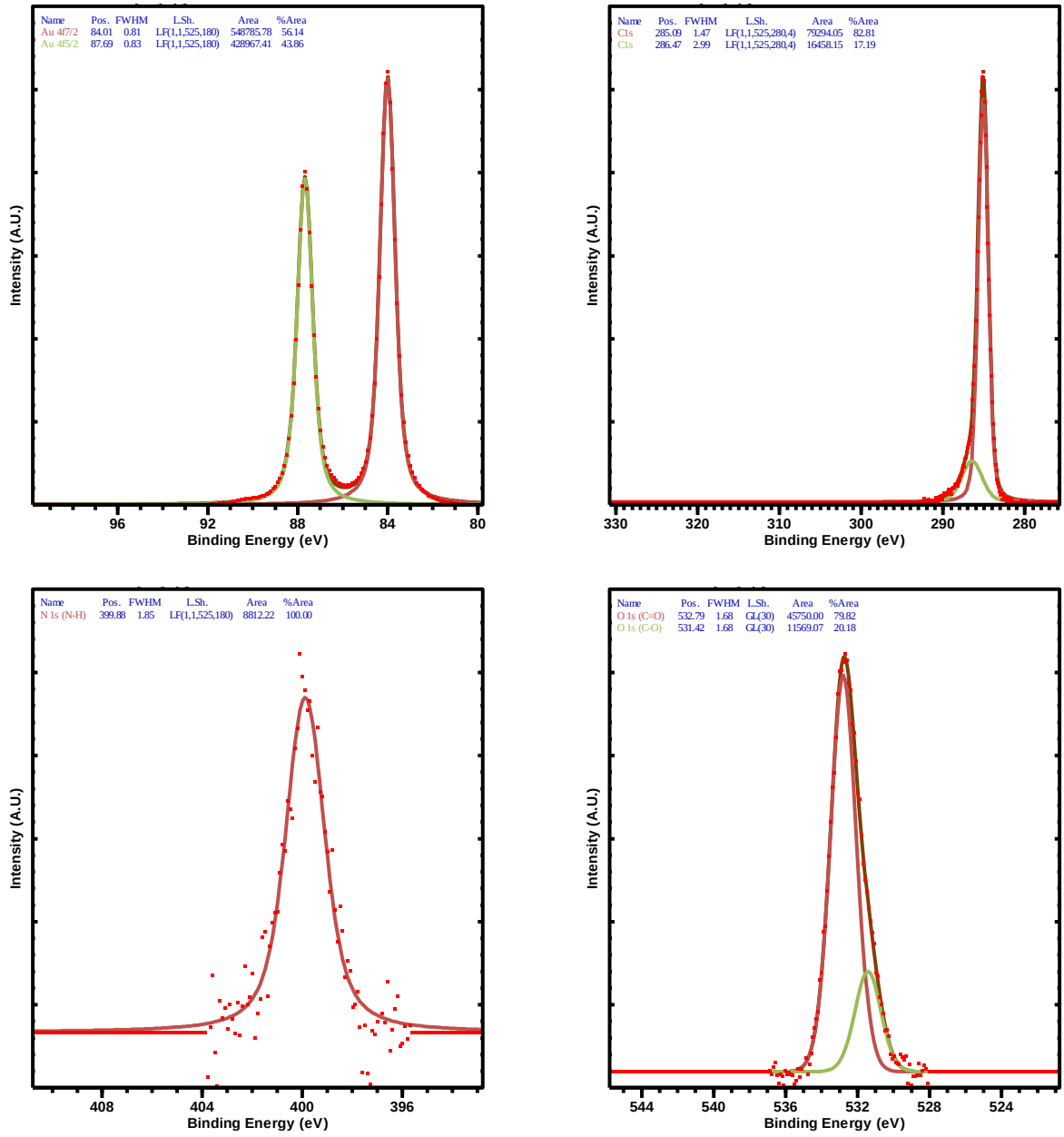


Figure S3.40: XPS spectra taken for Au surfaces coated with **IrC6bpySS** displaying the energy regions of (top, left) Au 4f, (top, right) C1s, (bottom, left) N1s and (bottom, right) O1s

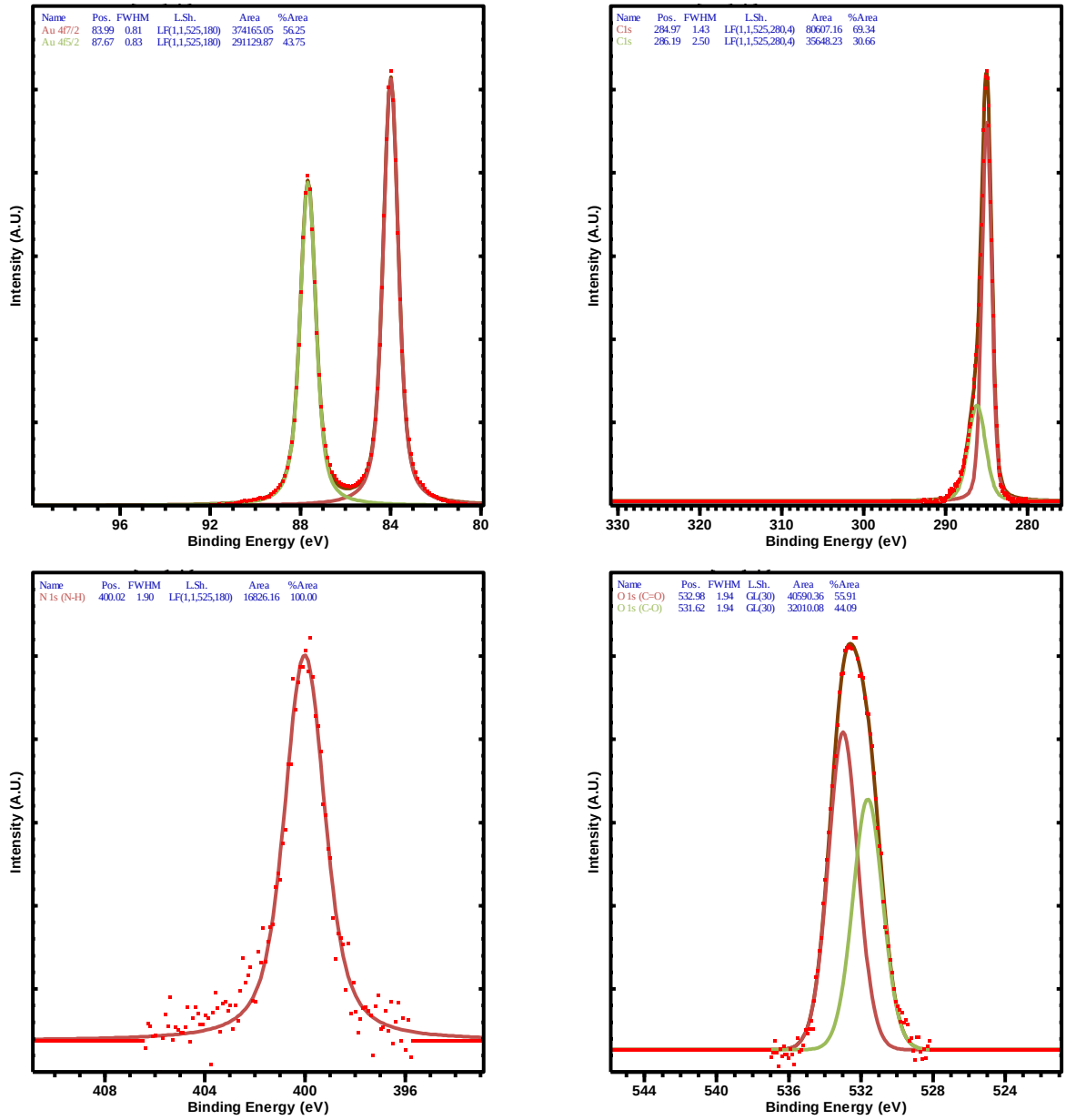


Figure S3.41: XPS spectra taken for Au surfaces coated with **IrC12bpySS** displaying the energy regions of (top, left) Au 4f, (top, right) C1s, (bottom, left) N1s and (bottom, right) O1s

77K emission

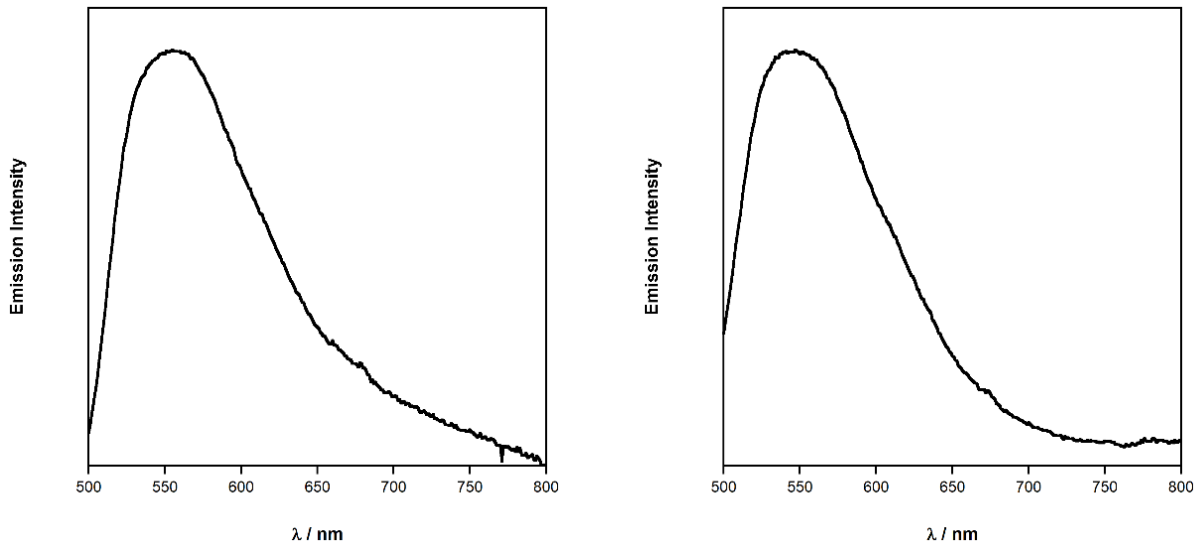


Figure S3.42: Emission spectra collected at 77 K for (left) IrC6bpySS and (right) IrC12bpySS, in a 4:1 EtOH:MeOH glass, λ_{exc} = 310 nm

5.3 Conferences Attended

Poster: *Optical Sensing of Environmentally Harmful Fluorosurfactant Molecules on Surfaces Decorated with Luminescent Metal Complexes and Surfactant*, ISPPCC, Hong Kong, 2019

Oral: *Sugar Sensing via an iridium(III) Complex, through Photoluminescence and Electrochemiluminescence*, PhotoUK-IT joint Italian-UK Photophysics Conference, Lipari, Italy, 2019

Oral: *Surface Bound Ir(III) Sensors for Environmentally Harmful Fluorosurfactants*, RSC Photochemistry Conference, Swansea, UK, 2018

Poster: *Sensing of Biomolecules with Ir(III) sensors*, European Biological Inorganic Chemistry Conference, Birmingham, UK, 2018

Poster: *Luminescent Ir(III) Compounds for Fluorosurfactant Sensing*, PhotoIUPAC, Dublin, Republic of Ireland, 2018

Poster: *Luminescent Metal Complexes on Surfaces for Sensing of Biomolecules*, Applications of photoactive coordination compounds, St. Andrews, 2017

5.4 Publications

1. Dita Davis*, Andrew J. Carrod*, Zhilin Guo, Benson M. Kariuki, Yuan-Zhu Zhang and Zoe Pikramenou, *Inorg. Chem.*, 2019, **58**, 13268. *Authors contributed equally to this work
2. Samuel J. Adams, Andrew J. Carrod, Luke A. Rochford, Marc Walker and Zoe Pikramenou, *ChemistrySelect,* 2018*,* **3**, 3251.
3. Siobhan M. King, Sunil Claire, Rodolfo I. Teixeira, Abiola N. Dosumu, Andrew J. Carrod, Hamid Dehghani, Michael J. Hannon, Andrew D. Ward, Roy Bicknell, Stanley W. Botchway, Nikolas J. Hodges and Zoe Pikramenou, *J. Am. Chem. Soc.*, 2018*,* **140**, 10242.